To the Graduate Council:

I am submitting herewith a thesis written by Ye-Lin Shen entitled "Microstructural and Hardness Evaluation of $Ni_4Mo$ Alloy with Aluminum Additions." I have examined the final copy of this thesis for form and content and recommend that it be accepted in partial fulfillment of the requirements for the degree of Master of Science, with a major in Metallurgical Engineering.

Charlie R. Brooks

Charlie R. Brooks, Major Professor

We have read this thesis and
recommend its acceptance:

Dan T. Allen

R. A. Buchanan

Accepted for the council:

Associate Vice Chancellor and
Dean of the Graduate School

# Microstructural and Hardness Evaluation of $Ni_4Mo$ Alloy with Aluminum Additions

A Thesis
Presented for the
Master of Science
Degree
University of Tennessee, Knoxville

Ye-Lin Shen
August 1996

# DEDICATION

This thesis is dedicated to the following family members,

my husband, Cong Yue Qiao

my son, Jonathan Y. Qiao

My parents, and my parents in-laws

without their love, support and patience, it would not have been possible.

# ACKNOWLEDGMENTS

The author would like to express her greatest appreciation to her major advisor, Dr. Charlie R. Brooks, for his advice, inspiration, encouragement, guidance, and support throughout this investigation. The work could not have been accomplished without his continued support. The author also like to express her deep appreciation to Dr. Ben F. Oliver and Dr. Raymond A. Buchanan for their continued advice, support and encouragement during the course of the work. The author gratefully acknowledges Dr. Eugene E. Stansbury for his interest in the topic and many good discussions.

The author wishes to acknowledge Dr. Edward A. Kenik and Dr. Neal D. Evans for their support and assistance during the TEM examination experiments and much excellent advise. The support through the SHaRE program operated at Oak Ridge National Laboratory, which provides the research facilities and makes it possible to obtain many unique results through this study, is appreciated.

The author also like to thank all the staff members of the Materials Science and Engineering Department and Chemical Engineering Department for their encouragement and assistance whenever the author needed help.

Last, but not the least, the author appreciates the assistance obtained from her colleague graduate students for their help during experimental work namely, Mr. Tim Newport, Mr. Michael Strauss, Dr. Ping Li, and Mr. Robert Perrier.

# ABSTRACT

The Ni-20 at.% Mo alloy, here referred to as $Ni_4Mo$, is a single phase face-centered cubic structure ($\alpha$) above 868°C; below this temperature it becomes long-range ordered ($\beta$). The conversion of $\alpha$ to $\beta$ (ordering reaction) on cooling or by other heat treatment causes a marked increase (e.g., doubling) in the hardness and yield strength. However, extreme embrittlement also occurs. A major purpose of the present study was to see if the addition of moderate amount of aluminum would prevent the embrittlement yet retain the strengthening during ordering. Aluminum was chosen because if might allow the alloys to retain the good corrosion resistance of $Ni_4Mo$.

The alloys studied were the base $Ni_4Mo$ alloy and $Ni_4Mo$ with addition of 2, 5, 7, and 9 at.% aluminum. All samples were small arc melted buttons. They were solution heat treated at 1280°C for 50 hours in quartz tubes filled with argon, then quenched by breaking the tube under water. Samples were then aged at 600, 650, 700, 750, 850, and 950°C for up to 100 hours. Microhardness was measured and ductility was examined by bending thin slices. The microstructures were evaluated using optical, scanning electron and transmission electron microscopy. Corrosion resistance was evaluated using cyclic anodic polarization and polarization resistance testing.

A major finding was that aluminum increased considerably the hardness for all aging treatment and for all alloys (a maximum of about 650 HV after aging the 5, 7, and 9 at.% Al alloys for 100 hours at 700°C), but did not prevent embrittlement. However, in the solution heat treated condition the hardness of the 9 at.% Al alloy (440 HV) was approximately double that of the $Ni_4Mo$ alloy (220 HV), and good ductility was retained.

$Ni_4Mo$ and 7 at.% Al alloys possesses good corrosion resistance in 14% hydrochloric solution with air condition.

The specific results are summarized in the list below.

Hardness Measurements

1. For the same heat treatments (with minor exceptions), the hardness of the 2 at.% Al alloy was the same as the base $Ni_4Mo$ alloy.
2. The hardness increased with increasing Aluminum contents from 5, 7, and 9 at.% aluminum for all heat treatments.
3. The maximum hardness (about 650 HV Vickers) was attained in the 5, 7 and 9 at.% Al alloys after aging for 100 hours at 700°C.
4. Upon aging at 750°C, the hardness for all alloy increased significantly (approximately doubled) after 10 hours, then increased about another 20% upon aging for 50 hours, then remained the same after 50 hours (100 hours total).

Microstructural Examination

1. The binary $Ni_4Mo$ alloy was SRO $\alpha$ in the as-quenched condition, prior to aging. For all the aging treatment, the $\alpha$ was converted to a domain structure of long-range order $\beta$. For some treatments, there was grain boundary migration, with accompanying domain growth. In come regions, the migration was accompanied by the precipitation of $\gamma$, showing that the composition of the base alloy was slightly to the Mo-rich side of the stoichiometric $Ni_4Mo$.
2. The optical light microscopy observation indicated that the aluminum alloys were single phase in the as-quenched condition. However, transmission electron microscopy revealed that the short-range order $\alpha$ was retained. Apparently

aluminum enhances the kinetics of the decomposition of $\alpha$, and the quenched structures consisted of a very fine domain structure of the nonequilibrium phases $DO_{22}$ and $Ni_2Mo$. This was the starting structure for the aging treatment of all the alloys.

3. The identification of the microstructures and the phases in them is based on the optical light, scanning electron and transmission electron microscopy observations. The results are summarized in Table 4-13.

(a) Aging at 750°C for 10, 50 and 100 Hours

The 2 at.% Al alloy progressed from a fine domain structure of SRO $\alpha$ + $DO_{22}$ to a fine domain structure of $\beta$ plus the nonequilibrium phases $DO_{22}$ and $Ni_2Mo$.

The 5 at.% Al alloy progressed from a fine domain structure of the nonequilibrium $DO_{22}$ phase to the formation of a lamellar structure of $\gamma$ and $\gamma'$ forming from the grain boundaries. The $DO_{22}$ matrix changed to a fine domain structure of $DO_{22}$ and $Ni_2Mo$.

The 7 and 9 at.% Al alloys progressed from an initial structure of fine domains of the nonequilibrium phases $DO_{22}$ and $Ni_2Mo$ to a lath structure of $\gamma$ and $\gamma'$ growing from the grain boundaries. The remaining matrix formed a fine tweed structure of $Ni_2Mo$ and $DO_{22}$ phases.

(b) Aging for 100 Hours at 600, 650, 700, 750, 850 and 950°C

At 650°C, the $Ni_4Mo$ alloy consisted of a matrix of fine β domains. There was some discontinuous precipitation of γ associated with grain boundary migration. At 750°C the structure was all fine domains of β. The precipitation of γ distributed in matrix.

The 2 at.% Al alloy showed little change in the structure until 750°C, where fine domains of β formed in the $DO_{22}$ + $Ni_2Mo$ matrix. Some δ particles appeared. At 850°C, the matrix was fine domains of the $DO_{22}$ structure, and a lath structure began to form from the grain boundaries. At 950°C, the matrix was SRO α.

The 5 at.% Al alloy consisted of only a fine domain structure of $DO_{22}$ phase. At 650°C, the matrix consisted of fine domains of $DO_{22}$ and $Ni_2Mo$, and a lamellar structure of γ and γ' began to form from the grain boundaries. At 700°C and 750°C, the entire structure was lamellar. At 850°C and 950°C, the needle-like structure of γ formed and particles of δ distributed along grain boundaries.

The 7 at.% Al alloy, after aging at 600 and 650°C, had a structure similar to that of the 5 at.% Al alloy. At 750°C, the matrix consisted of the fine domains of the $Ni_2Mo$ and $DO_{22}$ phases, and a lamellar γ + γ' structure had formed from the grain boundaries. At 850°C and 950°C, microstructure is same as that of the 5 at % Al alloy.

The 9 at.% Al alloy was only aged at 600, 700 and 750°C. At 600°C and 700°C, the matrix was a fine domain structure of $DO_{22}$ and $Ni_2Mo$ phases. There were some δ laths present and some pure Mo particles. At 750°C, the matrix was a fine domain structure of $DO_{22}$ and $Ni_2Mo$. A lamellar structure of $\gamma + \gamma'$ had formed from the grain boundaries. Some Mo rich particles was found along grain boundaries.

Fractographic Evaluation

1. In the solution heat treated at 1250°C and aging at 950°C conditions, alloys were ductile.
2. Based on the bend tests, all alloys were brittle in the aged at 750°C for 100 hours. In the matrix, fracture occurred along the high angle, former α boundaries. In the alloys in which the lamellar structure had formed from the grain boundaries, cracking occurred along the location of the original a boundaries. In the 7 and 9 at.% Al alloys, some cracks crossed through the lamellar structure. In the lamellar structure, cracking occurred mainly by interphase interface separation, but there was some cleavage across the phases.

Corrosion Resistance Evaluation

1. In general, the corrosion rate of all alloys was in the acceptable range based on a calculated surface loss rate.
2. The corrosion rate of $Ni_4Mo$ and 7 at.% Al alloys was in a range of 5-20 mils per year which is considered good corrosion resistance. The corrosion rate of 2, 5 and 9 at.% Al alloys was in a range of 20-50 mils per year which is considered fair corrosion resistance.

3. Aluminum can influence the phase transformation and also changed the corrosion rate in Ni-Mo-Al alloy.

# TABLE OF CONTENTS


| CHAPTER | | | PAGE |
|---|---|---|---|
| 1. | INTRODUCTION | | 1 |
| 2. | LITERATURE REVIEW | | 4 |
| | 2.1 | Hastelloy Alloy Systems | 4 |
| | 2.2 | Nickel-Molybdenum Alloys | 7 |
| | 2.3 | Physical and Mechanical Properties of Ni-Mo Alloys | 9 |
| | 2.4 | Ordered and Disordered Structure in Ni-20 at.% Mo Alloys | 26 |
| | 2.5 | The Effect of Alloy Elements in Ni-Base Alloys | 28 |
| | 2.6 | Heat Treatment | 31 |
| | 2.7 | Microstructural Evaluation | 33 |
| | 2.8 | X-Ray and Electron Diffraction | 35 |
| | 2.9 | Corrosion Resistance Evaluation | 38 |
| 3. | MATERIALS AND EXPERIMENTAL PROCEDURES | | 41 |
| | 3.1 | Chemical Composition | 41 |
| | 3.2 | Materials Fabrication | 42 |
| | 3.3 | Heat Treatment | 44 |
| | 3.4 | Microhardness Measurement | 44 |
| | 3.5 | Optical Light Microscopic (OLM) Evaluation | 46 |
| | 3.6 | Scanning Electron Microscopy (SEM) and Energy Disperse Spectrometer (EDS) Investigation | 47 |
| | 3.7 | Fractographic Study Using SEM and EDS | 47 |
| | 3.8 | Transmission Electron Microscopy (TEM) | 48 |
| | 3.9 | Corrosion Resistance Evaluation | 52 |
| 4. | RESULTS AND DISCUSSION | | 58 |
| | 4.1 | Hardness Measurements | 58 |
| | 4.2 | Optical Light Microscopic (OLM) Microstructural Evaluation in $Ni_4Mo$ and Ni-Mo-Al Alloys | 68 |

4.3 Scanning Electron Microscopy (SEM) Microstructural Evaluation ..... 112
4.4 Fracture Surface Topology Investigation ..... 164
4.5 Transmission Electron Microscopy (TEM) Microstructure and Electron Diffraction Pattern Analysis ..... 183
4.6 Corrosion Resistance Evaluation ..... 249

5. CONCLUSIONS AND RECOMMENDATIONS ..... 263
5.1 Conclusion ..... 263
5.2 Recommendations ..... 265

REFERENCES ..... 266
VITA ..... 275

# LIST OF TABLES


Table 2-1. Nominal chemical compositions (wt.%) of some typical nickel-base alloys [8] ..... 6

Table 3-1. Chemical composition (at.%/wt.%) of the $Ni_4Mo$ alloy studied ..... 41

Table 3-2. Composition of laboratory Ni-Mo-Al alloys (at.%/wt.%) ..... 42

Table 3-3. Heat treatment conditions employed ..... 45

Table 3-4. Etching solution for OLM microstructural study ..... 46

Table 3-5. Chemical composition (wt.%) of the Hastelloy B2 alloy studied ..... 50

Table 3-6. Jet polishing solution 1 ..... 51

Table 3-7. Jet polishing solution 2 ..... 51

Table 4-1. Microstructure feature as reviewed by OLM examination in alloys in all aging conditions ..... 114

Table 4-2. SEM examination of phase transformation of alloys in all aging conditions ..... 165

Table 4-3. The microstructure of Ni-Mo-Al alloys after solution treated (1250°C, 50 hours) and water quenched ..... 197

Table 4-4. The microstructure of Ni-Mo-Al alloys aged at 600°C ..... 202

Table 4-5. The microstructure of Ni-Mo-Al alloys aged at 650°C ..... 207

Table 4-6. The microstructure of Ni-Mo-Al alloys aged at 750°C for 10 hours ..... 209

Table 4-7. The microstructure of Ni-Mo-Al alloys aged at 750°C for 50 hours ..... 216

Table 4-8. Chemical composition of the lamellar structures in Figure 4-130 ..... 218

Table 4-9. The microstructure of Ni-Mo-Al alloys aged at 750°C for 100 hours ..... 226

Table 4-10. The microstructure of Ni-Mo-Al alloys aged at 850°C hours..... 228

Table 4-11. Chemical composition of precipitates ..... 230

Table 4-12. The microstructure of Ni-Mo-Al alloys aged at 950°C..... 233

Table 4-13. Summary examination of phase transformation in alloys ..... 234

Table 4-14. Microstructural feature in Hastelloy B2 alloys ..... 249

Table 4-15. Anodic polarization parameter measurement in $Ni_4Mo$ alloy ..... 252

Table 4-16. Summary of polarization resistance results (average values based on 2 to 4 independent tests for each alloy) ..... 262

# LIST OF FIGURES


Figure 2-1. Ni-Mo phase diagram and phases [2, 14] ..... 8

Figure 2-2. Specific heat of Ni-20 at.% Mo, slowly cooled and quenched from 950°C [17] ..... 10

Figure 2-3. Electrical resistivity-temperature relationship for Ni-20 at.% Mo in three initial conditions [18] ..... 11

Figure 2-4. Thermal expansion of 6.4, 11.9, and 20 at.% Mo alloys [2] ..... 13

Figure 2-5. Effect of Mo content on yield strength of α-phase alloys [2] ..... 13

Figure 2-6. The effect of aging temperature and time on the 0.2% yield strength of Hastelloy B2 alloy [20] ..... 14

Figure 2-7. The effect of aging temperature and time on the tensile elongation of Hastelloy B2 alloy [20] ..... 14

Figure 2-8. The effect of aging time and temperature on hardness for two different initial α grain sizes of Hastelloy B2 alloy [22] ..... 16

Figure 2-9. Tensile properties of solution annealed Hastelloy B alloy as a function of temperature [23] ..... 17

Figure 2-10. Tensile properties (at 25°C) of Hastelloy B Alloy as a function of aging time and temperature [23] ..... 18

Figure 2-11. (a) The amount of recrystallization versus aging time for 43% cold worked material, (b) Arrhenius plot based on the time 50% recrystallization from the curves in (a) [24] ..... 20

Figure 2-12. The effect of the amount of cold work on the hardness of α in the Ni-20 at.% Mo alloy [25] ..... 21

Figure 2-13. The effect of aging time at 850°C on the hardness of the Ni-20 at.% Mo alloy initially in the cold worked α condition [25] ..... 21

Figure 2-14. The effect of aging time at 850°C on the hardness of the Ni-20 at.% Mo alloy initially in the cold worked α condition [25] ..... 22

Figure 2-15. The effect of aging time at 775°C on the hardness of the Ni-20 at.% Mo alloy initially in the cold worked α condition [25] ..... 22

Figure 2-16. The effect of aging time at 700°C on the hardness of the Ni-20 at.% Mo alloy initially in the cold worked α condition [25] ..... 23

Figure 2-17. Summary of the structure changes which occur during aging cold worked α at 850°C [27] ..... 25

Figure 2-18. Summary of the structure changes which occur during aging cold worked α at 700°C [27] ..... 25

Figure 2-19. Crystal structure of β phase ($Ni_4Mo$) [2] ..... 27

Figure 2-20. β-lattice with relationship between FCC α-lattice and bct ordered lattice; positions of Mo atoms in adjacent planes indicated by x [2] ..... 29

Figure 2-21. Effect of ordering in $Ni_4Mo$ on room temperature tensile ductility: (a) dependence of ductility on exposure time at 700°C for alloys free of boron and (b) effect of boron content on the ductility of alloy ordered to $Ni_4Mo$ alloy.[33] ..... 32

Figure 2-22. Isothermal time-temperature-transformation diagram for ordering reaction in Ni-20 at.% Mo [2] ..... 34

Figure 2-23. Ordered phase in $Ni_4Mo$ alloy [18] ..... 36

Figure 2-24. [001] electron diffraction pattern form a Ni-20 at.% Mo alloy [47] ..... 37

Figure 2-25. Comparative behavior of several nickel-base alloys in pure $H_2SO_4$ [49] ..... 39

Figure 2-26. Comparative isocorrosion plots of various nickel-base alloys in hydrochloric solution [49] ..... 40

Figure 3-1. Samples sealed in a quartz tube and ready for a heat treatment..... 43

Figure 3-2. (a) Schematic diagram of the three-point bending-fixture used to initiate cracking, (b) The real bending-fixture..... 49

Figure 3-3. (a) The specimen was deformed into the U shape with a designed fixture, (b) Schematic diagram of the U-bend test working circuit..... 55

Figure 3-4. (a) Schematic diagram of electrochemical polarization cell, (b) Schematic diagram of the electrochemical polarization working circuit..... 57

Figure 4-1. The hardness as a function of aluminum content in as-cast condition, aged at 650°C and 750°C without solution heat treatment and homogenization treatment at 1250°C..... 60

Figure 4-2. The hardness as a function of aging at 650°C and 750°C for 100 hours in the as-cast condition (without homogenization treatment) and solution heat treatment at 1250°C for 50 hours with different aluminum content..... 61

Figure 4-3. The hardness as a function of aluminum content at different aging temperature for 100 hours (solution heat treated at 1280°C for 50 hours), and solution heat treated at 1250°C for 50 hours..... 63

Figure 4-4. The hardness as a function of aluminum content aged at 750°C for different times..... 64

Figure 4-5. Hardness as a function of aging temperature for 100 hours in samples with different aluminum contents..... 66

Figure 4-6. Hardness as a function of aging time at 750°C with different aluminum contents..... 67

Figure 4-7. OLM microstructure of $Ni_4Mo$ alloy (as-received condition) aged at 750°C for 100 hours showing β recrystallization and β phase..... 70

Figure 4-8. OLM microstructure of 2 at.% Al alloy in as-cast condition (no homogenization) aged at 750°C for 100 hours showing dendritic structure at low magnification..... 70

Figure 4-9. OLM microstructure of 9 at.% Al alloy in as-cast condition (no homogenization) aged at 750°C for 100 hours showing dendirtic structure at low magnification..... 71

Figure 4-10. OLM microstructure of 2 at.% Al alloy in as-cast condition (no homogenization) aged at 750°C for 100 hours showing coarse lamellar structure..... 71

Figure 4-11. OLM microstructure of 5 at.% Al alloy in as-cast condition (no homogenization) aged at 750°C for 100 hours showing dark and bright regions..... 72

Figure 4-12. OLM microstructure of 7 at.% Al alloy in as-cast condition (no homogenization) aged at 750°C for 100 hours showing dark and bright regions..... 72

Figure 4-13. OLM microstructure of 9 at.% Al alloy in as-cast condition (no homogenization) aged at 750°C for 100 hours showing lamellar structure, dark and bright regions..... 73

Figure 4-14. OLM microstructure of $Ni_4Mo$ alloy at as-received condition (hot forged) single $\alpha$ phase with annealing twins..... 73

Figure 4-15. OLM microstructure of $Ni_4Mo$ alloy homogenized at 1250°C for 50 hours showing single $\alpha$ phase with annealing twins..... 75

Figure 4-16. Ni-Mo-Al ternary alloy phase diagram at 1260°C [65]..... 76

Figure 4-17. OLM microstructure of 2 at.% Al alloy homogenized at 1250°C for 50 hours showing single $\alpha$ phase with annealing twins..... 77

Figure 4-18. OLM microstructure of 5 at.% Al alloy homogenized at 1250°C for 50 hours showing single $\alpha$ phase with annealing twins..... 77

Figure 4-19. OLM microstructure of 7 at.% Al alloy homogenized at 1250°C for 50 hours showing single $\alpha$ phase with annealing twins..... 78

Figure 4-20. OLM microstructure of 9 at.% Al alloy homogenized at 1250°C for 50 hours showing particles along grain boundaries and in matrix..... 78

Figure 4-21. OLM microstructure of 2 at.% Al alloy aged at 600 °C for 100 hours showing single α phase..... 80

Figure 4-22. OLM microstructure of 5 at.% Al alloy aged at 600 °C for 100 hours showing single α phase ..... 80

Figure 4-23. OLM microstructure of 7 at.% Al alloy aged at 600°C for 100 hours showing grain boundary migration and secondary phase starting to form along the grain boundaries, (a) 200X, (b) 400 X..... 81

Figure 4-24. OLM microstructure of 9 at.% Al alloy aged at 600°C for 100 hours showing lamellar structure, particles and grain boundaries migration, (a) 400X, (b) 1000X..... 82

Figure 4-25. OLM microstructure of $Ni_4Mo$ alloy aged at 650°C for 100 hours showing β domain phase formation along the primary grain boundaries..... 85

Figure 4-26. OLM microstructure of 2 at.% Al alloy aged at 650°C for 100 hours showing shingle phase with intergranular cracking..... 85

Figure 4-27. OLM microstructure of 5 at.% Al alloy aged at 650°C for 100 hours showing lamellar structure with intergranular cracking..... 86

Figure 4-28. OLM microstructure of 7 at.% Al alloy aged at 650°C for 100 hours showing grain boundary migration with secondary phases nucleated along the grain boundaries and grains..... 86

Figure 4-29. Ni-Mo-Al ternary alloy phase diagram at 700°C [65]..... 88

Figure 4-30. OLM microstructure of 2 at.% Al alloy aged at 700°C for 100 hours showing single phase with intergranular cracking..... 89

Figure 4-31. OLM microstructure of 5 at.% Al alloy aged at 700°C for 100 hours showing lamellar structure..... 89

Figure 4-32. OLM microstructure of 7 at.% Al alloy aged at 700°C for 100 hours showing phase transformation along grain boundaries..... 90

Figure 4-33. OLM microstructure of 9 at.% Al alloy aged at 700°C for 100 hours showing (a) particles precipitation, (b) lamellar structure with particles..... 91

Figure 4-34. OLM microstructure of $Ni_4Mo$ alloy aged at 750°C for 10 hours showing Widmanstatten pattern β phase..... 93

Figure 4-35. OLM microstructure of 2 at.% Al alloy aged at 750°C for 10 hours showing single α phase..... 93

Figure 4-36. OLM microstructure of 5 at.% Al alloy aged at 750°C for 10 hours showing lamellar structure with intergranular cracking ..... 94

Figure 4-37. OLM microstructure of 7 at.% Al alloy aged at 750°C for 10 hours showing grain boundary migration and phase transformation along the grain boundaries..... 94

Figure 4-38. OLM microstructure of $Ni_4Mo$ alloy aged at 750°C for 50 hours showing Widmanstatten pattern β and grain boundary migration..... 95

Figure 4-39. OLM microstructure of 2 at.% Al alloy aged at 750°C for 50 hours showing phase transformation along the grain boundaries..... 97

Figure 4-40. OLM microstructure of 5 at.% Al alloy aged at 750°C for 50 hours showing lamellar structure..... 97

Figure 4-41. OLM microstructure of 7 at.% Al alloy aged at 750°C for 50 hours showing lamellar structure formation along the grain boundaries..... 98

Figure 4-42. OLM microstructure of $Ni_4Mo$ alloy aged at 750°C for 100 hours showing (a) widmanstatten pattern β phase and coarse β associated with grain boundary migration, (b) coarse β along grain boundaries, (c) Widmanstatten pattern β phase..... 98

Figure 4-43. OLM microstructure of 2 at.% Al alloy aged at 750°C for 100 hours showing (a) single phase with annealing twins, (b) high magnification of secondary phases formation ..... 100

Figure 4-44. OLM microstructure of 5 at.% Al alloy aged at 750°C for 100 hours showing (a) lamellar structure, (b) coarsening lamellar structure formed along grain boundaries..... 102

Figure 4-45. OLM microstructure of 7 at. % Al alloy aged at 750°C for 100 hours showing (a) lamellar structure formation along grain boundaries, (b) coarse structure starting to form along grain boundaries..... 103

Figure 4-46. OLM microstructure of 9 at.% Al alloy aged at 750°C for 100 hours showing (a) lamellar structure nucleating inside of grains, (b) high magnification of lamellar structure and particles along grain boundaries..... 104

Figure 4-47 Ni-Mo-Al ternary alloy phase diagram at 800°C [65]..... 105

Figure 4-48. OLM microstructure of 2 at.% Al alloy aged at 850°C for 100 hours showing (a) striation line along the grain boundaries, (b) coarse lamellar structure and fine striation structure..... 107

Figure 4-49. OLM microstructure of 5 at.% Al alloy aged at 850°C for 100 hours showing needle-like structure..... 108

Figure 4-50. OLM microstructure of 7 at.% Al alloy aged at 850°C for 100 hours showing needle-like structure..... 108

Figure 4-51. Ni-Mo-Al ternary alloy phase diagram at 950°C [65]..... 109

Figure 4-52. OLM microstructure of 2 at.% Al alloy aged at 950°C for 100 hours showing single phase and particles along grain boundaries..... 110

Figure 4-53. OLM microstructure of 5 at.% Al alloy aged at 950°C for 100 hours showing needle-like structure and particles along the grain boundaries, (a) 400X (b) 1000X..... 111

Figure 4-54 OLM microstructure of 7 at.% Al alloy aging at 950°C for 100 hours showing needle-like precipitates and particles along the grain boundaries, (a) 400X (b) 1000X..... 113

Figure 4-55. (a) SEM microstructure (BSE) in $Ni_4Mo$ alloy in hot forged condition showing single α phase with particles, (b) EDS analysis from A point for matrix. The ratio of Ni to Mo is 1.9, (c) EDS analysis from B point for black particles, (d) EDS analysis from C point for black particles (bright particles in SE) ..... 117

Figure 4-56. (a) SEM microstructure (BSE) of $Ni_4Mo$ alloy aged at 800°C for 10 minutes showing δ phase particles and β phase, (b) EDS analysis from A point for bright particles..... 119

Figure 4-57. (a) SEM microstructure (SE) of $Ni_4Mo$ alloy (hot forged) aged at 750°C for 100 hours showing β phase β phase recrystallization, (b) EDS analysis from A point (particles), (c) β domains..... 121

Figure 4-58. (a) SEM microstructure (SE) of 2 at.% Al alloy in as-cast condition (without homogenization) aged at 750°C for 100 hours showing two phase structure (see arrow), (b) EDS analysis from bright particles, (c) EDS analysis from matrix..... 122

Figure 4-59. SEM microstructure (BSE) of 5 at.% Al alloy in as-cast condition (without homogenization) aged at 750°C for 100 hours showing precipitates, lamellar structure and single α phase, (a) low magnification, (b) high magnification, (c) EDS analysis form single phase, (d) EDS analysis from bright area..... 124

Figure 4-60. SEM microstructure (SE) of 7 at.% Al alloy in as-cast condition (without homogenization) aged at 750°C for 100 hours showing, (a) lamellar structure (arrow B) with flower-like structure (arrow A), (b) lamellar structure, (c) EDS analysis from flower-like structure, (d) EDS analysis from lamellar structure..... 127

Figure 4-61. (a) SEM microstructure (SE) of 9 at.% Al alloy in as-cast condition (without homogenization) aged at 750°C for 100 hours showing lamellar structure with bright precipitates, (b) EDS analysis from bright precipitates, (c) EDS analysis from coarse structure..... 129

Figure 4-62. (a) SEM microstructure (SE) of 9 at.% Al alloy solution treated at 1250°C for 50 hours showing Mo-rich precipitates along grain boundaries and in matrix, (b) EDS analysis from particles, (c) EDS analysis from matrix..... 130

Figure 4-63. SEM microstructure (SE) of 7 at.% Al alloy aged at 600°C for 100 hours showing (a) grain boundaries migration and secondary phase formation along grain boundaries, (b) high magnification of grain boundary migration and secondary phase formation along grain boundaries, (c) EDS analysis from matrix, (d) EDS analysis from striation line..... 133

Figure 4-64. SEM microstructure (SE) of 9 at.% Al alloy solution treated at 1280°C for 50 hours and aged at 600°C for 100 hours showing (a) lamellar structure with precipitates, (b) high mignificationlamellar structure, (c) EDS analysis from particles, (d) EDS analysis from striation line of lamellar structure, (e) EDS analysis from dark lamellar structure..... 135

Figure 4-65. (a) SEM microstructure (BSE) of $Ni_4Mo$ alloy solution treated at 1280°C for 50 hours and aged at 650°C for 100 hours showing β domain phase along the grain boundaries, (b) EDS analysis from particles in domain region, (c) EDS analysis from matrix, (d) EDS analysis from beside particles..... 139

Figure 4-66. SEM microstructure (SE) of 7 at.% Al alloy solution treated at 1280°C for 50 hours and aged at 650°C for 100 hours showing (a) secondary phase formation along grain boundaries, (b) high magnification lamellar structure..... 141

Figure 4-67. SEM microstructure (SE) of 9 at.% Al alloy solution treated at 1280°C for 50 hours and aged at 600°C for 100 hours showing (a) high magnification of lamellar structure, (b) and (c) high magnification of coarse lamellar structure and fine lamellar structure..... 142

Figure 4-68. SEM microstructure (SE) of $Ni_4Mo$ alloy solution treated at 1280°C for 50 hours and aged at 750°C for 100 hours showing grain boundary migration..... 145

Figure 4-69. SEM microstructure (SE) of $Ni_4Mo$ alloy solution treated at 1280°C for 50 hours and at 750°C for 100 hours showing (a) β Widmanstatten pattern and β domains along migrated grain boundaries, (b) high magnification of β phase..... 146

Figure 4-70. SEM microstructure (SE) of 2 at.% Al alloy solution treated at 1280°C for 50 hours and aged at 750°C for 50 hours showing (a) coarsen grain boundaries, (b) precipitates in matrix..... 147

Figure 4-71. (a) SEM microstructure (SE) of 2 at.% Al alloy solution treated at 1280°C for 50 hours and aged at 750°C for 100 hours showing precipitates in matrix, (b) EDS analysis from particles along grain boundaries..... 148

Figure 4-72. SEM microstructure (SE) of 5 at.% Al alloy solution treated at 1280°C for 50 hours and aged at 750°C for 100 hours showing (a) coarse grain boundaries and lamellar structure, (b) high magnification of coarse grain boundary structure..... 149

Figure 4-73. SEM microstructure (SE) of 7 at.% Al alloy solution treated at 1280°C for 50 hours and aged at 750°C for 100 hours showing lamellar structure..... 151

Figure 4-74. SEM microstructure (SE) of 2 at.% Al alloy solution treated at 1280°C for 50 hours and aged at 850°C for 100 hours showing (a) striation lines and particles, (b) particles across the striation lines, (c) EDS analysis from the particles, (d) coarse lamellar structure..... 151

Figure 4-75. SEM microstructure (SE) of 5 at.% Al alloy solution treated at 1280°C for 50 hours and aged at 850°C for 100 hours showing (a) needle-like structure, (b) high magnification of needle-like structure, (c) EDS analysis from the lath, (d) EDS analysis from the matrix, (e) EDS analysis from the particles along grain boundaries..... 153

Figure 4-76. SEM microstructure of 7 at.% Al alloy solution treated at 1280°C for 50 hours and aged at 850°C for 100 hours showing coarse grain boundary particles and needle-like structure..... 157

Figure 4-77. (a) SEM microstructure of 2 at.% Al alloy solution treated at 1280°C for 50 hours and aged at 950°C for 100 hours showing particles along grain boundaries, (b) EDS analysis from particles along grain boundaries in 2 at.% Al alloy..... 157

Figure 4-78. (a) SEM microstructure (SE) of 5 at.% Al alloy solution treated at 1280°C for 50 hours and aged at 950°C for 100 hours showing particles along grain boundaries and needle-like structure, (b) EDS analysis from particles along grain boundaries..... 158

Figure 4-79. SEM microstructure of 7 at.% Al alloy solution treated at 1280°C for 50 hours and aged at 950°C for 100 hours showing (a) particles and needle-like structure, (b) coarse grain boundary particles and needle-like structure, (c) EDS analysis from particles along the grain boundaries, (d) EDS analysis from matrix..... 159

Figure 4-80. (a) SEM microstructure (BSE) of 7 at.% Al alloy solution treated at 1280°C and aged at 950°C for 100 hours showing sample in the as-polished condition, (b) EDS analysis from darken area, (c) EDS analysis from matrix, (d) EDS analysis from bright particles..... 161

Figure 4-81. Intergranular cracking of $Ni_4Mo$ alloy aged at 750°C for 100 hours..... 168

Figure 4-82. Interface cracking between coarsened β phase and Widmanstatten pattern β structure in $Ni_4Mo$ alloy aged at 750°C for 100 hours. The arrow indicated the γ phase..... 168

Figure 4-83. EDS analysis from the bright lath in coarsened β region in $Ni_4Mo$ alloy..... 169

Figure 4-84. The cleavage morphology at grain boundaries between coarsened β and Widmanstatten pattern β structure in $Ni_4Mo$ alloy ..... 169

Figure 4-85. Molybdenum segregated along grain boundaries in $Ni_4Mo$ alloy ..... 170

Figure 4-86. Intergranular cracking in 2 at.% Al alloy aged at 750°C for 100 hours ..... 172

Figure 4-87. Fracture morphology of 2 at.% Al alloy aged at 750°C for 100 hours ..... 172

Figure 4-88. EDS analysis from particles in 2 at.% Al alloy ..... 173

Figure 4-89. Intergranular dimple morphology in 2 at.% Al alloy aged at 750°C for 100 hours ..... 173

Figure 4-90. Intergranular cracking in 5 at.% Al alloy aged at 750°C for 100 hours ..... 174

Figure 4-91. The fracture surface of 5 at.% Al alloy aged at 750°C for 100 hours ..... 174

Figure 4-92. Secondary cracking along the lamellar plates and interface between lamellar structure and coarsened structure ..... 175

Figure 4-93. The fracture surface of 5 at.% Al alloy aged at 750°C for 100 hours ..... 175

Figure 4-94. The fracture surface of 5 at.% Al alloy aged at 750°C for 100 hours in high magnification ..... 176

Figure 4-95. Intergranular and transgranular cracking in 7 at.% Al alloy aged at 750°C for 100 hours ..... 178

Figure 4-96. Transgranular cracking along the lamellar plates and interface between lamellar structure and a matrix in 7 at.% Al alloy ..... 178

Figure 4-97. Intergranular cracking along the coarse structure and grain boundaries in 7 at.% Al alloy ..... 179

Figure 4-98. Dimple fracture morphology in a matrix in 7 at.% Al alloy ..... 179

Figure 4-99. (a) Intergranular cracking in 9 at.% Al alloy aged at 750°C for 100 hours, (b) Transgranular cracking in 9 at.% Al alloy aged at 750°C for 100 hours ..... 180
Figure 4-100. The fracture morphology (SE) of 9 at.% Al alloy aged at 750°C for 100 hours ..... 181

Figure 4-101. Backscattered electron image of 9 at.% Al alloy aged at 750°C for 100 hours ..... 181

Figure 4-102. EDS analysis from bright area showing Mo-rich plates in 9 at.% Al alloy ..... 182

Figure 4-103. EDS analysis from darken area showing Ni-rich plates in 9 at.% Al alloy ..... 182

Figure 4-104. (a) Schematic diagram of the [001] zone axis electron diffraction pattern for α, β, $DO_{22}$, $Ni_2Mo$, and γ' structure, (b) Schematic electron diffraction of γ structure ..... 185

Figure 4-105. Schematic diagram of [112] zone axis electron diffraction pattern for α, β, $DO_{22}$, $Ni_2Mo$, and γ' structure ..... 187

Figure 4-106. Schematic diffraction patterns showing the location of maxima for the fcc fundamental lattice and the β. $DO_{22}$, $Ni_2Mo$ and γ' superlattices, (a) [001] zone, (b) [112] zone ..... 188

Figure 4-107. TEM microstructure of $Ni_4Mo$ alloy solution treated at 1250°C for 50 hours, (a) SRO α phase with dislocations pile-ups at grain boundary, (b) corresponding different pattern at [001] zone, (c) [112] zone ..... 190

Figure 4-108. TEM microstructure 2 at.% Al alloy solution treated at 1250°C for 50 hours, (a) $DO_{22}$ precipitates in SRO α phase matrix, and dislocation pile-ups at grain boundary and stacking faults, (b) corresponding the [001] zone diffraction pattern ..... 191

Figure 4-109. TEM microstructure of 2 at.% Al alloy solution treatment at 1250°C for 20 minutes, (a) [112] zone diffraction pattern showing SRO α superlattice spots, (b) and (c) SRO α phase and dense dislocation ..... 192

Figure 4-110. TEM microstructure of 5 at.% Al alloy solution treated at 1250°C for 50 hours, (a) [112] zone diffraction pattern showing $DO_{22}$ superlattice spots, (b) corresponding microstructure and stacking faults..... 194

Figure 4-111. TEM microstructure of 7 at.% Al alloy solution treated at 1250°C for 50 hours, (a) and (b) [001] and [112] zone diffraction pattern showing $DO_{22}$ and $Ni_2Mo$ superlattice spots, (c) corresponding microstructure of [112]zone showing uniform $DO_{22}$ and $Ni_2Mo$ phases..... 195

Figure 4-112. TEM microstructure of 9 at.% Al alloy solution treated at 1250°C for 50 hours, (a) [112] zone diffraction pattern showing $DO_{22}$ and $Ni_2Mo$ superlattice spots, (b) corresponding microstructure, (c) particles and stacking faults in matrix..... 196

Figure 4-113. TEM microstructure of 2 at.% Al alloy aged at 600°C for 100 hours, (a) [001] zone diffraction pattern showing SRO $\alpha$, LRO $\beta$ and $DO_{22}$ superlattice spots, (b) [112] zone diffraction pattern showing SRO $\alpha$, $\beta$ and $DO_{22}$ superlattice spots, (c) corresponding microstructure of [112] zone diffraction pattern..... 198

Figure 4-114. TEM microstructure of 5 at.% Al alloy aged at 600°C for 100 hours, (a) $DO_{22}$ phase, (b) corresponding [001] zone diffraction pattern..... 200

Figure 4-115. TEM microstructure of 7 at.% Al alloy aged at 600°C for 100 hours, (a) [112] zone diffraction pattern showing $DO_{22}$ and $Ni_2Mo$ superlattice spots, (b) corresponding microstructure of $DO_{22}$ and $Ni_2Mo$ phase..... 200

Figure 4-116. TEM microstructure of 9 at.% Al alloy aged at 600°C for 100 hours, (a) microstructure of $DO_{22}$ and $Ni_2Mo$ phase, (b) corresponding [112] zone diffraction pattern..... 201

Figure 4-117. TEM microstructure of $Ni_4Mo$ alloy aged at 650°C for 100 hours, (a) [112] zone diffraction pattern showing $\beta$ superlattice spots, (b) corresponding microstructure of $\beta$ phase..... 203

Figure 4-118. TEM microstructure of 2 at.% Al alloy aged at 650°C for 100 hours, (a) microstructure of $DO_{22}$ and $Ni_2Mo$ phase, (b) corresponding [321] zone diffraction pattern..... 203

Figure 4-119. TEM microstructure of 5 at.% Al alloy aged at 650°C for 100 hours, (a) [112] zone diffraction pattern showing strong intensity $DO_{22}$ and weak intensity $Ni_2Mo$, (b) corresponding microstructure of $DO_{22}$ and $Ni_2Mo$ phases, (c) lamellar structure..... 205

Figure 4-120. TEM microstructure of 7 at.% Al alloy aged at 650°C for 100 hours, (a) [001] zone diffraction pattern showing $DO_{22}$ and $Ni_2Mo$ superlattice spots, (b) corresponding microstructure of $DO_{22}$ and $Ni_2Mo$ phases, (c) lamellar structure, (d) diffraction pattern at c region..... 206

Figure 4-121. TEM microstructure of $Ni_4Mo$ alloy aged at 750°C for 10 hours, (a) [001] diffraction pattern showing β superlattice spots, (b) β domains stacking faults..... 208

Figure 4-122. TEM microstructure of 2 at.% Al alloy aged at 750°C for 10 hours, (a) [001] zone diffraction pattern showing SRO α superlattice spots, (b) SRO α phase..... 209

Figure 4-123. TEM microstructure of 5 at.% Al alloy aged at 750°C for 10 hours, (a) lamellar structure, (b) diffraction pattern $[100]_\gamma // [011]_{fcc}$, (c) schematic diffraction pattern $[100]_\gamma // [011]_{fcc}$..... 210

Figure 4-124. TEM microstructure of $Ni_4Mo$ alloy aged at 750°C for 50 hours, (a) β phase and stacking faults, (b) [001] zone diffraction pattern showing β superlattice spots..... 211

Figure 4-125. TEM microstructure of 2 at.% Al alloy aged at 750°C for 50 hours, (a) stacking faults and precipitates, (b) [111] diffraction pattern showing $DO_{22}$ superlattice spots..... 213

Figure 4-126. TEM microstructure of 5 at.% Al alloy aged at 750°C for 50 hours, (a) and (b) lamellar structure, (c) stacking faults and precipitates..... 214

Figure 4-127. TEM microstructure of 7 at.% Al alloy aged at 750°C for 50 hours, (a) [112] zone diffraction pattern showing $DO_{22}$ and $Ni_2Mo$ superlattice spots, (b) microstructure of $DO_{22}$ and $Ni_2Mo$ phase..... 215

Figure 4-128. TEM microstructure of $Ni_4Mo$ alloy aged at 750°C for 100 hours, (a) microstructure of β and $Ni_2Mo$ phases, (b) [112] zone diffraction pattern showing β and $Ni_2Mo$ superlattice spots..... 218

Figure 4-129. TEM microstructure of 2 at.% Al alloy aged at 750°C for 100 hours, (a) [112] zone diffraction pattern showing β, $DO_{22}$ and $Ni_2Mo$ superlattice spots, (b) microstructure of β, $DO_{22}$ and $Ni_2Mo$ phase..... 217

Figure 4-130. TEM microstructure of 5 at.% Al alloy aged at 750°C for 100 hours, (a) lamellar structure of γ and γ' phases, (b) corresponding diffraction pattern, (c) schematic diffraction pattern, (d) lamellar structure, (e) Ni-rich particles, EDS analysis from lamellar structure (f) A, (g) B, (h) C, (I) D, (j) E, (k) F..... 219

Figure 4-131. TEM microstructure of 7 at.% Al alloy aged at 750°C for 100 hours, (a) tweed structure, (b) lamellar structure, (c) [001]diffraction pattern showing strong intensity $Ni_2Mo$ and γ' and weak intensity $DO_{22}$ superlattice spots..... 223

Figure 4-132. TEM microstructure of 9 at.% Al alloy aged at 750°C for 100 hours, (a) [111] diffraction pattern showing $DO_{22}$ superlattice spots, (b) corresponding microstructure of tweed structure, (c) lamellar structure, (d) [001] diffraction pattern, (f) EDS analysis from the lamellar structure and matrix..... 224

Figure 4-133. TEM microstructure of 2 at.% Al alloy aged at 850°C for 100 hours, (a) microstructure of $DO_{22}$, (b) [112] diffraction pattern showing $DO_{22}$ superlattice spots, (c) dislocations, (d) lamellar structure..... 227

Figure 4-134. TEM microstructure of 5 at.% Al alloy aged at 850°C for 100 hours, (a) and (b) different shape precipitates and dislocation pile-ups at precipitates..... 229

Figure 4-135. TEM microstructure of 5 at.% Al alloy aged at 950°C for 100 hours, (a) lath shape precipitates and dislocation pile-ups at precipitates, (b) [112] zone diffraction pattern..... 231

Figure 4-136. TEM microstructure of 7 at.% Al alloy aged at 950°C for 100 hours, (a) and (b) precipitates and dislocations, (c) EDS analysis from matrix (A), (d) from precipitates (B, C), (e) from precipitates (D)..... 231

Figure 4-137. [001] zone diffraction pattern showing intermediate stage of SRO α phase transformation to LRO β phase in Hastelloy B2 alloy aged at 550°C for 200 hours..... 237

Figure 4-138. TEM microstructure of Hastelloy B2 alloy aged at 550°C for 800 hours, (a) secondary phase precipitates in matrix, (b) corresponding [112] zone diffraction pattern showing the β and $DO_{22}$ superlattice position..... 237

Figure 4-139. TEM microstructure of Hastelloy B2 alloy aged at 550°C for 1200 hours, (a) and (b) [001] and [112] zone diffraction patterns showing $DO_{22}$ and b superlattice spots, (c) corresponding microstructure for [112] zone diffraction pattern showing early stage of striation of plates of $DO_{22}$ phase..... 238

Figure 4-140. TEM microstructure of Hastelloy B2 alloy aged at 650°C for 200 hours, (a) [112] zone diffraction pattern showing $DO_{22}$ and β superlattice spots, ( b) corresponding microstructure showing $DO_{22}$ phase precipitates in β phase matrix..... 239

Figure 4-141. TEM microstructure of Hastelloy B2 alloy aged at 650°C for 800 hours, (a) [001] zone diffraction pattern showing diffuse intensity maxima at $DO_{22}$ and β superlattice spots, (b) corresponding microstructure showing $DO_{22}$ phase precipitates in β phase matrix, (c) in some regions, the early stage of $DO_{22}$ phase striation formation..... 241

Figure 4-142. TEM microstructure of Hastelloy B2 alloy aged at 60°C for 1200 hours, (a) and (b) [001] and [112] zone diffraction patterns showing diffuse intensity maxima at $DO_{22}$ and β superlattice spots, (c) corresponding microstructure at [112] zone diffraction pattern showing fine $DO_{22}$ and β phases mixture..... 242

Figure 4-143. TEM microstructure of Hastelloy B2 alloy aged at 750°C for 200 hours, (a) the lath of $DO_{22}$ phase form in matrix, (b) corresponding [112] zone diffraction pattern showing $DO_{22}$ and β phases..... 243

Figure 4-144. TEM microstructure of Hastelloy B2 alloy aged at 750°C for 400 hours, (a) SRO α phase recrystallization at grain boundaries and stacking faults, (b) corresponding [112] zone diffraction pattern at recrystallization region showing diffuse intensity at {1 1/2 0} positions..... 243

Figure 4-145. TEM microstructure of Hastelloy B2 alloy aged at 750°C for 800 hours, (a) [111] zone diffraction pattern showing $DO_{22}$ superlattice spots, (b) and (c) coarsened microstructure made of lathe and diamond-shape particles..... 244

Figure 4-146. TEM microstructure of Hastelloy B2 alloy aged at 750°C for 1200 hours, (a) lamellar structure formed along grain boundaries, (b) corresponding diffraction pattern..... 245

Figure 4-147. TEM microstructure of Hastelloy B2 alloy aged at 850°C for 200 hours, showing dense dislocations..... 247

Figure 4-148. TEM microstructure of Hastelloy B2 alloy aged at 850°C for 400 hours, (a) select area diffraction pattern at [001] zone showing diffuse intensity maxima at {1 1/2 0} positions, (b) corresponding microstructure showing the SRO α phase formation..... 247

Figure 4-149. TEM microstructure of Hastelloy B2 alloy aged 850°C for 400 hours, (a) coarse lamellar structure, (B) [001] zone select area diffraction pattern showing the SRO α superlattice spots..... 248

Figure 4-150. TEM microstructure of Hastelloy B2 alloy aged at 850°C for 1200 hours, (a) [001] zone diffraction pattern showing diffuse intensity maxima at SRO α superlattice spots, (b) corresponding microstructure showing SRO α phase and dislocation pile-ups grain boundary ..... 248

Figure 4-151. OLM microstructure of $Ni_4Mo$ alloy showing result of ASTM A262 Practice A ..... 251

Figure 4-152. Potentiodynamic anodic polarization curve in $Ni_4Mo$ alloy ..... 251

Figure 4-153. SEM microstructure of $Ni_4Mo$ alloy showing intergranular cracking in U-bend test ..... 253

Figure 4-154. Schematic diagram of cyclic polarization curve ..... 255

Figure 4-155. Cyclic polarization behavior of $Ni_4Mo$ alloy in 14% hydrochloric solution upon aging at 750°C for 100 hours ..... 256

Figure 4-156. Cyclic polarization behavior of 2 at.% Al alloy in 14% hydrochloric solution upon aging at 750°C for 100 hours ..... 257

Figure 4-157. Cyclic polarization behavior of 5 at.% Al alloy in 14% hydrochloric solution upon aging at 750°C for 100 hours ..... 258

Figure 4-158. Cyclic polarization behavior of 7 at.% Al alloy in 14% hydrochloric solution upon aging at 750°C for 100 hours ..... 259

Figure 4-159. Cyclic polarization behavior of 9 at.% Al alloy in 14% hydrochloric solution upon aging at 750°C for 100 hours ..... 260

# CHAPTER 1

# INTRODUCTION

Nickel-base alloys are one of the most complex and the most widely used group for our present-day society. They can withstand a wide variety of severe operating conditions involving corrosion environments, high temperature, high stress, and/or the combinations of these conditions, and have special, important mechanical and metallurgical characteristics. nickel-base alloys are used in instruments and control equipment to measure and regulate electrical characteristics because of their high electrical resistance. Nickel-base alloys also are used up to the highest homologous temperature of any common alloy systems. They currently are used in aircraft engines, space vehicles, nuclear power systems, chemical and petrochemical industries, pollution control equipment and heat-treating equipment because of their significant corrosion resistance and excellent elevated temperature properties [1].

Pure nickel is ductile and tough and it possesses a face-centered cubic crystal structure up to its melting point. Nickel and many of its alloys are readily fabricated by conventional methods and offer freedom from the ductile to brittle transformation behavior of most body-centered cubic and non-cubic metals. Nickel can accommodate large amounts of alloying elements, such as Cr, Al, Mo, Ti, Fe, B, Cu and V in solid solution. However, for the developed nickel-base alloys, emphases have been placed on the applications that require corrosion-resistance, heat-resistance, low-expansion and high electrical resistance.

Some alloying elements are added purposely in nickel-base alloys for obtaining special required physical and/or mechanical properties. However, some unexpected intermetallic phases may appear in modified alloy systems during materials fabrication or heat treatment. Specifically in Ni-Mo alloys, the intermetallic phases $Ni_4Mo$ ($\beta$), $Ni_3Mo$ ($\gamma$)/$DO_{22}$, and NiMo ($\delta$) can form, and the phase transformations associated with the formation of these phases generates spectacular microstructures and property changes. These phase transformations vary the material's corrosion resistance and mechanical properties. Alloying elements can alter the phase transformation behavior and the properties. Further study of the Ni-Mo alloys will lead to a better understanding of principles important to all nickel-base alloy systems [2].

Hastelloy B2 alloy was developed base on $Ni_4Mo$ alloy, which contains 29 wt.% molybdenum and 71 wt.% nickel, offered the best resistance to hot hydrochloric acid environments among the nickel-base alloys. The existing metallurgical issue of $Ni_4Mo$ alloy is that the material becomes brittle upon heating in the 600-800°C temperature range or upon slow cooling from this temperature range. This process is associated with the transformation of $\alpha$ to $\beta$ phase, which takes place through a disorder-order phase transformation.

The disorder-order transformation only involves a redistribution of atoms among the atomic locations from a random arrangement to a more regular arrangement, whereby designated sites are occupied predominantly by one kind of atom. In general, there is a critical disorder-order transformation temperature $T_c$. Above the disorder-order transformation temperature, long-range order disappears; when the temperature is lowered through the critical point, long-range order is reestablished.

$Ni_4Mo$ alloy exists as a face-centered cubic (FCC) solid solution above 868°C, but transforms by a long-range ordering reaction when it is equilibrated below this

temperature. The ordered intermetallic phase (β phase) is the major reaction product. The transformation has been studied by transmission electron microscopy, scanning electron microscopy, optical microscopy and x-ray diffraction in $Ni_4Mo$ alloy with quenched, aging and cold worked conditions.

The intermetallic phase (β phase) is a long-range ordered structure and $Ni_4Mo$ alloy becomes brittle when the β phase forms. The brittleness may result from strong resistance to the motion of dislocations leading to intergranular fracture being favored [3]. Therefore, suppressing the disorder-order (α to β) transformation is important to maintain good mechanical properties during service and for required heat treatments during material fabrication.

Aluminum offers the potential for addition to alloys for high temperature structural applications due to good corrosion resistance combined with oxidation resistance at a high temperature. Thus, additions of aluminum contents with 2 at.%, 5 at.%, 7 at.% and 9 at.% were proposed for the modifications of $Ni_4Mo$ alloy in order to determine if aluminum can prevent the embrittlement. In addition, aluminum is also used in a minor amount in $Ni_4Mo$ alloy for the purpose of deoxidization, controlling carbon and nitrogen, to prevent the ordered intermetallic phase β forming, and to improve high-temperature corrosion resistance.

It is believed that this study will benefit not only the fundamental understanding of the nickel-base alloy systems and provide a data base for the alloy development, but also the investigation may lead to a practical importance of property improvement of available $Ni_4Mo$ alloy.

# CHAPTER 2

# LITERATURE REVIEW

## 2.1 Hastelloy Alloy Systems

Conventional Hastelloy alloys belong to the nickel-base alloy systems. Hastelloy alloys can be classified into two groups based upon their applications. One group is high-performance, corrosion-resistance alloys including alloys B-2, C-4, C-22, C-276, G-3, G30, H-9M, N and F. The other group is high-performance, heat-resistance alloys including alloys X, S and W. Hastelloy alloys of the corrosion resistance group are often used in the chemical and petroleum industries for manufacturing containment vessels and pipes while the heat resistance alloy group can be used for high temperature corrosion resistance applications.

The physical metallurgy of Hastelloy alloys is complex, subtle and sophisticated. Hastelloy B2 alloy, for example, is an improved wrought version of Hastelloy B alloy. Hastelloy B2 alloy, a Ni-Mo alloy, has the same excellent corrosion resistance as Hastelloy B alloy, but with improved resistance to knife-line attack adjacent to the weld metal and to heat-affected zone attack at some distance from a weld. The lower carbon content of Hastelloy B2 alloy provides better resistance to the formation of grain boundary carbide precipitates in the weld heat-affected zone, thus making it suitable for most chemical process applications in the as-welded condition [4-6]. Hastelloy B2 alloy also has an excellent resistance to pitting and stress-corrosion cracking. However, Hastelloy B2 alloy can develop decreased ductility when it is cooled too slowly or reheated, either treatment leading to long-range ordering (formation of $\beta$ phase).

Hastelloy C alloy contains nominally 16 wt.% Cr and 16 wt.% Mo, and form intermetallic phases within the temperature 700-1050°C. Two types of precipitates, $Ni_7Mo_6$ and $M_6C$, often form in Hastelloy C alloy, but are not of great concern from a weldability viewpoint. The intermetallic phase $Ni_7Mo_6$ was found to form primarily at grain boundaries either as a continuous or discontinuous chain-type structure. In Hastelloy C-276 alloy, 4 wt.% W is added along with a controlled carbon and silicon content. Hastelloy C-276 alloy resists the formation of grain boundary precipitates in the heat-affected zones of welds, and it frequently is suitable in the as-welded condition for chemical process equipment [7]. However, Hastelloy C-276 alloy does not reduce intermetallic $Ni_7Mo_6$ precipitation, which is rich in molybdenum and creates adjacent areas of alloy depletion that can be selectively attacked [8-10].

Hastelloy S alloy, a Ni-Cr-Mo alloy, is a high-temperature alloy with a unique combination of properties. It has excellent thermal stability, low thermal expansion and excellent oxidation resistance up to 2000°F (1093°C). In addition, the alloy has good high-temperature and thermal fatigue strengths. Hastelloy S alloy retains its strength and ductility after aging at temperatures of 800 to 1600°F (427 to 871°C) [11].

Hastelloy W alloy, a Ni-Cr-Mo alloy with an increased Mo and a decreased Cr content compared to Hastelloy S alloy, is a solid-solution-strengthened alloy and was developed primarily for the welding of dissimilar alloys. The principal alloying elements in alloy tungsten are molybdenum and chromium. It is available as straight cut length wire for gas-tungsten-arc welding, layer-wound wire for gas-metal-arc welding, and coated electrodes for shielded-metal-arc welding [12]. The nominal chemical composition (wt.%) of the above described alloys is documented in Table 1.

Table 1. Nominal chemical compositions (wt.%) of some typical nickel-base alloys.

| | Cr | Ni | Co | Mo | Fe | C | W | Cu | Al | Si |
|---|---|---|---|---|---|---|---|---|---|---|
| Hastelloy B | 1.0 max. | bal | 2.5 max. | 28.0 | 5.0 | 0.05 max. | - | - | - | 1.0 |
| Hastelloy B2 | 1.0 max. | bal | - | 28.0 | 2.0 max. | 0.01 | - | - | - | 0.1 |
| Hastelloy C-4 | 16.0 | 65.0 | - | 15.5 | 3.0 max. | 0.01 | - | - | - | 0.08 |
| Hastelloy C-276 | 14.5-16.5 | bal | 2.5 | 15.0-17.0 | 4.0-7.0 | 0.01 | 3.0-4.5 | - | - | 0.08 |
| Hastelloy G-3 | 21.0-23.5 | bal | 5.0 | 6.0-8.0 | 19.5 | 0.015 | 1.5 max. | 1.5-2.5 | - | 1.0 |
| Hastelloy G-30 | 29.5 | 43.0 | - | 5.5 | 15.0 | 0.03 | 2.5 | 2.0- | - | 0.08 |
| Hastelloy W | 5.0 | 63.0 | 2.5 max. | 24.0 | 6.0 | 0.12 max. | - | - | - | 1.0 |
| Hastelloy S | 14.5-17.0 | bal | 2.0 | 14.0-16.5 | 3.0 | 0.02 max. | - | 0.35 | 0.10-0.50 | 0.2-0.75 |

SOURCE: Metals Handbook, 9th Edition, Vol 13, ASM Metals Park, Ohio, 1992.

## 2.2 Nickel-Molybdenum Alloy

For the Ni-Mo binary alloy, the intermetallic phases $Ni_4Mo$ (β-phase), $Ni_3Mo$ (γ-phase), unstable $Ni_2Mo$, and NiMo (δ-phase) can form with modest exposure in the temperature range 600-800°C. Formation of these intermetallic phases can render Ni-Mo alloys brittle [2 and 13]. The amount of molybdenum in nickel is one of the factors leading to embrittlement of Ni-Mo alloys. Figure 1 [2 and 14] presents the Ni-Mo phase diagram. When stoichiometric ratio of nickel to molybdenum is at or very close to 1:4, the short-range ordered phase (α phase) transforms to the long-range ordered phase (β phase) on cooling. On heating, intermetallic phases β and γ decompose by a peritectoid reaction, and the intermetallic phase δ decomposes by a peritectic reaction.

In the Ni-20 at.% Mo alloy, the SRO α phase to LRO β phase transformation has been studied extensively because formation of the β phase from α phase increases the strength but renders the alloy brittle. Fracture occurs on the former high angle α boundaries. Guthrie and Stansbury [15] conducted an x-ray diffraction investigation of Ni-Mo alloys and observed lines attributable to α phase and β phase in a diffraction pattern of 19.99 at.% Mo alloy and β lines and faint γ lines in a 20.77 at.% Mo alloy, and placed the β region between 20-20.5 at.% Mo. Casselton and Hume-Rothery [16] investigated the equilibrium diagram of the Ni-Mo alloy system by a combination of thermal, microscope and x-ray methods. The result is the same as that of Guthrie and Stansbury. Many investigators believe that the intermetallic β phase encompasses the stoichiometric $Ni_4Mo$. The solubility of molybdenum in α is one of the important factors affecting the transformation of long-range ordered phase β from short-range ordered phase α. Thus, alloys developed for corrosion resistance in the α-phase should be used at temperatures which place them in the α-field at equilibrium or at temperatures

H. Okamoto, 1991

| Phase | Composition, wt% Mo | Pearson symbol | Space group |
|---|---|---|---|
| (Ni) | 0 to 38(a) | *cF*4 | $Fm\bar{3}m$ |
| $Ni_4Mo$ | 29.0 | *tI*10 | *I*4/*m* |
| $Ni_3Mo$ | 35:3 | *oP*8 | *Pmnn* |
| NiMo | 63.9 to 65.7 | *oP*112 | $P2_12_12_1$ |
| (Mo) | 98.9 to 100(b) | *cI*2 | $Im\bar{3}m$ |
| **Metastable phases** | | | |
| $Ni_2Mo$ | ... | *oI*6 | ... |
| $Ni_3Mo$ | ... | *tI*8 | *I*4/*mmm* |
| $Ni_4Mo$ | ... | *tI*10, *cF*4 | ... |
| $Ni_{17}Mo_5$ | ... | ... | ... |

(a) At 1317 °C. (b) At 1362 °C

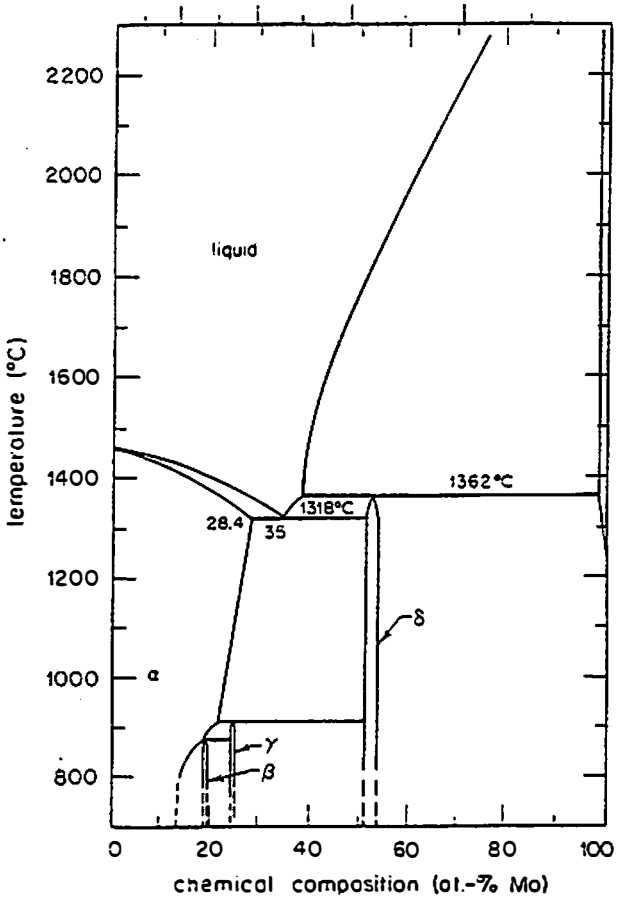



Figure 2-1. Ni-Mo phase diagram and phases.

SOURCE: (a) ASM Handbook, Alloy Phase Diagrams, 10 Edition, Vol. 3, ASM Metals Park, Ohio, 1992. (b) C.R. Brooks, J.E. Spruiell, and E.E. Stansbury, Physical Metallurgy of Nickel-Molybdenum Alloys, International Metals Reviews, 29:210-248 (1984).

low enough for no β phase to form within the design life of the component [2].

## 2.3 Physical and Mechanical Properties of Ni-Mo Alloys

### 2.3.1 Physical Properties

The physical properties are different for the long-range ordered (LRO) state and the short-range ordered (SRO) state in Ni-Mo alloys. They are affected by the temperature, heat treatment and cold working condition as well as chemical composition. The specific heat of Ni-20 at.% Mo alloy that was slowly cooled and quenched from 950°C was reported by Norem [17]. The result for an initial LRO state and an initial SRO state is shown in Figure 2. On heating the LRO state, the specific heat increases gradually to about 800°C, and then rapidly increases up to 868°C, the transformation temperature as the β phase transforms to the α phase. This peak corresponds to an enthalpy change of approximately 2900 J-mol$^{-1}$. On heating from the quenched condition (SRO state), thermal energy is released in two stages, one having a maximum rate near 600°C and the other near 725°C, as the α phase transformation to the β phase occurs. Then, the specific heat increases as the β phase transforms to the α phase.

The electrical resistivity with temperature relationship for a Ni-20 at.% Mo alloy in three initial conditions (annealed, cooled at 60 Kmin$^{-1}$, and quenched from 950°C and swaged to 75% reduction in area) is represented in Figure 3 [18]. At 25°C, the electrical resistivity is the lowest for an initial condition of annealed and is highest for an initial condition of cooled 60 Kmin$^{-1}$ . When the initial condition is annealed, the electrical resistivity increases with increase of temperature; when the initial condition is cooled 60 Kmin$^{-1}$ or quenched then swaged 75% reduction in area, the electrical resistivity decreases with increase of temperature in the range 650-825°C, then increases with increase of

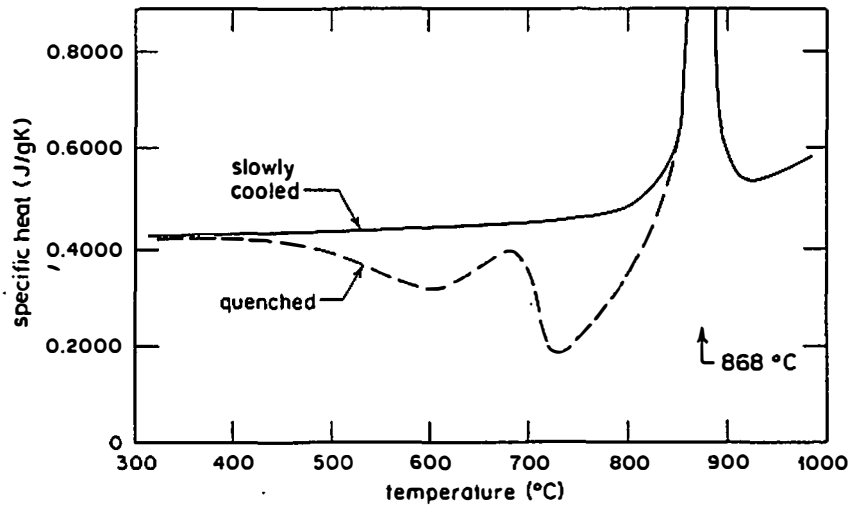



Figure 2-2. Specific heat of Ni-20at% Mo, slowly cooled and quenched from 950°C.

SOURCE: W.E. Norem, Ph.D. dissertation, University of Tennessee, 1963.

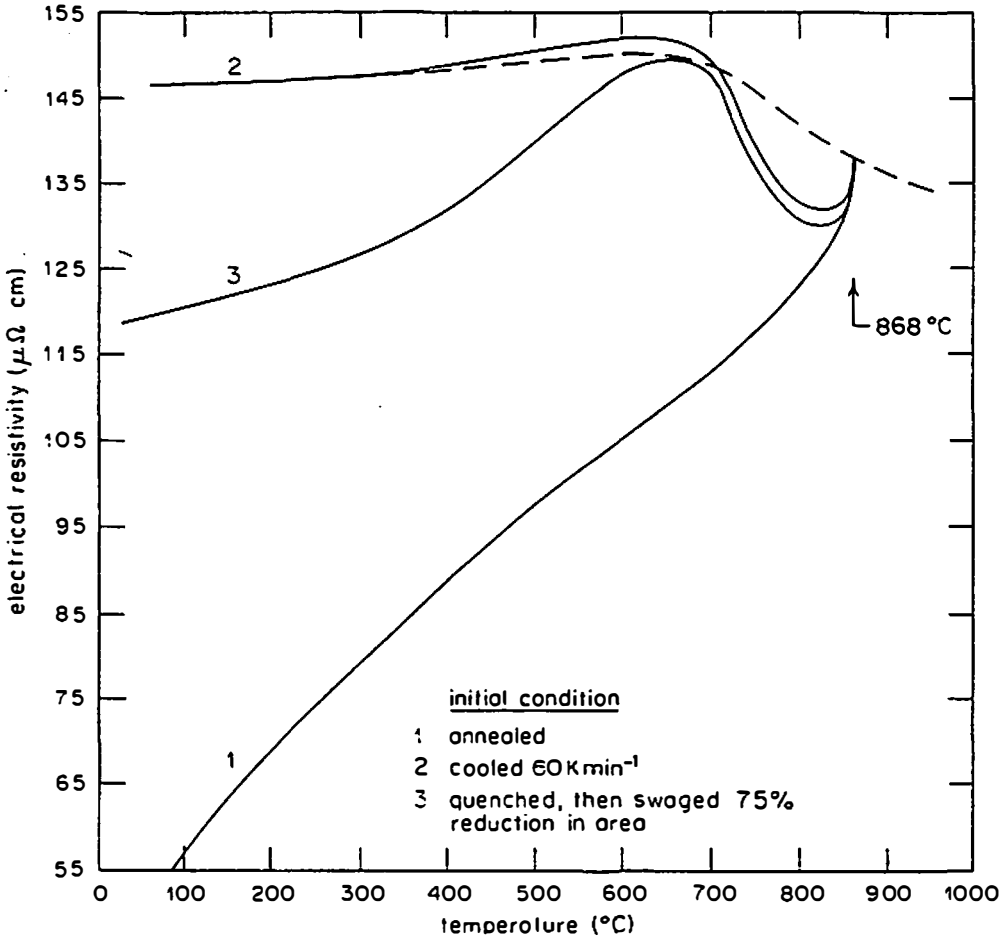



Figure 2-3. Electrical resistivity-temperature relationship for Ni 20 at.% Mo alloy in three initial conditions.

SOURCE: T.S. Lei, Ph.D. Dissertation, University of Tennessee, 1979.

temperature. Lei [18] reported that during the disorder-order transformation the electrical resistivity decreases while the hardness increases and SRO decreases at about 600°C. Brauwers et al. [19] stated that the electrical resistivity increases when the temperature rises up to the critical order-disorder transformation temperature for general ordered alloys. Therefore, temperature, heat treatment and cold working condition affect the electrical resistivity.

The thermal expansion from 25 to 1000°C was measured in Ni-Mo alloys. The result is shown in Figure 4. The curve for 20 at.% Mo alloy shows a smaller slope in the long-range ordered state than in the short-range ordered state. An isothermal expansion accompanying the transformation of LRO to SRO near 870°C is followed by expansion in the SRO range essentially coincident with that observed for the alloys with lower molybdenum contents [2].

### 2.3.2 Strength Properties

The addition of molybdenum to nickel in the α-phase significantly increases the strength (see Figure 5) and hardness [2]. This effect can be attributed to the influence of molybdenum on the stacking-fault energy, to the formation of SRO, and to the elastic strain resulting from the presence of the larger molybdenum atom.

The ordered intermetallic β (LRO) phase and deformation considerably affect the strength in Ni-20 at.% Mo alloy. Brooks et al. [20-22] investigated the effect of aging time on the tensile and yield strengths, the fracture elongation and microhardness of Hastelloy B2 alloy aged at different temperatures. The results are illustrated in Figures 6 and 7. Aging for up to 1200 hours from 550°C and 850°C increased the strength significantly [20]. Upon aging at 750°C, the strength passed through a maximum then decreased. In the solution annealed condition, the ductility was approximately 60%,

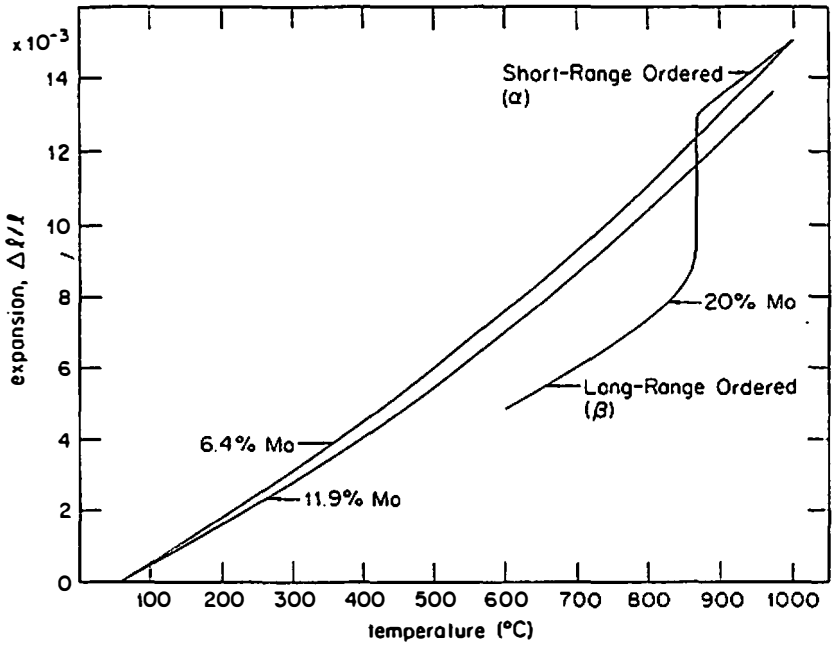



Figure 2-4. Thermal expansion of 6.4, 11.9 and 20 at.% Mo alloys.

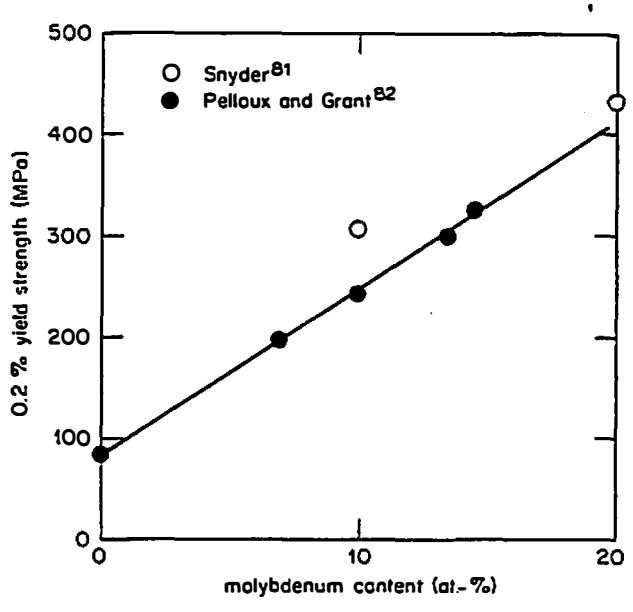



Figure 2-5. Effect of Mo content on yield strength of α-phase alloys.

SOURCE: C.R. Brooks, J.E. Spruiell, and E.E. Stansbury, "Physical Metallurgy of Nickel-Molybdenum Alloys," International Metals Reviews, 29:210-248 (1984). (for Figure 2-4 and 2-5)

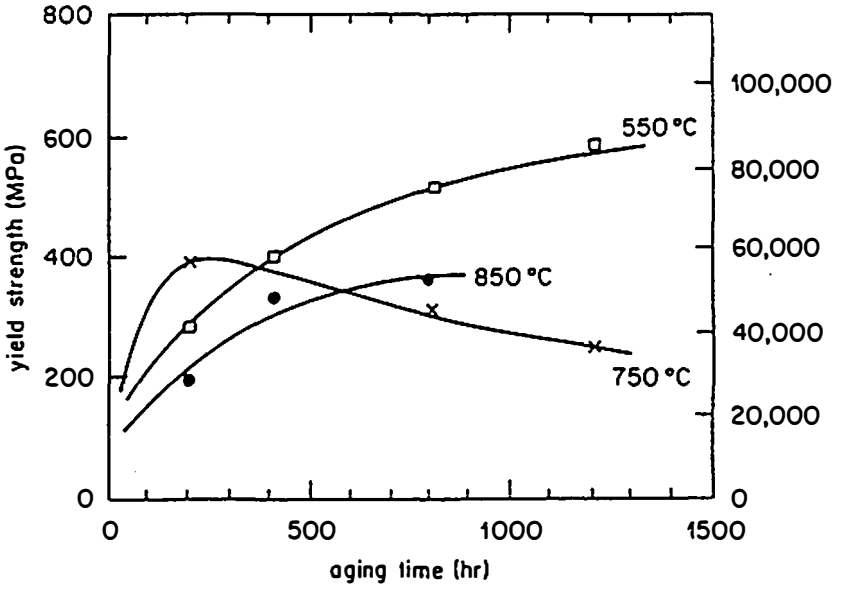



Figure 2-6. The effect of aging temperature and time on the 0.2% yield strength of Hastelloy B2 alloy.

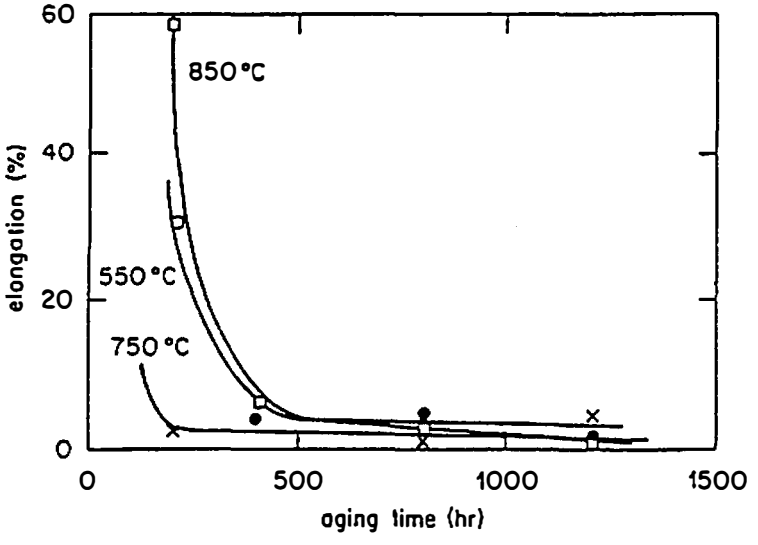



Figure 2-7. The effect of aging temperature and time on the tensile elongation of Hastelloy B2 alloy.

SOURCE: C.R. Brooks and Y.M. Wang, Tensile Properties and Fractography of Aged Hastelloy B2 (550-850°C for up to 1200H), Materials Characterization 25:185-197 (1990). (for Figure 2-6 and 2-7)

but after aging at 550°C and 850°C for 400 hours or more, the ductility was less than 5%. Upon aging at 750°C, ductility was less than 5% for aging 200 hours or more, even though the strength decreased.

The effect of grain size effect on hardness at all aging temperature and time is shown in Figure 8 [22]. For both initial grain sizes of 50 mm and 800 mm, the results of hardness are essentially the same. Aging at a higher temperature, 850°C, causes a measurable hardening, and aging at the lower temperature, 550°C, causes the hardness to approximately double in 1,200 hours. Upon aging at 650°C, the hardness increases appreciably, and for the 800 mm grain size material, it began to decrease after aging 1,200 hours, whereas for the 50 mm grain size material it was also slightly increased. At 750°C, both materials had a maximum hardness after aging 400 hours, then decreased appreciably [22].

Roan and Brooks [23] studied the dependency of the tensile properties of Hastelloy B alloy on test temperature with a solution annealed condition and the results are illustrated in Figure 9. The influence of aging time at several different temperatures on the tensile properties of Hastelloy B alloy is shown in Figure 10. The elongation sharply decreases at about 700°C, and corresponds to a change in the fracture mode from transgranular to intergranular above 700°C. However, the cause of the phenomenon is not clear. Roan and Brooks [23] reported that the type of precipitate present can be correlated with the mechanical properties. The feather-like precipitate causes the strengthening. Aging can make the retained $\alpha$ phase transform to the ordered $\beta$ phase. The rate of ordering is a maximum at about 750°C.

In Hastelloy B2 alloy, the phase transformations affect its strength, elongation, and hardness and phase transformations are quite sensitive to the molybdenum content and the amount of chromium and iron. The phase transformation involves the exchange of

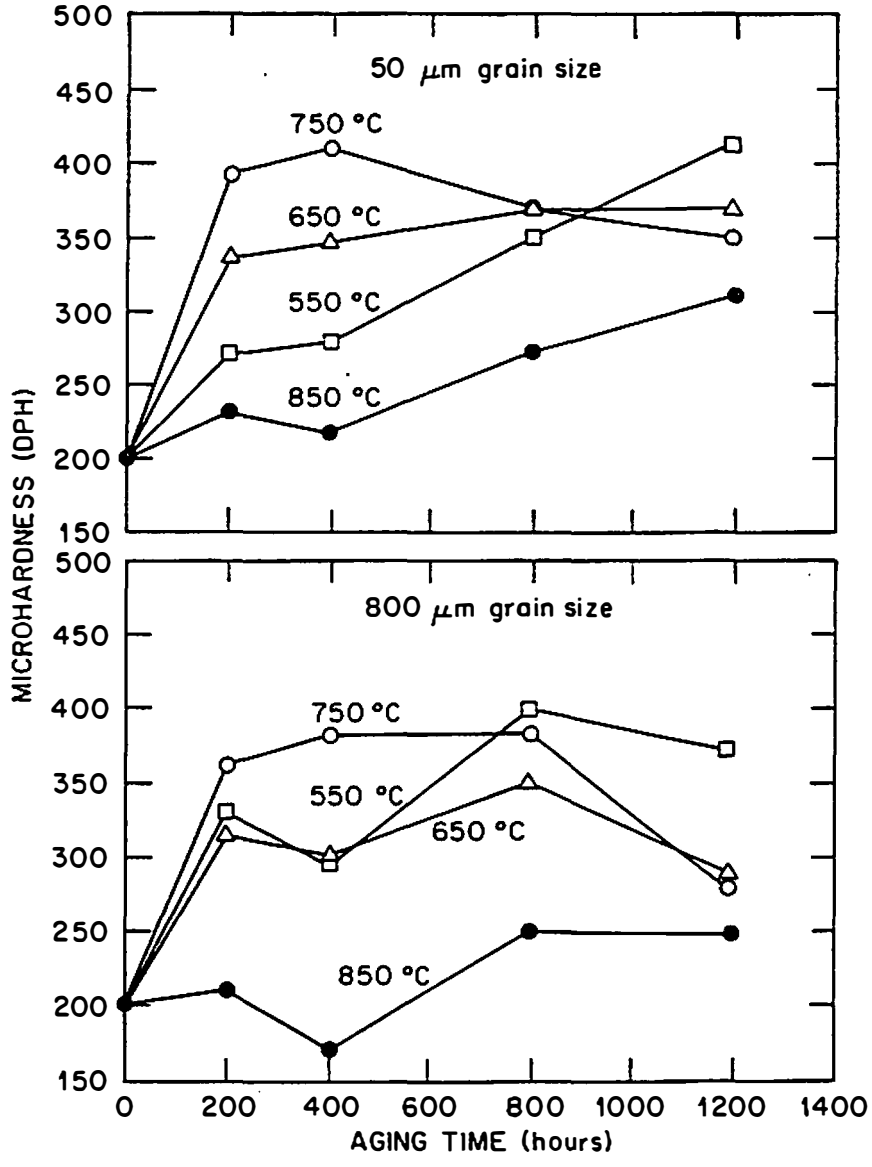



Figure 2-8. The effect of aging time and temperature on hardness for two different initial α grain sizes of Hastelloy B2 alloy.

SOURCE: C. R. Brooks and Y. M. Wang, Effect on the Microstructure of Aging Hastelloy B2 from 550 to 850°C for 1,200 Hours, Metallography, 23:57-86 (1989).

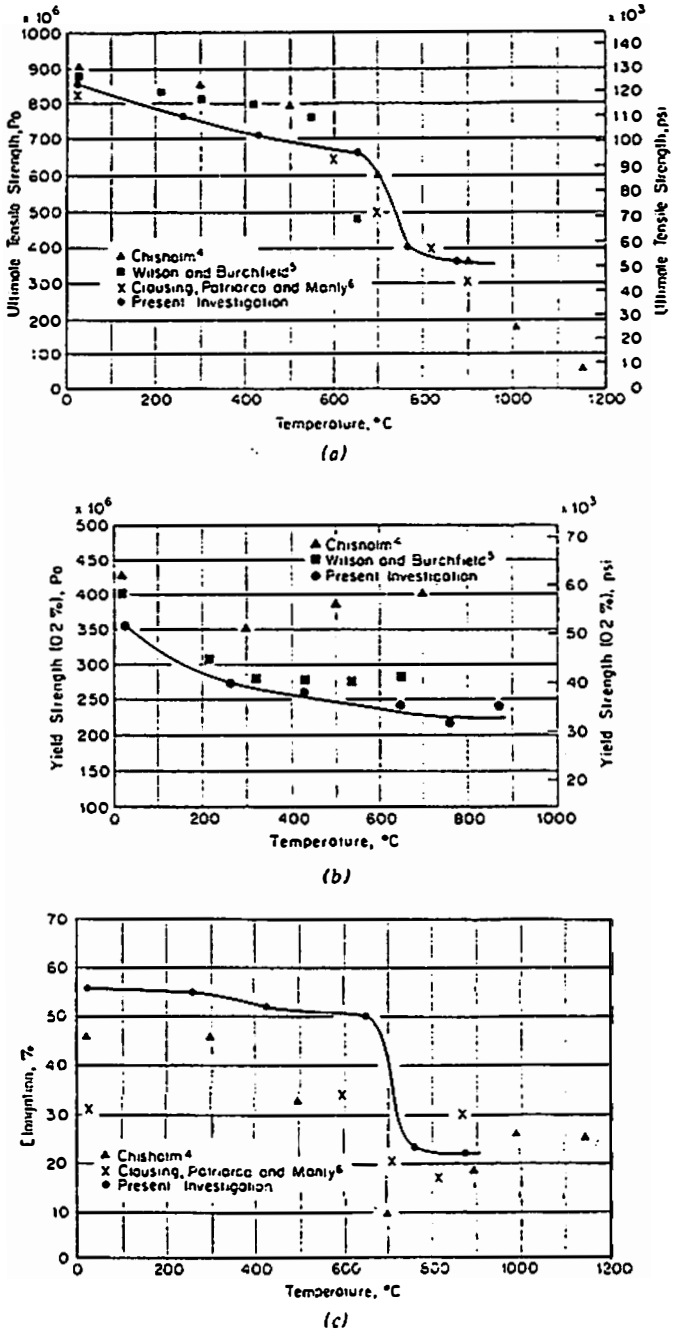



Figure 2-9. Tensile properties of solution annealed Hastelloy B alloy as a function of temperature.

SOURCE: D.F. Roan and C.R. Brooks, The Effect of Aging on the Mechanical Properties of a Nickel-Molybdenum-Iron Alloy (Hastelloy B), Metallurgical Transactions, 6A:1892-1831 (1975).

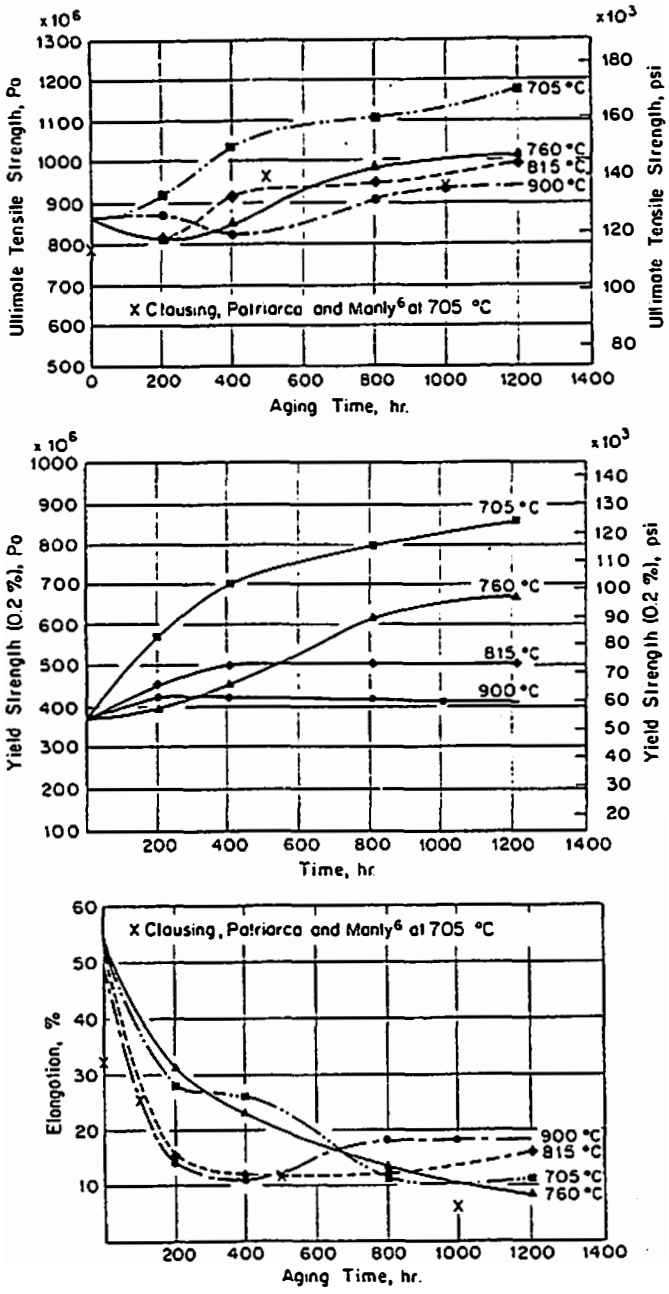



Figure 2-10. Tensile properties (at 25°C) of Hastelloy B as function of aging time and temperature.

SOURCE: D.F. Roan and C.R. Brooks, The Effect of Aging on the Mechanical Properties of a Nickel-Molybdenum-Iron Alloy (Hastelloy B), Metallurgical Transaction 6A:1829-1831 (1975).

nickel and molybdenum atoms on the parent lattice and the ordered phase β retains a crystallographic relation with the parent α phase. Hastelloy B2 alloy shows common characteristics of the phase transformations that occur in the Ni-Mo binary alloy. Thus, aging allows the formation of β phase with accompanying strengthening as well as embrittlement.

### 2.3.3 Effect of Aging Cold Worked α on Hardness

The disordered phase α can be retained by quenching. The kinetics of the disorder-order (α to β) transformation has allowed an examination of the interaction of recrystallization and ordering. Cao and Brooks [24] researched cold worked α upon aging to produce the ordered structure. They found that the cold worked α phase transformed to β phase which inherited the deformation structure of the α phase, and then the cold worked β recrystallized. The amount of recrystallization was a function of time and temperature. Recrystallization of the α structure was about 100 times slower than in the ordered β structure (see Figure 11).

Sanganeria and Brooks [25] investigated the effect of different aging temperatures and aging times on microhardness of the cold worked α phase. The results of their study are shown in Figures 12-16. The hardness of Hastelloy B2 alloy in the disordered α condition increased from about 200 DPH to 500 DPH after cold work by swaging (Figure 12). The cold worked specimens upon aging became long-range ordered (β) below 868°C. Aging at 850°C resulted in recrystallization of the α phase, with a reduction in hardness, then the formation of the ordered β, with the hardness increasing to about 550 DPH (Figure 13). Aging at 885°C, the hardness in the cold worked α condition decreased because of recrystallization of the α phase (see Figure 14). Aging at 700 and 775°C (Figures 15 and 16) resulted in the transformation of the cold worked α to cold worked,

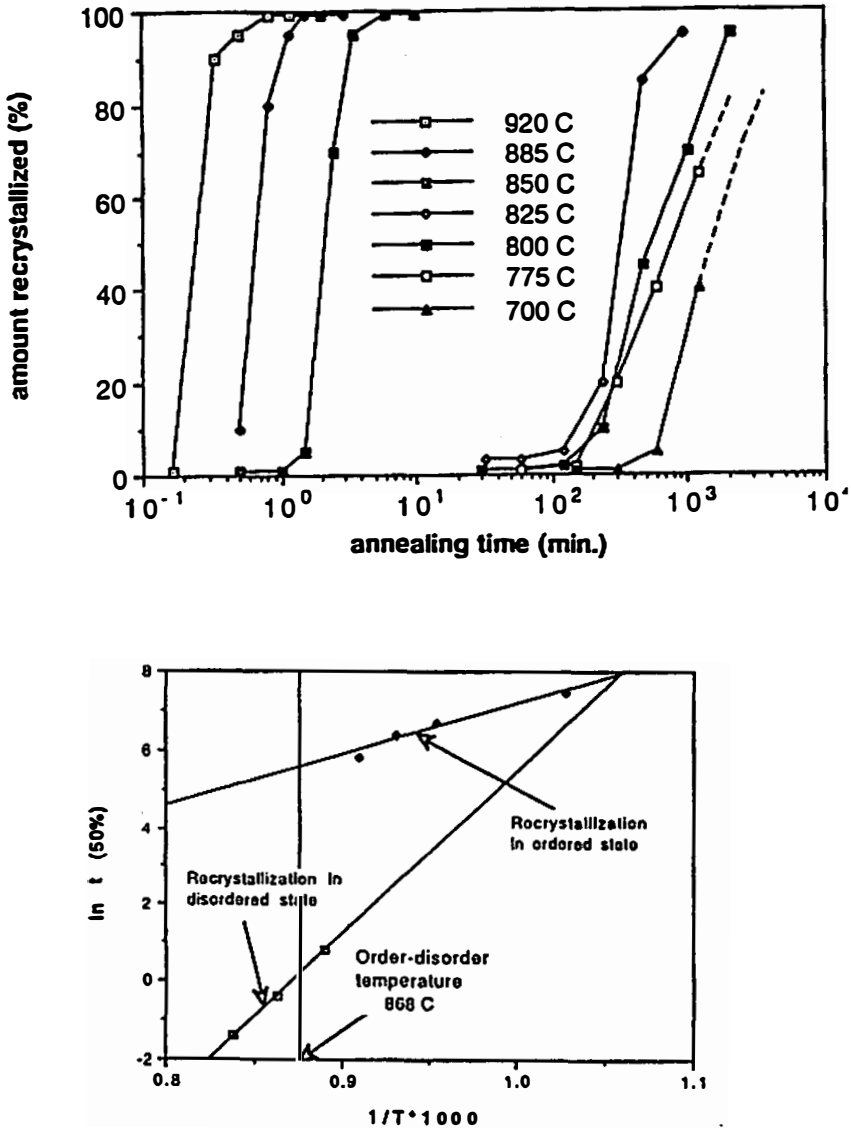



Figure 2-11. (a) The amount of recrystallization versus aging time for 43% cold worked material. (b) Arrhenius plot based on the time 50% recrystallization from the curves in (a). (The activation energies derived from the slopes for recrystallization from the disordered α structure and from the ordered β structure).

SOURCE: Siqi Cao and C.R. Brooks, Recrystallization of the Disordered and Ordered Structure in Ni-20 at.% Mo Alloy, Microstructural Science, 21:277-288 (1994).

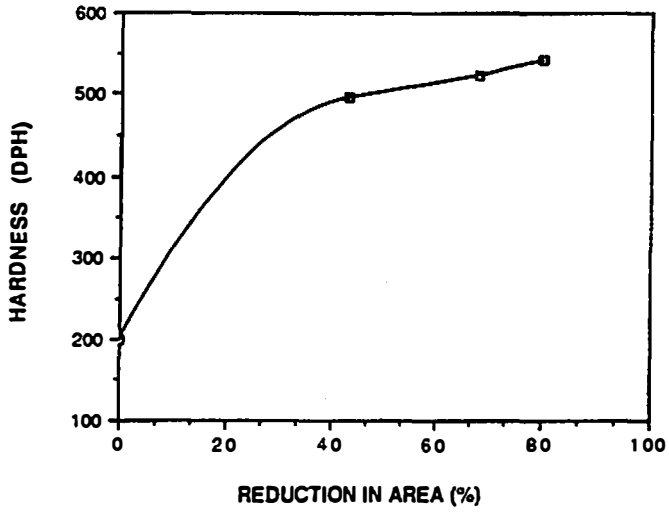



Figure 2-12. The effect of the amount of cold work (% reduction in area by swaging) on the hardness of a in the Ni-20 at.% Mo alloy.

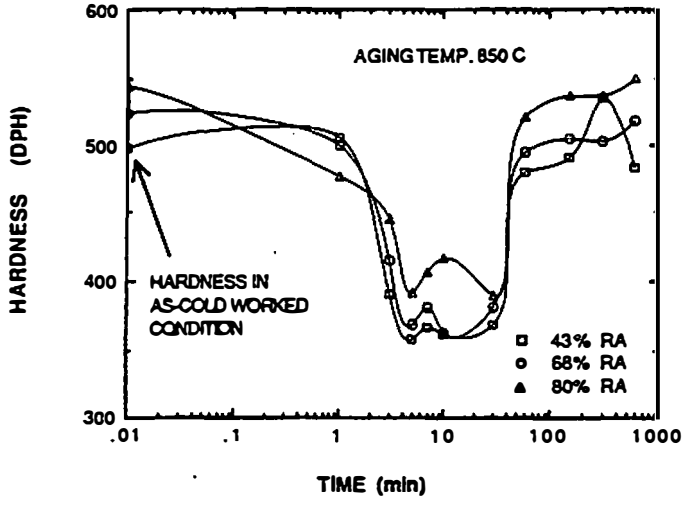



Figure 2-13. The effect of aging time at 850°C on the hardness of the Ni-20 at.% Mo alloy initially in the cold worked α condition.

SOURCE: M. Sanganeia and C.R. Brooks, The Effect of Cold Working on the Ordering Reaction in $Ni_4Mo$, Microstructural Science, 18:237-253, Editors T.A. Place, J.D. Braun, W.E. White and G.F. Vander Voort, ASM International, Materials Park, OH (1990). (for Figure 2-12 and 2-13)

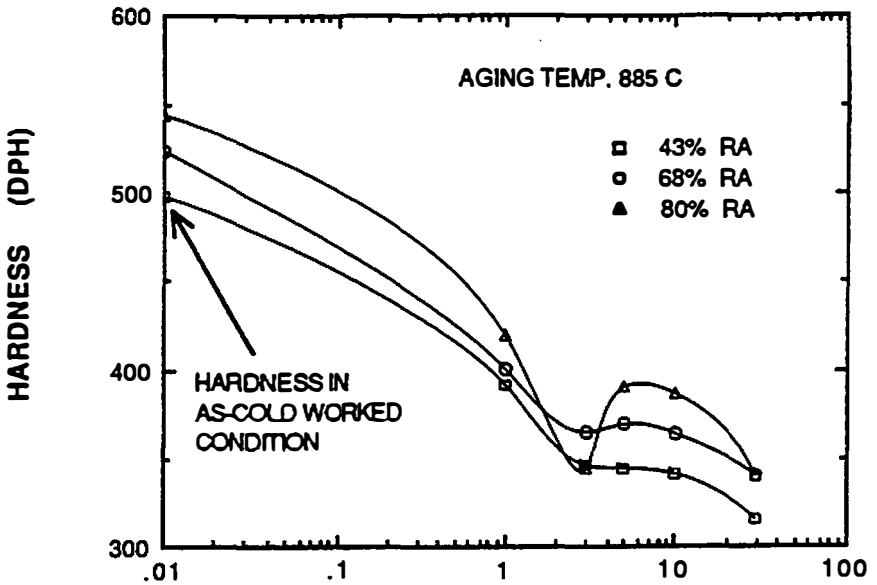



Figure 2-14. The effect of aging time at 885°C on the hardness of the Ni-20 at.%. Mo alloy initially in the cold worked α condition.

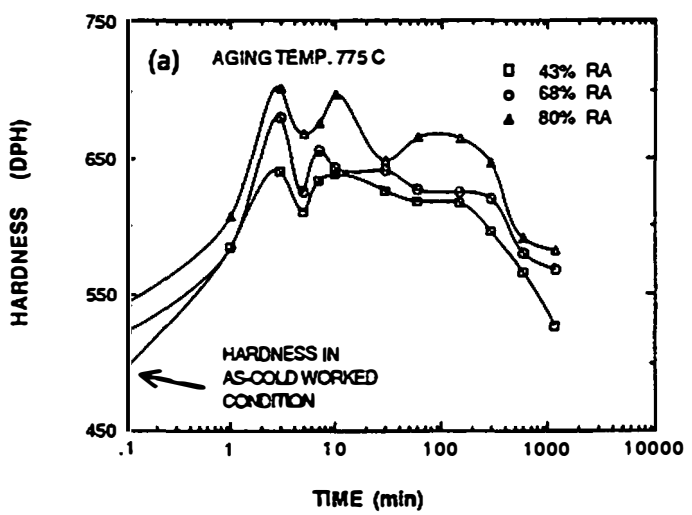



Figure 2-15. The effect of aging time at 775°C on the hardness of the Ni-20 at.% Mo alloy initially in the cold worked α condition.

SOURCE: M. Sanganeria and C.R. Brooks, The Effect of Cold Working on the Ordering Reaction in $Ni_4Mo$, Microstructural Science, 18:237-253, Editors T.A. Place, J.D. Braun, W.E. White and G.F. Vander Voort, ASM International, Materials Park, OH (1990). (for Figure 2-14 and 2-15)

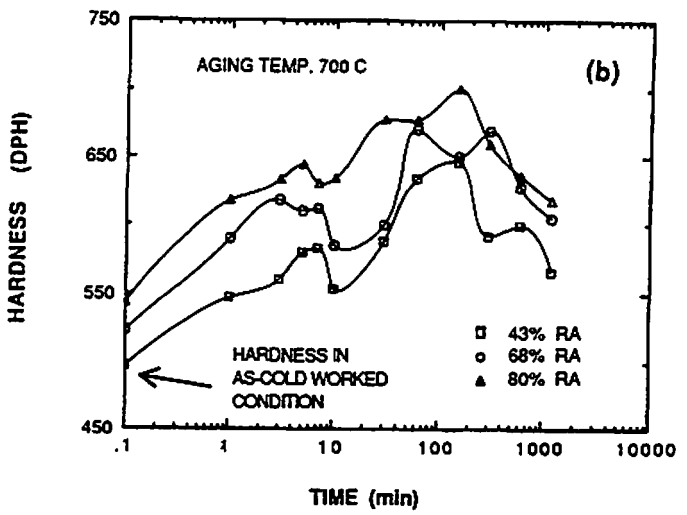



Figure 2-16. The effect of aging time at 700°C on the hardness of the Ni-20 at.% Mo alloy initially in the cold worked α condition.

SOURCE: M. Sanganeria and C.R. Brooked, The Effect of Cold Working on the Ordering Reaction in $Ni_4Mo$, Microstructural Science, 18:237-253, Editors T.A. Place, J.D. Braun, W.E. White and G.F. Vander Voort, ASM International, Materials Park, OH (1990). (for Figure 2-16)

ordered β, with the hardness approaching 700 DPH, followed by recrystallization of the β phase, with an associated decrease in hardness.

Ling et al. [26] studied the ordering transformation in an initially disordered and the cold-worked Ni-20 at.% Mo alloy. They investigated that by comparing changes in the hardness, the ordering transformation in an initially disordered and then cold-worked Ni-20 at.% Mo compared to an initially as-quenched Ni-20 at.% Mo alloy during progressive ordering. After same aging temperature and time, the maximum hardness in a cold-worked and ordered $Ni_4Mo$ (β phase) is attained faster than that for α phase as-quenched sample. The β domains in the cold-worked sample were apparently much finer than these formed from the quenched sample. In both the cold-worked and as-quenched alloys a recrystallization process was observed.

The energy introduced by cold-working is one of major driving forces for the recrystallization process. Brooks and Cao [27] obtained a group of curves of microhardness as a function of aging time at 850°C and 700°C and their results agreed with those obtained by Sanganeria and Brooks [25]. The appearance of recrystallization in the cold worked α phase prior to ordering at 850°C is attributed to the low disorder-order energy change compared with the stored energy of cold work. At 700°C, the disorder-order energy change is higher than the stored energy, and the deformed α phase is converted to deformed β phase, then recrystallization occurs. The reduction in hardness at long aging times is attributed to an increase in the long-range ordered β domain size. However, some deformed structure still remains at this point. The recrystallization process is heterogeneous due to the heterogeneity of the deformation structure. Brooks and Cao [27] summarized schematically the microhardness change with aging time during cold working at 850°C and 700°C (Figures 17 and 18). At 850°C (see Figure 17), the nucleation of recrystallized grains of α phase is associated with decrease of hardness.

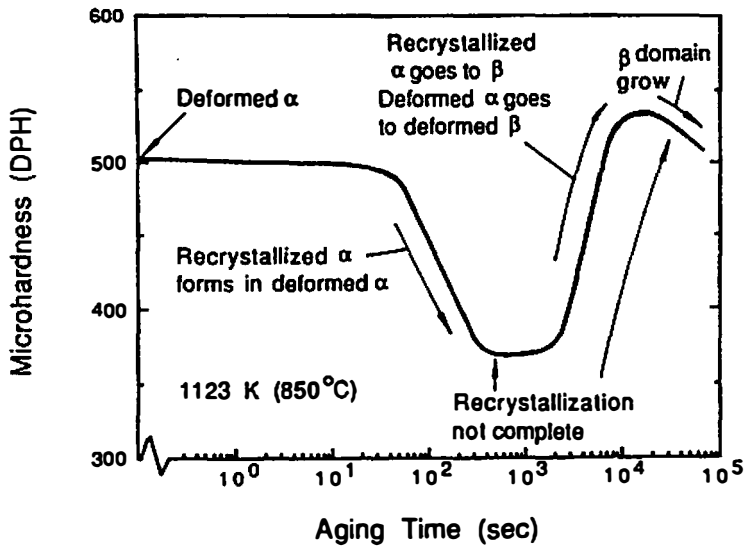



Figure 2-17. Summary of the structure changes which occur during aging cold worked α at 850°C.

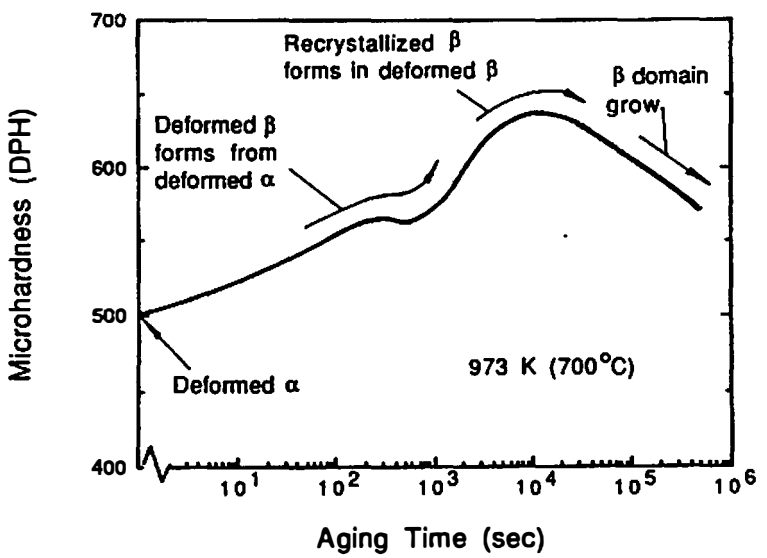



Figure 2-18. Summary of the structure changes which occur during aging cold worked α at 700°C.

SOURCE: C.R. Brooks and S. Cao, The Development of the Ordered Structure from Cold Worked Disordered Alpha in $Ni_4Mo$, Philosophical Magazine A, 65:327-353 (1992). (for Figure 2-17 and 2-18)

When the recrystallized region becomes ordered, there is an increasing hardness associated with this ordering. As β domains structure forms and coarsens with aging time, the hardness begins to decrease. Upon aging 700°C (see Figure 18), the deformed α phase quickly begins to form the ordered β phase, with a rise in hardness. When recrystallized β grains appear in deformed β which is ordered β phase, they continue to nucleate and grow to consume the deformed β structure. As the β domains increase in size, the hardness begins to decrease. However, the recrystallization response, whether occurring in the disordered α phase or the ordered β phase, has the expected dependence on temperature and amount of cold work.

## 2.4 Ordered and Disordered Structures in Ni-20 at.% Mo Alloy

Ordering reactions have been observed in many solid solutions, usually occurring on cooling, resulting in long-range ordered or short-range ordered states. In the LRO state specific atomic species occupy a specific set of lattice sites. The solubility of nickel in molybdenum is limited, but Mo is readily soluble in nickel. There are three intermetallic (ordered) compounds which occur at or near stoichiometry: $Ni_4Mo$ (β), $Ni_3Mo$ (γ), and NiMo (δ) (Figure 1). On heating, β and γ decompose by a peritectoid reaction, and δ decomposes by a peritectic reaction. Above 868°C the Ni-20 at.% Mo alloy exists face-centered cubic (FCC) terminal solid solution called the α-phase (short-range ordered state). Below this temperature, the structure is body-centered tetragonal β-phase (long-range ordered state) [28]. The atomic arrangement of molybdenum and nickel atoms in β is shown in Figure 19. The β structure consists of the molybdenum atoms occupying the (420) planes of the parent FCC lattice and nickel atoms occupying all other sites. A schematic diagram of β-lattice with relationship between FCC α-lattice and bct

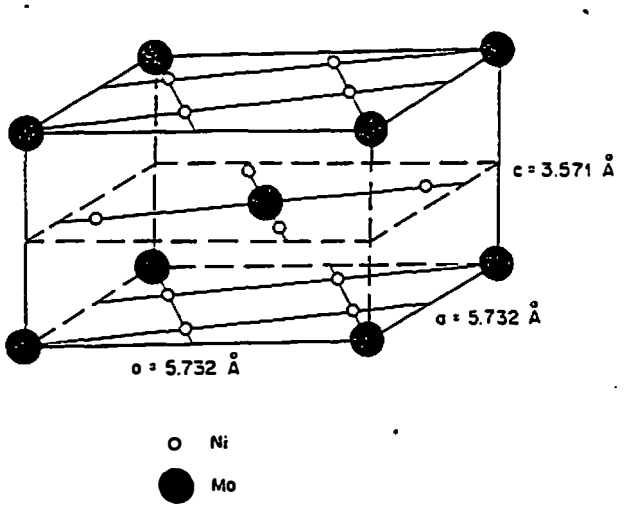



Figure 2-19. Crystal structure of b phase ($Ni_4Mo$).

SOURCE: C.R. Brooks, J.E. Spruiell, and E.E. Stansbury, Physical Metallurgy of Nickel-Molybdenum Alloys, International Metals Reviews, 29:210-248 (1984).

ordered lattice is shown in Figure 20. Thus, the transformation can occur just by nickel and molybdenum atoms locating properly on the parent α lattice [2]. Spruiell and Stansbury [28] studied the crystal structures of the Ni-10.7 at.% Mo and Ni-20 at.% Mo alloys using x-ray diffuse scattering measurement of quenched, and quenched and aged Ni-20 at.% Mo alloy. The α phase is not a random solid solution, but exhibits short range order (SRO). The SRO state is characterized by a diffuse peak at {1,1/2,0} in reciprocal space, which does not coincide with the fundamental FCC spots nor the 1/5 {420} LRO spots.

The long-range ordered β phase forms by randomly nucleations in the short-range ordered α matrix and growth. After impingement, long-range ordered β domains coalesce towards a configuration characterized by perpendicular twin plates. This rearranged domains structure is composed of a number of colonies [29].

## 2.5 The Effect of Alloy Elements in Ni-Base Alloys

The major alloying elements significantly affect the nickel-base alloys in their properties. Lecomte-Beckers [30] pointed out that the microstructure in nickel-base superalloys was found to depend greatly on aluminum and titanium contents. During solidification, the liquid metal in front of solid-liquid interface is enriched in titanium and molybdenum, whereas the dendrite cores are richer in cobalt. Kiriyenko et al. [31] stated that titanium, tungsten, zirconium, vanadium and niobium are stronger carbide formers than molybdenum. These alloying elements are used to improve the anticorrosion properties of Ni-Mo alloys in the temperature range near 1300°C, by transforming the carbon present in the alloy to a carbide phase without denuding the matrix of molybdenum. At 700-800°C the influence of these elements is obviously not due to

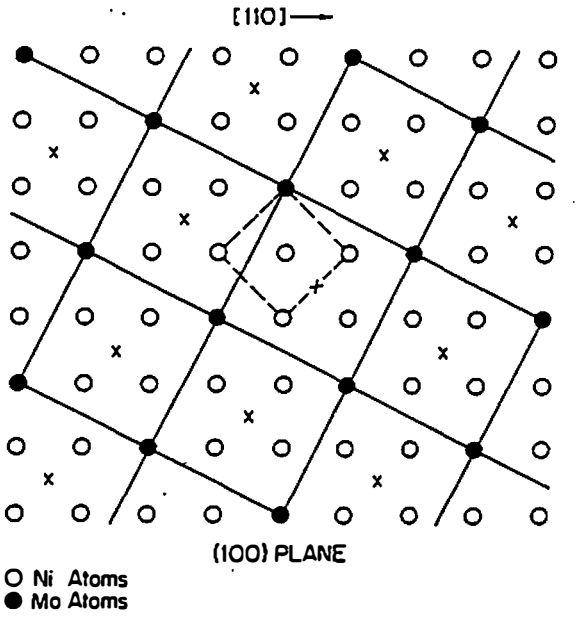



Figure 2-20. β-lattice with relationship between FCC α-lattice and bct ordered lattice; positions of Mo atoms in adjacent planes indicated by x.

SOURCE: C.R. Brooks, J.E. Spruiell, and E.E Stansbury, Physical Metallurgy of Nickel-Molybdenum Alloys, International Metals Reviews, 29:210-248 (1984).

carbide formation but other processes. Between 600 and 800°C ordering processes occur in Ni-Mo alloy systems, and these process mainly govern the corrosion properties. It is natural to suggest that the role of these elements in altering corrosion properties must be due to the effect on the processes of ordering.

However, additions of copper provide an improvement in the resistance of nickel to nonoxidizing acids and chromium added to Ni-Mo alloys improves resistance to oxidizing media [32]. Chromium also improves the resistance to high temperature oxidation and to attack by hot sulfur-bearing gases [7, 33]. Vasudevan and Stansbury [34] stated that addition of chromium is seen to have significant effects on $Ni_4Mo$ alloys for both short-range and long-range order. The degree of short-range ordering in as-quenched alloys decreases with an increase of chromium content, the formation of long-range order $Ni_4Mo$ is deterred with addition of chromium (3.84 wt.% Cr), and the retention of SRO state is independent of cooling rate. Iron increases the solubility of carbon in nickel and improves resistance to high-temperature carbonizing environments. Alloying with molybdenum is essential for corrosion resistance in reducing media and for resistance to localized corrosion attack. The solubility of molybdenum in $\alpha$ phase is of importance from a practical viewpoint because the precipitation of $\beta$ phase from $\alpha$ phase can lead to embrittlement. Thus, alloys developed for corrosion resistance in the $\alpha$ phase should be used at temperatures which place them in the $\alpha$ field at equilibrium within the design life of the component [2]. Molybdenum in nickel-base alloys markedly improves the pitting and crevice corrosion resistance [35, 36]. Tungsten behaves similarly to molybdenum in providing improved resistance to nonoxidizing acids and to localized corrosion [7]. Cobalt, like iron, increases the solubility of carbon in nickel-base alloys, and increases the resistance to carbonization [8]. Boron added to a Ni-27 wt.% Mo alloy caused the tensile ductility to increase from about 5 to 30 pct and changed the fracture mode from

predominantly intergranular into predominantly transgranular (Figure 21) [37]. When more than 10 at.% boron is added to Ni-Mo alloys (20-30 at.% Mo), they have high tensile strength and high hot hardness. These properties are derived from fine boride dispersions with good high temperature stability and the presence of ordered phases in a fine grained matrix [38]. Niobium and tantalum are added as stabilizing elements to tie up carbon and prevent intergranular corrosion attack due to grain-boundary carbide precipitation, but they reduce the tendency of nickel alloys toward hot cracking during welding [7, 39]. Aluminum and titanium are often used in minor amounts for the purpose of deoxidation or to tie up carbon. These elements enable the formulation of age-hardenable high-strength alloys for low and elevated temperature service. Aluminum can also be used to promote the formation of a tightly adherent alumina scale at high temperature that resists attack by oxidation, carbonization and chlorination [40]. The residual element sulphur at the migrated boundaries of Ni-20 at.% Mo alloy would be accumulation of sulphur from the bulk lattice as the boundary moves. At the aging temperature, the rate of sulphur diffusion was sufficiently high to allow it to maintain segregation to migrating boundaries. Thus, the residual element sulphur is segregated in the ordered $Ni_4Mo$ alloy and maintained at the moving boundaries [41, 42].

## 2.6 Heat Treatment

The physical metallurgy of Ni-Mo alloys was reviewed in detail by Brooks et al. [2]. Rapid cooling Hastelloy B2 alloy from 900°C to 25°C will prevent the formation of $\beta$ phase from $\alpha$ phase, and then the $\beta$ phase can be formed by aging below 868°C. Stansbury [43] stated that classical ordering phase transformations typically occur by nucleation and growth leading to C-type time-temperature-transformation curves. The

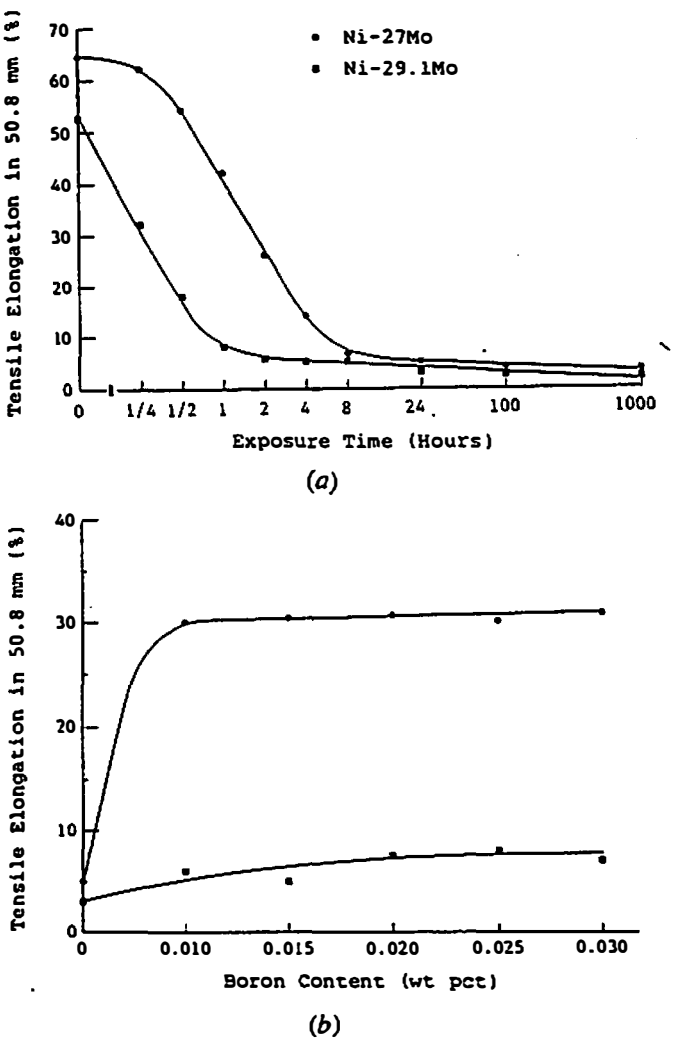



Figure 2-21. Effect of ordering in $Ni_4Mo$ on room temperature tensile ductility: (a) dependence of ductility on exposure time at 700°C for alloys free of boron and (b) effect of boron content on the ductility of alloys ordered to $Ni_4Mo$ (exposed 24 h at 700°C prior to testing).

SOURCE: H.M. Tawancy, Ductility of Ni- $Ni_4Mo$ Alloys by Boron Additions, Metallurgical Transactions A, 22:3067-3071 (1991).

transformation by a typical C-shaped curve is shown in Figure 22. It is clear that the transformation kinetics of α phase to β phase is very slow below 600°C. In the temperature range of 750°-868°C, the SRO to LRO transformation occurs by nucleation and growth of LRO domains in a SRO matrix [43]. The β phase can be formed in the α crystal by proper rearrangement of the atoms on the FCC lattice in local regions, and then the growth of these ordered regions by the interface movement.

Hastelloy B2 alloy displays some of the characteristics of Ni-20 at.% Mo binary alloy. The structure of the binary alloy is a face-centered cubic solid solution (α) above 868°C, and below this temperature the Hastelloy B2 alloy is composed of the compound, $Ni_4Mo$ (β phase). The ordering reaction can be suppressed by cooling rapidly from the α phase region, but the β phase forms rapidly upon holding in a temperature range of 600-850°C. The ordering reaction causes remarkable strengthening. The quantity of SRO α and LRO β is a function of temperature and time. Brooks et al. [20] reported that in the Hastelloy B2 binary alloy, the strengthening which occurs during aging is accompanied by embrittlement with fracture occurring along the former α high angle boundaries. Tillack [44] stated that the addition of aluminum and certain other alloying elements to nickel and nickel-base alloys produces an appreciable response to age hardening. The effect is dependent on both chemical composition and aging temperature. The precipitation of submicroscopic particles throughout the grains results in a significant increase in hardness and strength.

## 2.7 Microstructural Evaluation

It is important to study the microstructure evolution process in Ni-Mo alloys because it controls the mechanical properties. A number of investigations [22, 41, 42, 43,

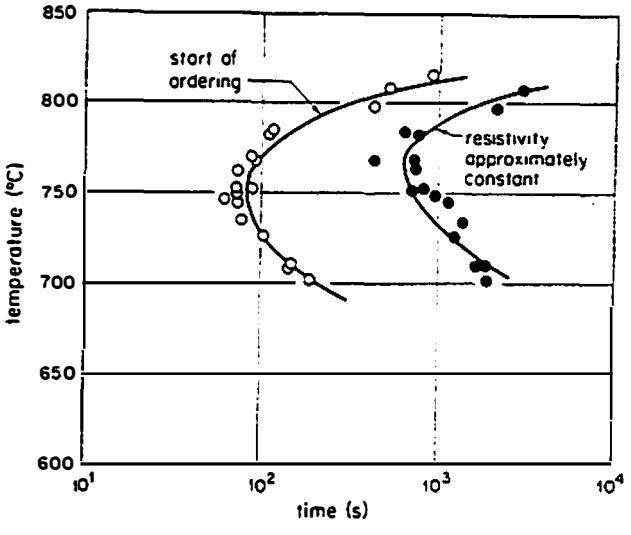



Figure 2-22. Isothermal time-temperature-transformation diagram for ordering reaction in Ni-20 at.% Mo.

SOURCR: C.R. Brooks, J.E. Spruiell and E.E. Stansbury, Physical Metallurgy of Nickel-Molybdenum alloys, International Metals Reviews, 29:210-248 (1984).

44, 47] have been carried out metallographic examination of the $Ni_4Mo$ system. Optical and electron microscopes were employed to evaluate the microstructures. Lei [18] observed the LRO state ($\beta$ phase) domains and SRO state ($\alpha$ phase) regions in Ni-20 at.% Mo alloy after aging one hour at 850°C. A typical microstructural morphology is shown the Widmanstatten pattern $\beta$ phase formation (Figure 23). Irani et al. [45] used plane-polarized light to follow an ordering reaction of Ni-20 at.% Mo alloy. Brooks et al. [42] conducted a microstructural examination of Hastelloy B2 alloy which was aged from 550 to 850°C for 200, 400, 800 and 1200 hours by using optical and scanning electron microscopes. They believed that the $\alpha$ phase has, at least initially, transformed to the $\beta$ phase, as this is known to cause hardening. Therefore, both OLM and SEM can be successfully used during the microstructural evaluation on Ni-Mo alloys.

## 2.8 X-Ray and Electron Diffraction

X-ray and electron diffraction are the best methods for detecting SRO-LRO phase transformation. Spruiell and Stansbury [28] used x-ray diffuse scattering measurements to investigate the structure of SRO in Ni-Mo alloy. They found that the diffuse scattering produced by SRO contained maxima located at the {1,1/2, 0} position in reciprocal space. Using electron diffraction to investigate the SRO-LRO transformation was frequently reported [6, 9, 27, 46, 48, 49]. Electron diffraction patterns from a Ni-20 at.% Mo alloy for order, disorder, and both order-disorder are exhibited in Figure 24 [48]. The TEM microstructure in $Ni_4Mo$ alloy was studied by many researchers [50 to 57]. TEM microstructure and electron diffraction approaches can be efficiently employed to define the SRO-LRO transformation.



Figure 2-23. Optical microstructure of β phase in $Ni_4Mo$. Note etched Widmanstatten pattern characteristic of the ordered domain structure.

SOURCE: T.S. Lei, Ph.D. Dissertation, University of Tennessee (1979).

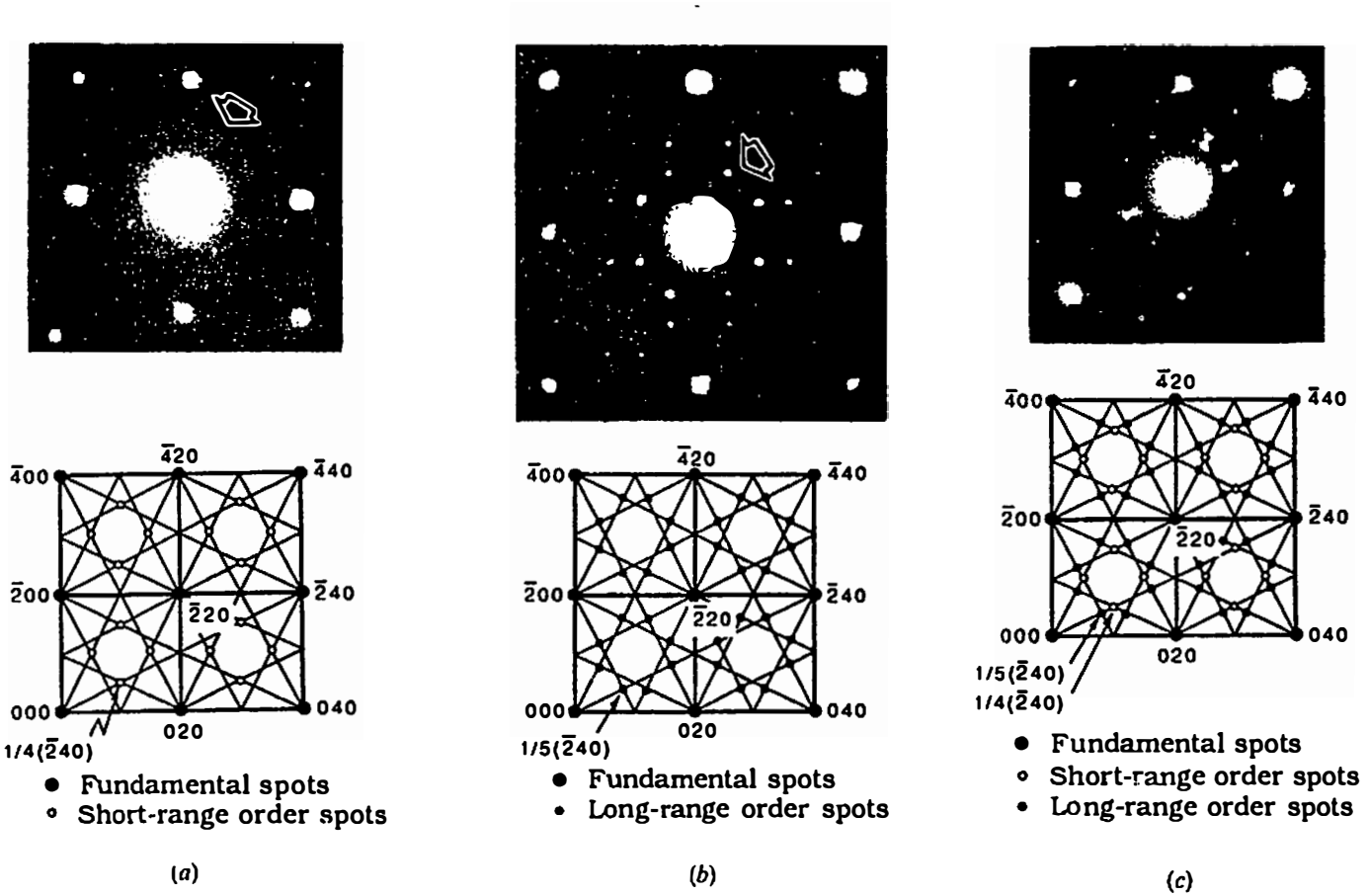



Figure 24. [001] electron diffraction patterns from a Ni-20 at.% Mo alloy a) disordered a showing SRO spots only arrow; b) ordered b showing LRO spots only arrow; c) pattern showing the LRO and SRO spots at an intermediate step in the disorder to order process.

SOURCE: S. Cao, C.R. Brooks and L. Allard, An in situ Transmission Electron Microscopy Study of Ordering in a splat Cooled Ni-20 at.% Mo alloy, Materials Characterization, 34:87-95, (1995).

## 2.9. Corrosion Resistance

Nickel offers very useful corrosion resistance itself and it is an excellent base on which to develop specialized alloys. The atomic size of nickel and nearly a complete 3d electron shell enable nickel to receive large amounts of alloying addition. When molybdenum is added in nickel, an alloy has been developed for service in environments of nonoxidizing solutions of HCl, $H_3PO_4$, HF and $H_2SO_4$. It is well known that sulfuric and hydrochloric acid are two of the most aggressive environments in the chemical industry. Hastelloy B2 alloy in a dilute deaerated sulfuric acid solution exhibits a low corrosion rate because the corrosion potential determined by the hydrogen reduction reaction is low. Sridhar [58, 59] claimed that the Hastelloy B and B2 alloys can be used to a higher temperature for all concentrations of acid. The high corrosion resistance of Hastelloy B2 alloy is shown in Figure 25. Hastelloy B2 alloy shows the highest resistance in HCl of all the Ni-base alloys. Thus this alloy is used in a variety of processes involving hot HCl or nonoxidizing chloride salts hydrolyzing to produce HCl. An illustration of corrosion behavior of Hastelloy B2 alloy is illustrated in Figure 26. [58, 59]. As indicated in Figure 26, Hastelloy B2 alloy shows two corrosion curves, one at high temperature near the boiling point and the other at low temperature. The different behavior is due to the variations of the oxygen content in the solution. At the higher temperature, the oxygen solubility is lower and, therefore, the corrosion rate is lower.

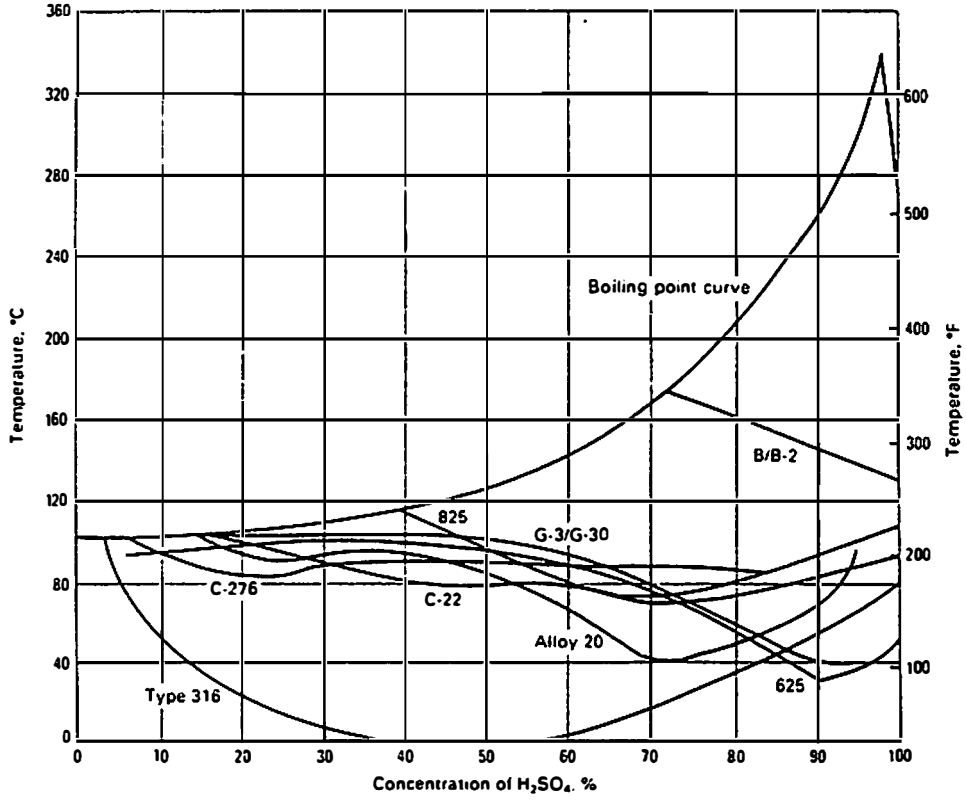



Figure 2-25. Comparative behavior of several nickel-base alloys in pure $H_2SO_4$. (The isocorrosion lines indicate a corrosion rate of 0.5 mm/yr.)

SOURCE: N. Sridhar, Behavior of Nickel-Base Alloys in Corrosive Environment in hydrochloric solution, Metals Handbook 9th Edition, Corrosion, 13:643-647 (1989).

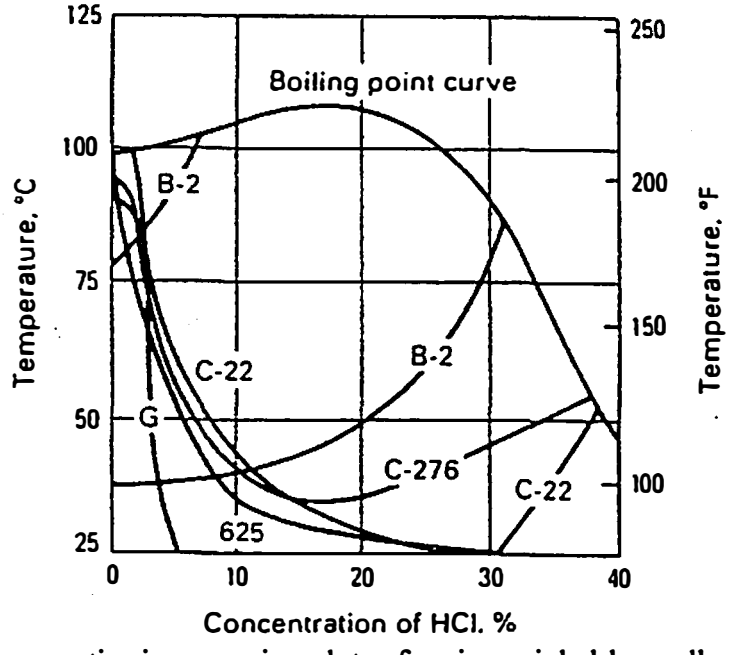



Figure 2-26. Comparative isocorrosion plots of various nickel-base alloys in hydrochloric solution. (The lines indicate a corrosion rate 0.13 mm/yr.)

SOURCE: N. Sridhar, Behavior of Nickel-Base Alloys in Corrosive Environment in hydrochloric solution, Metals Handbook 9th Edition, Corrosion, 13:643-647 (1989).

CHAPTER 3

# MATERIALS AND EXPERIMENTAL PROCEDURES

## 3.1. Chemical Composition

The base material of Ni-Mo alloy was received in the form of a hot forged bar. Its chemical composition is documented in Tables 3-1.

Table 3-1. Chemical composition (at.%/wt.%) of the $Ni_4Mo$ alloy studied.

| Ni | | Mo | | Al | | O | |
|---|---|---|---|---|---|---|---|
| at.% | wt.% | at.% | wt.% | at.% | wt.% | at.% | wt.% |
| 80.0 | 70.5 | 20.0 | 29.5 | <0.0003 | <0.01 | 0.0001 | 0.003 |

Four groups of laboratory type Ni-Mo-Al alloys with Al levels of 2, 5, 7, and 9 at.% (1, 2, 3, and 4 wt.%) were made. They were fabricated by remelting pieces of the $Ni_4Mo$ bar with pure aluminum additions using an arc-melting device in an argon atmosphere. The alloy systems studied are designated $Ni_4Mo$, 2 at.% Al, 5 at.% Al, 7 at.% Al, and 9 at.% Al alloys. The corresponding compositions are shown in Table 3-2. The aluminum content is based on the weighed aluminum added to the $Ni_4Mo$ bars, but the ingots were not chemically analyzed.

Table 3-2. Composition of laboratory Ni-Mo-Al alloys (at.%/wt.%).

| | Ni | | Mo | | Al | |
|---|---|---|---|---|---|---|
| | at.% | wt.% | at% | wt.% | at.% | wt.% |
| 2 at.% Al alloy | 78 | 69.8 | 20 | 29.2 | 2.0 | 1 |
| 5 at.% Al alloy | 76 | 69.1 | 19 | 28.9 | 5.0 | 2 |
| 7 at.% Al alloy | 74 | 68.4 | 19 | 28.6 | 7.0 | 3 |
| 9 at.% Al alloy | 73 | 67.7 | 18 | 28.3 | 9.0 | 4 |

## 3.2. **Materials Fabrication**

The alloys were produced in a conventional multi-hearth arc-casting furnace using a nonconsumable tungsten electrode and a low partial pressure of argon atmosphere. The samples were flipped 4 to 5 times and remelted during the process to ensure homogeneity. For each group of the test samples, the amount of aluminum content of 2, 5, 7 and 9 at.% (1, 2, 3, and 4 at.%) was added to the base $Ni_4Mo$ alloy to make the modified alloys. Then, all the samples in each group were capsulated in a quartz tube. The tube was evacuated and then backfilled with high purity argon at a reduced pressure. The argon pressure in the quartz tube was based upon a calculated value to accommodate less than 0.3 atm pressure for the homogenization temperature left out and each group samples were evacuated again on the tube sealed. The argon pressure in the quartz tube was less than 0.5 atm at various aging temperatures. Figure 3-1 shows some samples in the quartz tube.

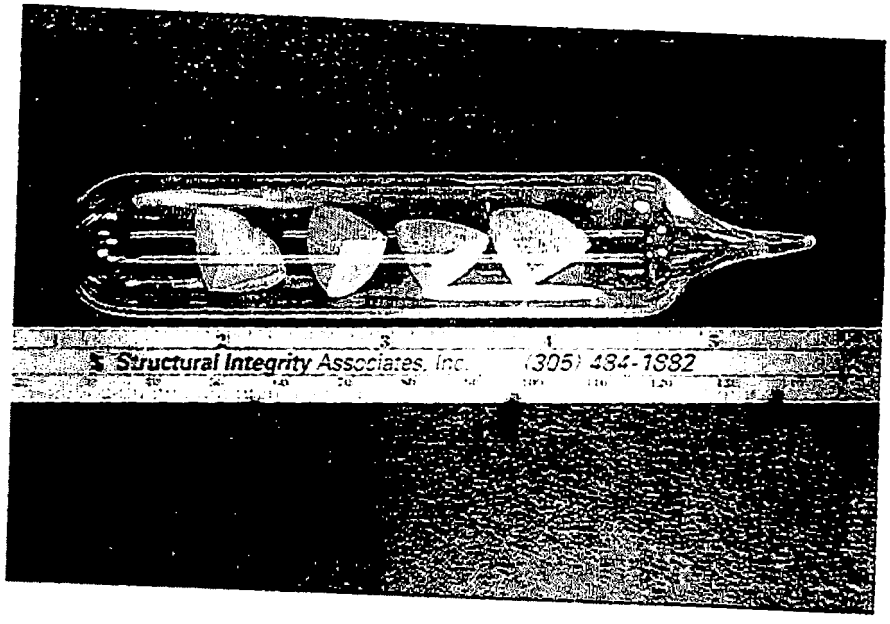



Figure 3-1. Samples sealed in a quartz tube and ready for heat treatment.

## 3.3. Heat Treatment

The heat treatments used in this study included homogenization heat treatment and elevated temperature aging. Each quartz tube contained 3 to 5 (with different aluminum contents) samples. The furnace temperature was checked randomly through out the period of each of the heat treatments. The temperature variations were within $\pm$ 5°C.

It was found that on aging at 650°C and 750°C for 100 hours without homogenization treatment, the microstructure in the alloys still had the dendritic structural appearance. Therefore, all the samples were homogenized in an argon atmosphere to reduce the compositional gradients associated with solidification. The first homogenized parameter was selected as 1250°C for 50 hours, but the microstructure of 9 at.% Al alloy showed particles in the grain boundaries and matrix. However, according to Ni-Mo-Al ternary phase diagram [65] at 1300°C and at 1260°C only $\alpha$ phase should be presented, so the homogenization parameter was selected as 1280°C for 50 hours followed by water quenching by breaking the tube under water in order to obtain the single $\alpha$ phase by arresting further phase transformation. Each group of samples was aged at 600°C, 650°C, 700°C, 750°C, 850°C, and 950°C for 100 hours. At the aging temperature of 750°C, aging times of 10, 50 and 100 hours were employed. After aging, the quartz tubes were broken under water with a hammer. The heat treatment conditions are summarized in Table 3-3.

## 3.4. Microhardness Measurement

A LEGO (Model M-400-G1) Vickers microhardness tester was used to conduct the hardness measurements. A 500 gram load and 15 second loading time were applied. The standard Rockwell test blocks (65.3 HRC, 46.5 HRC and 36.3 HRC) were used for a

Table 3-3. Heat treatment conditions employed

| | SHT temperature (°C) | SHT time (h) | AHT temperature (°C) | AHT time (h) |
|---|---|---|---|---|
| group 1 | No | No | No | No |
| group 2 | 650 | 100 | - | - |
| group 3 | 750 | 100 | - | - |
| group 4 | 1250 | 50 | - | - |
| group 5 | 1280 | 50 | 950 | 100 |
| group 6 | 1280 | 50 | 850 | 100 |
| group 7 | 1280 | 50 | 750 | 100 |
| group 8 | 1280 | 50 | 750 | 50 |
| group 9 | 1280 | 50 | 750 | 10 |
| group 10 | 1280 | 50 | 700 | 100 |
| group 11 | 1280 | 50 | 650 | 100 |
| group 12 | 1280 | 50 | 600 | 100 |

SHT: solution heat treatment

AHT: aging heat treatment

careful calibration prior to each group of the hardness measurements. For each of the samples used, a minimum of five measurements were performed and an average hardness value is reported. The variation was about $\pm$ 9 HV in the same location.

### 3.5. Optical Light Microscopic (OLM) Evaluation

For microstructure examination, the samples were sectioned into two parts. One part was used for metallographic examination and the other was used for preparing TEM samples. OLM metallographic samples were mounted in conductive bakelite and the sectioned surface was used for the examination to avoid surface effects. All samples were wet ground up to 600 grade using SiC paper and the final surface finishing was a 0.05 μm $Al_2O_3$ slurry. Finally, the metallographic samples were chemically etched in the solution in Table 3-4.

Table 3-4. Etching solution for OLM microstructural study.

| HCl | $H_2O$ | $CrO_3$ |
|---|---|---|
| 150 ml | 100 ml | 25 g |

During etching, the sample was swabbed for 3 to 10 seconds with a cotton ball at room temperature. Then, the etched samples were washed with distilled water and methanol then dried immediately. The etched surface was examined under an EPIPHOT-TME Model metallurgical microscope at various magnifications and the typical images were documented.

## 3.6 Scanning Electron Microscopy (SEM) and Energy Disperse Spectrometer (EDS) Investigation

A scanning electron microscope (SEM) equipped with an energy dispersive spectrometer (EDS) possesses an unique capability to do microstructural analysis and surface chemical analysis. The resolution of a SEM is significantly higher than an OLM, thus detailed microstructural information can be gained by SEM examination. By using backscattered electron imaging (BSE), Z-contrast (chemical contrast) can reveal elemental distribution patterns in a sample. Therefore, the information of general chemical distribution can be manifested qualitatively by employing Z-contrast technique. Both secondary electron imaging (SE) and backscattered electron imaging (BSE) techniques were used in order to obtain maximum information.

In this research, the detailed microstructures of the modified alloys were evaluated using a Cambridge Stereoscan (Model 360) SEM equipped with a EDS analytical system (Model 10,000 LINK).

## 3.7. Fractographic Study Using SEM and EDS

Fractographic examination of bend-rupture samples was conducted utilizing Cambridge Steroscan Model 360 SEM. Samples in three different heat treatment conditions were chosen for fractographic examination. One condition was solution treatment alone, for which the sample had been heated to 1250°C, held at that temperature for 50 hours, then water quenched. Two other conditions were solution treatment (1280°C for 50 hours) plus an aging at 750°C and at 950°C for 100 hours followed by water quenching. The cracking tendency of the materials as a function of

aluminum content was studied through the bend-rupture specimens. A schematic drawing of the bending fixture used is shown in Figure 3-2. Two different bending radii, 10 mm and 13.5 mm, were applied.

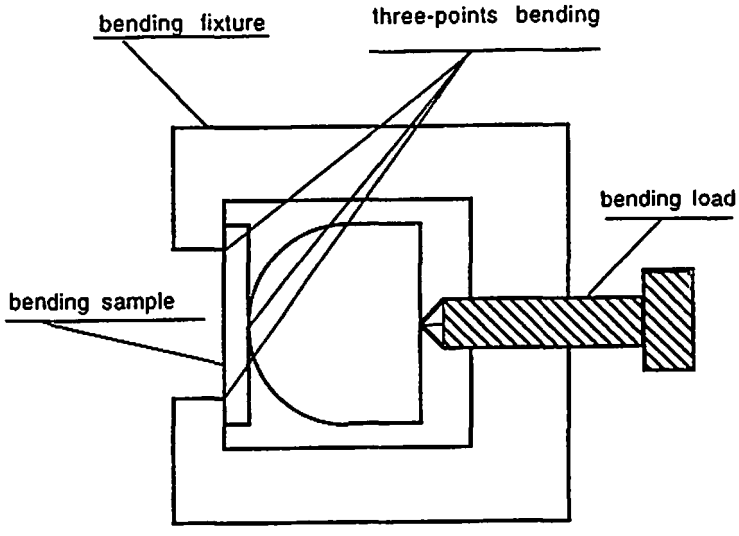
The bending rupture sample was machined in a plate form with a dimension of 1 x 25 x 28 mm. Prior to the bending process, one side of the larger surface of the plate was metallographic alloy polished to 0.05 μm $Al_2O_3$ slurry and etched in order to study the surface deformation and rupture phenomena. The sample was placed in the three-point bending fracture. The bending load was slowly applied until cracking was observed by naked eye. The sample was examined under SEM to determine the crack propagation direction relative to the microstructural features. The sample was further bent to advance the cracks until it was completely fractured after preliminary SEM examination. The fracture surface was examined again under SEM.

## 3.8. **Transmission Electron Microscopy (TEM)**

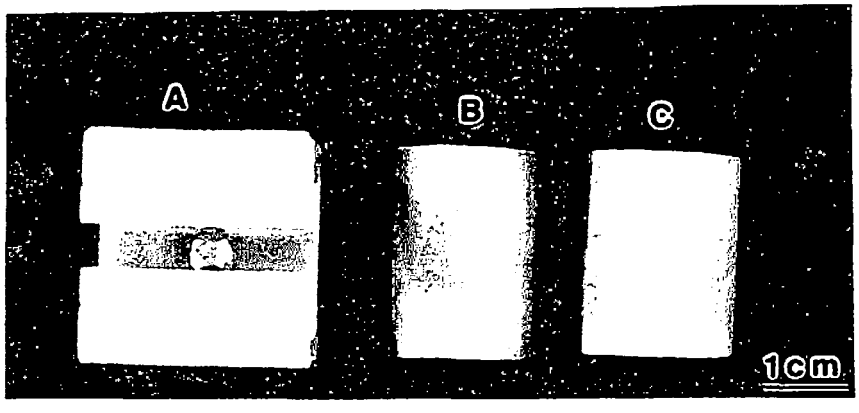
In this section, detailed information is given about the order of materials and heat treatment conditions used for TEM examination samples, preparation of TEM specimens, microstructural characterization, and constituents analysis.

### 3.8.1. Materials and Heat Treatments Applied for TEM Study

Two basic groups of materials were examined for TEM evaluation. The first group was prepared from a quarter bottom of the arc-melted ingot of the $Ni_4Mo$ alloy and the Ni-Mo-Al alloys. The TEM evaluation was undertaken for various heat treatments. The second group of materials used for TEM evaluation was commercial Hastelloy B2 alloy without aluminum additions. The chemical composition of the Hastelloy B2 alloy




(a)




A: Bending-fixture
B: Bending block, radius 10 mm
C: Bending block, radius 13.5 mm

(b)

Figure 3-2. (a). Schematic diagram of the three-point bending-fixture used to initiate cracking: (b). The real bending-fixture.

is in Table 3-5. The specimens were prepared in different aging conditions. The materials received were 6.4 mm in diameter swaged rods that were solution-annealed for 100 hours at 1065°C followed by water quenching. The rods were then further swaged to a diameter of 3.2 mm and solution annealed for 2 hours at 1065°C followed by water quenching. The solution heat treatments were carried out in an argon atmosphere. The samples were sealed in quartz tubes under an argon atmosphere, and then heated at 550°C, 650°C, 750°C, and 850°C for 200, 400, 800, and 1200 hours.

Table 3-5. Chemical composition (wt.%) of the Hastelloy B2 alloy studied

| Ni | Cr | Mo | Fe | Si | Mn | C | P | S |
|---|---|---|---|---|---|---|---|---|
| Bal. | 0.97 | 27.62 | 0.82 | 0.02 | 0.26 | <0.10 | 0.005 | <0.002 |

3.8.2. TEM Specimen Preparation

From the small arc-melted ingot samples ($Ni_4Mo$ alloy with aluminum additions), about I mm thickness thin discs were sliced from the heat treated materials with a high speed, thin abrasive blade with copious water for cooling. The thin discs were ground about 3 mm in diameter thinner plate. The thickness of these discs was wet ground at 600 grade using SiC paper by slow speed hand grinding, and reduced to an approximately 0.3 mm thickness.

For the Hastelloy B2 alloy, the disc specimens were cut from the aged rods at about I mm thickness, then they were wet ground at 600 grade using SiC paper by slow speed, hand grinding to approximately 0.3 mm in thickness.

The ready discs (about 0.3 mm in thickness) were further electrochemically thinned at their center by using a Struers Tenupol type twin jet polishing apparatus,

equipped with a photocell to detect light from the initial penetration of the specimen, by which the power of the cell could be automatically cut-off thereupon.

(a). For the arc-melted ingot samples, two different jet polishing solutions were used. One solution was composed of $H_4PO_3$, $H_2SO_4$, and HCl (Table 3-6). The operation parameters were voltage: 5 to 10 V, current: 0.3 to 0.5 A, temperature: -25°C to -10°C, followed by water and methanol rinses. If the jet polishing sample was too thick to clearly observe the microstructure under TEM, the specimen was jet polished again with a different solution (Table 3-7). The operation parameters were voltage: 30 to 40 V, current: 0.3 to 0.4 A, temperature: -5 to 0°C. The electrolytically polished samples were washed once in distilled water then methanol. The cleaned specimens were dried in air on lint-free paper.

Table 3-6. Jet polishing solution 1

| $H_4PO_3$ | $H_2SO_4$ | HCl | $H_2O$ |
|---|---|---|---|
| 640 ml | 150 ml | 35 ml | 210 ml |

Table 3-7. Jet polishing solution 2

| Butanol | HCl | Methanol |
|---|---|---|
| 175 ml | 30 ml | 300 ml |

(b). For Hastelloy B2 alloy without Al additions, the electrochemical polishing solution was composed of $H_4PO_3$, $H_2SO_4$, and HCl (Table 3-6). Electrolytic thinning conditions were: voltage 10 to 15 V, current 0.1 to 0.15 A; temperature -5°C to 0°C. The electrolytically polished specimens were washed in distilled water and methanol. The cleaned specimens were dried in air on lint-free paper.

In order to obtain the best prepared condition, an ion milling process was carried out on the twin jet polished specimens. A Model 600 Dif and 600 TMP Duo Mill™ type ion milling apparatus was employed. Liquid nitrogen was used to maintain a relatively low temperature for the specimen area. The ion milling conditions were voltage: 6V, beam angle: 12 to 15°, gun current: 0.5 to 0.7A, the time spent: 30 minutes.

### 3.8.3. TEM Microstructural and EDS Analyses

The TEM thin disc samples were examined in a Phillips Model CM-12 transmission electron microscope at 120 KV. The microstructural features were characterized by representative photomicrographs. The microstructure and microconstituents were also characterized by electron diffraction patterns. Typical TEM microstructure and electron diffraction patterns were obtained. A Model PV9900 energy dispersive spectrometer was used for obtaining chemical X-ray analysis.

## 3.9. Corrosion Resistance Evaluation

### 3.9.1 Investigation of the Corrosion Resistance of $Ni_4Mo$ Alloy

A $Ni_4Mo$ alloy has useful resistance to a variety of corrosives. But the subject of metallic corrosion is highly complex, involving consideration of the microstructural features of the alloy. The various reactions may occur at the metal and environment interface and depend on the chemical nature of the environment. Thus, the corrosion resistance investigation on the $Ni_4Mo$ alloy was performed consisting of three approaches described in the following sections.

a). ASTM A262 Practice A Examination

A262 Practice A test is used for acceptance of materials and also is used in connection with other evaluation tests to provide a method for identifying samples which are certain to be free of susceptibility to intergranular attack. After the A262 Practice A test, the etched surface is examined with an optical light microscopy. The etched structures are classified into the following types: step structure, dual structure, ditch structure, end-grain pitting I, and end-grain pitting II. Only a ditch structure is not acceptable.

The sample in the form of a hot forged bar was received for this test. The microstructure showed a single $\alpha$ phase and no $\beta$ phase was observed. The sample of surface area 10 X 10 mm was mounted in epoxy. It was wet ground to 600 grade using SiC paper and the final surface finishing was 0.05 $\mu$m $Al_2O_3$ slurry. The solution for A262 Practice A [60] was prepared by adding 100g of reagent grade oxalic acid crystals to 900 ml of distilled water (10% oxalic acid), then stirring until all crystals were dissolved.

A A225BR2 D-C Amplifier and a V202AR2 D-C Voltammeter was employed for the ASTM A262 test. After placing the specimen into the electrolyte (10% oxalic acid), it was contacted as an anode and an AISI 304 austenitic stainless steel container was employed as a cathode in the oxalic acid to form a circuit. A current density of 1 $A/cm^2$ was employed for 1.5 minutes. Then the sample was washed with distilled water immediately after etching. The etched surface was examined under an optical light microscope at 200X to document the corrosion results.

b). Potentiodynamic Anodic Polarization Testing

Potentiodynamic anodic polarization is the characterization of a metal specimen by its current-potential relationship. The results can give information about polarization

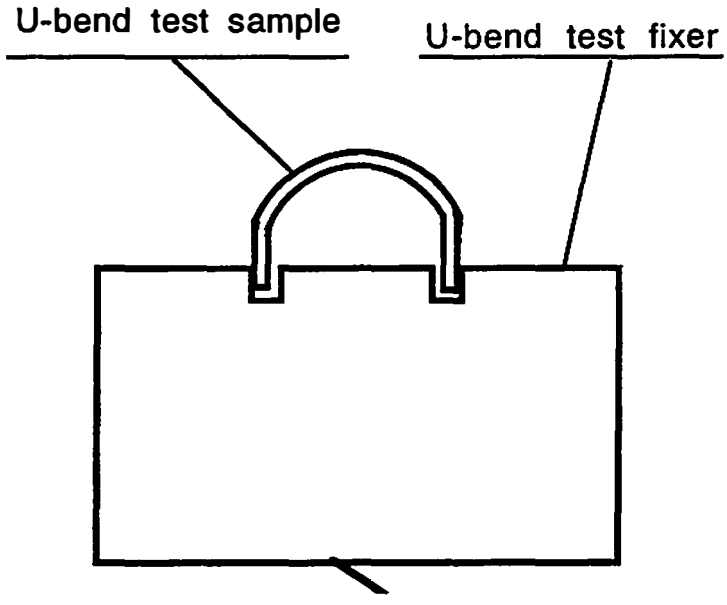
of an active-passive alloy and also may be used to judge the corrosion resistance of alloy and the corrosive strength of the solution.

An EG & G Model 273 Potentiostat with $Soft_{corr}$ Corrosion Measurement Software was used for the potentiodynamic anodic polarization test. The specimen surface was 10 X 10 mm with a final surface finish of 0.05 μm $Al_2O_3$ slurry. In accordance with ASTM G5-87 [61], the solution was prepared with 1000 ml of 1.0N $H_2SO_4$ reagent grade acid and distilled water (49g $H_2SO_4$, 1000 ml $H_2O$). The apparatus included a potentiostat, a working electrode (the specimen), a reference electrode (saturated calomel), a counter electrode (platinum), a high input impedance voltmeter, and a polarization cell. Reduction of oxygen level in the solution prior to immersion of the test specimen was accomplished by bubbling nitrogen for 30 minutes. Then, the specimen was moved into the test cell. The open circuit specimen potential was recorded until the potential was stable. In the potentiodymamic method, a potentiodynamic potential sweep rate of 0.6 V/h was utilized while recording the resultant current.

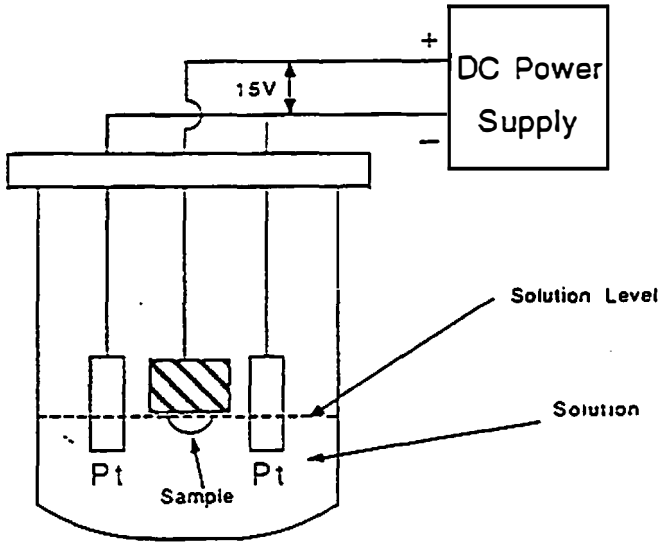
c). Modified ASTM G-30 U-Bend Test

The U-bend test can be used for evaluation of stress-corrosion cracking in metals. It is useful for determining the relative susceptibility of a metal to intergranular stress corrosion cracking.

The size of the simplified U-bend test specimen was 3 X 5 X 0.05 cm. The examined surface was wet ground by using 600 SiC paper prior to the final finishing of 0.05 μm $Al_2O_3$ slurry. The specimen was deformed in mainly plastic deformation into the U-shape with a designed fixture (Figure 3-3a). The fixture was made of 304 stainless steel. The bend specimen radius was 12 mm resulting in a total strain of $s = T/2R = 0.021$ (ASTM-G30) [62]. The testing was conducted using a DC power supply. The anode




(a)



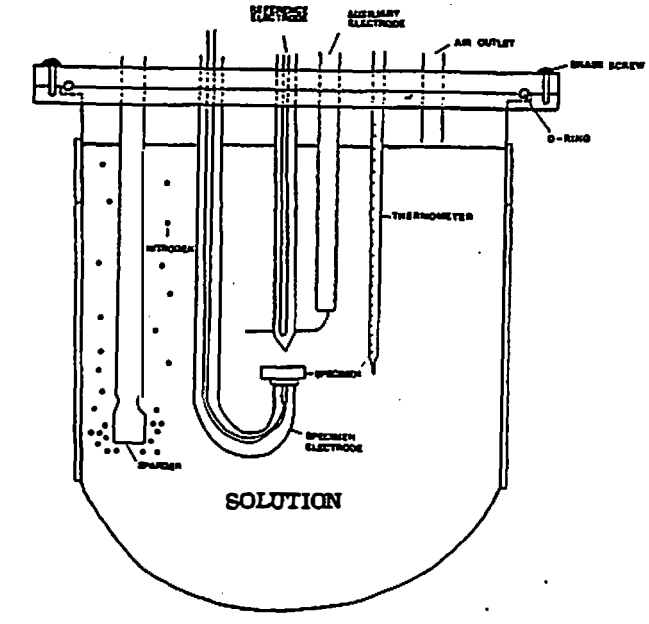

(b)

Figure 3-3. (a) The specimen was deformed into the U shape with a designed fixture
(b) Schematic diagram of the U-bend test working circuit.

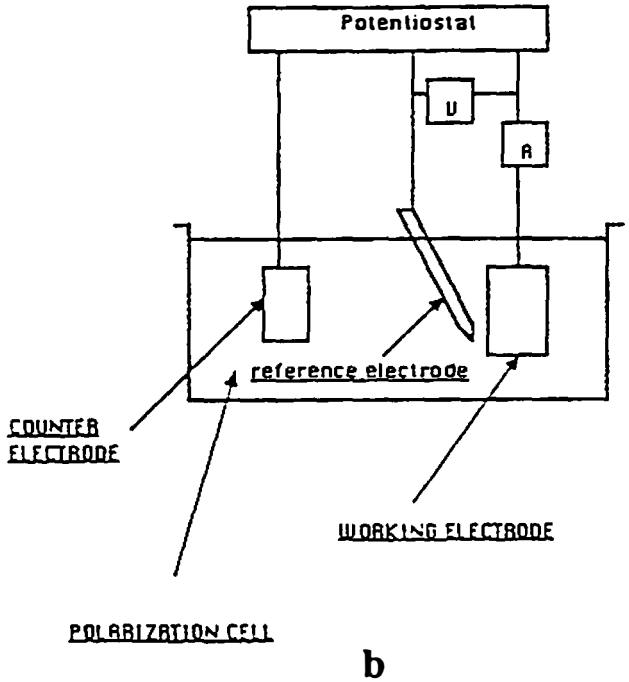
(the specimen) and cathode (platinum) were placed in the electrolyte (1N sulfuric + 0.5N NaCl [63]) and connected into an electronic circuit. During testing, the specimen was placed in a glass container containing the solution composed of $H_2SO_4$ + NaCl and distilled water (49 g $H_2SO_4$, 20 g NaCl, and 1000 ml $H_2O$). The current density was 0.25 $A/cm^2$ and the testing time was 2 hours. Under a microscope, the specimen surface was examined. The modified U-bend test apparatus is schematically shown in Figure 3-3b.

### 3.9.2. Potentiodynamic Evaluation for the Ni-Mo-Al Alloys

For the $Ni_4Mo$ bar alloy and the Ni-Mo-Al alloys, cyclic anodic polarization testing and the polarization resistance testing were selected for evaluation of corrosion. The alloys were electrochemically tested in terms of general corrosion resistance. A comparison of the corrosion tendencies between modified alloys and $Ni_4Mo$ alloy was carried out. $Ni_4Mo$ and Ni-Mo-Al samples aged at 750°C for 100 hours were used for this examination. The samples were mounted in epoxy and the surface area was 25 X 25 mm. The final surface finishing was made using 600 grade SiC paper. The solution was prepared with 800 ml distilled water and 200 ml HCl. The apparatus used for the test included an EG&G Model 273 Potentiostat, a working electrode (the specimen), a reference electrode (saturatedcalomel), a counter electrode (platinum), a high input impedance voltmeter, an ammeter, and a polarization cell. Maintaining a constant oxygen level in the solution prior to immersion of the test specimen was accomplished by sparging with air. Then, the specimen was placed into the test cell, the reference electrode adjusted, and the open circuit specimen potential (corrosion potential) was recorded. In the polarization resistance and cyclic anodic polarization methods, a potential scanning rate of 0.6 V/h was utilized. The experimental circuit is schematically illustrated in Figure 3-4.




a




b

Figure 3-4. (a) Schematic diagram of electrochemical polarization cell; (b) Schematic diagram of the electrochemical polarization working circuit (V: voltammeter, A: amperemeter).

## CHAPTER 4

# RESULTS AND DISCUSSION

The results of hardness measurements, microstructural observations, fractographic evaluation and corrosion resistance assessment are presented and discussed in this chapter. The emphasis is on the effect of the Al additions to the base $Ni_4Mo$ alloy. By far most of the research involved microstructural examination, especially transmission electron microscopy, and the results concentrate on this part of the study.

## 4.1. Hardness Measurements

The hardness results are discussed for two separate groups of materials. The first group of materials was not solution heat treated and therefore, in the sample with a low temperature aging condition, clear evidence of the casting structure is exhibited. The second group of materials was solution heat treated at 1280°C for 50 hours followed by water quenching, and a well homogenized solution-annealed microstructure is clearly manifested. Materials in both groups showed a trend of hardness as a function of aging parameters and aluminum content which will be further correlated to their microstructural evolution. For each sample, more than five measurements were conducted and an average hardness value is reported. The variation is $\pm$ 9 HV in the same phase.

### 4.1.1 Hardness Measurements in the Alloys in the As-Cast Condition (without Homogenization)

In this group, hardness measurement results are discussed in terms of aging parameters (temperature and time) and amount of aluminum addition for the as-cast condition. The relationship between hardness and aging condition and aluminum content especially reflects the microstructural changes.

#### 4.1.1.1 Aluminum Content Effect

The effect of aluminum on the hardness is shown in Figure 4-1. In the as-cast condition, the hardness remained stable from 0 to 2 at.% aluminum and increased slightly from 2 to 5 at.% aluminum. Then, on further increase of aluminum content from 5 to 7 at.%, the hardness increased dramatically. For all alminum additions, aging at 650°C produced hardnesses about 100 to 200 HV above those of the as-cast condition, and aging 750°C increased the hardness another 100 to 200 HV increment. Homogenizing the as-cast material for 50 hours at 1250°C gave the same hardness curve as the as-cast condition.

#### 4.1.1.2. Aging Parameter Effect

The hardness data are plotted against aging temperature in Figure 4-2. Also shown is the hardness in the as-cast condition and after a solution heat treatment of 1250°C for 50 hours. There is a marked increase in hardness upon aging at 650°C, and then an additional increase upon aging at 750°C. Note especially that the hardness of the 5 and 7 at.% Al alloys has increased to around 600 to 650 HV. The solution heat treated hardness was somewhat higher (about 100 HV) than that of the as-cast condition, but considerably lower than the peak hardness attained upon aging at 750°C.

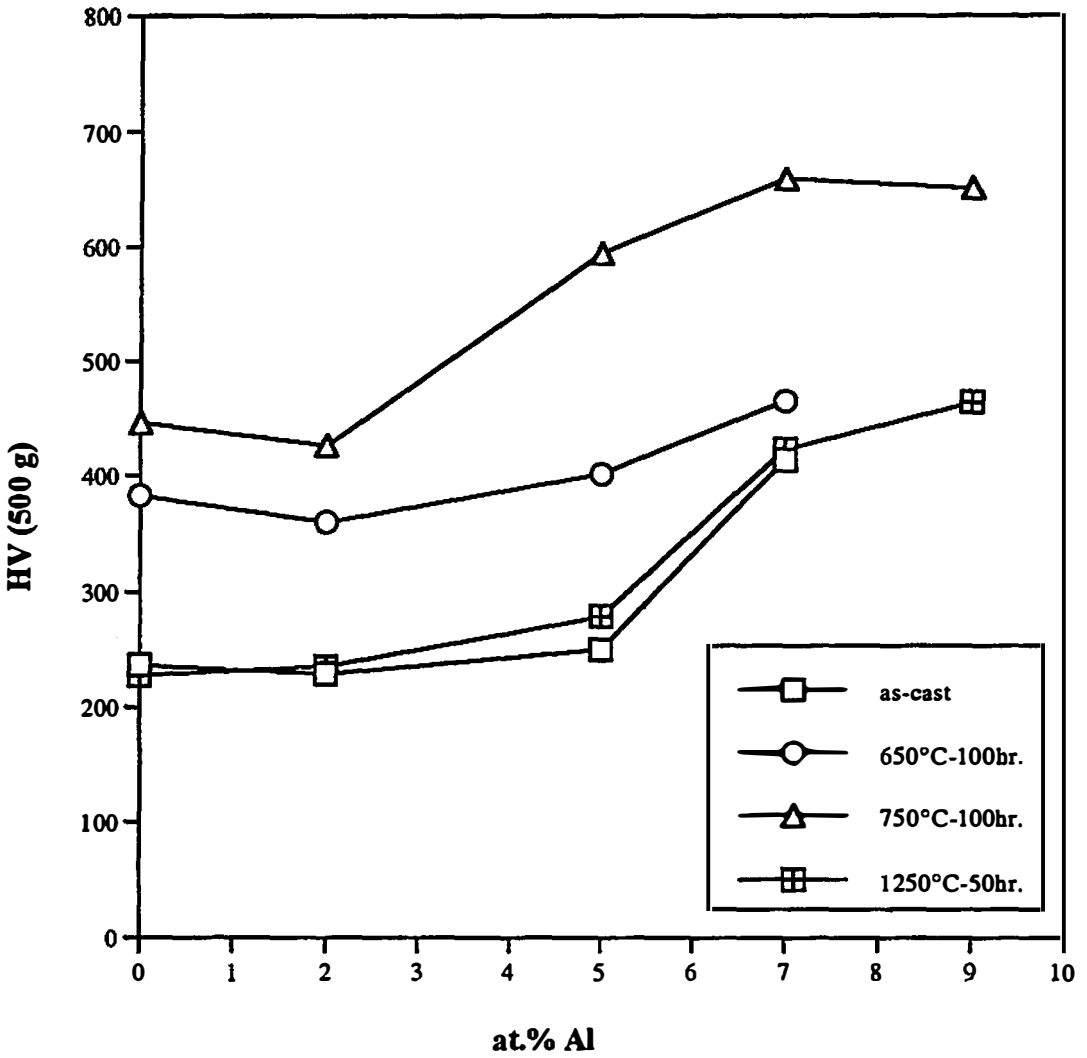



Figure 4-1. The hardness as a function of aluminum content in as-cast condition, aged at 650°C and 750°C without solution heat treatment, and homogenization treatment of 1250°C.

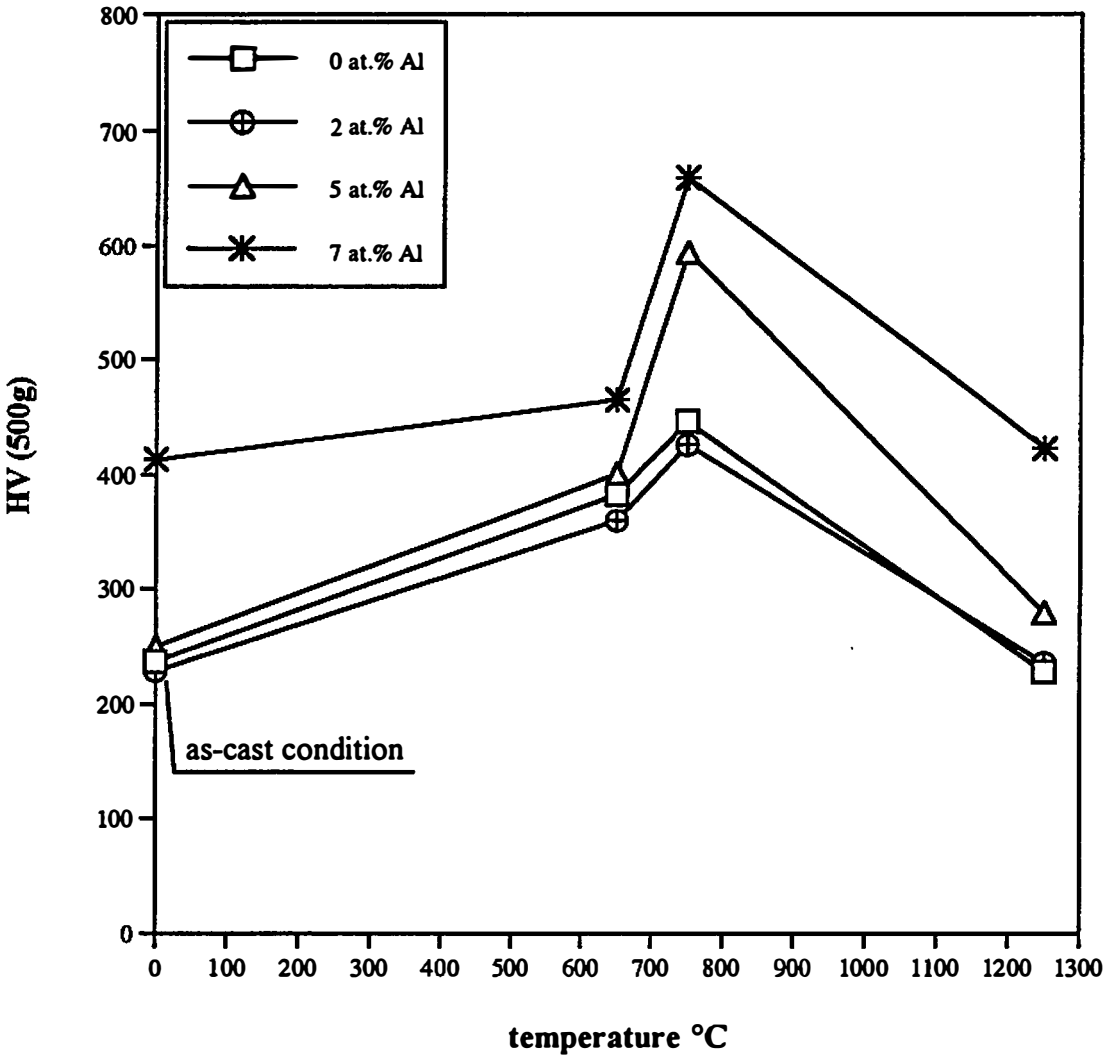



Figure 4-2. The hardness as a function of aging at 650°C and 750°C for 100 hours in the as-cast condition (without homogenization treatment) and solution heat treated at 1250°C for 50 hours with different aluminum content.

4.1.2. Hardness Measurement of the Solution Heat Treated Materials

In this group of materials, the solution heat treatment (1280°C, 50 hours) was performed prior to the aging study, thus, the microstructures in the alloys are significantly homogenized compared to the first group of materials, which was not solution heat treated. The hardness measurement data are analyzed as a function of aluminum content and aging parameter.

4.1.2.1. (a) Aluminum Content Effect (different aging temperature for 100 hours)

The effect of aluminum content and aging temperature (100 hours) on the hardness is shown in Figure 4-3. The solution heat treatment was 50 hours at 1280°C, but no hardness data were available. However, data are shown for a solution heat treatment of 50 hours at 1250°C, and subsequent microstructure analysis revealed no difference in the solution heat treated structure. The hardness increases gradually and considerably with an increase in aluminum content for the solution heat treated condition. This normally would be attributed to solid solution strengthening, as the structure revealed by optical microscopy appeared single phase (see Section 4.2). However, transmission electron microscopy revealed that the α phase was not always retained on quenching, and this is discussed later.

(b) Aluminum Content Effect (different aging time at 750°C)

Figure 4-4 gives the relationship of hardness and aluminum content upon aging at 750°C for different aging times. The hardness of solution heat treatment condition is also presented. The hardness of 2 at.% Al alloy upon aging for 10 hours shows a lower value than that of solution heat treatment condition. TEM shows the α phase in 2 at.% Al alloy after aging for 10 hours. With increase of aluminum content from 2 to 5 a.%, the hardenss

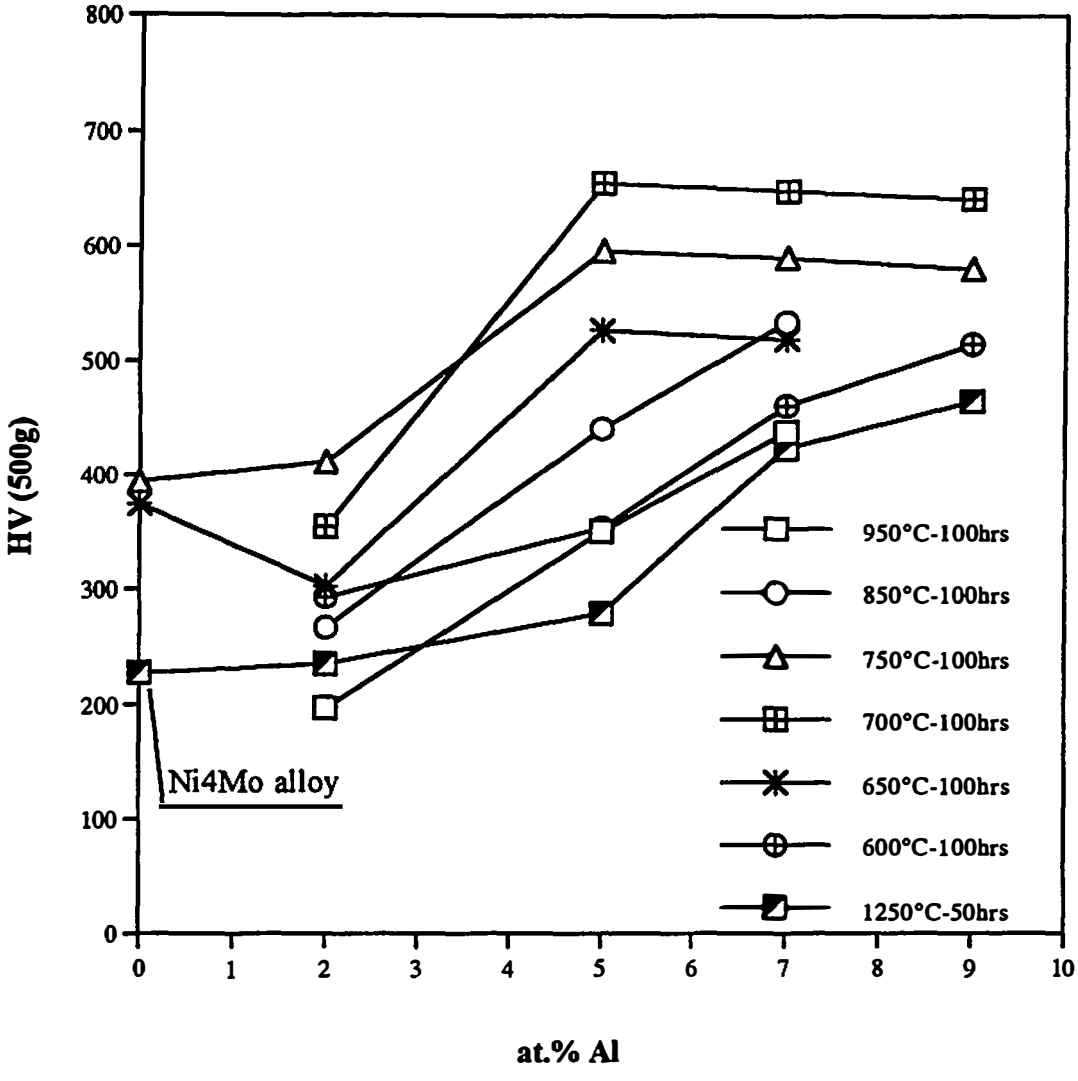



Figure 4-3. The hardness as a function of aluminum content at different aging temperatures for 100 hours (solution heat treated at 1280°C for 50 hours), and solution heat treated at 1250°C for 50 hours.

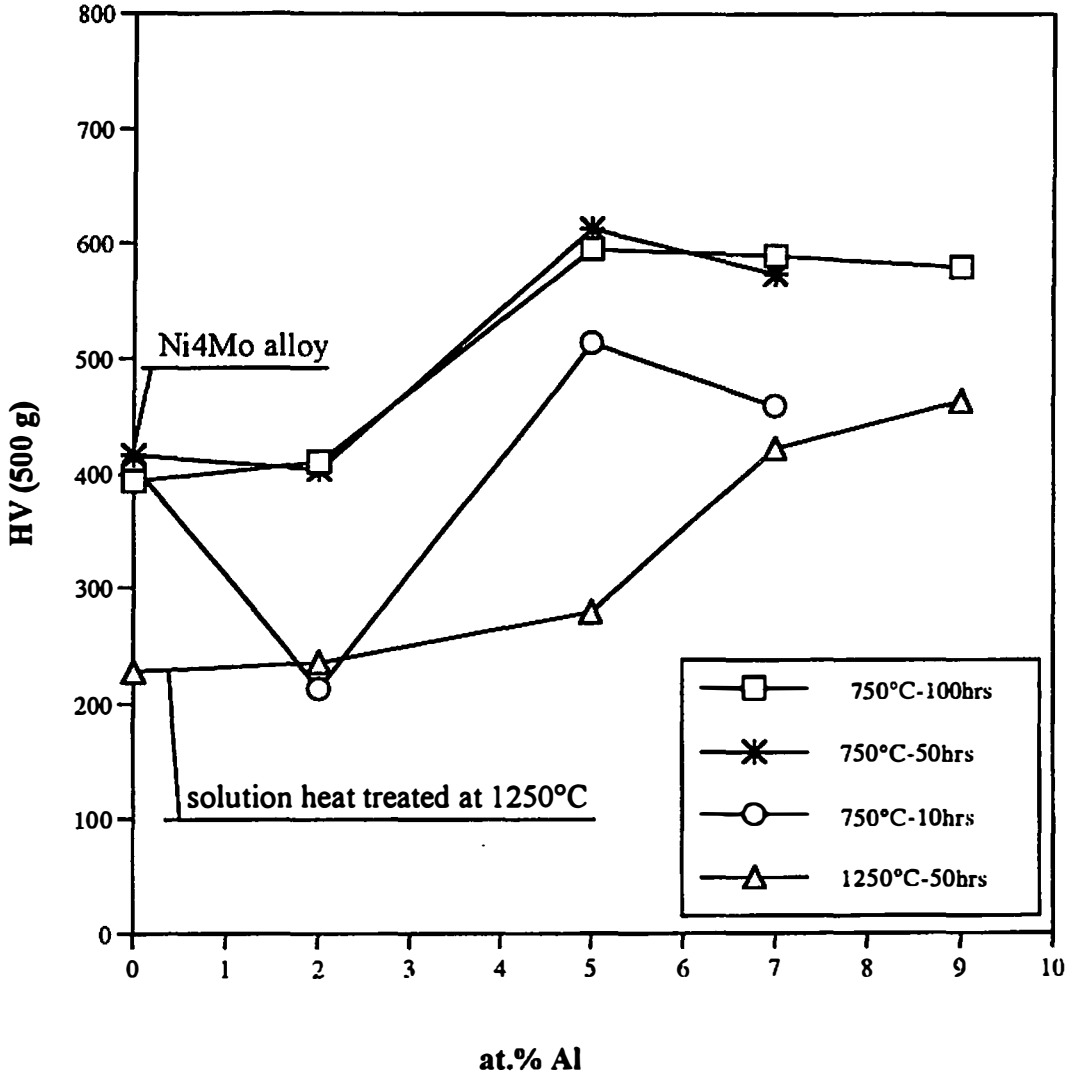



Figure 4-4. The hardness as a function of aluminum content for aging at 750°C for different times.

increases markly, but further increase of aluminum, the hardness decrased slightly. Upon aging for 50 hours, the hardness in alloys is similar to that for aging for 100 hours.

4.1.2.2. (a) Aging Temperature Effect

The $Ni_4Mo$ alloy increases in hardness from about 220 to about 380 upon aging at 650°C and 750°C. For the 2 % Al alloy, the hardness is about the same for all aging temperatures. The notable exception is a decrease of about 100 HV upon aging at 650°C. There is marked increase in hardness upon the addition of 5 at.% Al for all aging conditions. With higher aluminum addition of 7 and 9 at.%, the hardness is about constant upon aging from 650°C to 850°C, but increases for aging at 600°C. The highest hardness is attained upon aging at 700°C.

The hardness results are plotted in Figure 4-5 as a function of aging temperature. The base $Ni_4Mo$ alloy shows a marked increase in hardness (from about 220 to about 380 HV), attaining a maximum at 750°C. The 2 % Al alloy shows a similar response. The 5, 7 and 9 at.% Al alloys all attain about the same peak hardness of about 640 HV upon aging 100 hours at 700°C. The hardness result of $Ni_4Mo$ alloy is in agreement of the base $Ni_4Mo$ alloy with the data of Snyder and Brooks [64].

(b) Aging Time Effect (at 750°C)

The alloys were aged at 750°C for 10, 50 and 100 hours. The data is shown in Figure 4-6. As a base line, the solution heat treated data are also shown. With the exception of the 2 at.% Al alloy, aging for 10 hours decreased the hardness considerably, and there was a further increase upon aging for 50 hours. However, aging for 100 hours produced the same hardness as for 50 hours. The marked exception to the clear hardening trend is the lack of hardening of the 2 at.% Al alloy upon aging for 10 hours. TEM shows

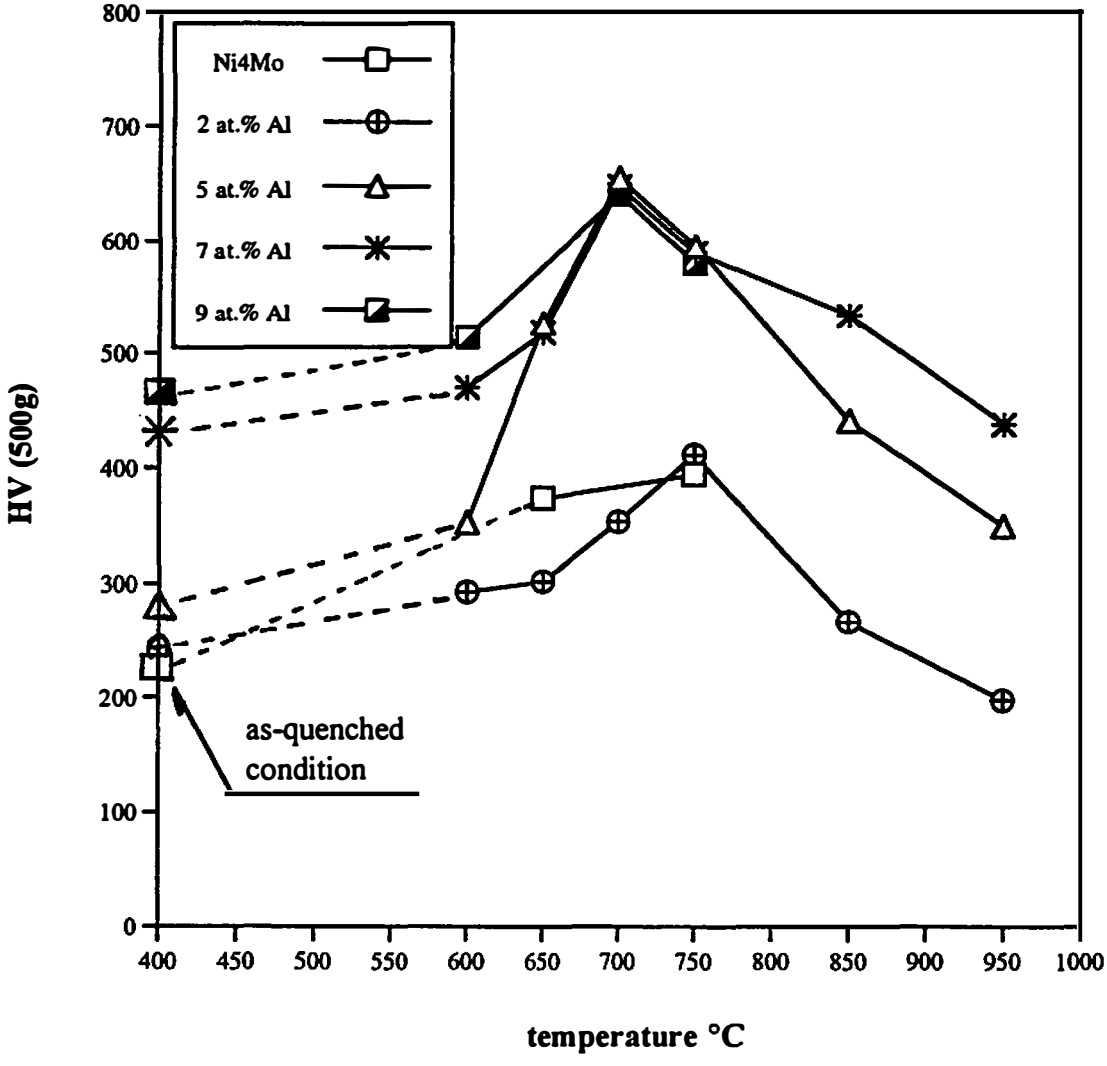



Figure 4-5. Hardness as a function of aging temperature for 100 hours in samples with different aluminum contents.

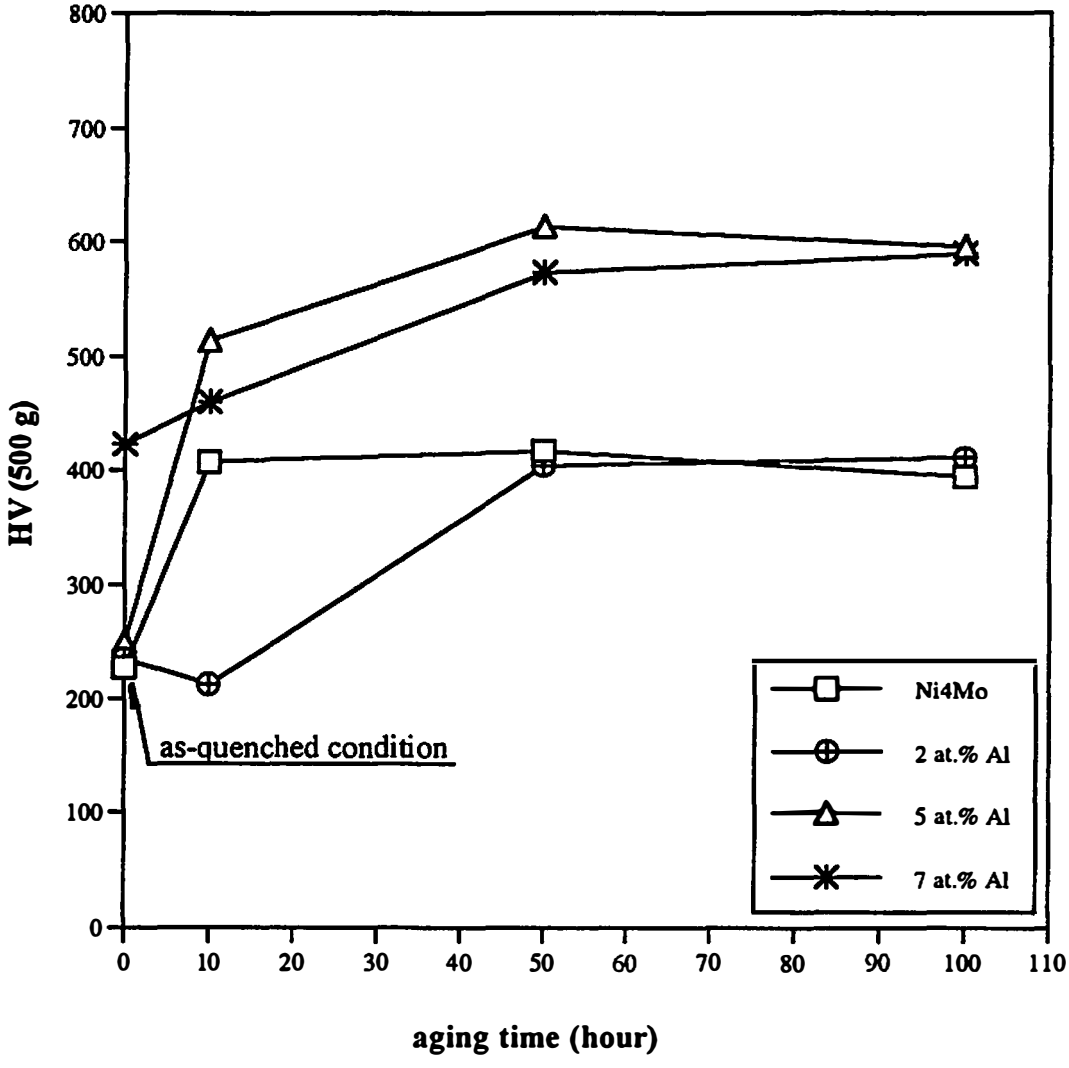



Figure 4-6. Hardness as a function of aging time at a fixed aging temperature of 750°C in sample with different aluminum content.

the α phase in 2 at.% Al alloy upon aging for 10 hours and is discussed in section 4.5.

## 4-2. Optical Light Microscopic (OLM) Microstructural Evaluation in $Ni_4Mo$ and Ni-Mo-Al Alloys

As shown in the above section, the hardness is a function of aging condition and aluminum content in the alloys studied. To help understand the effect of aluminum addition on hardness, in this section the results of OLM microstructural evaluation are given. In order to properly interpret the microstructural features, the phase constitution relationships and solidification behavior are also examined for the Ni-Mo-Al alloy system. The step by step description and discussion of aging effect on microstructures in the alloys studied are given in this section.

The low resolution of the OLM prevents determination of the fine structure and OLM provides no direct chemical analysis of the phases formed. The results of the examination using SEM and TEM are given in subsequent sections, where the basis of identifying the microstructural features is described. In this section, which describes only the OLM results, some of the labeling of the phases is based on the later work. For example, the OLM microstructure may indicate only a single phase α, whereas TEM reveals that it contains SRO α and the $DO_{22}$ structure.

### 4.2.1. Samples with an As-Cast Condition Plus Aged at 750°C for 100 Hours

As mentioned in the introduction, when the β phase forms from the α phase, the domains produce a Widmanstatten etching pattern, which can be taken as proof that β has formed. This pattern is found in the hot forged (without homogenization) $Ni_4Mo$ sample

after aging at 750°C for 100 hours (Figure 4-7). This transformation of the hot forged structure to the β approximately doubled the hardness (see Figure 4-1). Note that there is a mixture of former α grain sizes, indicating uneven grain growth. Also note that the etchant used did not reveal any dendritic segregation.

After aging at 750°C for 100 hours, the microstructures of the Ni-Mo-Al alloys (as-cast condition) showed clear interdendritic solidification structure. Figures 4-8 and 4-9 show typical dendritic structure of the 2 and 9 at.% Al alloys at low magnification (e.g. 100X).

A higher magnification micrograph for the 2 at.% Al alloy is presented in Figure 4-10. A lamellar structure (see arrow) started to form at selective locations (localized molybdenum and/or aluminum rich or poor area). The 5 at.% Al alloy shows mixed structures of dark and bright regions (Figure 4-11). The microstructure in 7 at.% Al alloy contains both dark and bright regions (Figure 4-12). In the dark regions, a lamellar structure was found (see arrow). The microstructure in 9 at.% Al alloy contained a lamellar structure, bright and dark regions (Figure 4-13).

In the as-forged condition, the grain size of the $Ni_4Mo$ alloy was uniform (Figure 4-14). However, after aging for 100 hours at 750°C, a rather duplex grain size is present (Figure 4-7) having an appearance of recrystallization. The origin of this effect was not established. For this heat treatment, the structure will be completely β phase in this binary alloy.

After aging for 100 hours at 750°C (without homogenization treatment), the as-cast dendritic structure can not be completely removed and/or homogenized. In the $Ni_4Mo$ alloy, the hardness increased because the β phase formed and recrystallization occurred. In the Ni-Mo-Al alloys, the secondary phase formed is due to the localized alloying element segregation which favors the formation of secondary phases. As indicated in Figure 4-1, the

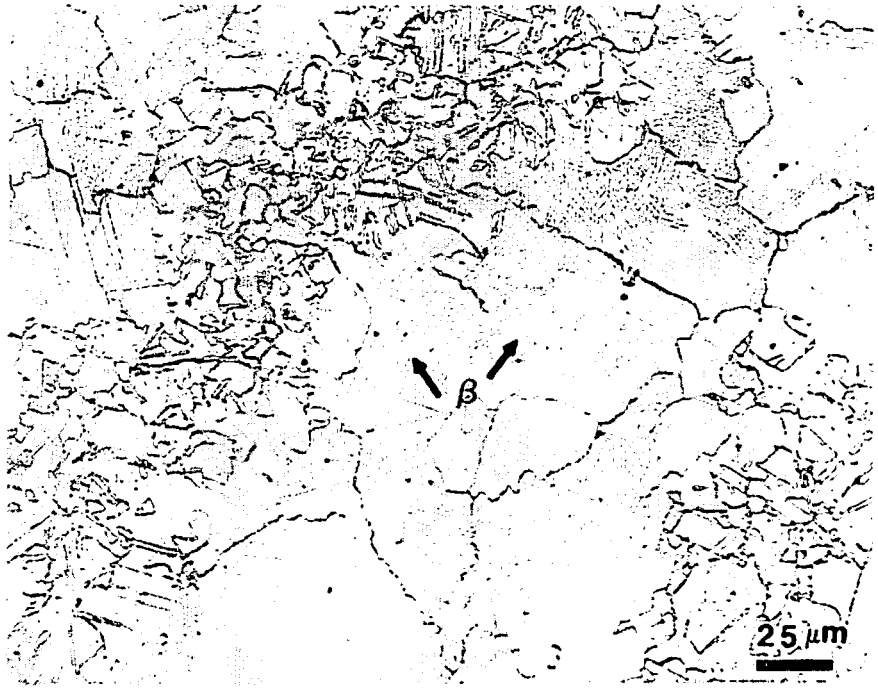



Figure 4-7. OLM microstructure of $Ni_4Mo$ alloy (as-received condition) aged at 750°C for 100 hours showing β recrystallization and β phase.

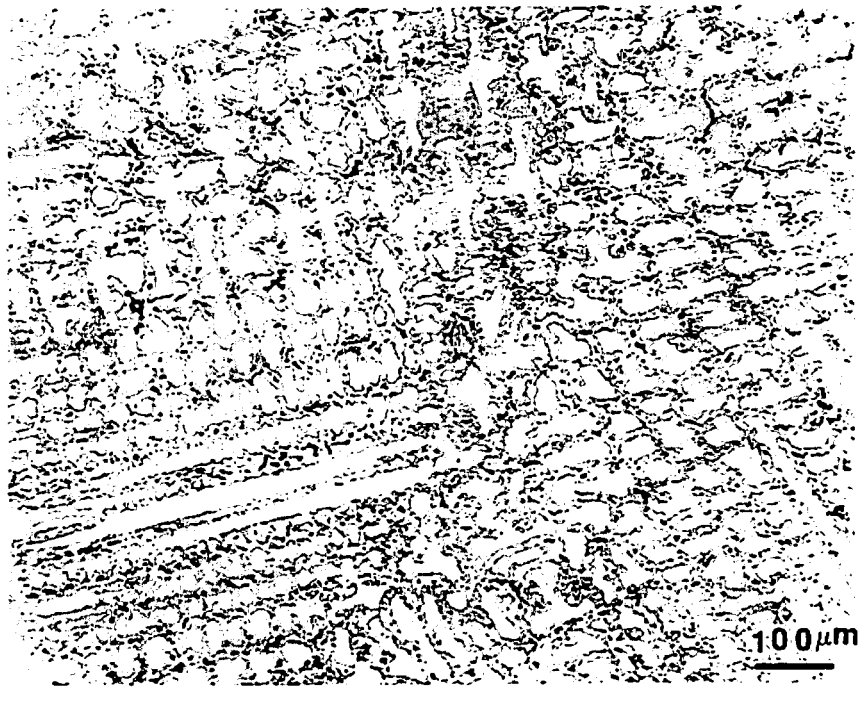



Figure 4-8. OLM microstructure of 2 at.% Al alloy in as-cast condition (no homogenization) aged at 750°C for 100 hours showing dendritic structure at low magnification.

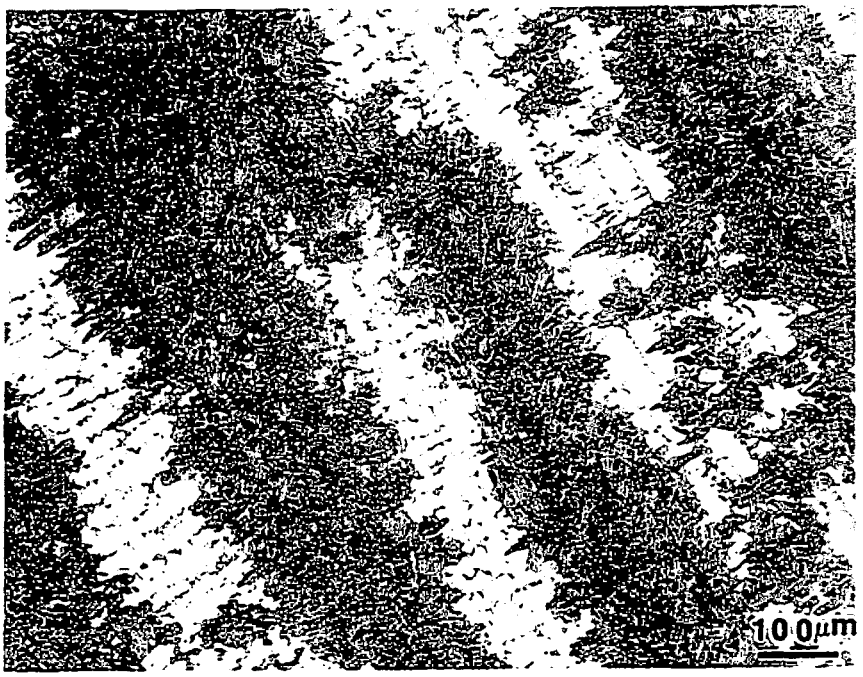



Figure 4-9. OLM microstructure of 9 at.% Al alloy in as-cast condition (no homogenization) aged at 750°C for 100 hours showing dendritic structure at low magnification.

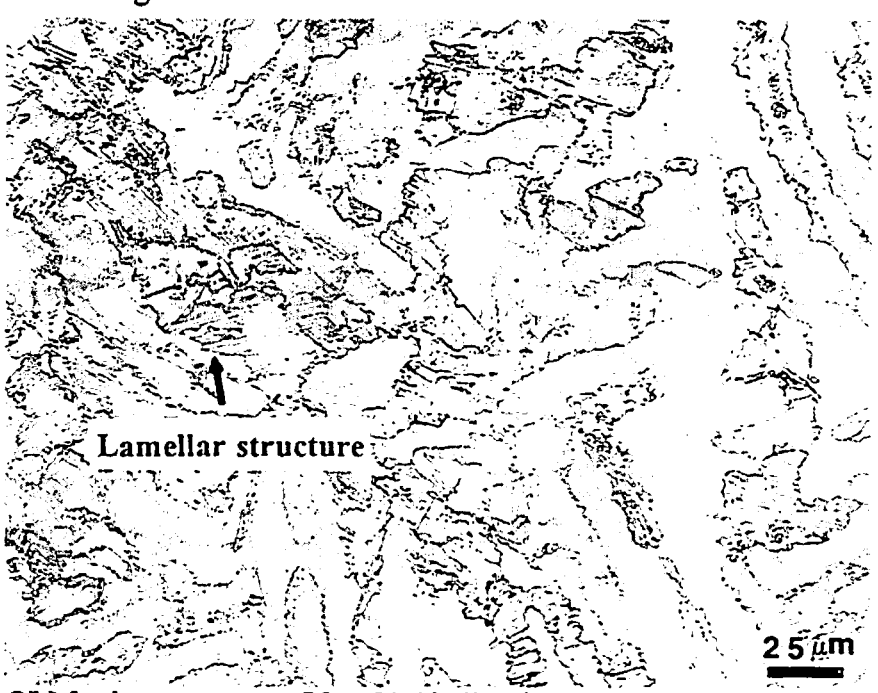



Figure 4-10. OLM microstructure of 2 at.% Al alloy in as-cast condition (no homogenization) aged at 750°C for 100 hours showing coarse lamellar structure.

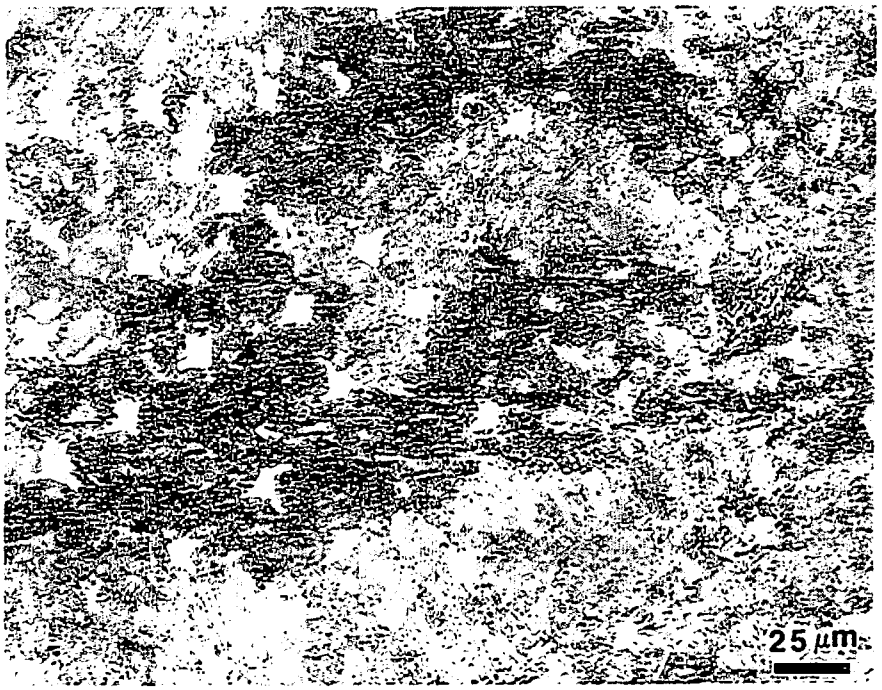



Figure 4-11. OLM microstructure of 5 at.% Al alloy in as-cast condition (no homogenization) aged at 750°C for 100 hours showing dark and bright regions.

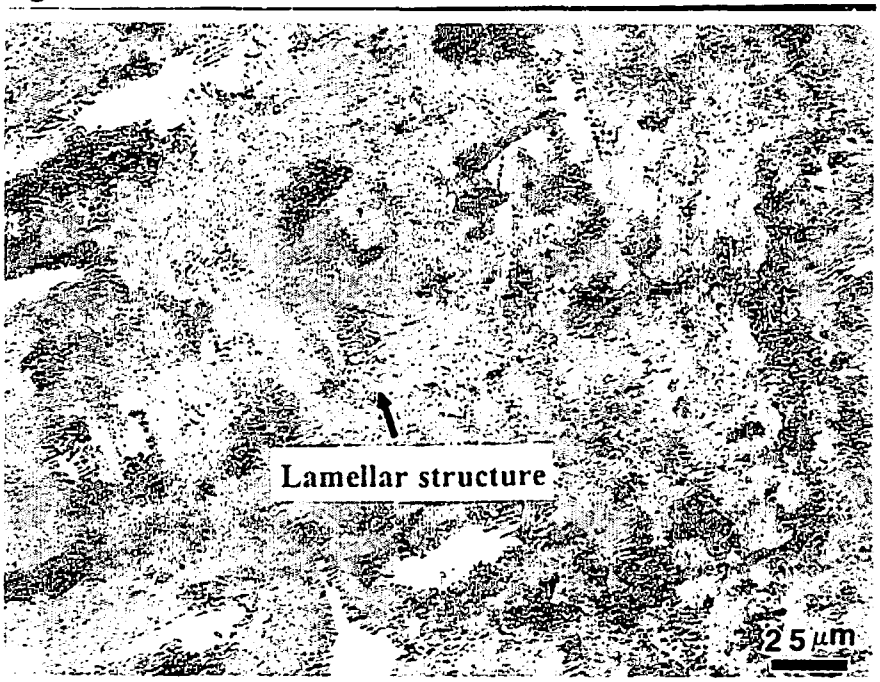



Figure 4-12. OLM microstructure of 7 at.% Al alloy in as-cast condition (no homogenization) aged at 750°C for 100 hours showing lamellar structure, dark and bright regions.




Figure 4-13. OLM microstructure of 9 at.% Al alloy in as-cast condition (no homogenization) aged at 750°C for 100 hours showing lamellar structure, dark and bright regions.

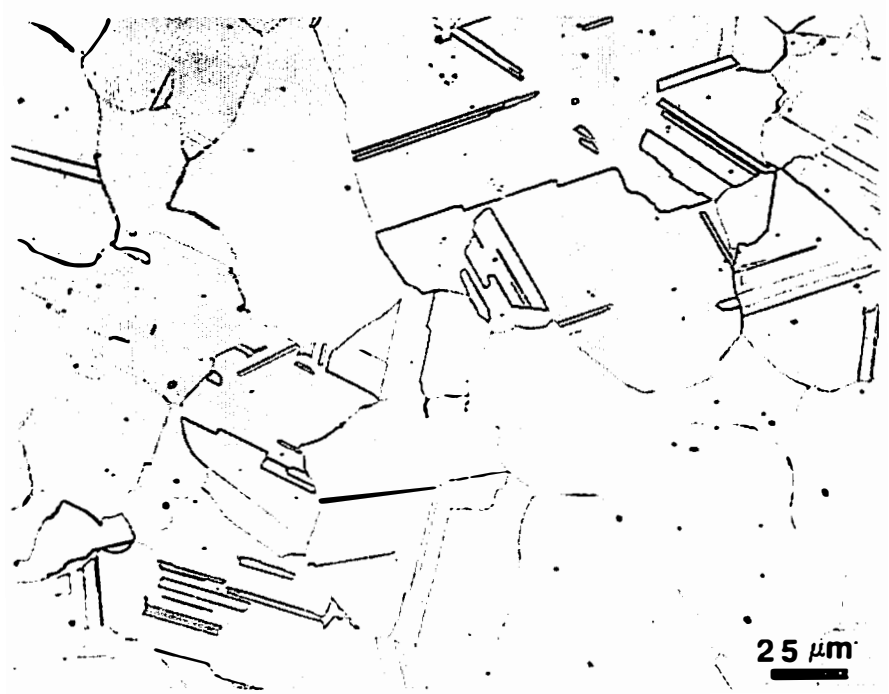



Figure 4-14. OLM microstructure of $Ni_4Mo$ alloy in as-received condition (hot forged) single $\alpha$ phase with annealing twins.

hardness in all alloys increased from that of the as-cast condition due to the secondary phase formation after aging. It is clearly shown that the hardness of secondary phases is greater than that of α phase.

The OLM microstructural study has shown that the hardness increased upon aging because of the formation of secondary phase including β, γ, δ, and γ', as shown in later sections.

### 4.2.2. Investigation of Proper Solution Treatment Condition

The $Ni_4Mo$ alloy shows single phase α after solution heat treatment at 1250°C for 50 hours (Figure 4-15), and grains have grown larger compared to that of the as-received condition (hot forged) (Figure 4-14). In order to obtain a completely homogenized single α phase, a designed solution heat treatment at 1250°C for 50 hours was applied based upon the ternary alloy phase diagram. The Ni-Mo-Al ternary phase diagram at 1260°C ( Figure 4-16 [65 and 66]) was used and it indicates that through 7 at.% aluminum, the alloy should be single phase α at this temperature. The 9 at.% Al alloy closed to border of two-phase region, and hence might not be single phase.

The microstructures of the 2, 5, and 7 at.% Al alloys show what appears to be single phase α (Figure 4-17 through 4-19). There is no sign of dendritic segregation, and this homogenization treatment produced a homogeneous structure. However, the microstructure of the 9 at.% Al alloy (Figure 4-20) shows what appears to be a sub-structure and a second phase.

Based on these results, to insure a homogenized microstructure for the aging treatment, all subsequent samples were heated for 50 hours at 1280°C in quartz tubes, then quenched by breaking the tubes in water. However, due to limited material, the microstructure for this treatment for the 9 at.% Al alloy was not available, and this

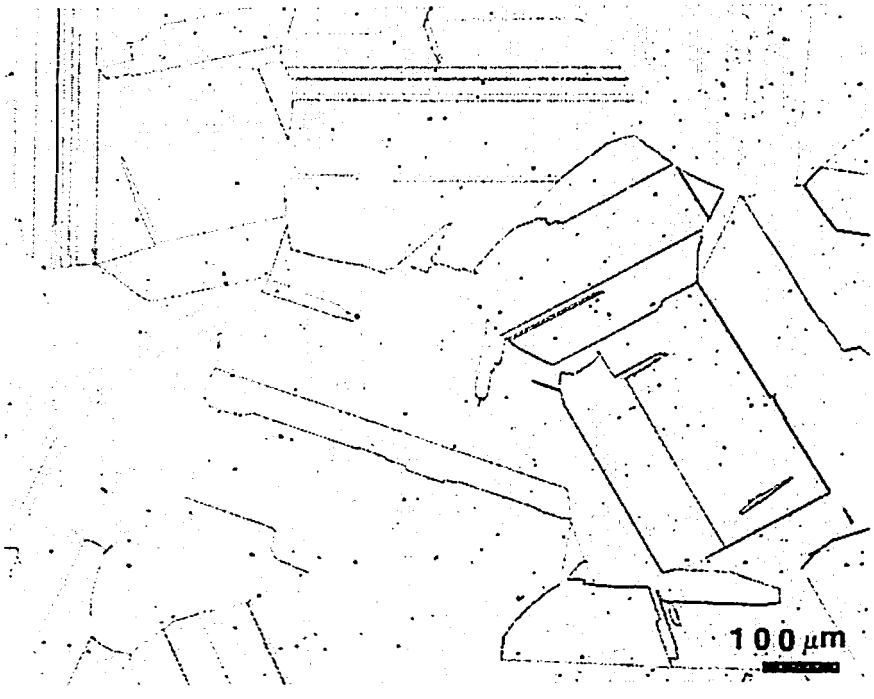



Figure 4-15. OLM microstructure of $Ni_4Mo$ alloy homogenized at 1250°C for 50 hours showing single $\alpha$ phase with annealing twins.

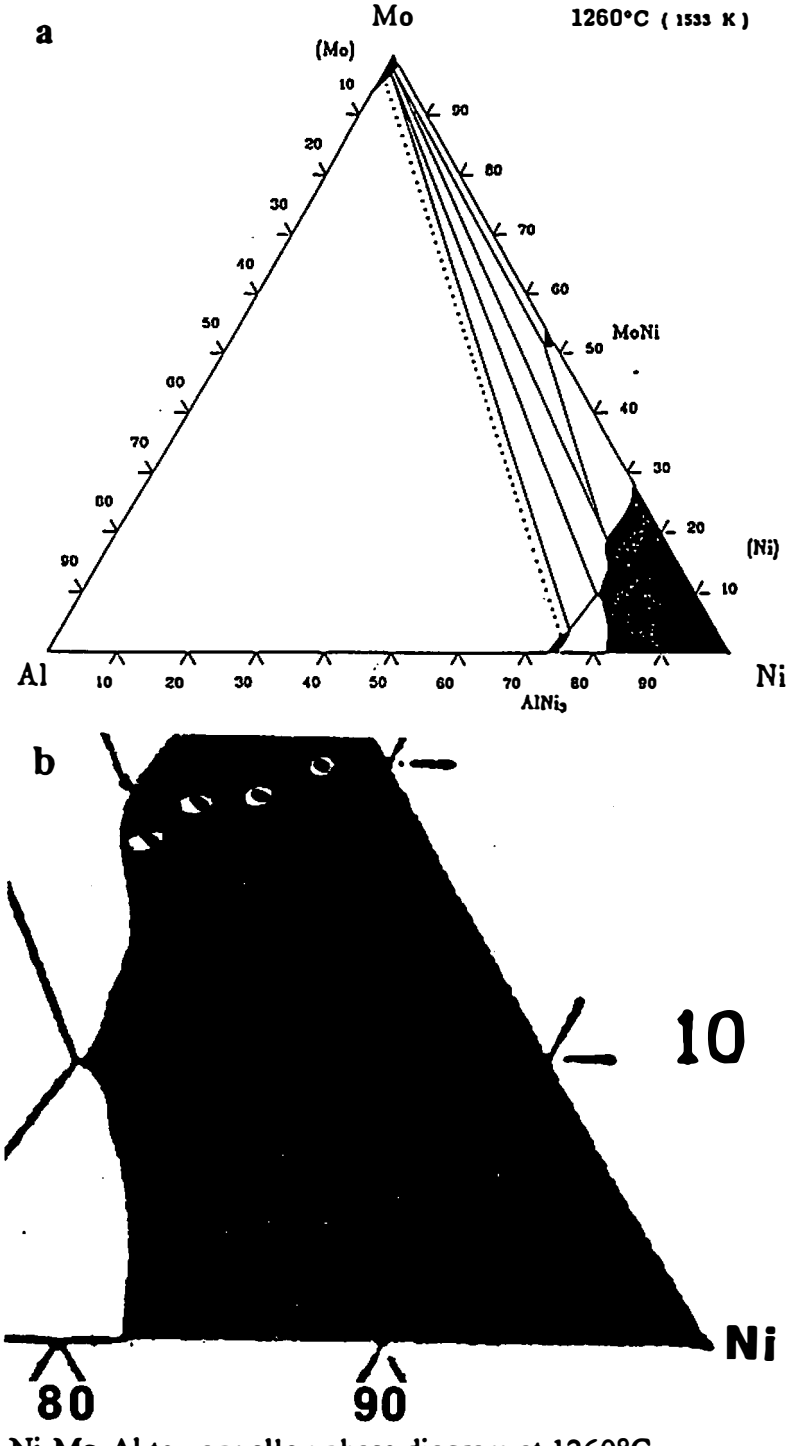



Figure 4-16. Ni-Mo-Al ternary alloy phase diagram at 1260°C.

Ref. P. Villars, A. Prince, and H. Okamoto, Handbook of Ternary Alloy Phase Diagrams, Vol. 4, pp. 4046-4066, ASM International, Materials Park, OH, 1995.

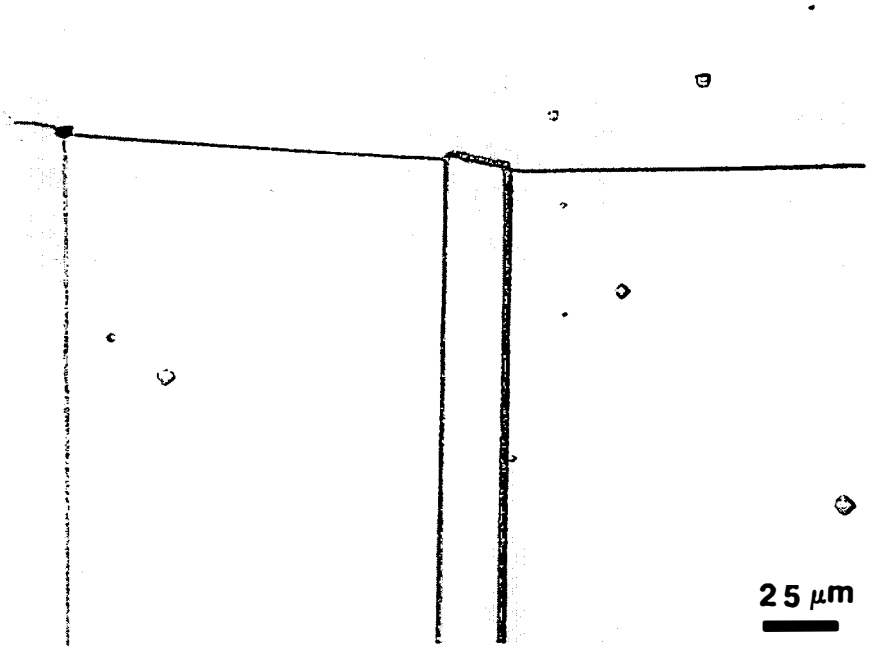



Figure 4-17. OLM microstructure of 2 at.% Al alloy homogenized at 1250°C for 50 hours showing single phase with annealing twins.

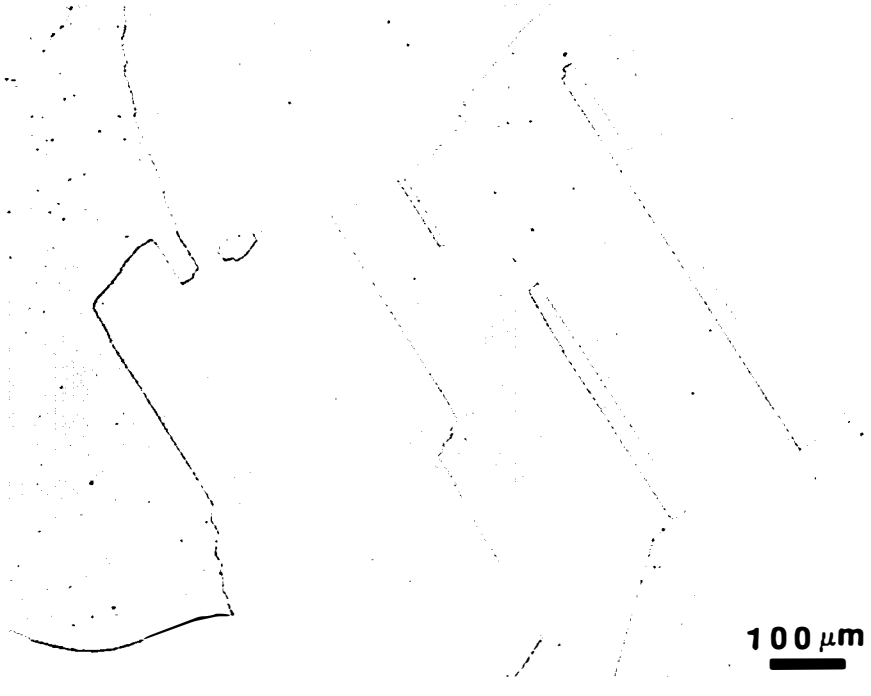



Figure 4-18. OLM microstructure of 5 at.% Al alloy homogenized at 1250°C for 50 hours showing single phase with annealing twins.




Figure 4-19. OLM microstructure of 7 at.% Al alloy homogenized at 1250°C for 50 hours showing single phase with annealing twins.

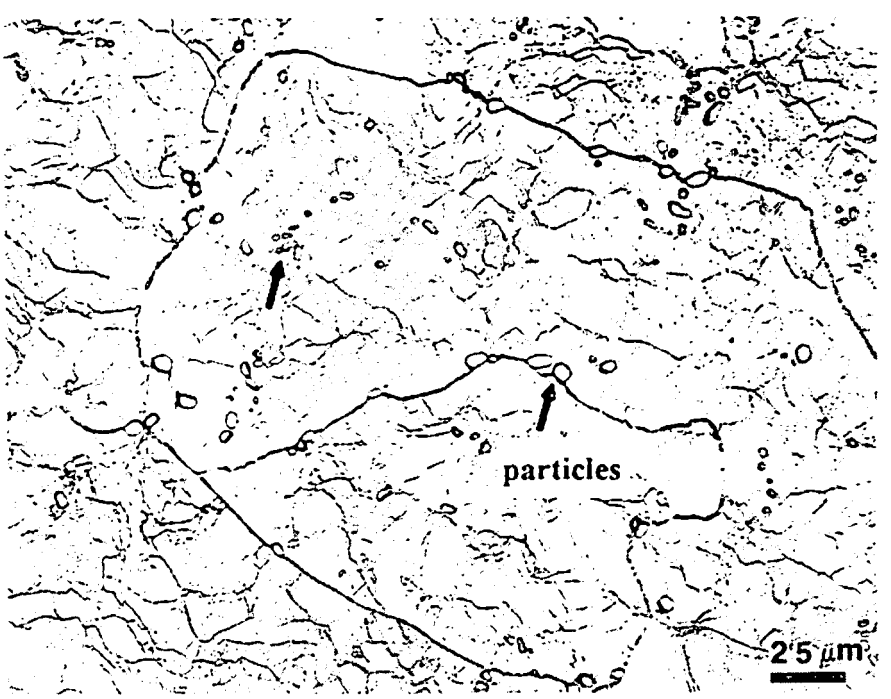



Figure 4-20. OLM microstructure in 9 at.% Al alloy homogenized at 1250°C for 50 hours showing particles along grain boundaries and in matrix.

situation will be commented on later.

Figure 4-1 shows that for this homogenization treatment the hardness increased considerably for aluminum additions of 7 and 9 at.%. This could be due to solid solution strengthening, but the TEM results discussed later will show that the structure is not single phase α, but ordered structures are presented.

### 4.2.3. OLM Microstructure of Ni-Mo-Al Alloys with a Solution Treated Plus Aged at 600°C for 100 Hours

The microstructures of the 2, 5, 7 and 9 at.% Al alloys are shown in Figures 4-21 to 4-24. A signle phase is exhibited in 2 and 5 at.% Al alloys (Figure 4-21 and 4-22) and the 7 at.% Al alloy appears to be single phase α, but there is slight grain boundary migration (Figure 4-23). There may be precipitation associated with this migration. In the 9 at.% Al alloy (Figure 4-24), migration of the grain boundaries has occurred, a lamellar structure has formed and some particles are present. Note that the lamellar spacing (Figure 4-24b) is greater at the edge of the structure than in the center.

As shown in Figure 4-3, upon aging at 600°C for 100 hours the hardness of the $Ni_4Mo$ alloy and the 2 and 5 at.% Al alloys remained about the same, or decreased slightly, from the solution heat treated condition. This is consistent with the microstructures which appear to have remained α phase. The hardness of the 7 at.% Al alloy increased somewhat, but the main obvious microstructural change was slight grain boundary migration, with an accompanying phase change. However, the amount of this feature is probably too slight to have effected this hardness change. The 9 at.% Al alloy showed a very marked hardness increase, and this is clearly associated, at least partially, with the presence of the lamellar structure. The relation of the microstructures and hardness will be discussed in more detail in the TEM section.

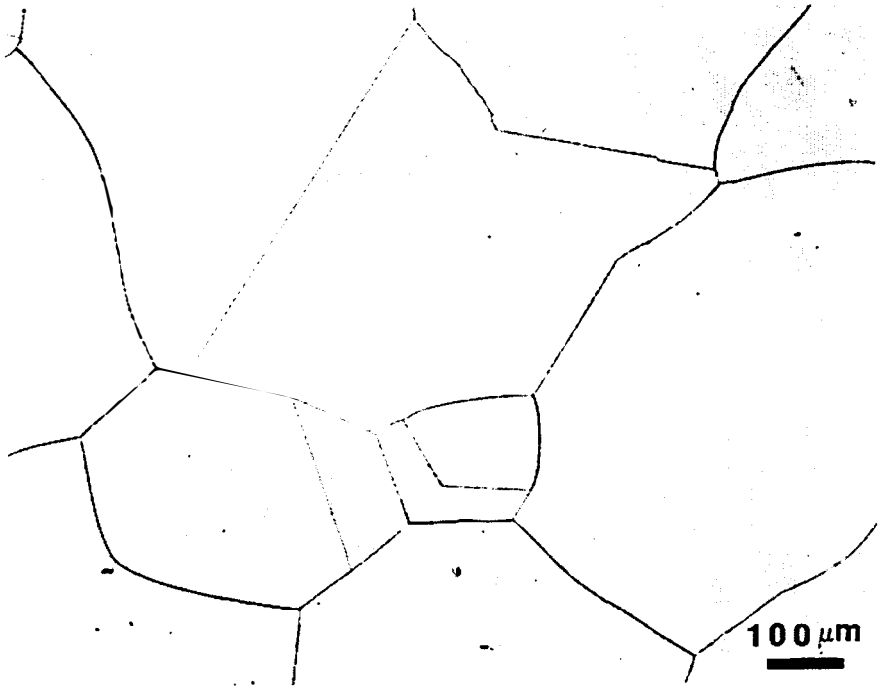



Figure 4-21. OLM microstructure of 2 at.% Al alloy aged at 600°C for 100 hours showing single phase.

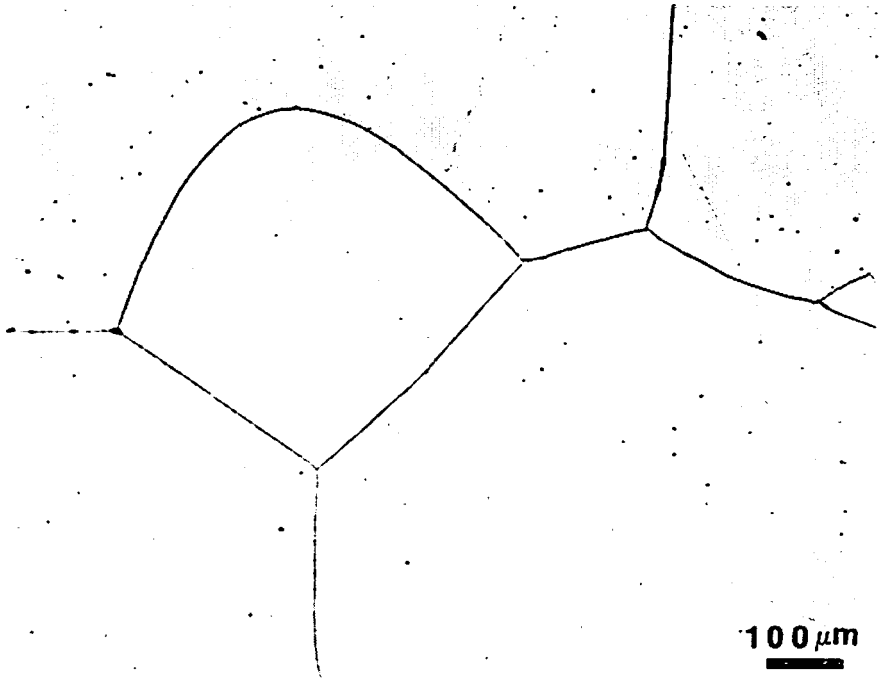



Figure 4-22. OLM microstructure of 5 at.% Al alloy aged at 600°C for 100 hours showing single phase.

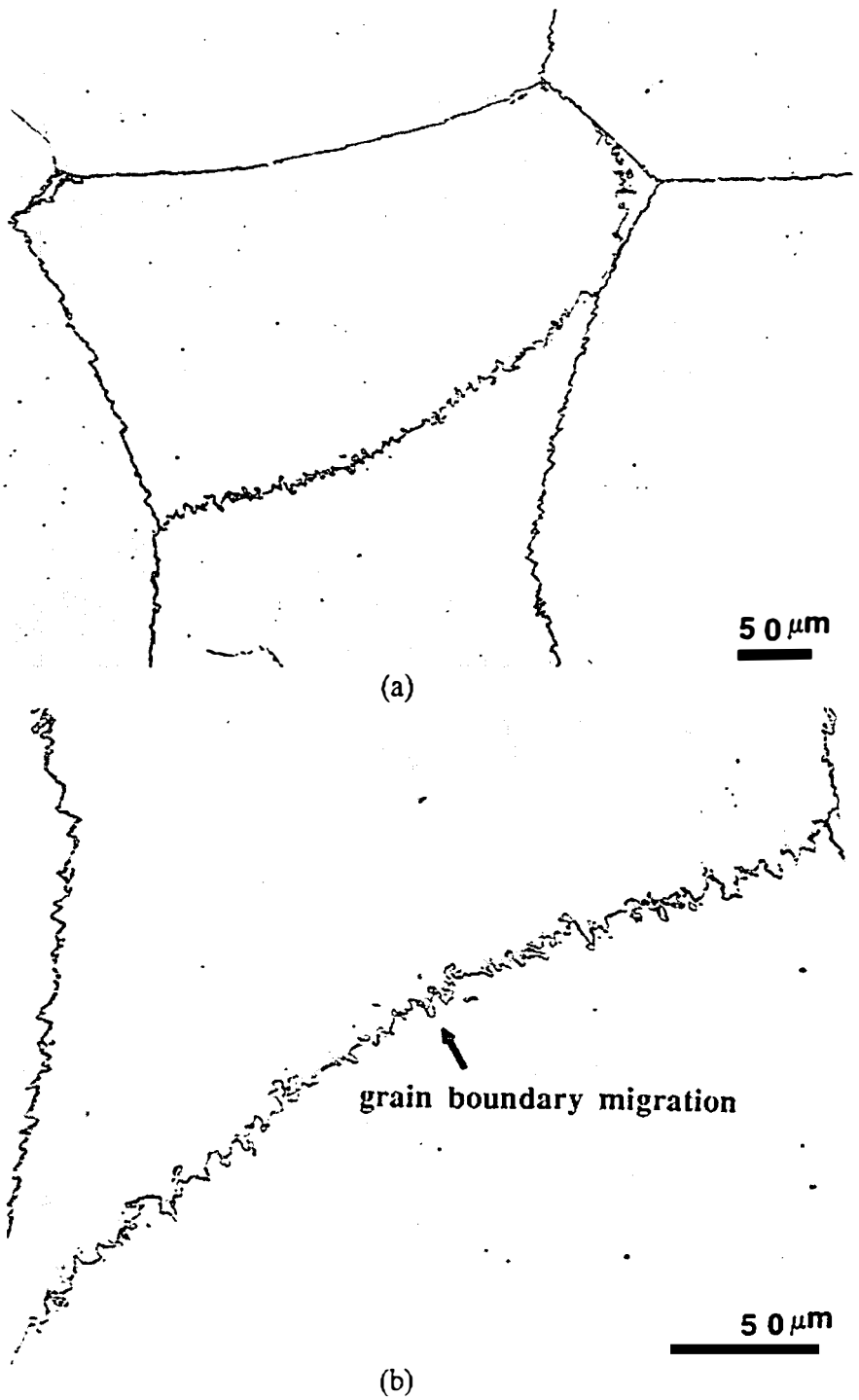



Figure 4-23. OLM microstructure of 7 at.% Al alloy aged at 600°C for 100 hours showing grain boundary migration and secondary phase starting to form along the grain boundaries. (a) 200X (b) 400X.

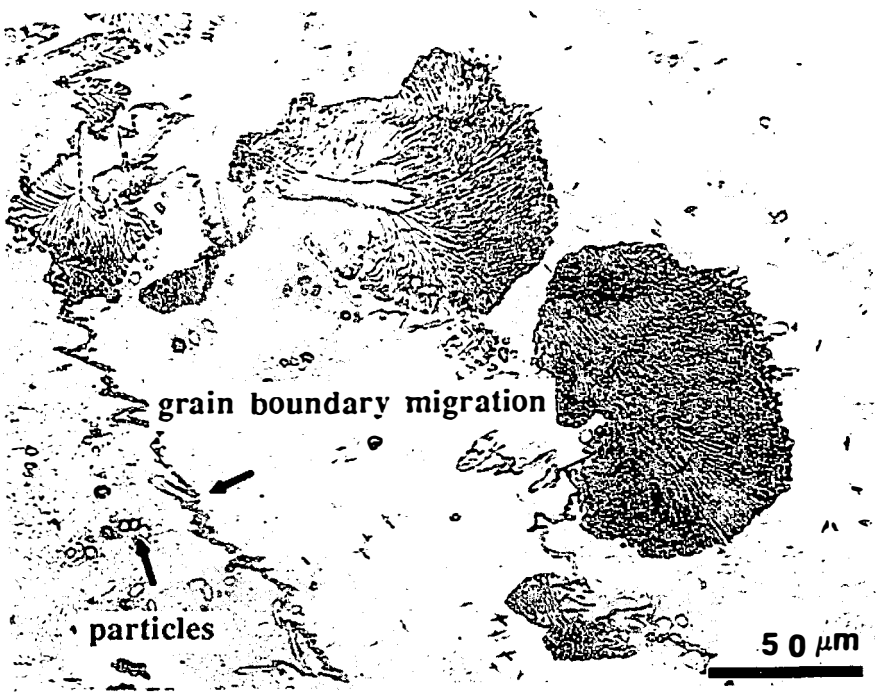



Figure 4-24. OLM microstructure of 9 at.% Al alloy aged at 600°C for 100 hours showing lamellar structure, particles, and grain boundaries migration. (a) 400X (b) 1000X.

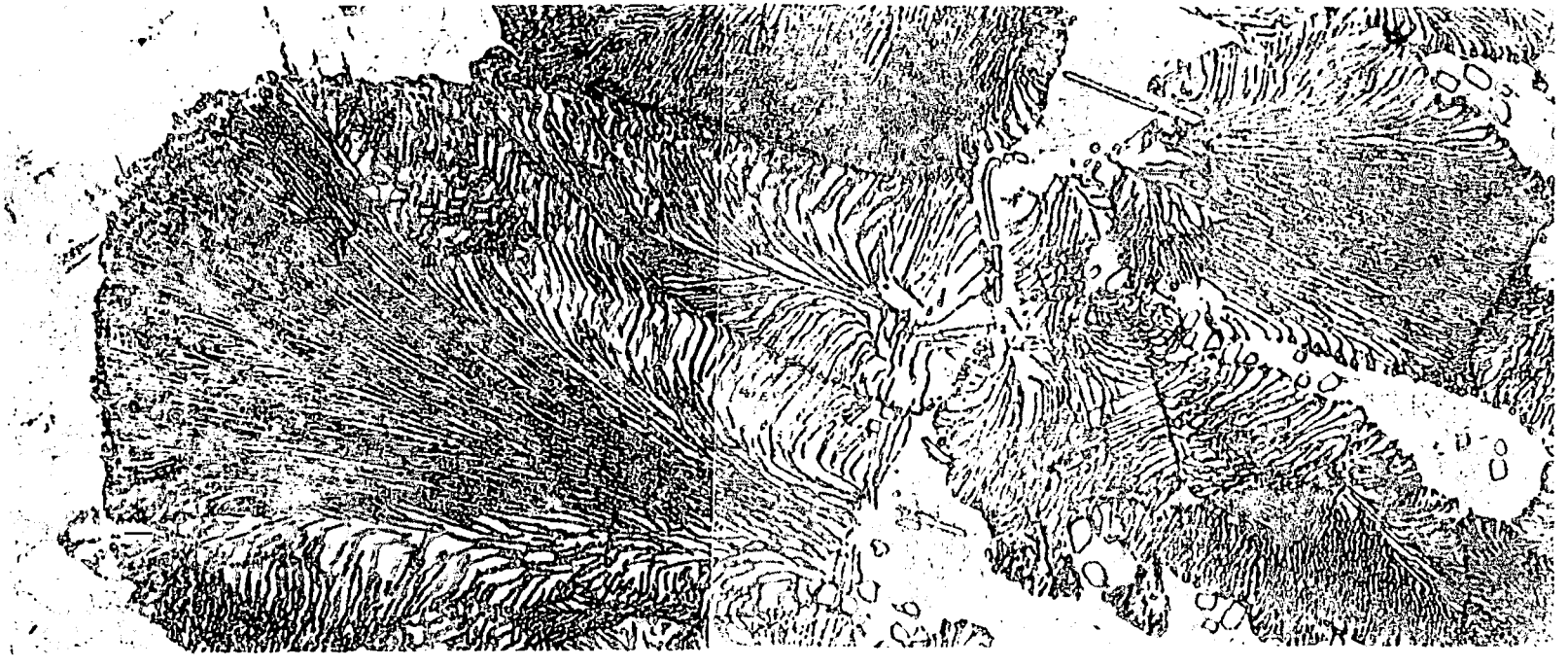


Figure 4-24. continue (b).

### 4.2.4. OLM Microstructure of Ni-Mo-Al Alloys with a Solution Treated Plus Aged at 650°C for 100 Hours

In the $Ni_4Mo$ alloy, the microstructure appears to be single phase α, but there is some slight grain boundary migration (Figure 4-25). Although a Widmanstatten structure did not etch out, this treatment probably converted the α to a fine domain β structure, as Figure 4-3 shows that the hardness has approximately doubled from this aging treatment. The boundary migration is probably accompanied by domain coarsening.

The 2 at.% Al alloy appears to be single phase α (Figure 4-26), and the hardness decreased slightly (Figure 4-3). In this alloy there was grain boundary cracking, indicating a decohesion of the high angle boundaries. This characteristic is common in the $Ni_4Mo$ alloy when the α converts to the ordered β, which causes hardening but produces cracking along the former α grain boundaries. However, Figure 4-3 shows that the hardness of the 2 at.% Al alloy has decreased slightly. The cracking is examined in more detail in the section on fractography.

During aging the 5 at.% Al alloy, extensive lamellar structure formed along the grain boundaries (Figure 4-27). There was also cracking along the location of the former α grain boundaries. At what stage this occurred is not known; that is, did these cracks form prior or after the formation of the lamellar structure? Figure 4-3 shows that there is a marked hardness increase.

In the 7 at.% Al alloy, there is a structure forming from the α grain boundaries, and some formation inside the grains. The grain boundary migration is observed. The matrix appears to be single phase (Figure 4-28). This alloy showed marked hardening (Figure 4-3), but no cracking was observed.

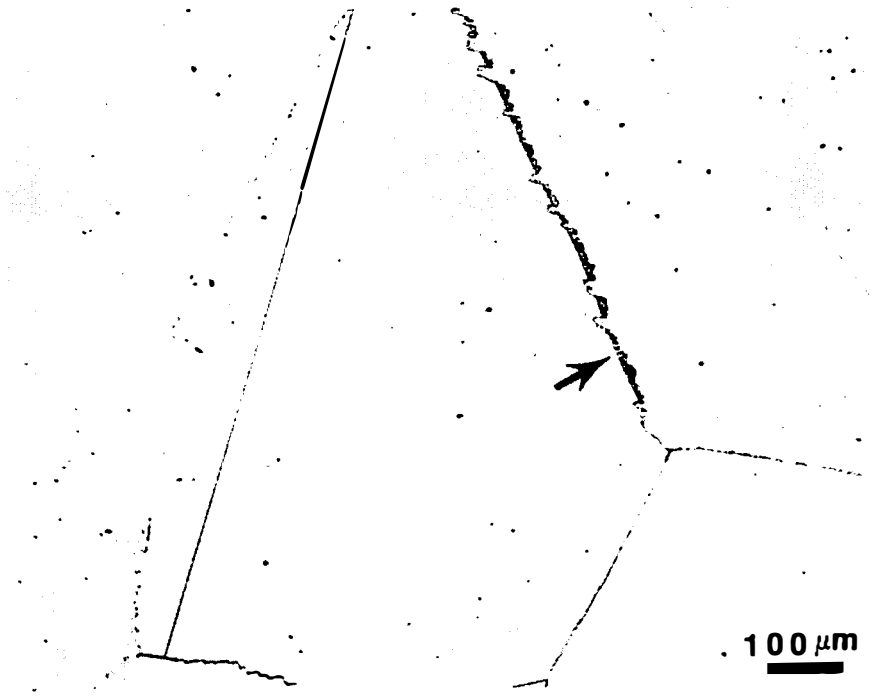



Figure 4-25. OLM microstructure of $Ni_4Mo$ alloy aged at 650°C for 100 hours showing β domain formation along the former α grain boundaries.

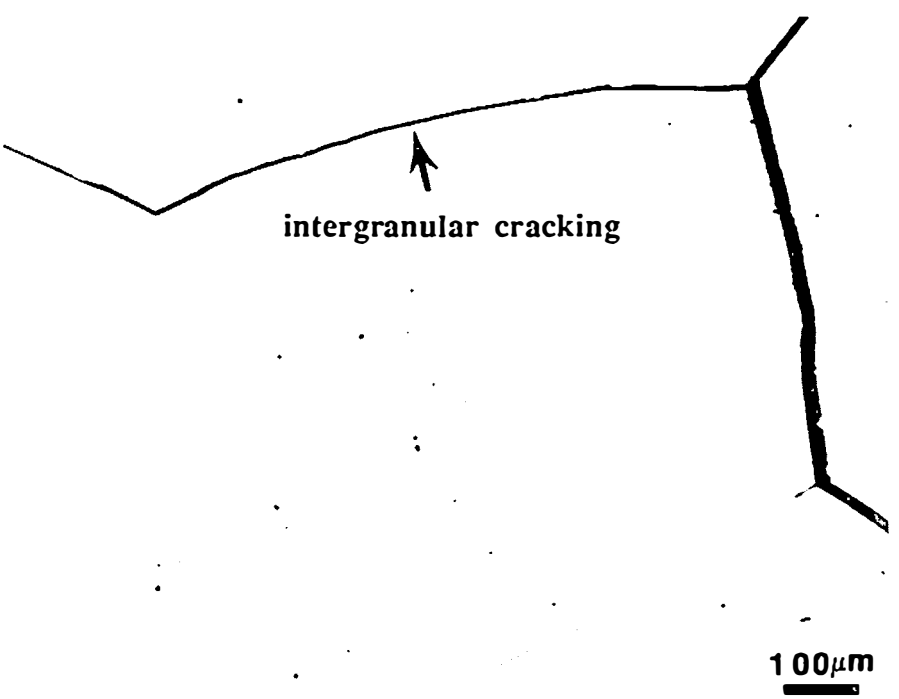



Figure 4-26. OLM microstructure of 2 at.% Al alloy aged at 650°C for 100 hours showing single phase with intergranular cracking.

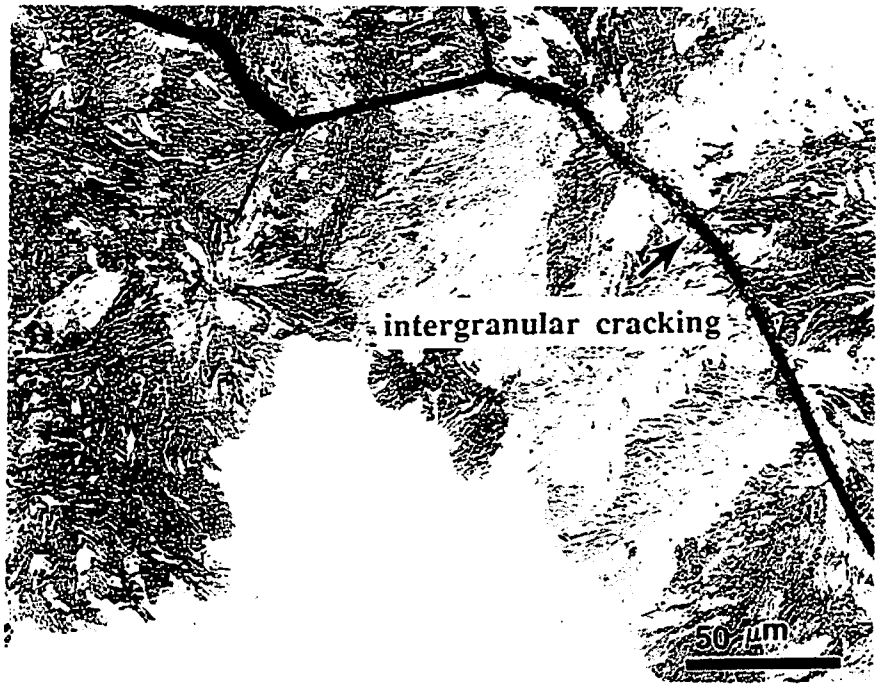



Figure 4-27. OLM microstructure of 5 at.% Al alloy aged at 650°C for 100 hours showing lamellar structure formation along grain boundaries with intergranular cracking.

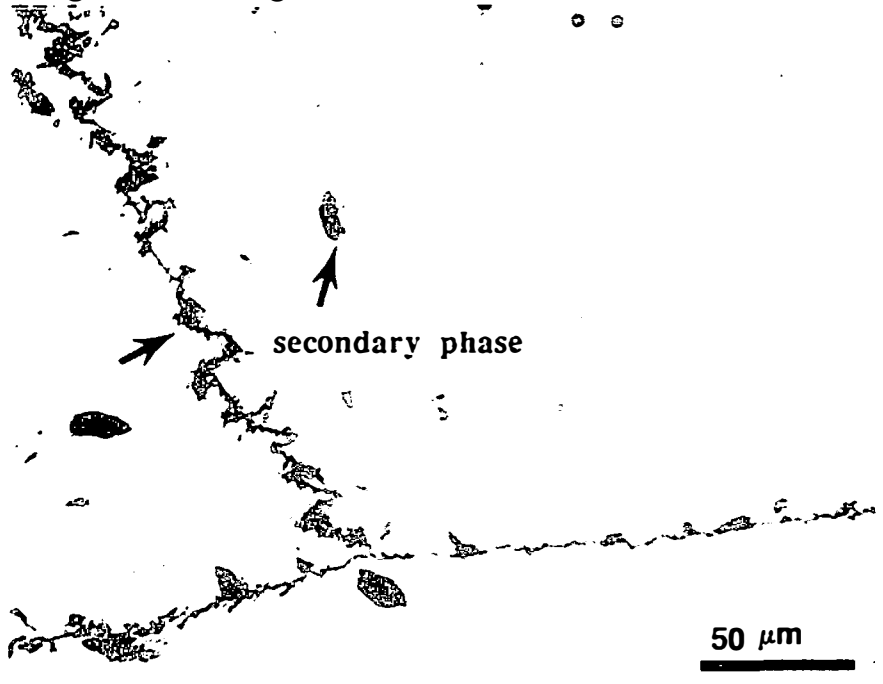



Figure 4-28. OLM microstructure of 7 at.% Al alloy aged at 650°C for 100 hours showing grain boundary migration with secondary phase nucleation along the grain boundaries and in the grains.

4.2.5. OLM Microstructure of Ni-Mo-Al Alloys with a Solution Treated Plus Aged at 700°C for 100 Hours

The phase diagram for the Ni-Mo-Al system at 700°C is shown in Figure 4-29 [65]. For each composition of the alloy, the equilibrium phases are noted. Although aging for 100 hours may not establish equilibrium, the diagram gives a guideline of what the microstructure may be.

The microstructure of the 2 at.% Al alloy (Figure 4-30) appears to be single phase. At equilibrium this composition should be $\beta$ and $\gamma$ phases. The precise structure is established in the TEM section. Figure 4-3 shows that the hardness of this alloy did not increase, but there is grain boundary cracking.

The 5 at.% Al alloy completely transformed to a lamellar structure (Figure 4-31). The phase diagram predicts this alloy should be $\beta$, $\gamma$ and $\gamma'$ phases. As discussed in the TEM section, this lamellar structure is composed of $\gamma$ and $\gamma'$. This structure caused the greatest hardening of all the alloys and heat treatments (Figure 4-3).

The 7 at.% Al alloy formed a lamellar structure along the grain boundaries, but the matrix appears to be single phase (Figure 4-32). The lamellar structure composes about 10% of the microstructure. Note that the hardness (Figure 4-3) is essentially the same maximum as that for the 5 at.% Al alloy. This implies that the matrix is not $\alpha$. The structure is discussed in the TEM section.

The microstructure of the 9 at.% Al alloy is heterogeneous, and has the appearance of retained dendritic segregation (Figure 4-33). In Figure 4-33a is an area showing uneven distribution of particles. There are also regions in which a lamellar structure has formed, but some regions appear to be untransformed $\alpha$. There are also discrete particles present (see arrows). It appears that the solution treatment of 1280°C for 50 hours did not homogenize the 9 at.% Al alloy. The hardness of this alloy was also

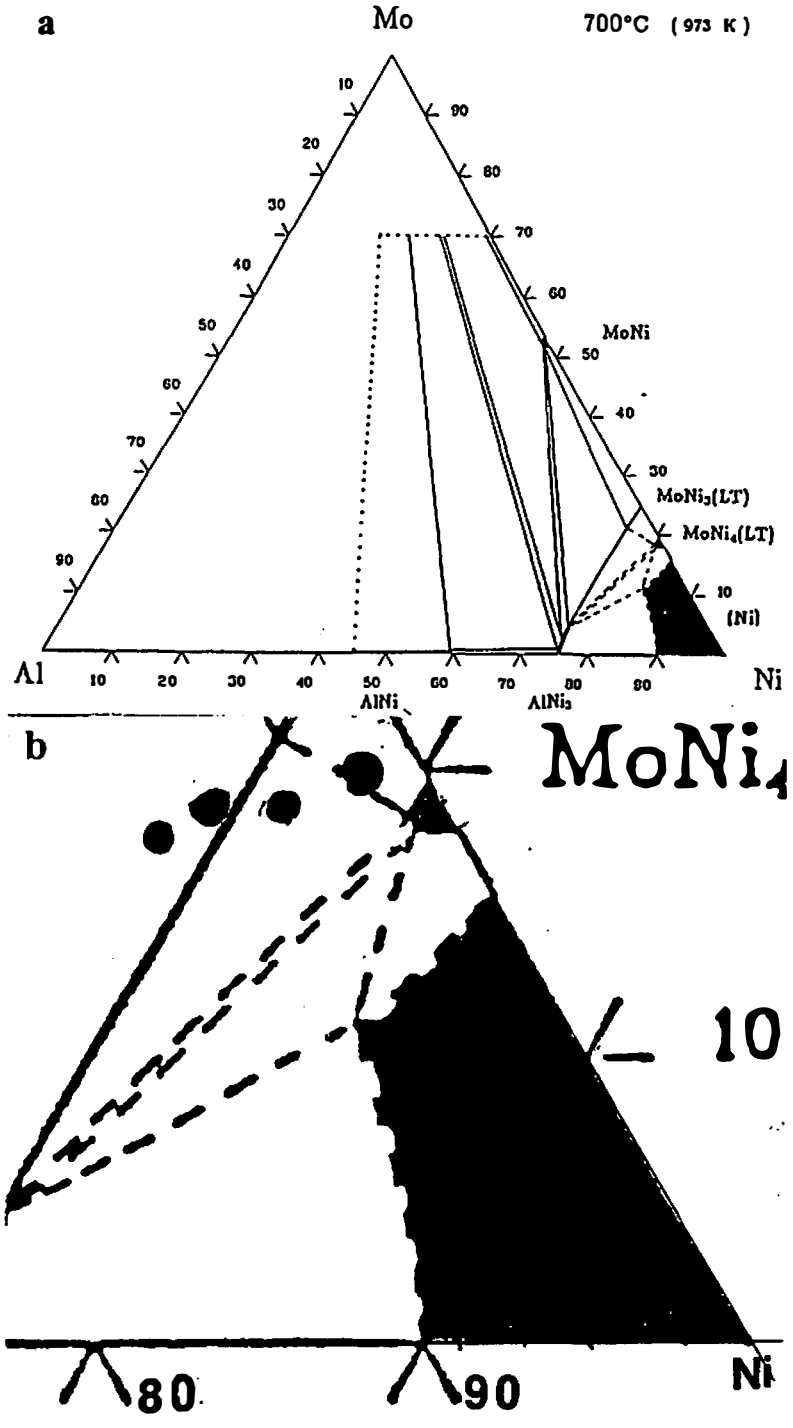



Figure 4-29. Ni-Mo-Al ternary alloy phase diagram at 700°C.

Ref. P. Villars, A. Prince, and H. Okamoto, Handbook of Ternary Alloy Phase Diagrams, Vol. 4, pp. 4046-4066, ASM International, Materials Park, OH, 1995.

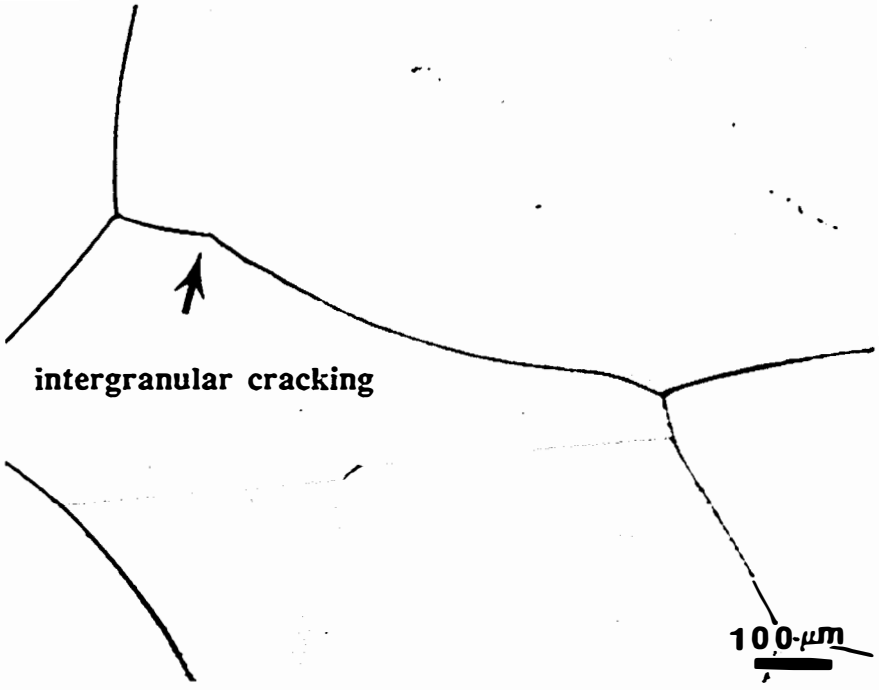



Figure 4-30. OLM microstructure of 2 at.% Al alloy aged at 700°C for 100 hours showing single phase with intergranular cracking.




Figure 4-31. OLM microstructure of 5 at.% Al alloy aged at 700°C for 100 hours showing lamellar structure.

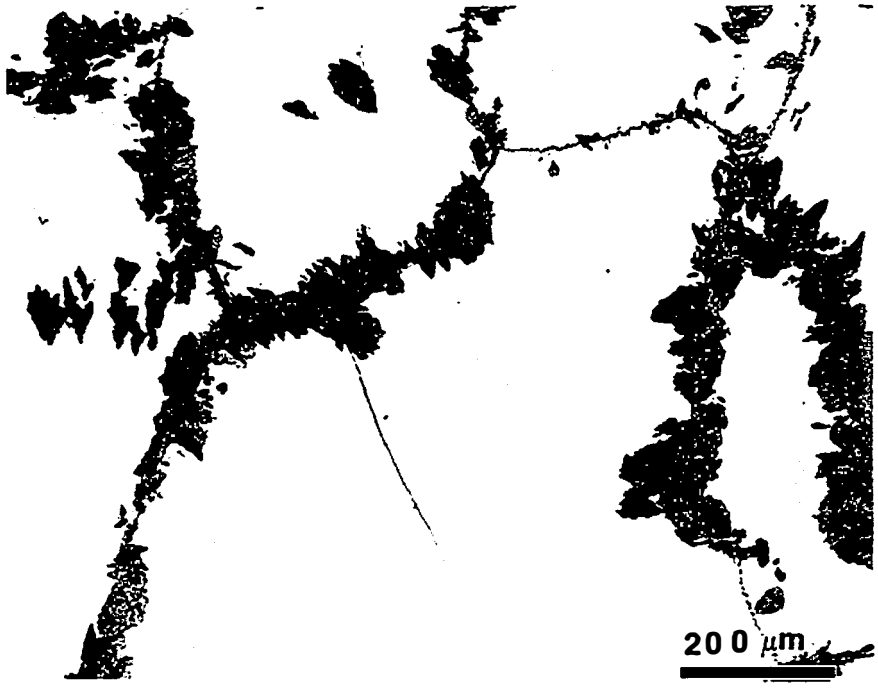



Figure 4-32. OLM microstructure of 7 at.% Al alloy aged at 700°C for 100 hours showing phase transformation along grain boundaries.

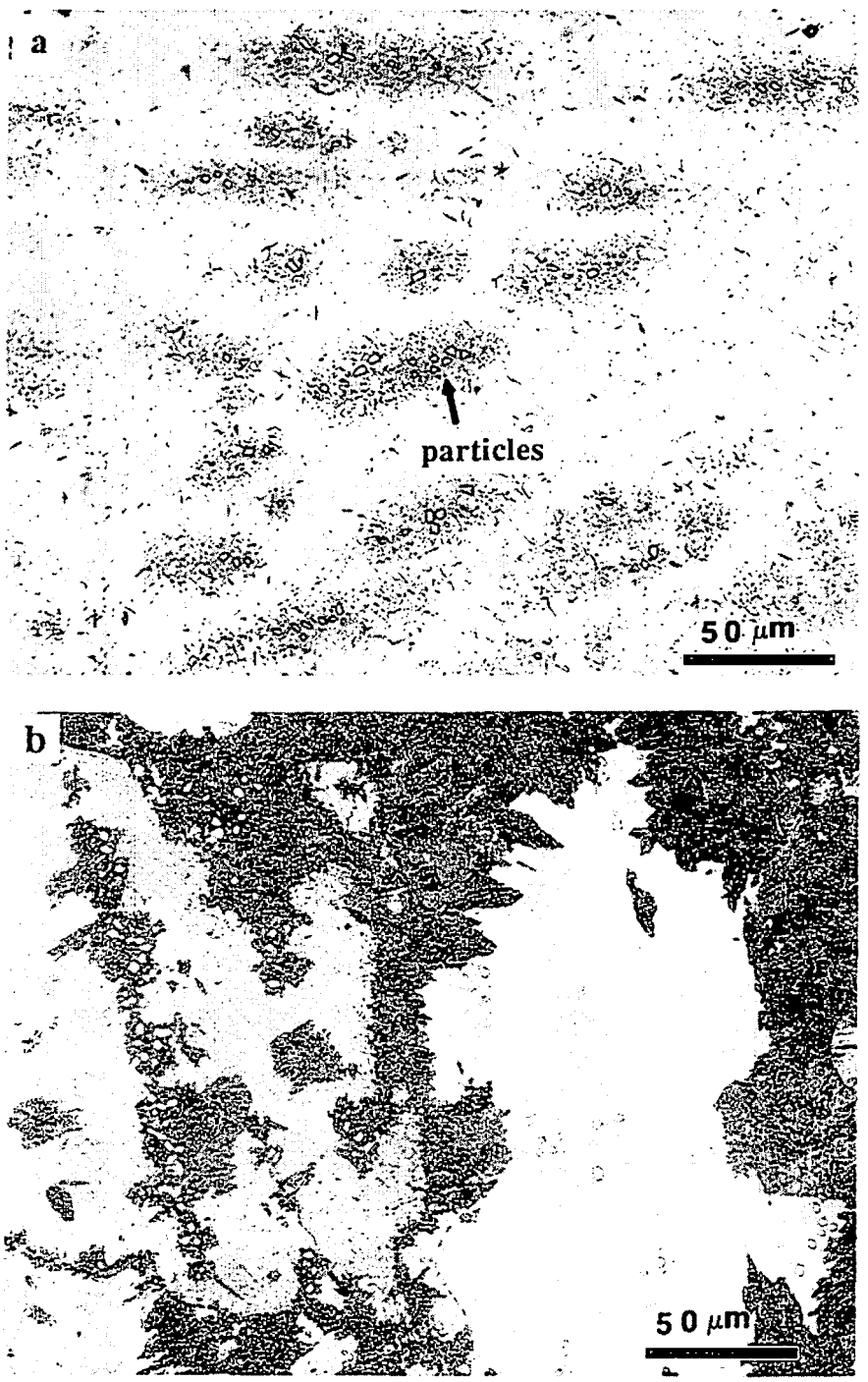



Figure 4-33. OLM microstructure of 9 at.% Al alloy aged at 700°C for 100 hours showing (a) particle precipitation, (b) lamellar structure and particles.

the maximum attained (Figure 4-3).

### 4.2.6. OLM Microstructure of Ni-Mo-Al Alloys with a Solution Treated Plus Aged at 750°C for 10 Hours

Upon aging the $Ni_4Mo$ alloy for 10 hours at 750°C, slight grain boundary migration is oserved and the Widmanstattern structure appeared (Figure 4-34), characteristic of the presence of a fine β domain structure. The hardness approximately doubled (Figure 4-4). The 2 at.% al alloy appears to be single phase (Figure 4-35). TEM (discussed later) showed that this structure is α, and this is consistent with the lack of hardness change (Figure 4-6). Thus the 2 at.% Al alloy has retarded the formation of the β phase. The 5 at.% Al alloy showed intergranular cracking and the formation of a considerable amount of lamellar structure along the α boundaries (Figure 4-36). Considerable hardening occurred during the 10 hours aging (Figure 4-6). The 7 at.% Al alloy showed some grain boundary migration accompanied by the formation of a lamellar structure (Figure 4-37). Note that there is less of this structure in this 7 at.% Al alloy than in the 5 at.% Al alloy, similar to that found upon aging at 700°C. This alloy only showed a slight increase in hardness (Figure 4-6).

### 4.2.7. OLM Microstructure of Ni-Mo-Al Alloys with a Solution Treated Plus Aged at 750°C for 50 Hours

The $Ni_4Mo$ alloy after aging for 50 hours at 750°C showed a prominent Widmanstatten pattern (Figure 4-38), showing that the β phase is still present. The slight boundary migration which occurred during 10 hours aging (see Figure 4-34) has progressed, and is presumably associated with domain coarsening. The hardness is about the same as that after 10 hours aging (Figure 4-4).




Figure 4-34. OLM microstructure of $Ni_4Mo$ alloy aged at 750°C for 10 hours showing Widmanstattern pattern β phase.

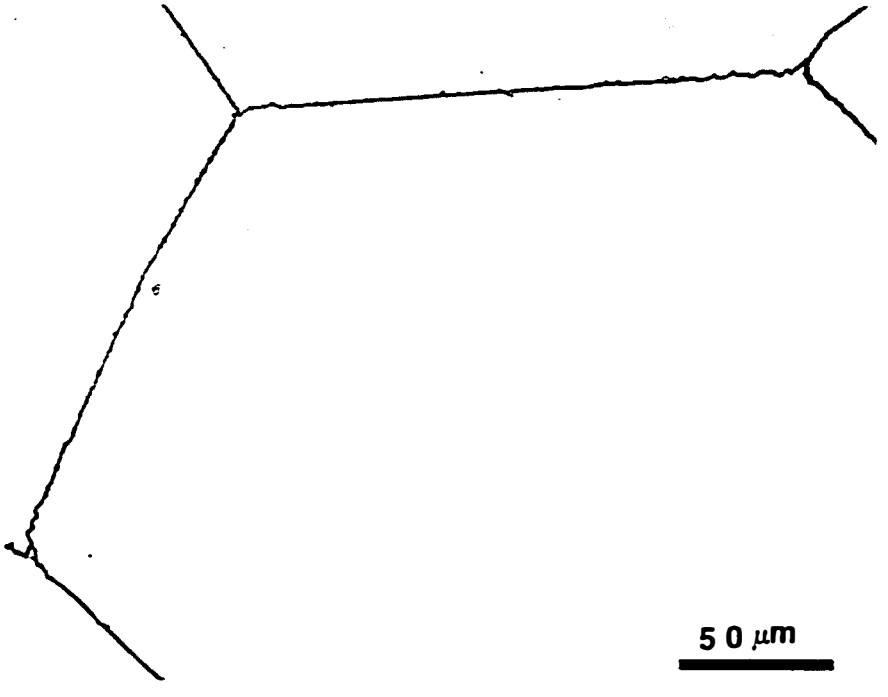



Figure 4-35. OLM microstructure of 2 at.% Al alloy aged at 750°C for 10 hours showing single α phase.

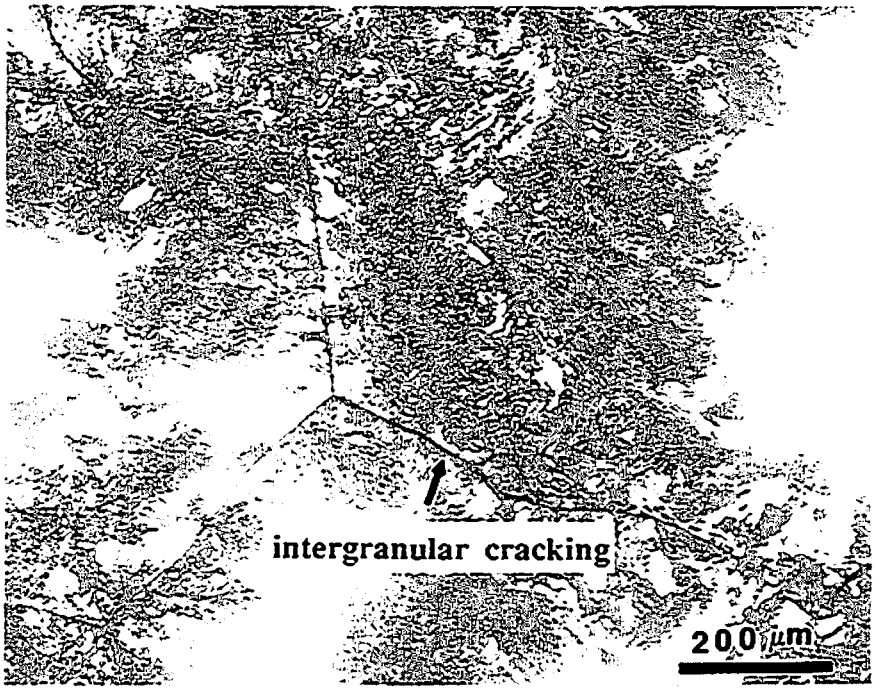



Figure 4-36. OLM microstructure of 5 at.% Al alloy aged at 750°C for 10 hours showing lamellar structure with intergranular cracking.

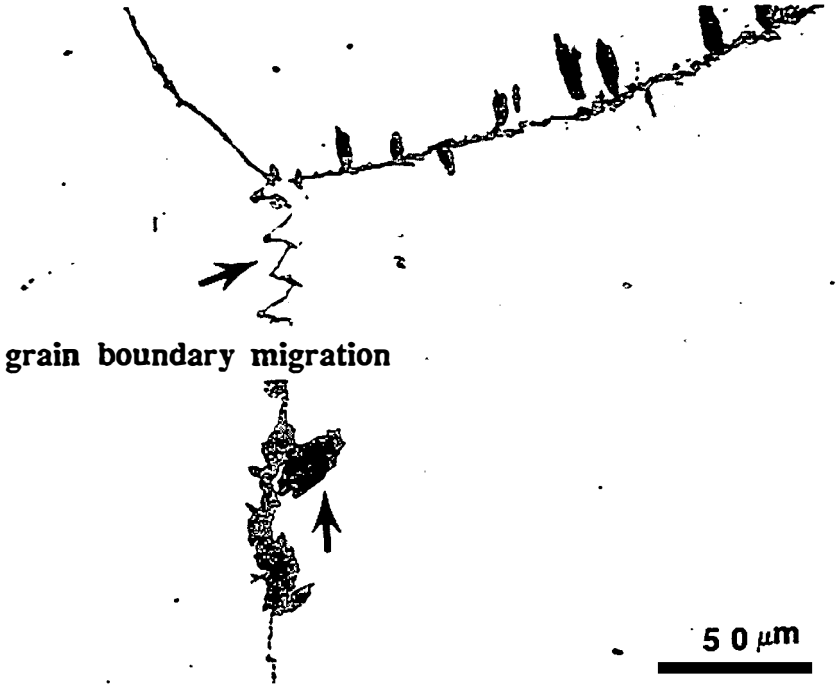



Figure 4-37. OLM microstructure of 7 at.% Al alloy aged at 750°C for 10 hours showing grain boundary migration and phase transformation along the grain boundaries.

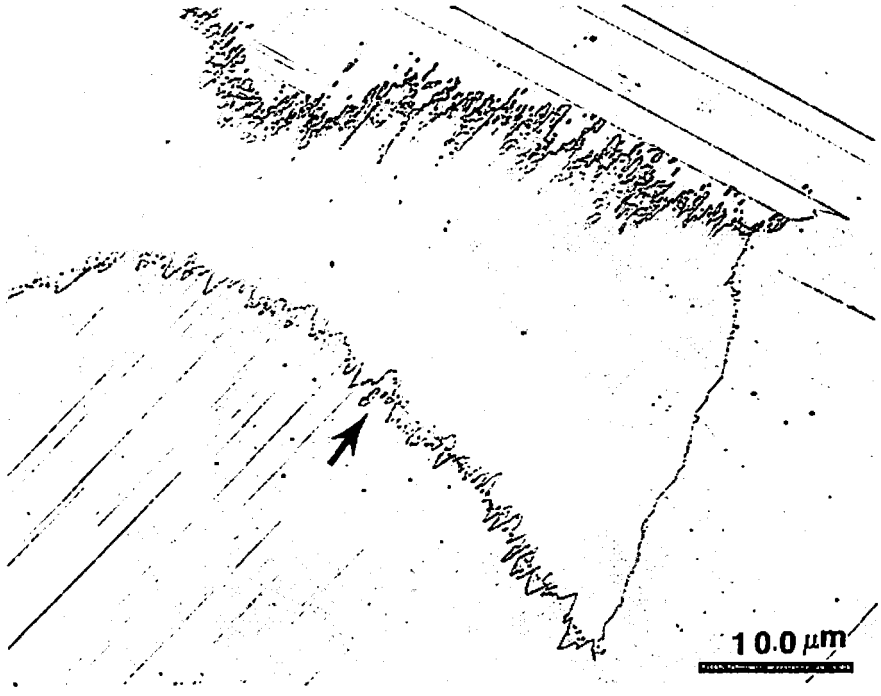



Figure 4-38. OLM microstructure of $Ni_4Mo$ alloy aged at 750°C for 50 hours showing Widmanstatten pattern β and grain boundary migration.

The 2 at.% Al alloy appears to be mainly single phase, but there is a structure growing from the grain boundaries (Figure 4-39). There is a marked increase in hardness compared to that after aging 10 hours (Figure 4-4), indicating that the matrix is probably not $\alpha$ phase. The structure is discussed in the TEM section. For the 5 at.% Al alloy, the amount of lamellar structure has continued to increase to completely consume the matrix (Figure 4-40). This alloy has the maximum hardness of all the alloys and heat treatments (Figure 4-4). The 7 at.% Al alloy shows the lamellar structure forming from the grain boundaries (Figure 4-41). A few regions of the formation of the lamellar structure within the grains were found, but are not shown in Figure 4-41.

With an increase of the aging time from 10 hours to 50 hours at 750°C, the amount of the lamellar structure increased in 5 at.% Al and 7 at.% Al alloys. In 2 at.% Al alloy, a thin layer of secondary phase started to nucleate along the grain boundaries. The intergranular cracking was found in both 2 at.% Al and 5 at.% Al alloys but not in 7 at.% Al alloy. Thus, the cohesion of grain boundaries decreases in 2 at.% Al and 5 at.% Al alloys under this aging condition but may be enhanced in 7 at.% Al alloy.

### 4.2.8 OLM Microstructure of Ni-Mo-Al Alloys with a Solution Treated Plus Aged at 750°C for 100 Hours

The microstructure of the $Ni_4Mo$ alloy after aging at 750°C for 100 hours is shown in Figure 4-42. The Widmanstatten pattern etches in a prominent fashion, and the grain boundary migration associated with presumably coarsened $\beta$ domains has progressed further. The hardness is about the same as that after aging for only 10 hours (Figure 4-4).

At low magnification, the microstructure of the 2 at.% Al alloy appears to be single phase (Figure 4-43a). However, high magnification (Figure 4-43b) reveals precipitates

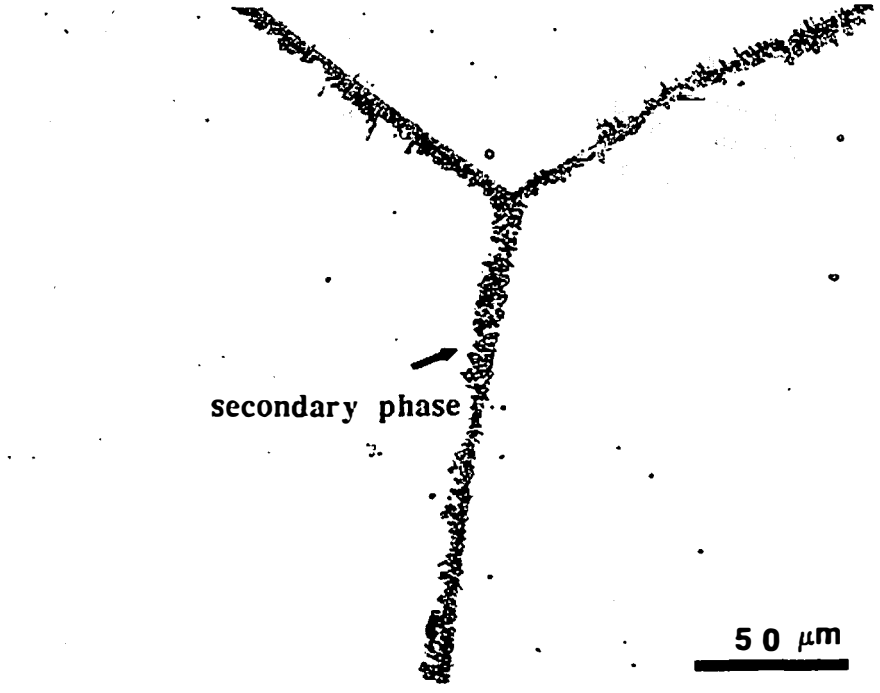



Figure 4-39. OLM microstructure of 2 at.% Al alloy aged at 750° for 50 hours showing phase transformation along the grain boundaries.

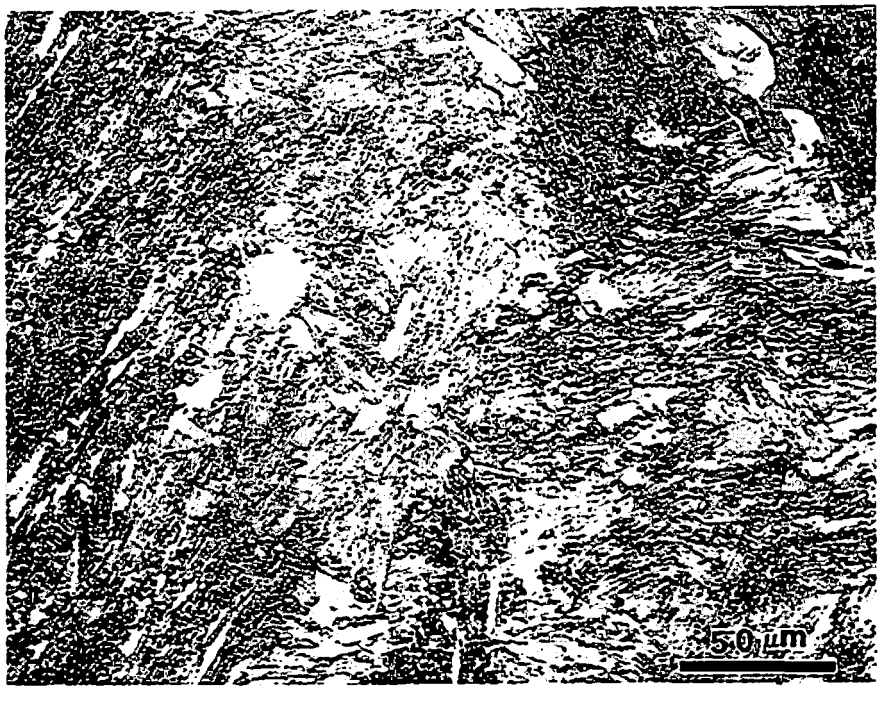



Figure 4-40. OLM microstructure of 5 at.% Al alloy aged at 750°C for 50 hours showing lamellar structure.

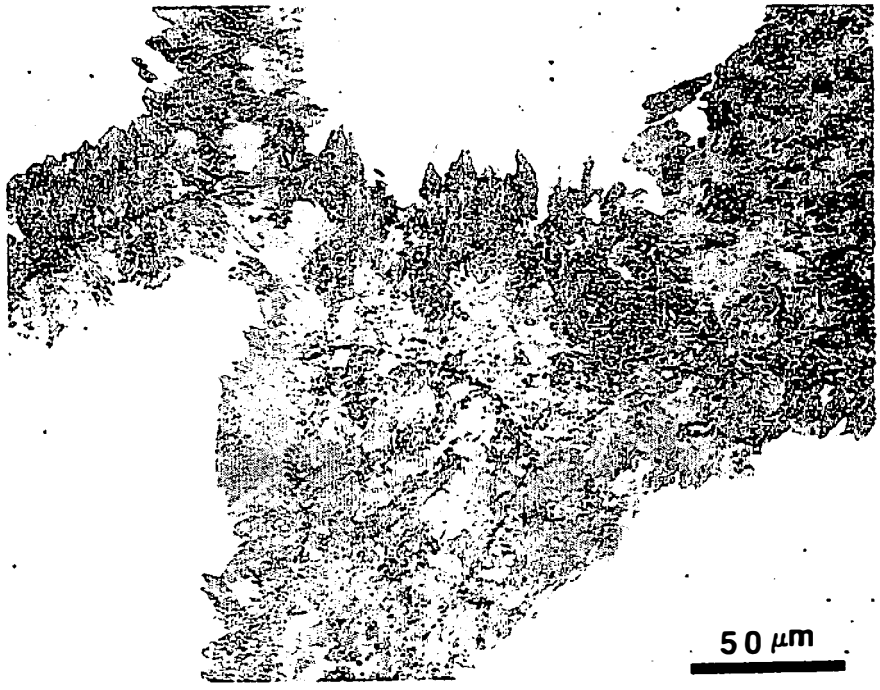



Figure 4-41. OLM microstructure of 7 at.% Al alloy aged at 750°C for 50 hours showing lamellar structure formation along the grain boundaries.

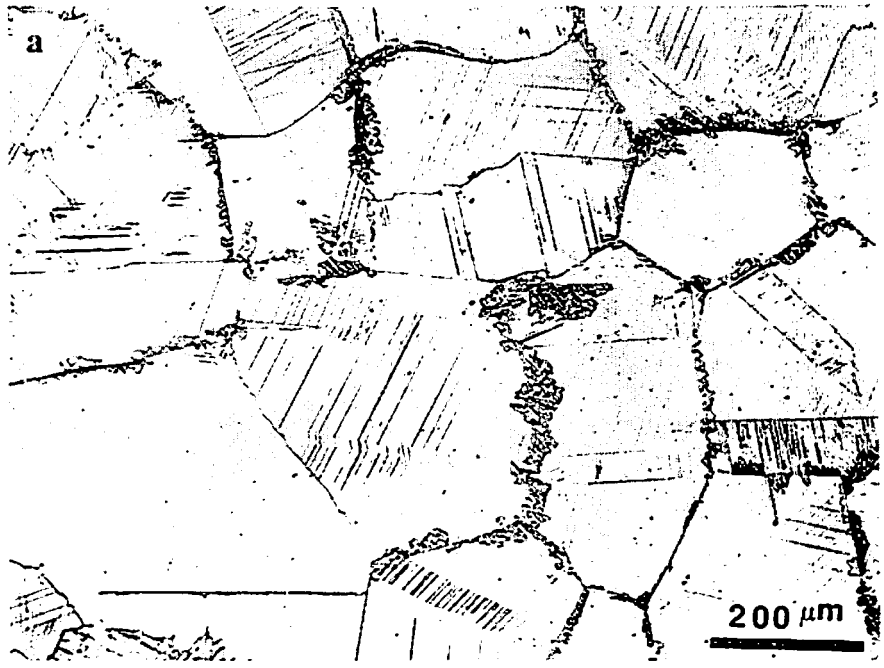



Figure 4-42. OLM microstructure of $Ni_4Mo$ alloy aged at 750°C for 100 hours showing (a) Widmanstatten pattern β phase and coarse β associated with grain boundaries migration, (b) high magnification of coarse β, (c) high magnification of Widmanstatten pattern β.



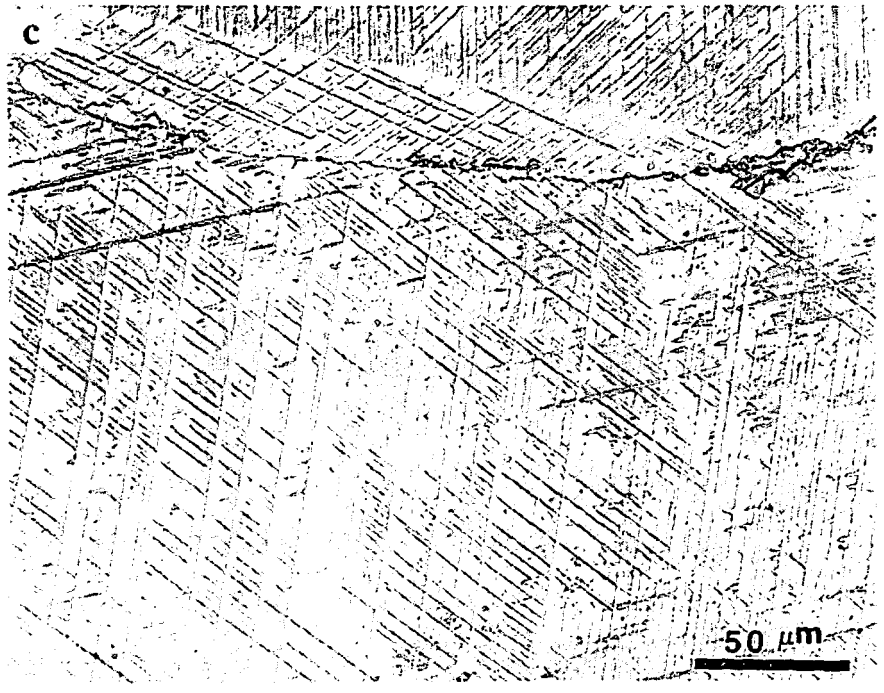




Figure 4-42. continue (b) and (c).

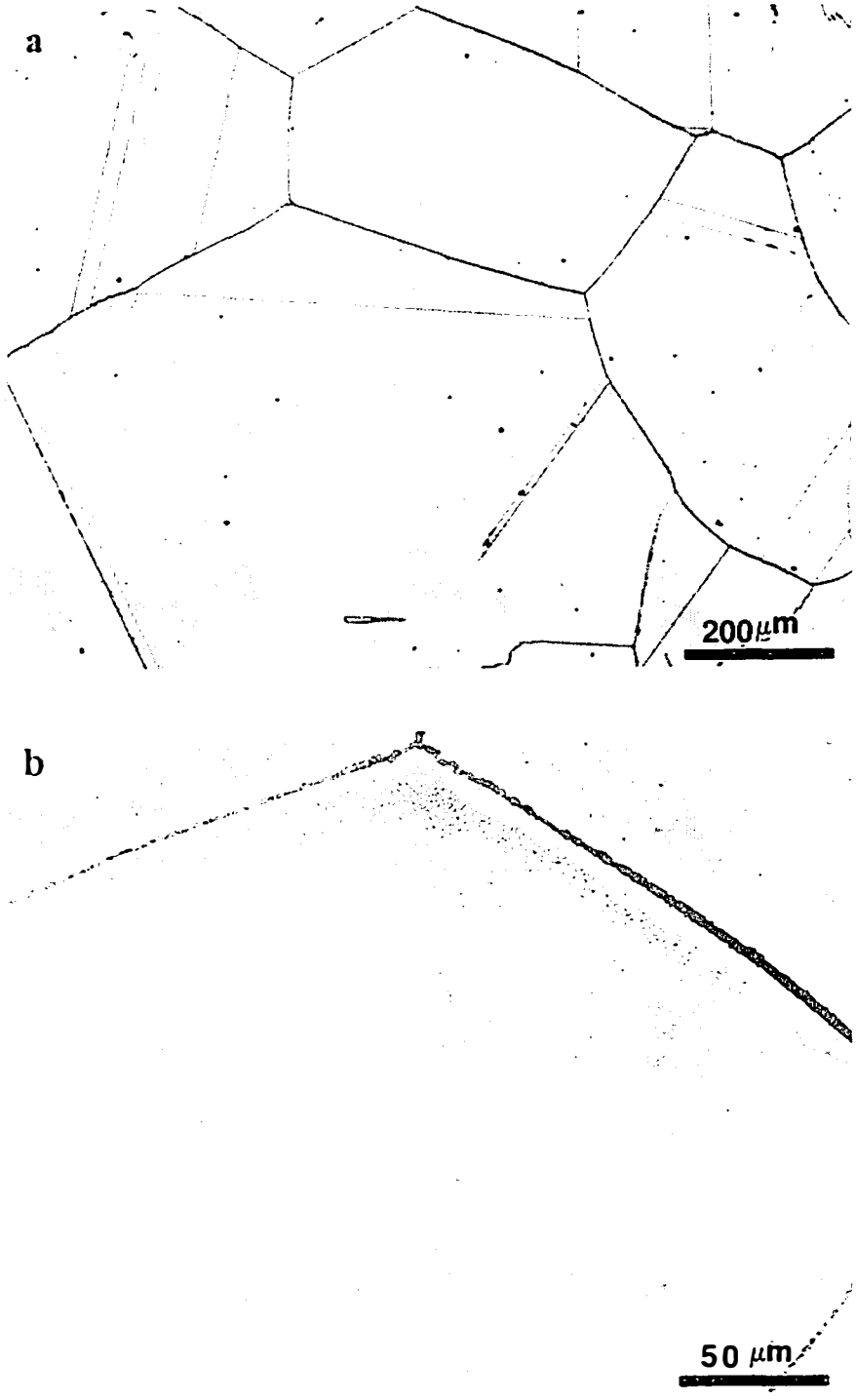



Figure 4-43. OLM microstructure in 2 at.% Al alloy aged at 750°C for 100 hours showing (a) single phase with annealing twins, (b) high magnification of secondary phase formation.

structure has formed along the grain boundaries and a denuded zone is produced bounded by a band of fine precipitates. Precipitates are also present within the grains. The 5 at.% Al alloy has converted almost entirely to a lamellar structure, which in regions appears to be converting to a coarser lamellar structure (Figure 4-44). The 7 at.% Al alloy shows a similar lamellar structure (Figure 4-45a), but less of it than in the 5 at.% Al alloy. There is also lamellar structure forming from the grain boundaries and inside the grains. There are also discrete particles along the grain boundaries (Figure 4-45b). Some of the features of these alloys are discussed in more detail in the section on fractography. For these alloys, the hardness is about the same as that for aging for 50 hours (Figure 4-4). The 9 at.% Al alloy shows about 50% lamellar structure in the matrix (Firgure 4-46a), and also particles along the grain boundaries are observed (Figure 4-46b).

After aging at 750°C for 100 hours, intergranular cracking was not found in the 2 at.% Al or 5 at.% Al alloys. Thus, it appears that with an increase of aging time, the cohesion of grain boundaries increases, although the hardness of 2 at.% Al and 5 at.% Al alloys is the same as that of samples after aging for 50 hours at the same temperature (Figure 4-4).

### 4.2.9. OLM Microstructure of Ni-Mo-Al Alloys with a Solution Treated Plus Aged at 850°C for 100 Hours

There is no Ni-Mo-Al phase diagram for 850°C, but as a guide to phase equilibrium the diagram shown in Figure 4-47 [65] for 800°C will be used. The equilibrium phases for the aluminum alloys are noted on the diagram. In this phase diagram, the δ phase region is not shown, the Ni-Mo phase diagram (see Figure 2-1) shows the δ phase region at 50 at.% molybdenum.

In the 2 at.% Al alloy, four different microstructural features are present

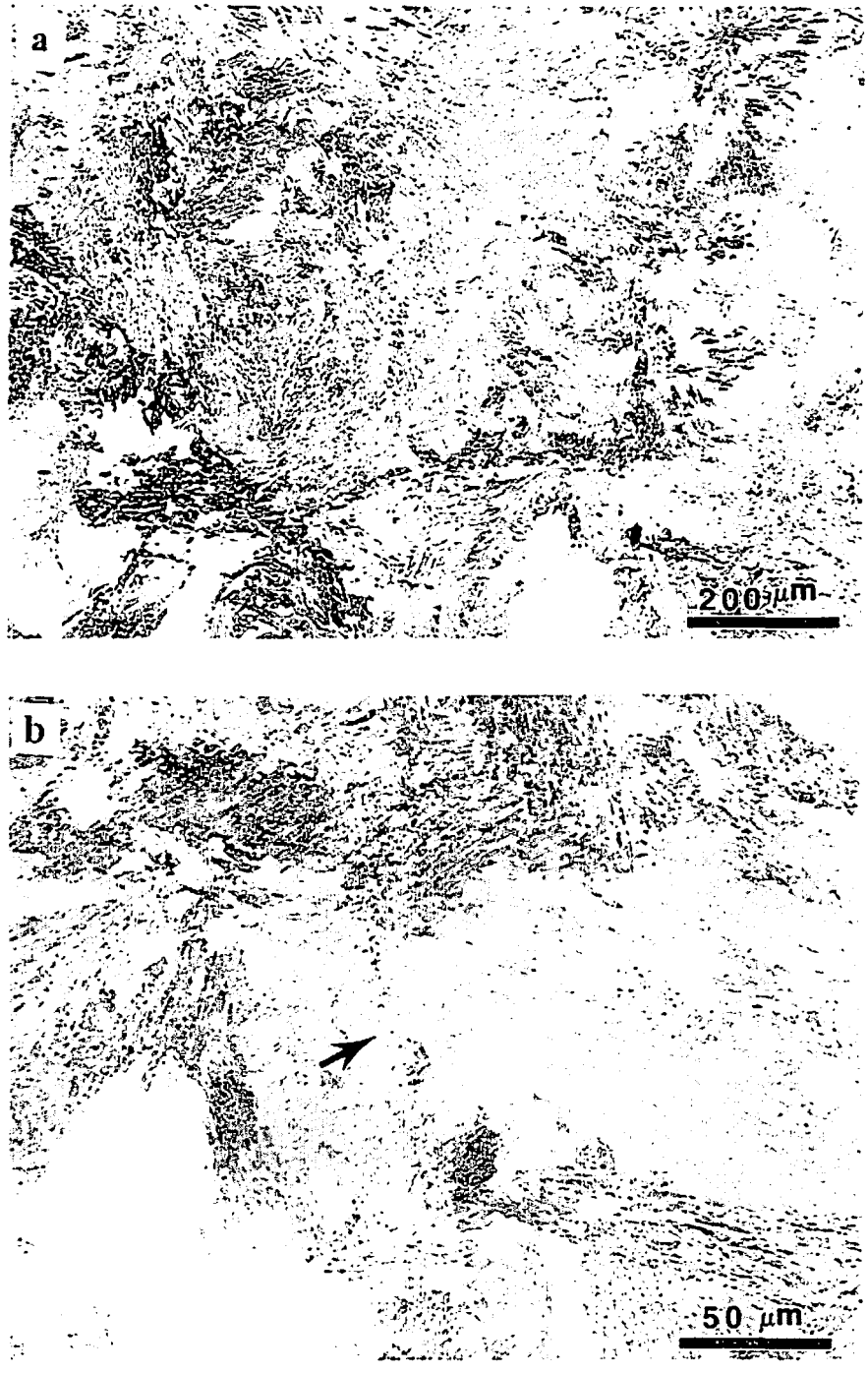



Figure 4-44. OLM microstructure of 5 at.% alloy aged at 750°C for 100 hours showing (a) lamellar structure, (b) coarse lamellar structure formed along grain boundaries.

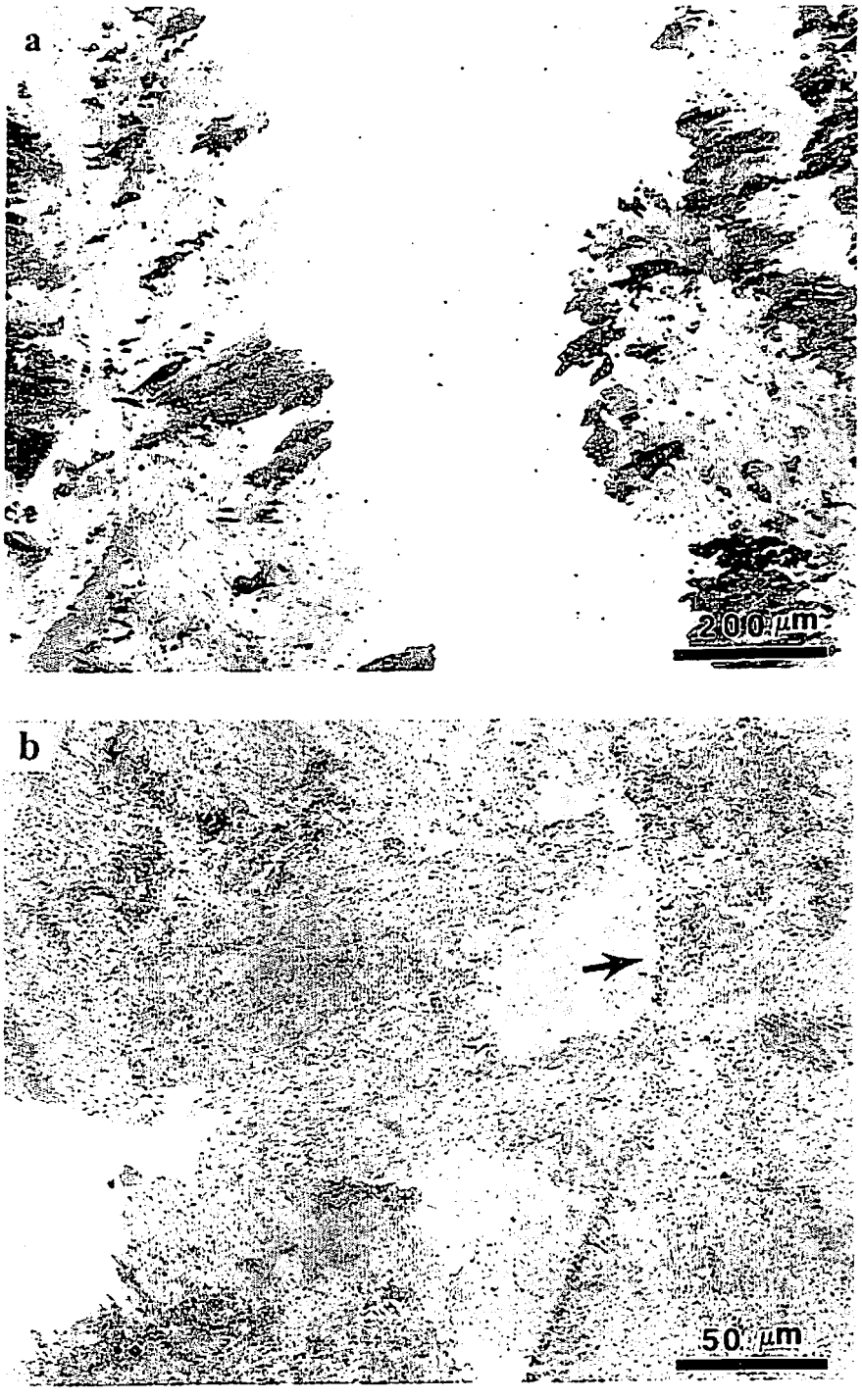



Figure 4-45. OLM microstructure of 7 at.% Al alloy aged at 750°C for 100 hours showing (a) lamellar structure formed along grain boundaries, (b) coarse lamellar structure along grain boundaries.

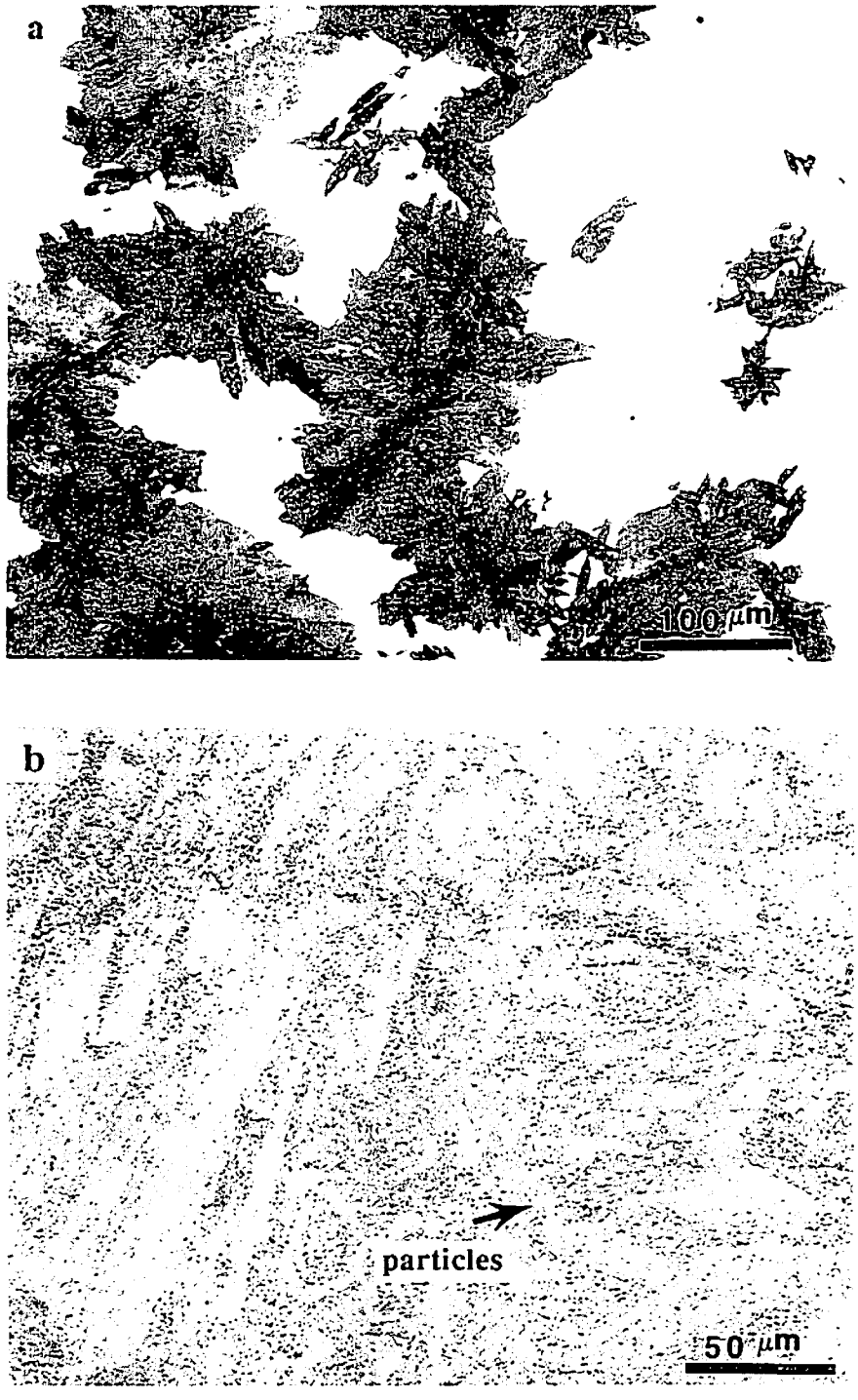



Figure 4-46. OLM microstructure of 9 at.% Al alloy aged at 750°C for 100 hours showing (a) lamellar structure nucleated in grains, (b) high magnification of lamellar structure and particles along the grain goundaries.

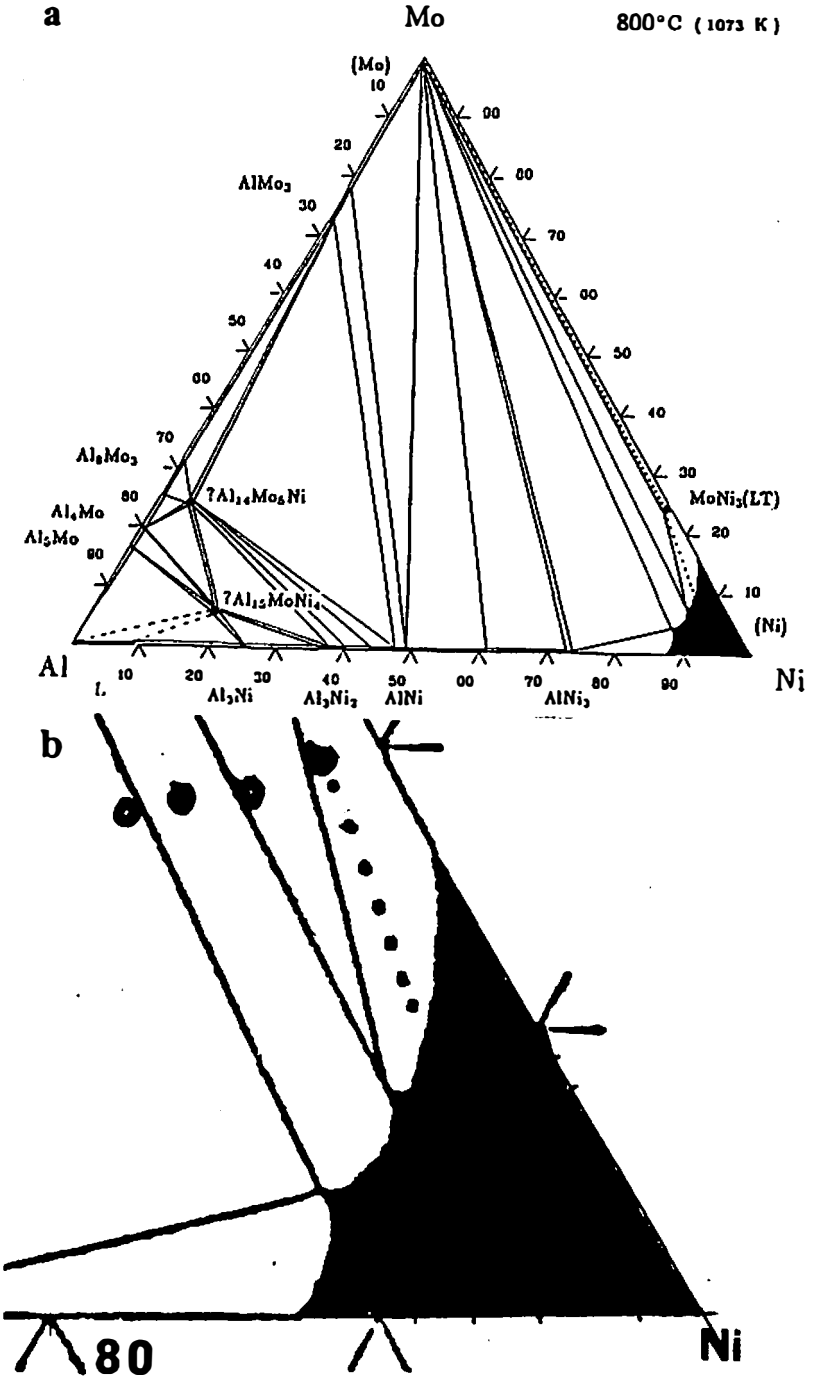



Figure 4-47. Ni-Mo-Al ternary alloy phase diagram at 800°C.

Ref. P. Villars, A. Prince, and H. Okamoto, Handbook of Ternary Alloy Phase Diagrams, Vol. 4, pp. 4046-4066, ASM International, Materials Park, OH, 1995.

(Figure 4-48): (a) fine striation structure; (b) thin Windmanstatten plates; (c) coarse lamellar structure; (d) the matrix. The 5 at.% Al alloy shows what appears to be a needle-like structure which is spheroidizing (Figure 4-49). The 7 at.% Al alloy shows a somewhat similar but finer structure (Figure 4-50). These structures are identified later in the section on SEM and TEM observations.

A similar thin plate structure was observed by Brooks and Wang [22] in the commercial Hastelloy B2 alloy after aging at 850°C for 200 hours. Vasudevan [67] found a similar structure in a $Ni_4Mo$ alloy containing 2.08 at.% Cr after aging at 850°C for 4500 hours. Williams [68] reported needle-like precipitates in a W and Ta modified Ni-Mo-Al alloy after prolonged exposure in the range 870 to 980°C.

After aging for 100 hours at 850°C, the hardness increases with aluminum content (Figure 4-3), although there are different microstructural features than those which formed at lower temperatures. However, the hardness of the alloys has decreased considerably from the peak values achieved near 700°C (Figure 4-5).

### 4.2.10. OLM Microstructure of Ni-Mo-Al Alloys with a Solution Treated Plus Aged at 950°C for 100 Hours

As a guide to the equilibrium phases at 950°C, the ternary phase diagram is shown in Figure 4-51 [65]. The phases are noted for the alloy studied.

After aging for 100 hours at 950°C, the 2 at.% Al alloy shows what appears to be single phase $\alpha$ (Figure 4-52). Note in Figure 4-3 that the hardness is about the same as that of the base $Ni_4Mo$ alloy. The 5 at.% Al alloy has transformed completely to fine precipitates (Figure 4-53a). There are also particles along the grain boundary (Figure 4-53b). These precipitates have increased the hardness considerably (Figure 4-3). The 7 at.% Al alloy shows an even finer precipitates structure, and some particles along the grain

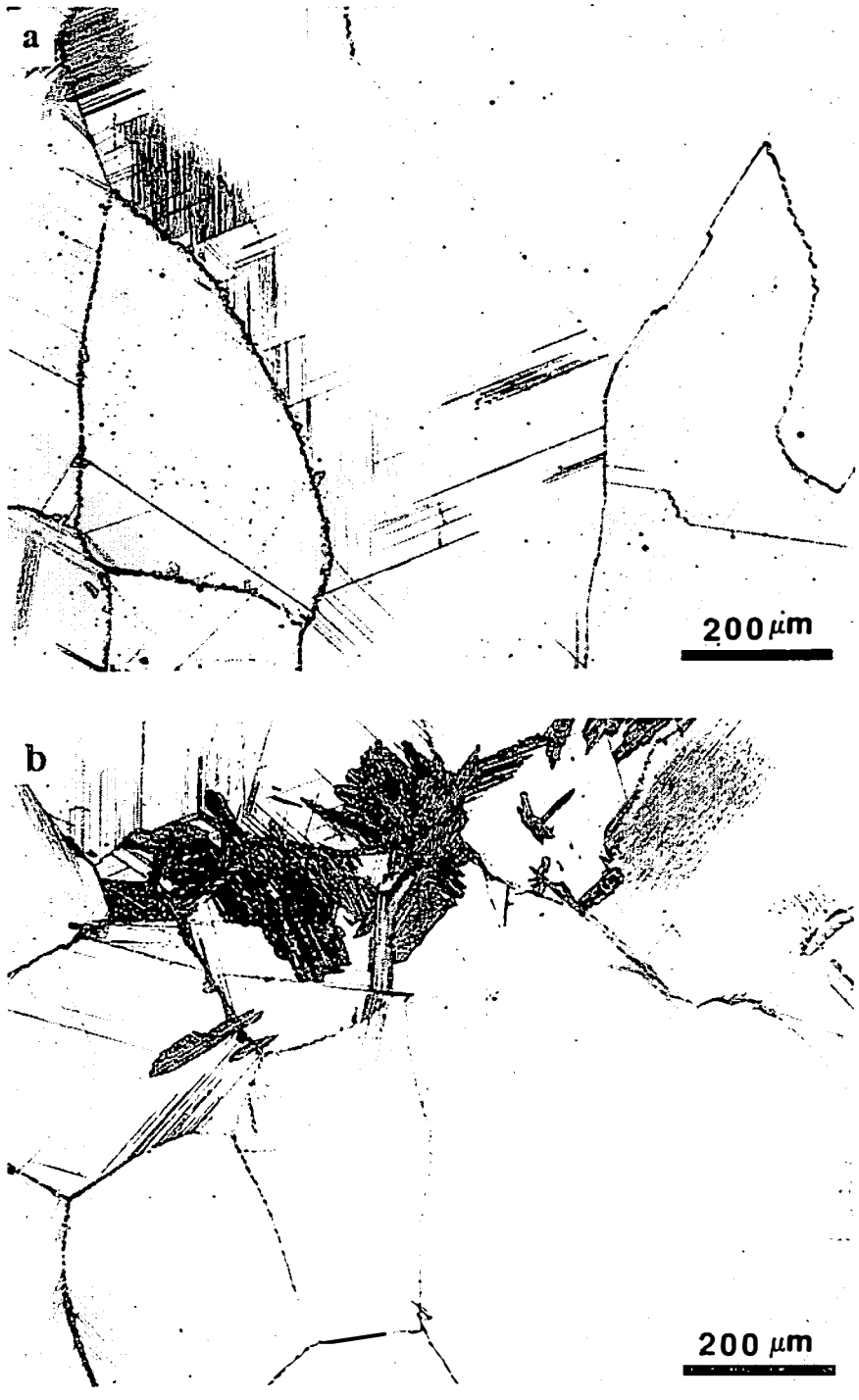



Figure 4-48. OLM microstructure of 2 at.% Al alloy aged at 850°C for 100 hours showing (a) Widmanstatten structure, (b) coarse lamellar structure and fine striation structure.

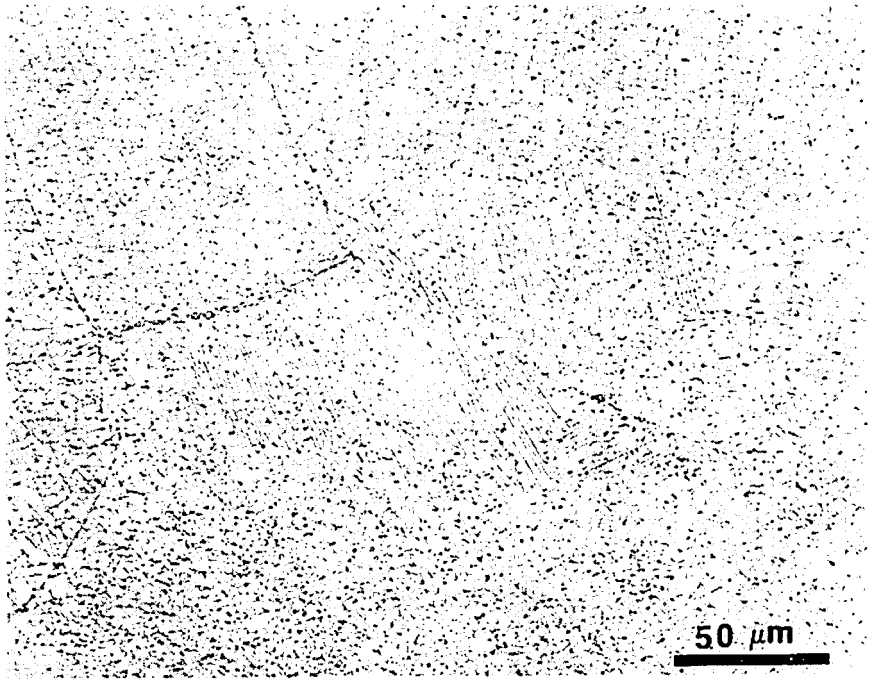



Figure 4-49. OLM microstructure of 5 at.% Al alloy aged at 850°C for 100 hours showing needle-like structure.

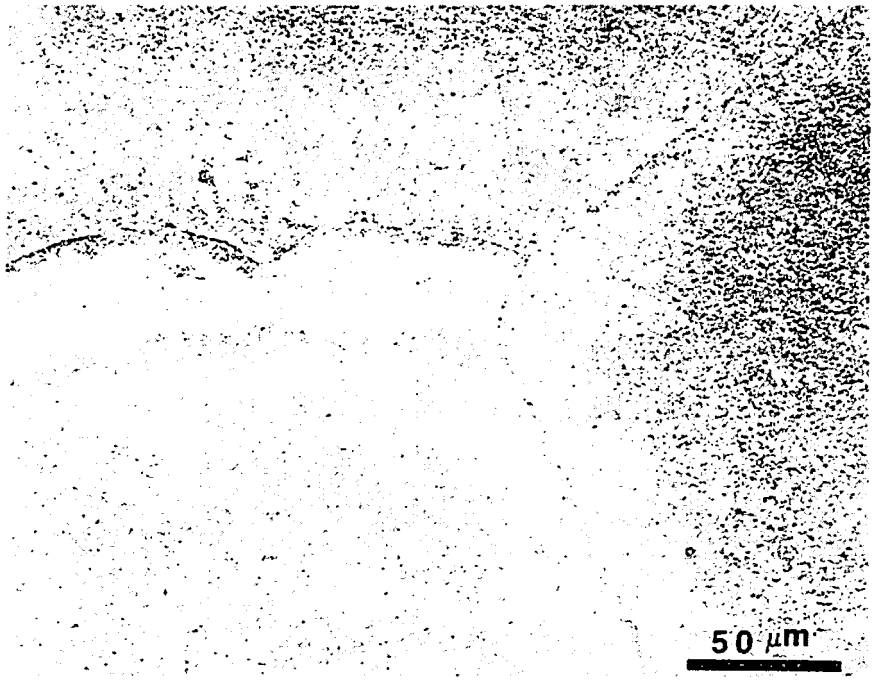



Figure 4-50. OLM microstructure of 7 at.% Al alloy aged at 850°C for 100 hours showing needle-like structure.

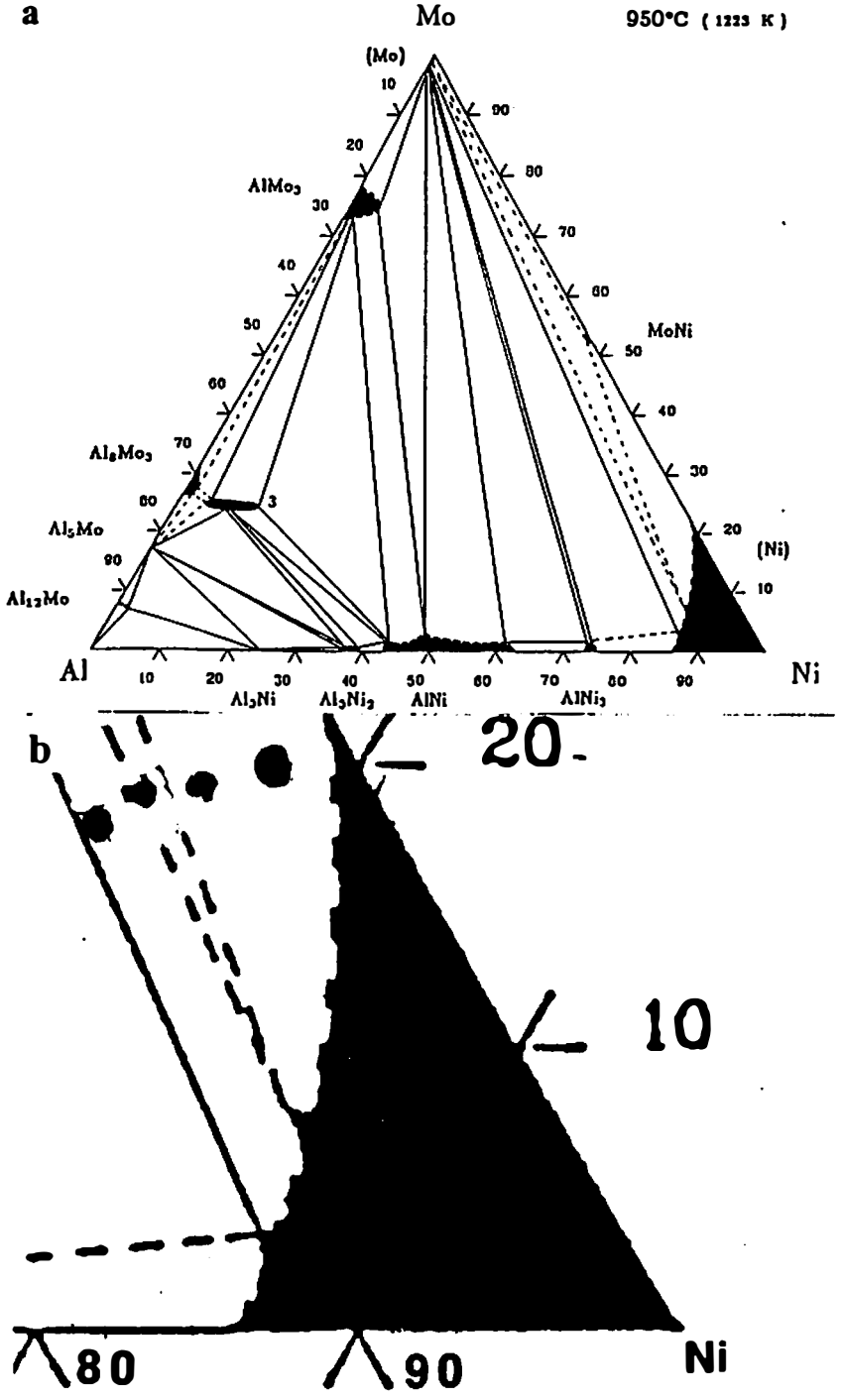



Figure 4-51. Ni-Mo-Al ternary alloy phase diagram at 950°C.

Ref. P. Villars, A. Prince, and H. Okamoto, Handbook of Ternary Alloy Phase Diagrams, Vol. 4, pp. 4046-4066, ASM International, Materials Park, 1995.

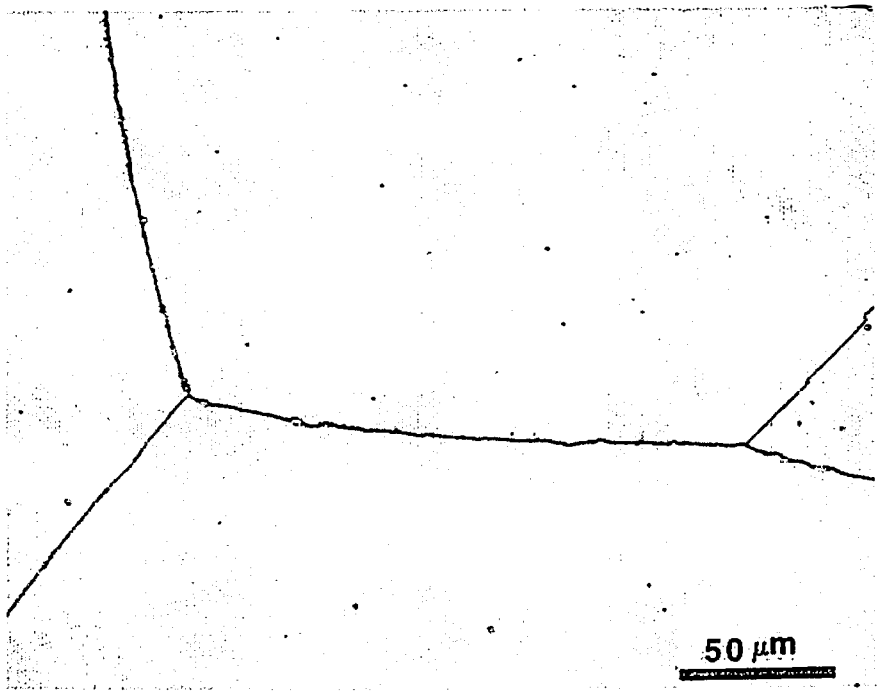



Figure 4-52. OLM microstructure of 2 at.% Al alloy aged at 950°C for 100 hours showing single phase and particles along grain boundaries.

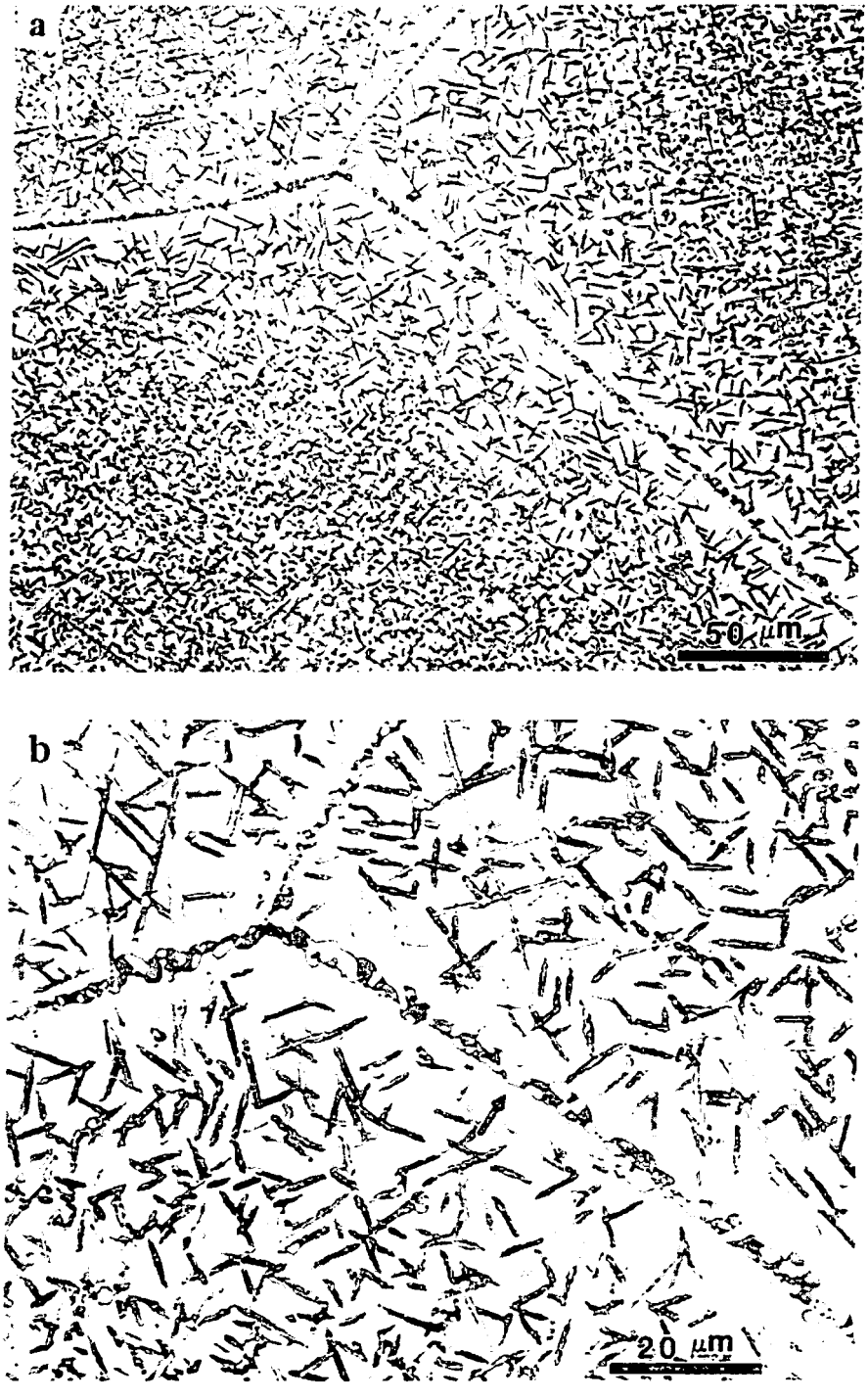



Figure 4-53. OLM microstructure of 5 at.% Al alloy aged at 950°C for 100 hours showing needle-like structure and particles precipitates along the grain boundaries. (a) 400X. (b) 1000X.

boundaries (Figure 4-54, a and b). This finer structure produced additional hardness over that of the 5 at.% Al alloy (Figure 4-3).

### 4.2.11. Summary of OLM Observations

The microstructural features observed by OLM are summarized in Table 4-1. Note that usually the phases present are not identified. This table will be upgraded to identify the phases associated with the microstructural features following the examination of the SEM and TEM results.

## 4.3 Scanning Electron Microscopy (SEM) Microstructural Evaluation

The OLM observations gave an overall picture of the phase transformations which occurred during aging, but the resolution restriction of the OLM prevented examination of the fine structural details. Also, there was no direct way to identify the phases which formed. In this section, the SEM microstructural observations are presented and analyzed. Of special use here is the qualitative chemical analysis of the phases obtained by EDS, which give strong clues to the identification of the phases. In some cases the phases are too fine for useful EDS analysis. Most of the SEM microstructures were obtained with secondary electrons (SE), which is most appropriate for high resolution imaging. However, some chemical discrimination can be obtained by imaging with the back-scattered electron (BSE), so some microgroaphs obtained by this imaging mode are presented. However, in the etched microstructure, topography changes (e.g. at the edge of a hole) may produce a somewhat false indication of chemical difference in BSE imaging.

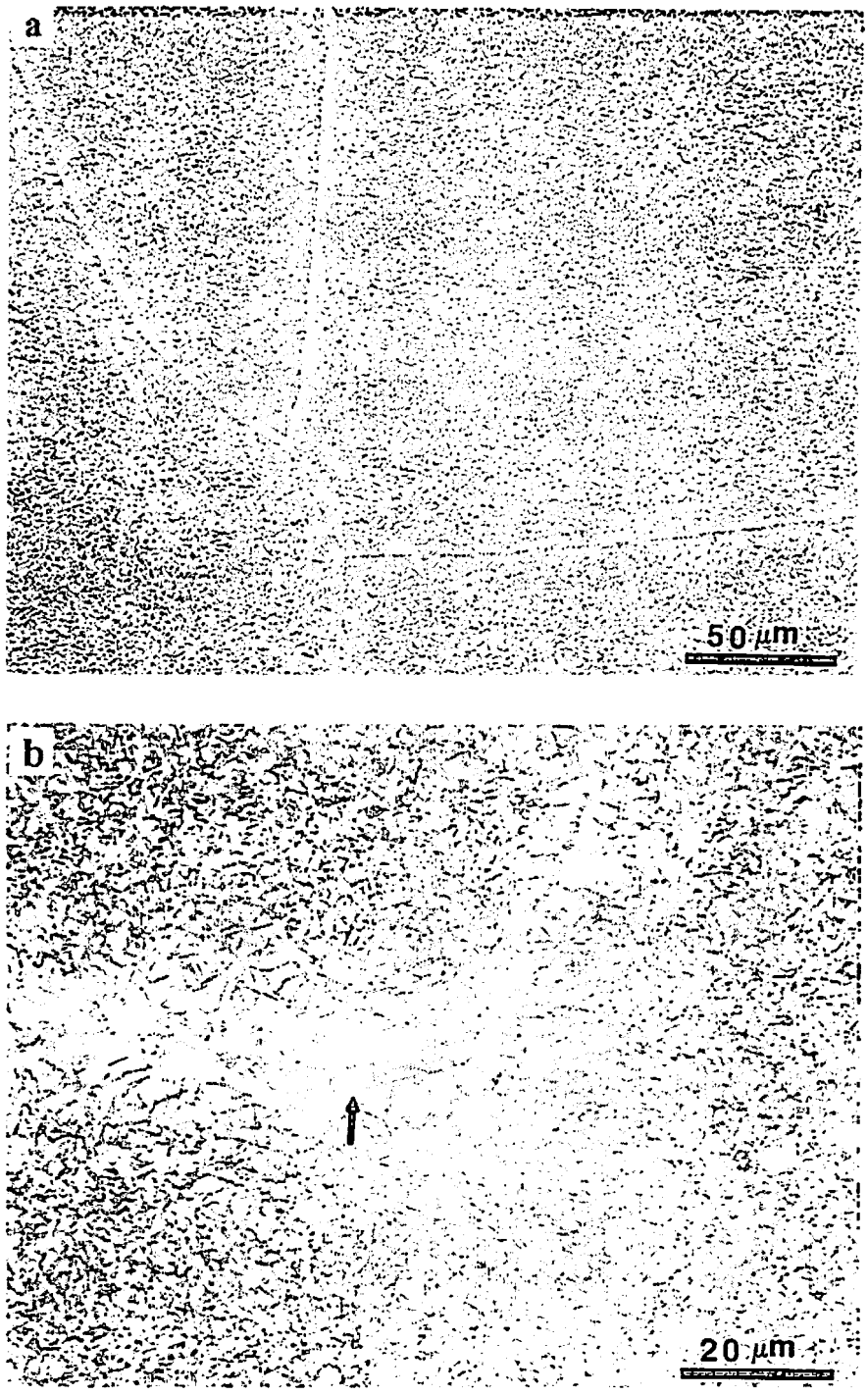



Figure 4-54. OLM microstructure of 7 at.% Al alloy aging at 950°C for 100 hours showing needle-like precipitates and particles along the grain boundaries. (a) 400X. (b) 1000X.

Table 4-1. OLM examination of phase transformation of alloys in all aging condition.

| | $Ni_4Mo$ | 2 at.% Al alloy | 5 at.% Al alloy | 7 at.% Al alloy | 9 at.% Al alloy |
|---|---|---|---|---|---|
| 1250°C, 50 hr. | single phase with annealing twins | single phase with annealing twins | single phase with annealing twins | single phase with annealing twins | particles with precipitates in matrix |
| 600°C, 100 hr. | - | single phase | single phase | secondary phase along grain boundaries with grain boundary migration | grain boundary migration, lamellar structure and particles |
| 650°C, 100 hr. | grain boundary migration | single phase, intergranular cracking | lamellar structure, intergranular cracking | grain boundary migration with secondary phase | - |
| 700°C, 100 hr. | - | single phase, intergraunlar cracking | lamellar structure | lamellar structure, grain boundary migration | particles, lamellar structure |

| | | | | | |
|---|---|---|---|---|---|
| 750°C, 10 hr. | β phase | single phase | lamellar structure, intergranular cracking | lamellar structure, grain boundary migration | - |
| 750°C, 50 hr. | β phase | single phase | lamellar structure | lamellar structure | - |
| 750°C, 100 hr. | β phase | secondary phase along grain boundaries | lamellar structure | lamellar structure | lamellar structure |
| 850°C, 100 hr. | - | fine and coarsened striation morphology and coarse lamellar structure | needle-like structure, particles along grain boundaries | needle-like structure, particles along grain boundaries | - |
| 950°C, 100 hr. | - | single phase, particles along grain boundaries | needle-like structure, particles along grain boundaries | needle-like structure, particles along grain boundaries and in matrix | - |

### 4.3.1. SEM Microstructural Evaluation for $Ni_4Mo$ in the Hot Forged Condition and After Aged at 800°C for 10 Minutes.

Figure 4-55a shows a BSE image of the $Ni_4Mo$ alloy in the as-received, hot forged condition. In the predominately $\alpha$ matrix there are annealing twins, black particles and holes where particles etched out. The EDS from these regions are shown in Figure 4-55, b, c and d. The black particles (at C) are rich in aluminum, and are presumed to be $Al_2O_3$ oxides. The black holes (at B), where particles were etched out, had a Ni-Mo peak ratio of 2.8, whereas the matrix (at A) has a value of 1.9. This indicates that the particles in the black hole are probably the $\gamma$ phase because the hole contains a low molybdenum content. Note that the matrix did not develop a Widmanstatten pattern upon etching which is characteristic of the presence of $\beta$ domains, and hence it is assumed that the material cooled sufficiently rapidly from the hot forging temperature to retain $\alpha$ phase. The presence of the $\gamma$ phase indicates that the composition of the alloy was slightly on the molybdenum-rich side of the exact $Ni_4Mo$ composition, placing the alloy in the $\beta + \gamma$ region of the phase diagram below the transformation temperature (see Ni-Mo phase diagram in Figure 2-1).

After aging for 10 min. at 800°C, the Widmanstatten pattern etched out in the matrix, showing that the $\alpha$ phase has decomposed to a $\beta$ domain structure (Figure 4-56a). There is some grain boundary migration, indicating domain coarsening. The EDS of the particles at A is shown in Figure 4-56b. These particles are rich in molybdenum, with a nickel to molybdenum ratio of 0.75. The high molybdenum content could indicate that these particles are the $\delta$ (NiMo) phase, but in this relatively pure Ni-Mo binary alloy this phase should not appear (see Figure 2-1, Ni-Mo phase diagram). The $\delta$ particles formed because of the element segregation.

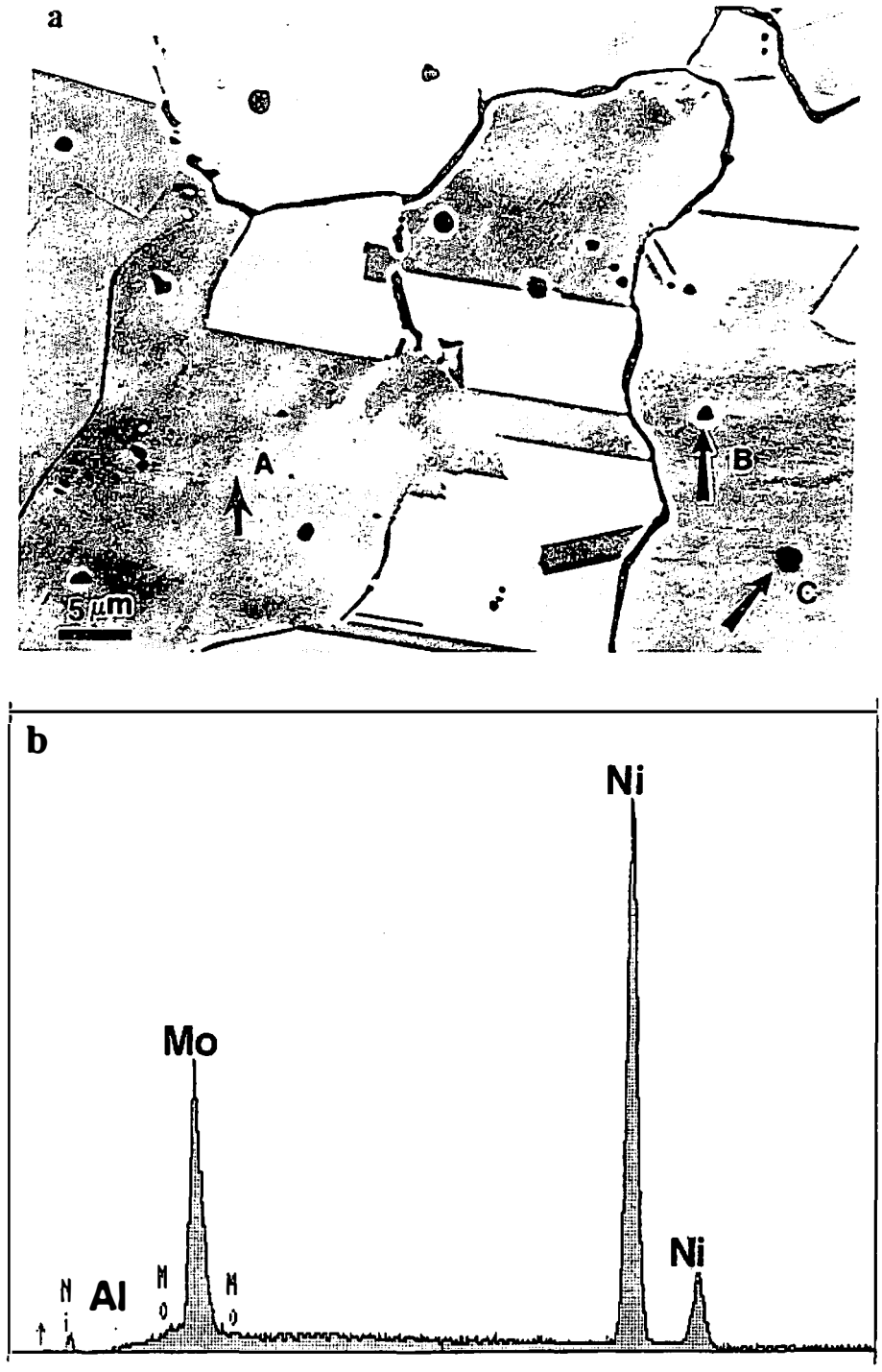



Figure 4-55. (a) SEM microstructure (BSE) of $Ni_4Mo$ alloy (hot forged condition) showing single α phase with particles. (b) EDS analysis from A for matrix, the ratio of Ni to Mo is 1.9, (c) EDS analysis from B for black particles, (d) EDS analysis from black particles (bright particles in SE).

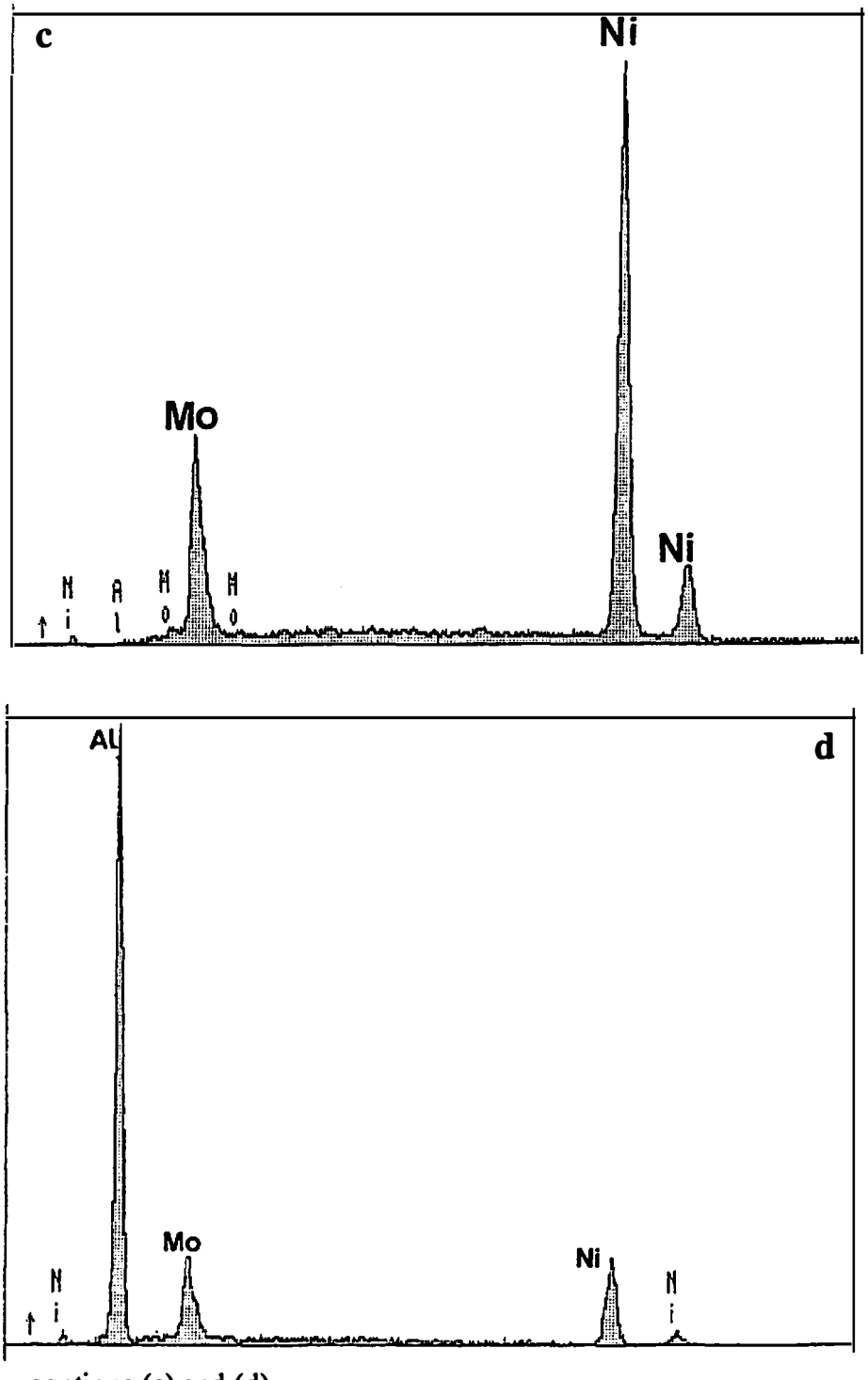



Figure 4-55. continue (c) and (d).

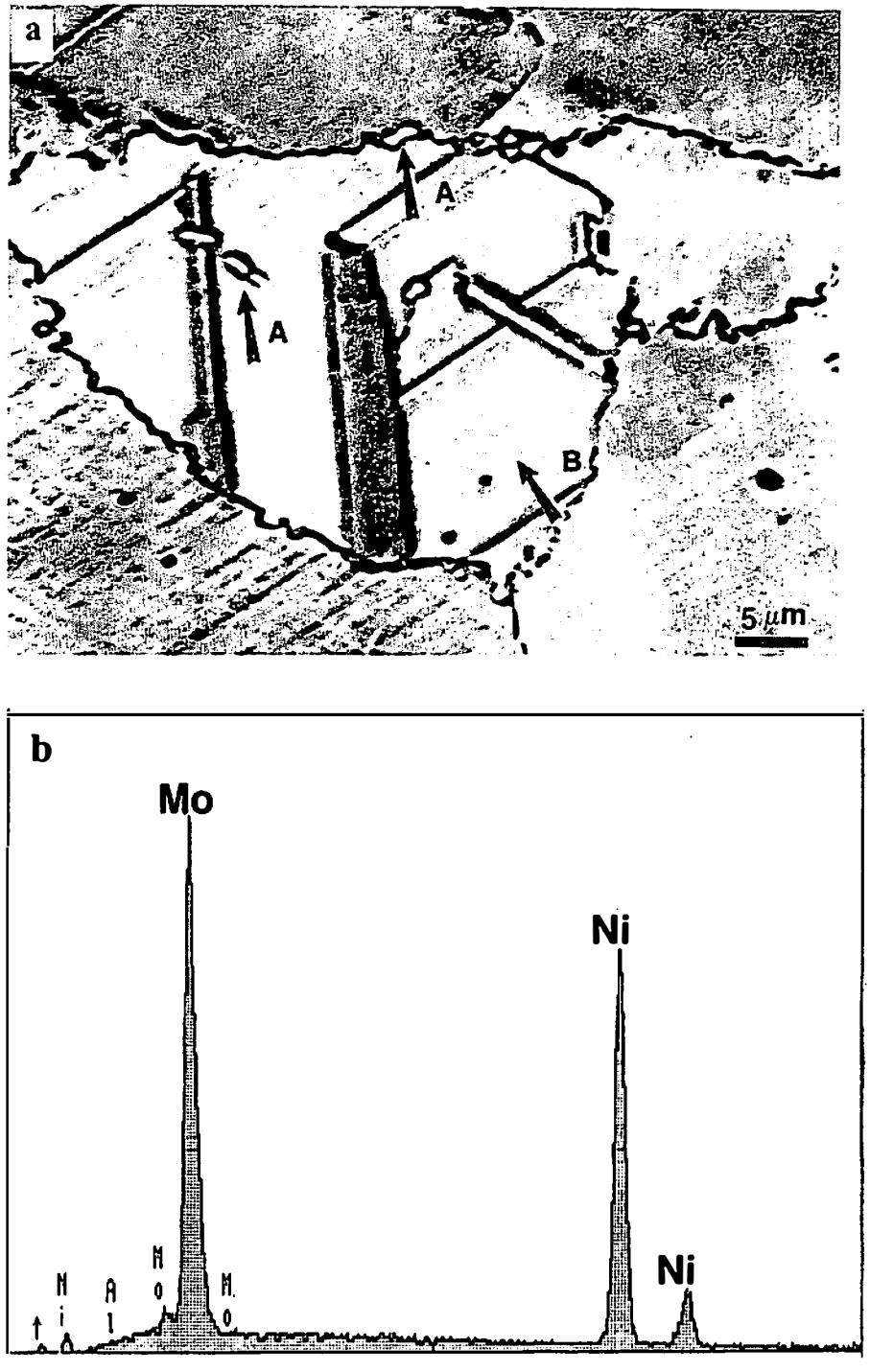



Figure 4-56. (a) SEM microstructure (BSE) of $Ni_4Mo$ alloy aged at 800°C for 10 minutes showing δ phase particles and β phase, (b) EDS analysis from A for bright particles.

### 4.3.2. SEM Microstructure of Ni-Mo-Al Alloys in As-Cast Condition (No Homogenization Treatment) Aged at 750°C for 100 Hours

In the $Ni_4Mo$ alloy in the hot forged condition, the $\alpha$ phase transformed to $\beta$ phase with Widmanstatten plates and bright particles distributed in the matrix (Figure 4-57a) after aging at 750°C (without solution heat treatment). The Ni-Mo-Al alloys which were aged at 750°C for 100 hours received no prior homogenization, but were aged in the as-cast condition, and hence it should be remembered that a segregated structure is being aged.

Figures 4-57, a and c show the microstructure of the $Ni_4Mo$ alloy. The Widmanstatten pattern has etched out indicating that the structure consists of $\beta$ domains. There is a range of grain sizes present, indicating some recrystallization during aging (see Figure 4-7). The EDS of the bright particle in Figure 4-75a (see arrow) is shown in Figure 4-57b. The nickel to molybdenum ratio is 0.5, indicating that this is the $\delta$ phase.

The OLM observation of the microstructure for the 2 at.% Al alloy (Figure 4-10) showed a structure forming from the grain boundaries, and was referred to as lamellar. This identification was based on the SEM observations, as shown in Figure 4-58a. EDS analysis of the matrix (B) is shown in Figure 4-58c, and that of the bright plates (A) in Figure 4-58b. These plates are taken to be the $\delta$ phase which formed in the elemental segregated region because of on homogenization treatment. Sever micro and macro-segregation existed in the alloy. In molybdenum rich regions, significant amount of $\delta$ phase was formed whereas areas of less Mo were free of the $\delta$ phase.

The microstructure of the 5 at.% Al alloy is shown in Figure 4-59, a and b. There are regions which appear single phase and the rest is a lamellar structure. The single phase regions did not develop a Widmanstatten pattern, indicating that these are still $\alpha$ phase, and the EDS of the single phase region (A) (Figure 4-59c) is consistent with these

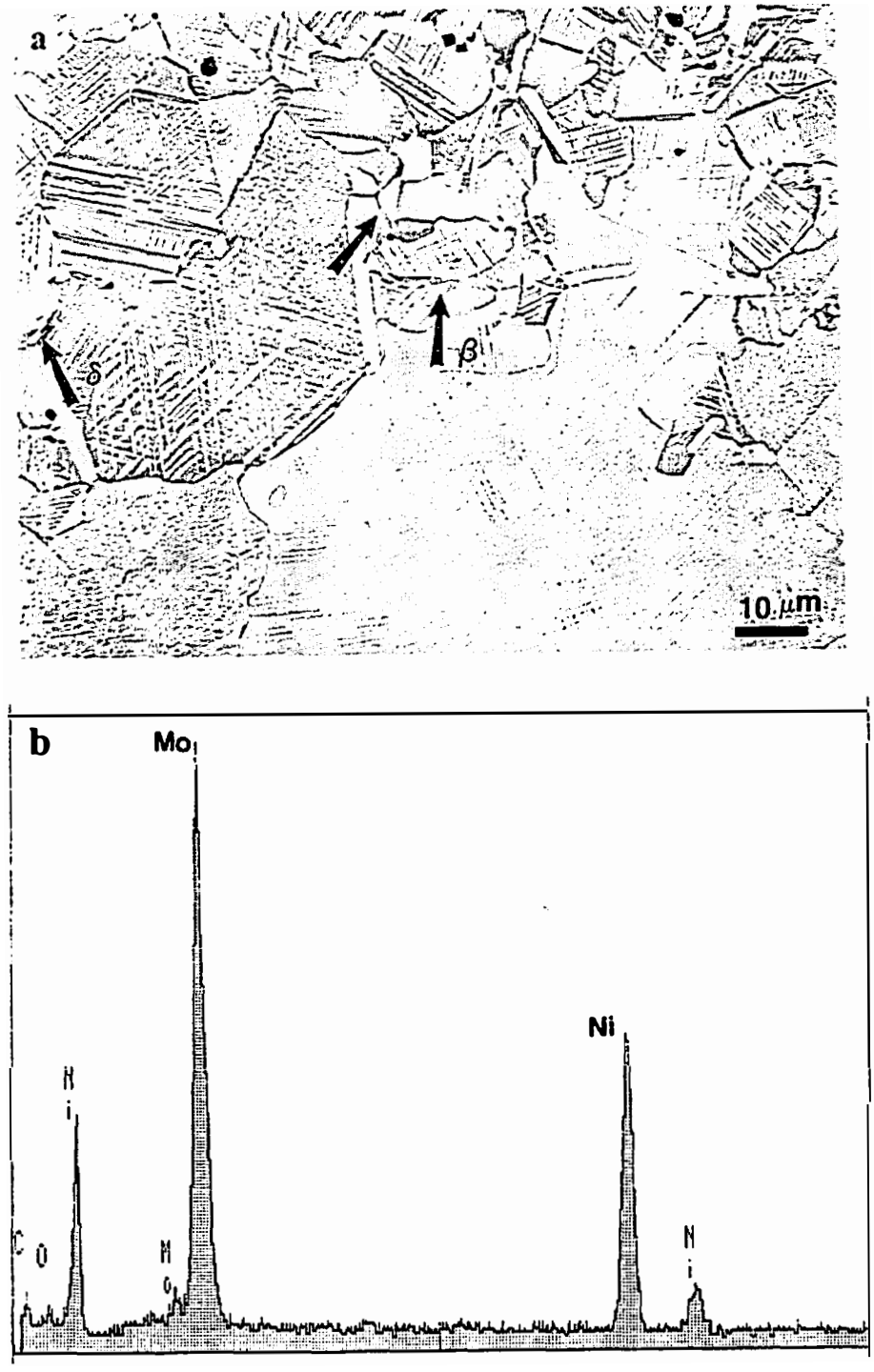



Figure 4-57. (a) SEM microstructure (SE) of $Ni_4Mo$ alloy (hot forged) aged 750°C for 100 hours showing β phase and β recrystallization. (b) EDS analysis from particles (see arrow), (c) β domains.

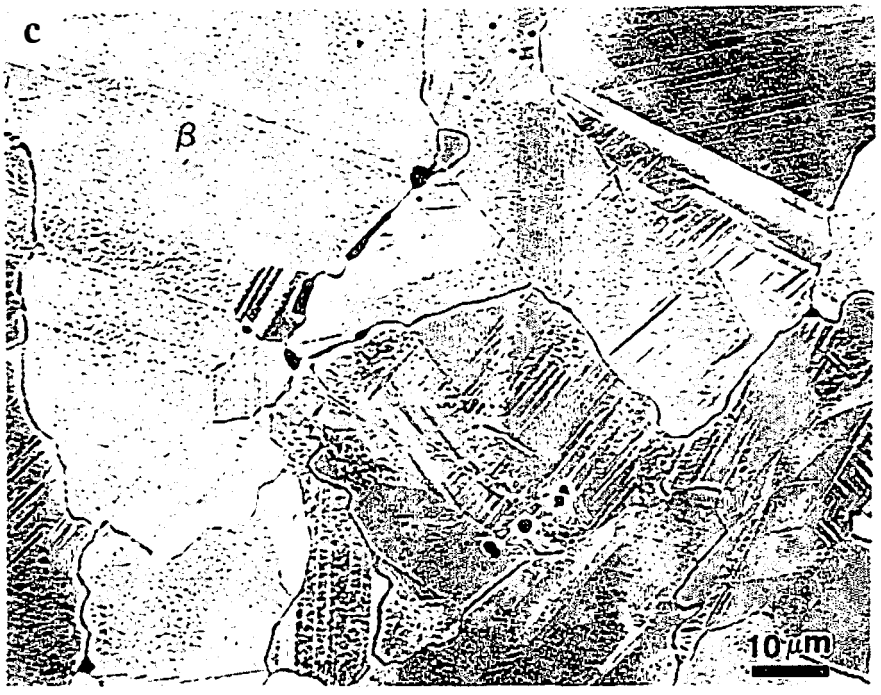



Figure 4-57. continue (c).

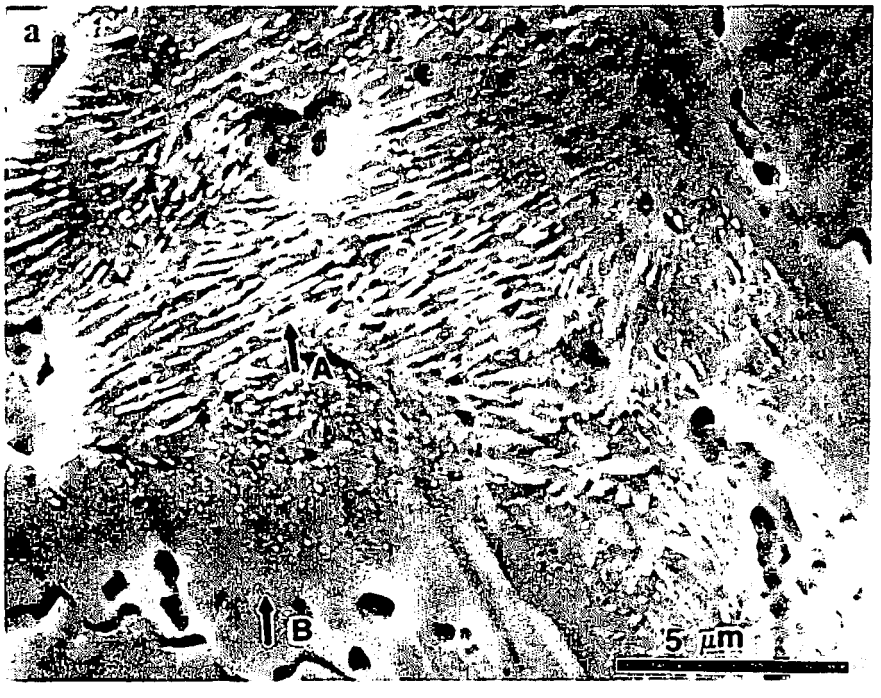



Figure 4-58a. (a) SEM microstructure (SE) of 2 at.% Al alloy in as-cast condition (without homogenization) aged at 750°C for 100 hours showing two phase structures, (b) EDS analysis from bright particles, (c) EDS analysis from matrix.

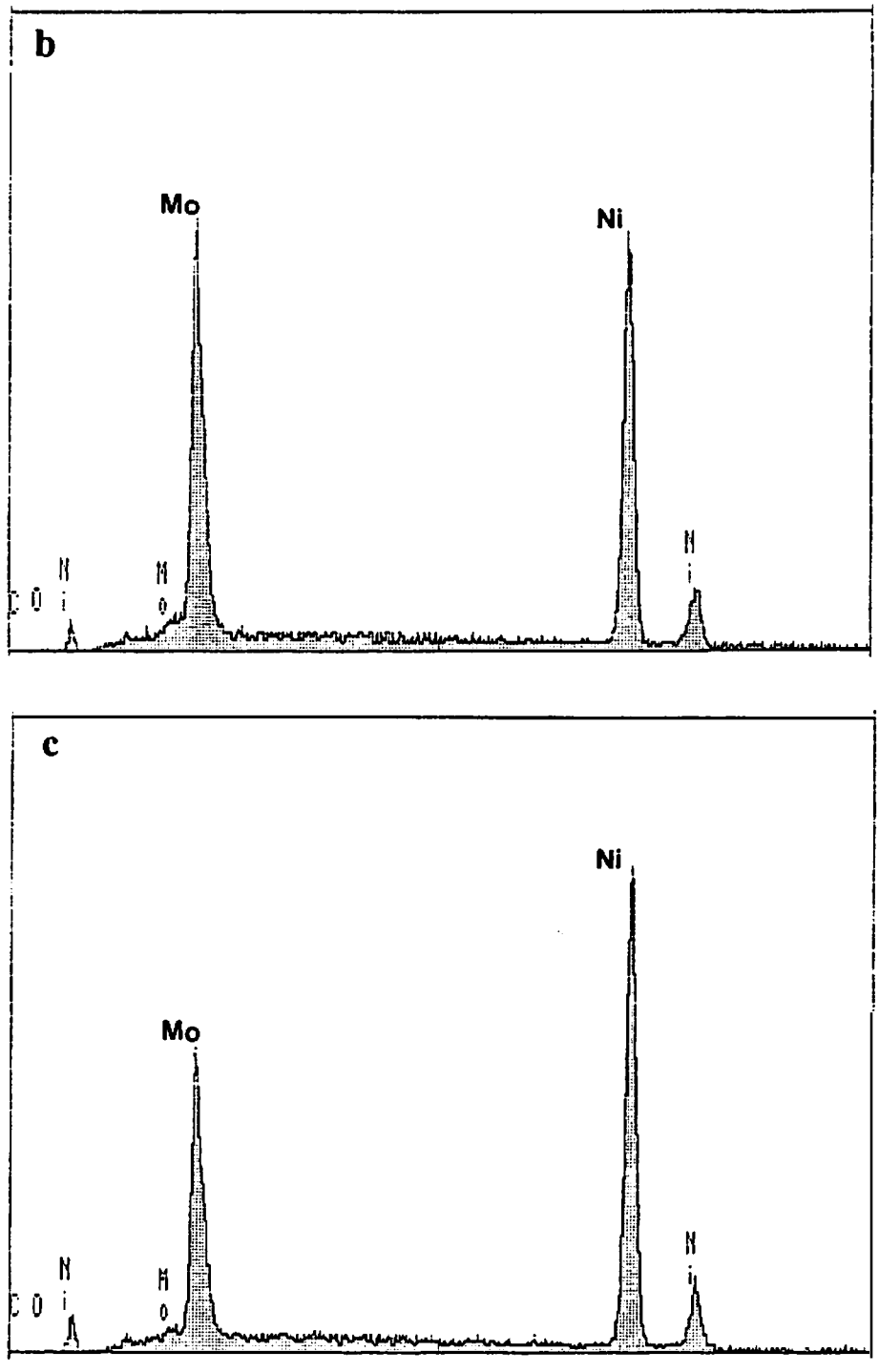



Figure 4-58. continue (b) and (c).

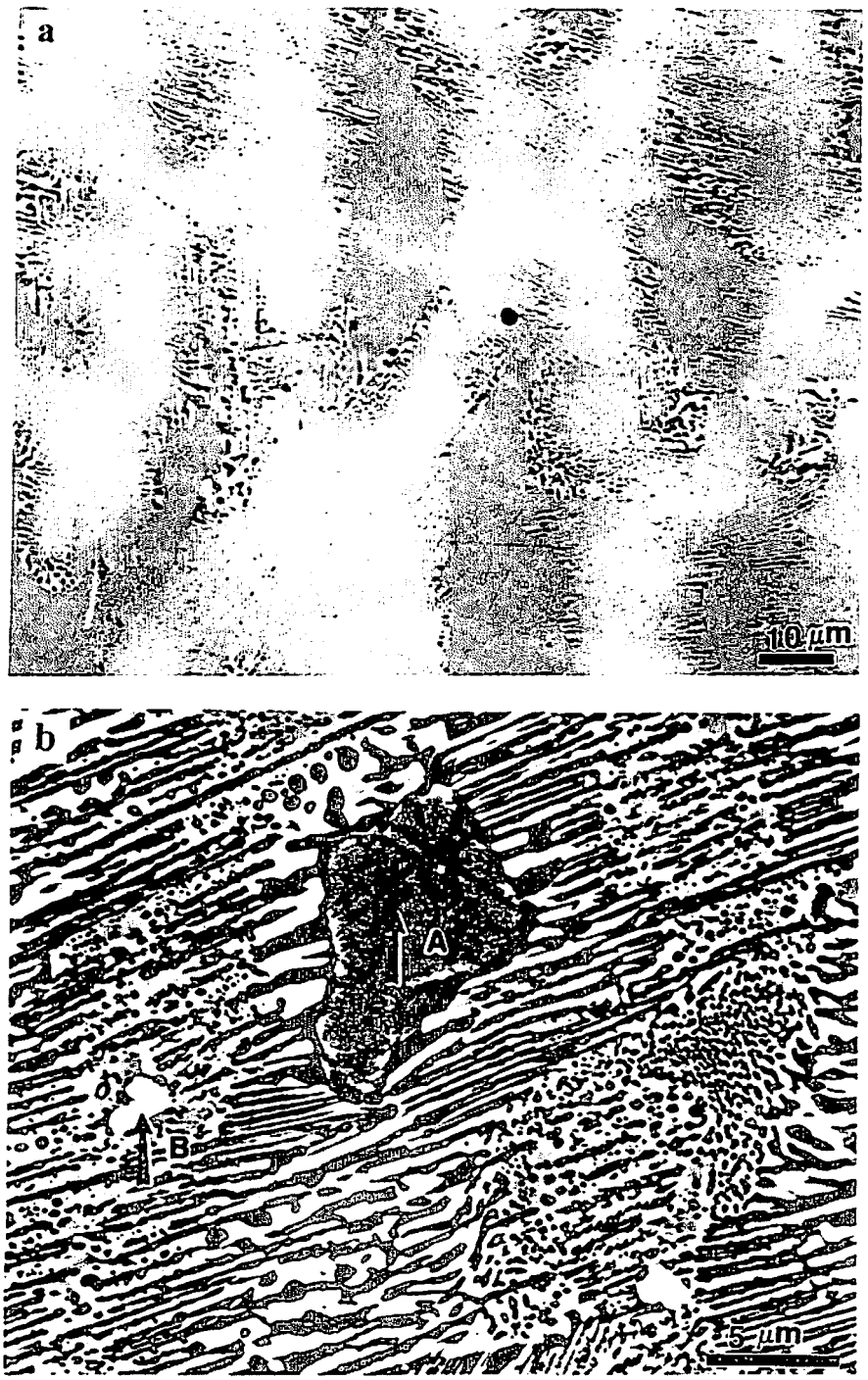



Figure 4-59a. SEM microstructure of 5 at.% Al alloy in as-cast condition (without homogenization) aged at 750°C for 100 hours showing (a) (BSE) precipitates, lamellar structure, and α phase, (b) (SE) lamellar structure with α phase, (c) EDS analysis from single phase, (d) EDS analysis from bright particles.

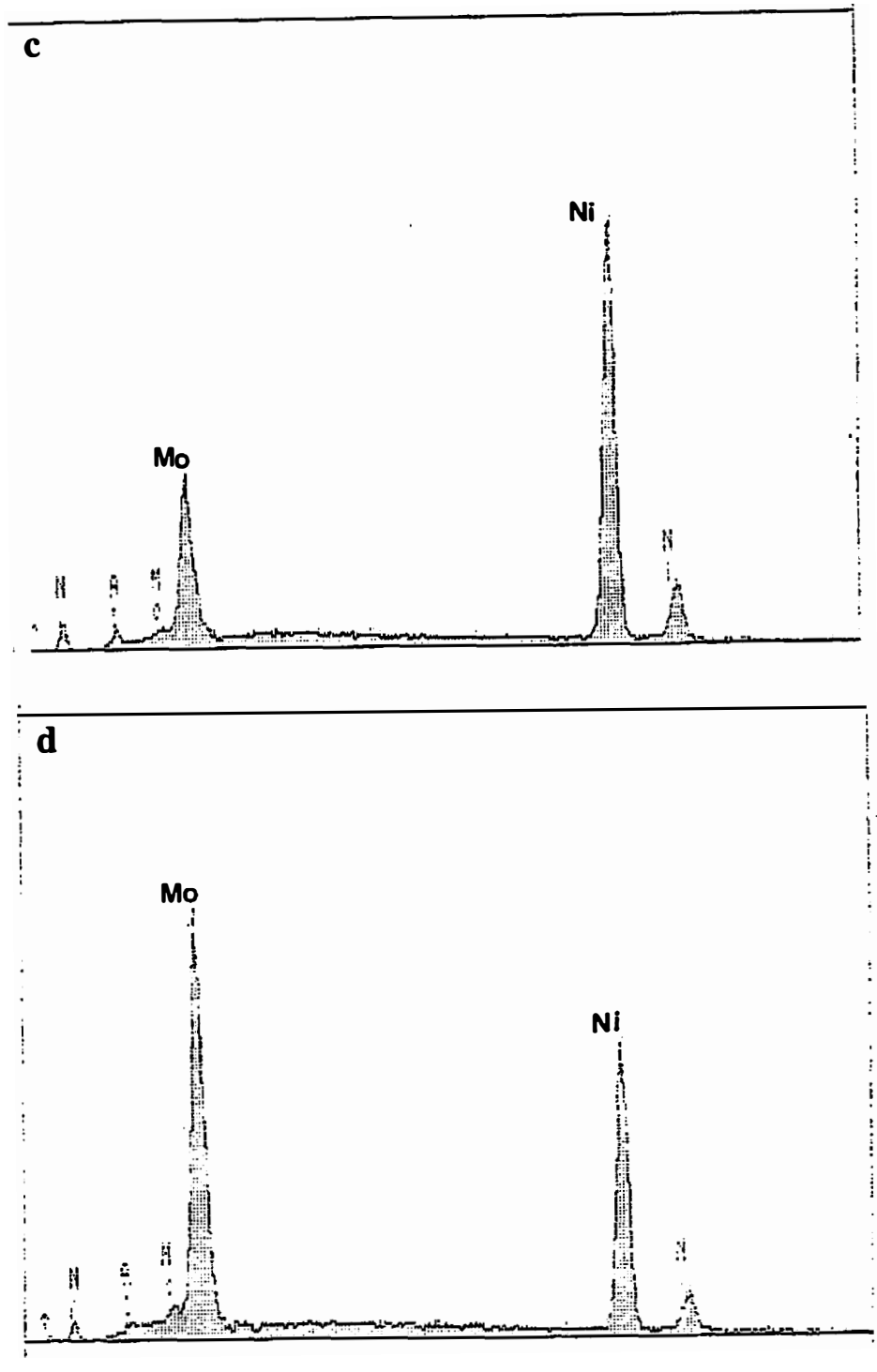



Figure 4-59. continue (c) and (d).

regions being α phase. The EDS analysis of the regions marked B in Figure 4-59d indicates that these are δ phase.

The 7 at.% Al alloy contained a considerable amount of a two phase structures (Figure 4-60, a and b). There were regions of a lamellar structure (B in Figure 4-60a) and a flower-like structure (A in Figure 4-60a). The EDS analyses from these two structure are shown in Figure 4-60 c and d, and they are not the same, indicating that the two phases in the two structures may not be identical. However, the individual phases are too fine for meaningful EDS analysis. The identification of the phases is discussed in the TEM section.

Figure 4-61a shows the microstructure for the 9 at.% Al alloy. A clear dendritic structure is still present. EDS analyses from the two regions noted (A and B) are shown in Figure 4-61, b and c. There is marked segregation of nickel and molybdenum between these two regions.

### 4.3.3. SEM Microstructure of Ni-Mo-Al Alloys Homogenized at 1250°C for 50 Hours

The initial homogenization treatment was chosen as 1250°C for 50 hours. The microstructure of the $Ni_4Mo$ and the 2, 5, and 7 at.% Al alloys all appeared to be single phase α. However, the exact structure for this condition is discussed in the TEM section. For this homogenization treatment, there were particles in the grain boundaries and matrix for the 9 at.% Al alloy, as shown in Figure 4-62a. EDS analyses from the particles and the matrix are shown in Figure 4-62, b and c. The particles are very rich in molybdenum, and are assumed to be pure molybdenum. The matrix is assumed to be α phase. These two phases are consistent with the phase diagram (see Figure 4-14).

Based on the inability to obtain a single phase for the 9 at.% Al alloy, the homogenization temperature was increased to 1280°C and all subsequent aged samples

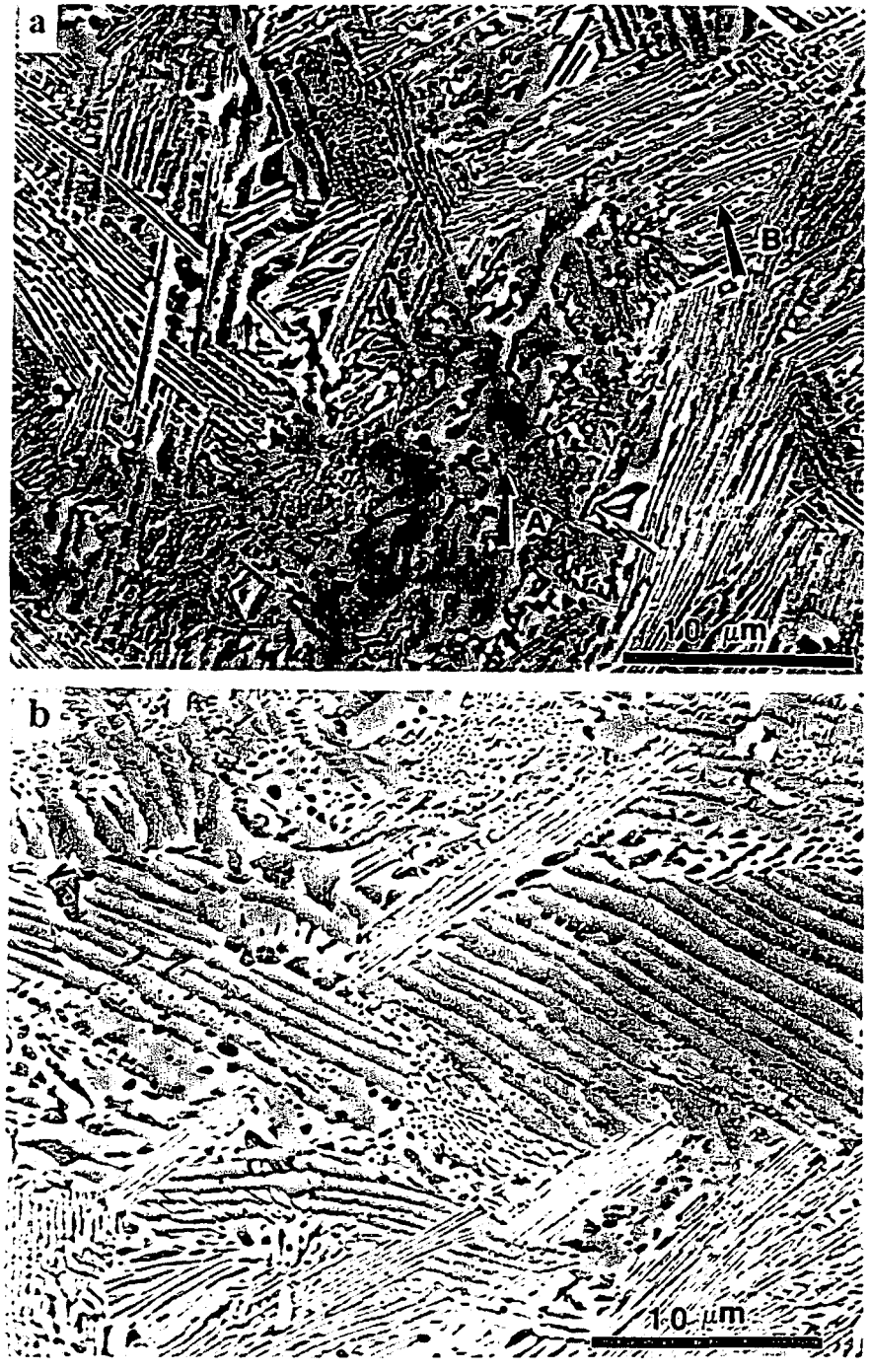



Figure 4-60. SEM microstructure (SE) of 7 at.% Al alloy in as-cast condition (without homogenization) aged at 750°C for 100 hours showing (a) lamellar structure with flower-like structure, (b) lamellar structure, (c) EDS analysis from flower-like structure, (d) EDS analysis from lamellar structure.

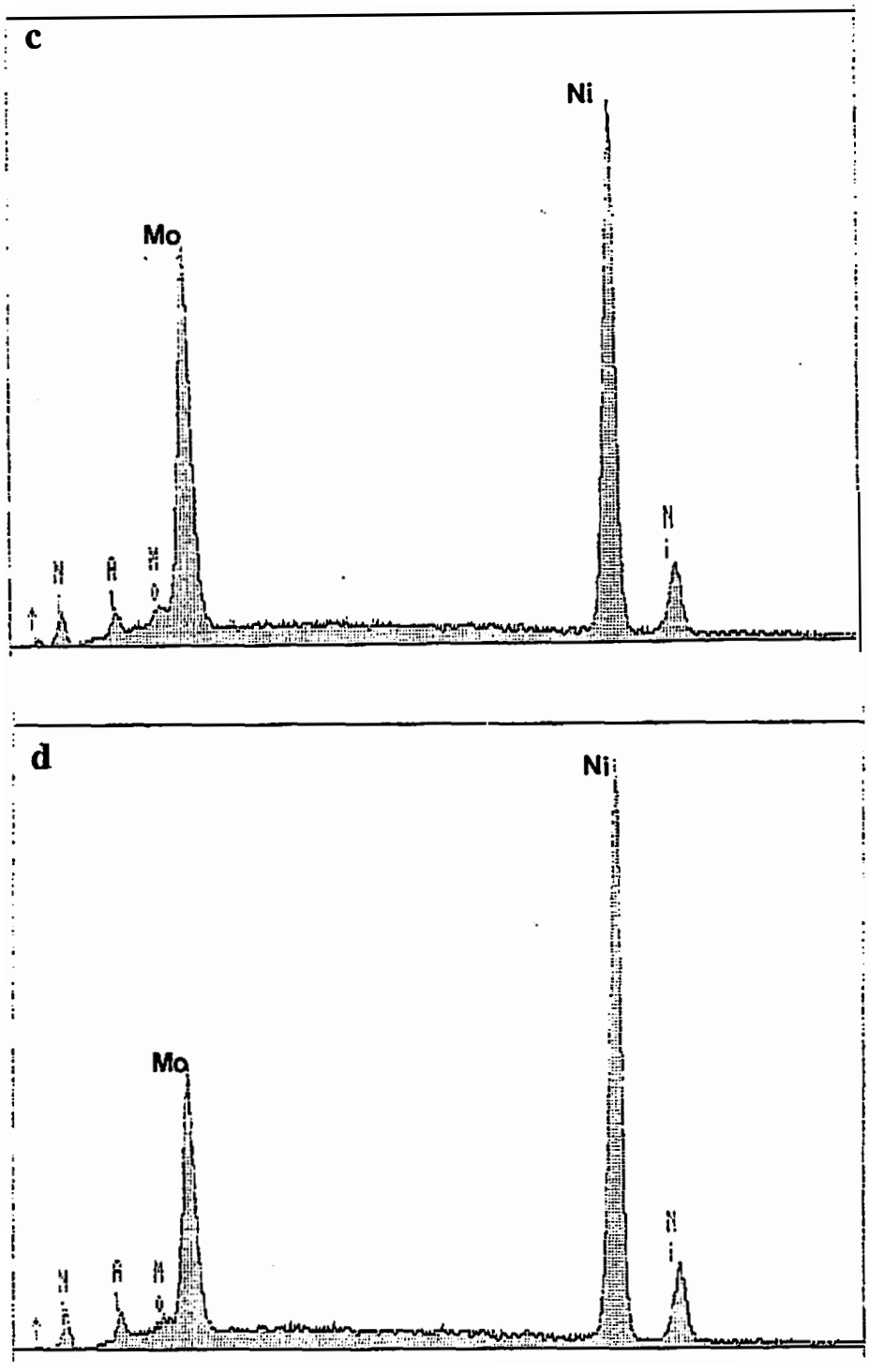



Figure 4-60. continue (c) and (d).

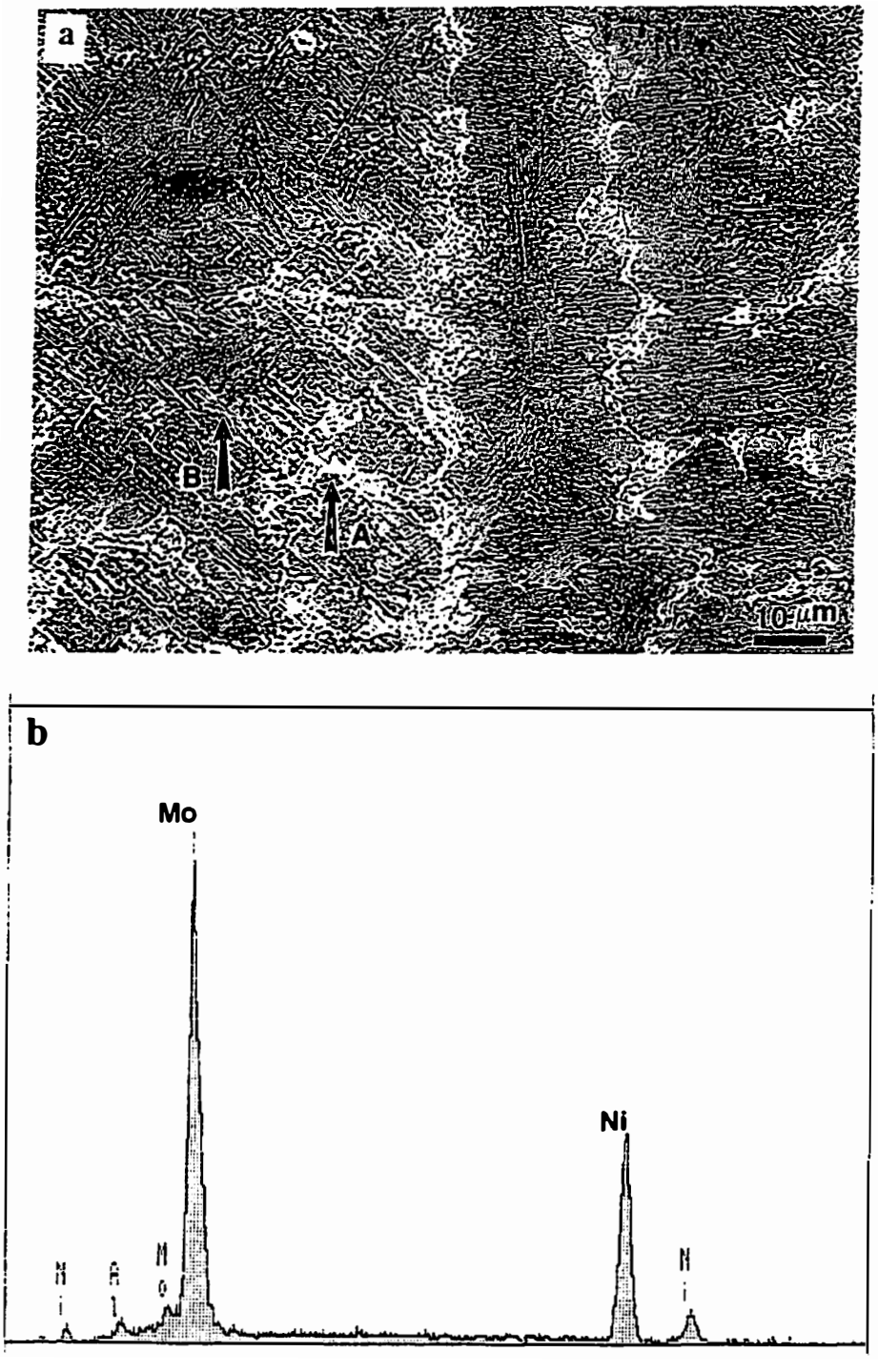



Figure 4-61. (a) SEM microstructure (SE) of 9 at.% Al alloy in as-cast condition (without homogenization) aged 750°C for 100 hours showing lamellar structure with bright precipitates, (b) EDS analysis from bright area, (c) EDS analysis from coarse structure.

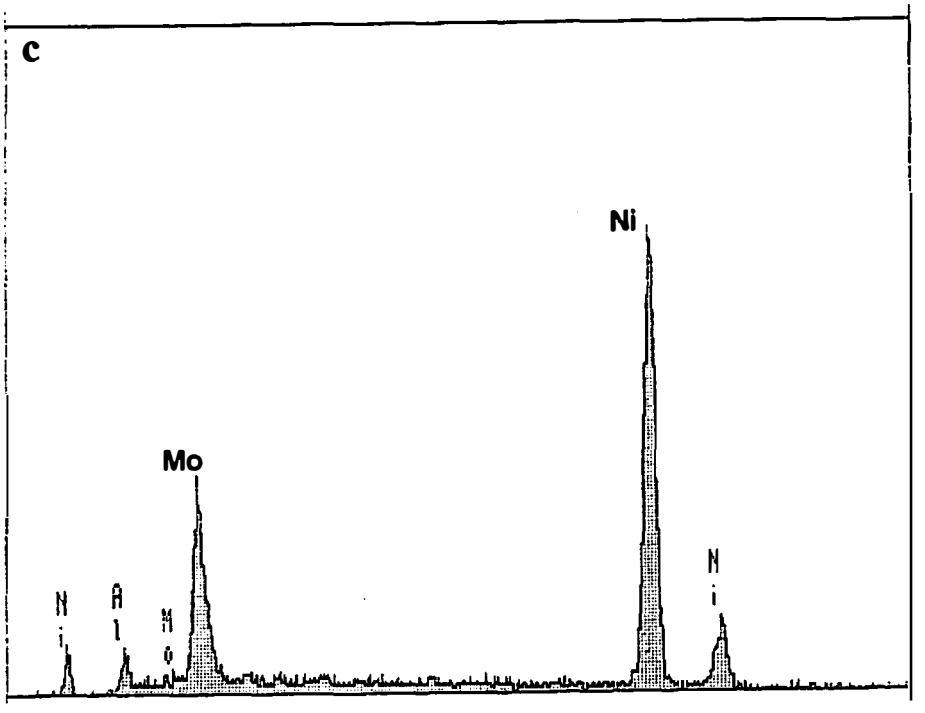



Figure 4-61. continue (c).

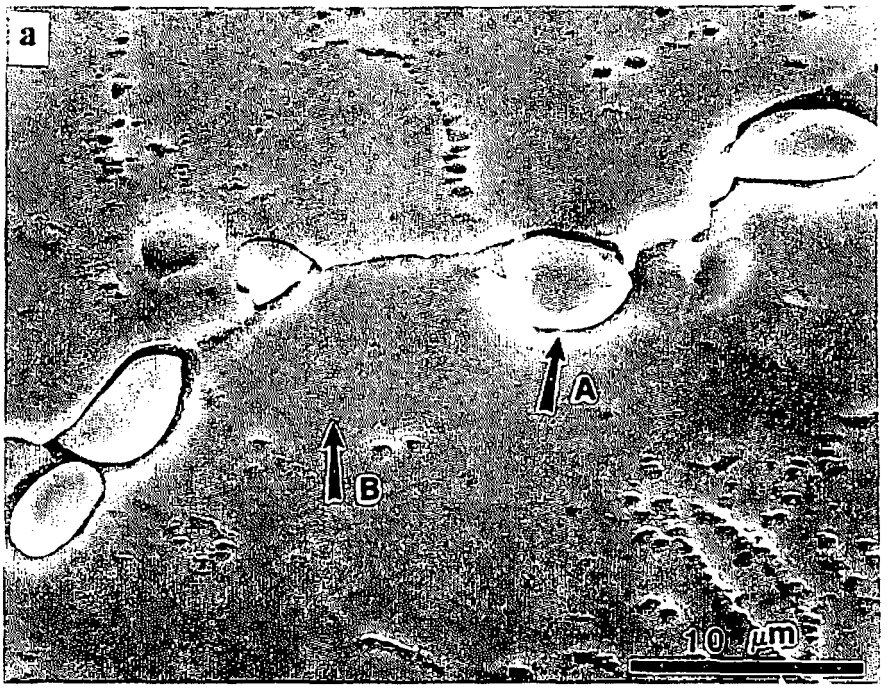



Figure 4-62. (a) SEM microstructure (SE) of 9 at.% Al alloy solution treated at 1250°C for 50 hours showing molybdenum-rich particles along grain boundaries and matrix, (b) EDS analysis from particles, (c) EDS analysis from matrix.

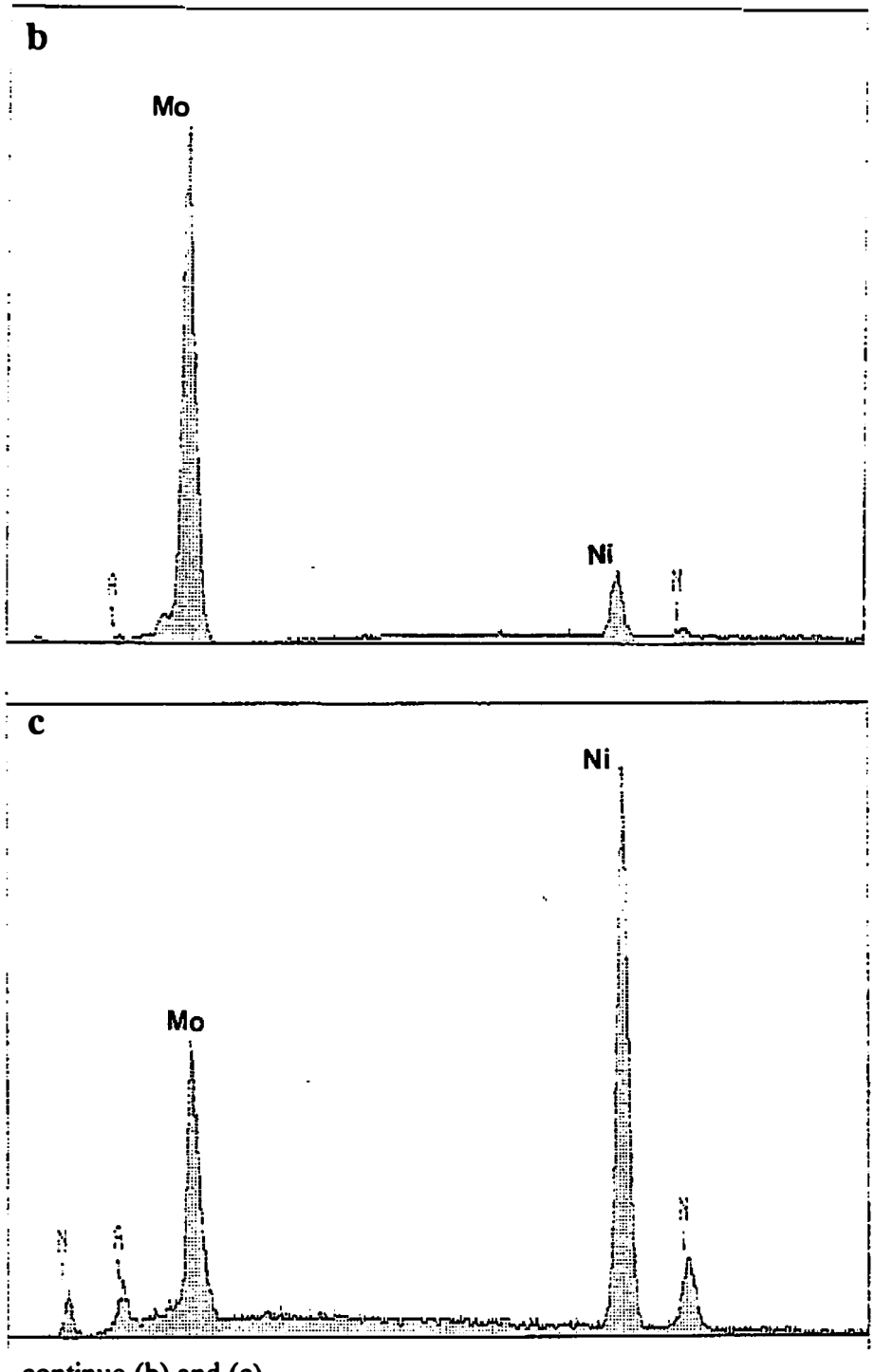



Figure 4-62. continue (b) and (c).

were homogenized for 50 hours at this temperature.

### 4.3.4. SEM Microstructure of Ni-Mo-Al Alloys Solution Treated and Aged at 600°C for 100 hours

The $Ni_4Mo$ alloy and the 2 and 5 at.% Al alloys all appeared in OLM to be single phase after aging for 100 hours at 600°C, so they were not examined with SEM. However, their fine structure is discussed in the TEM section.

In the 7 at.% Al alloy, OLM revealed that there was some grain boundary structure forming (see Figure 4-23). This is shown in Figure 4-63a. The region at the arrow is shown imaged with SE and BSE in Figure 4-63b. The striation line at B is bright in BSE image, consistent with its high molybdenum content (Figure 4-63d), and this may be the $\delta$ phase. The matrix (at A) is relatively rich in nickel and probably has the composition of the $\alpha$ phase (but see TEM section) (Figure 4-63c).

The 9 at.% Al alloy showed the formation of a lamellar structure (Figure 4-24), as revealed in Figure 4-64, a and b. The small rounded particles (A) are pure molybdenum (Figure 4-64c). In the lamellar structure, one lamellae is rich in molybdenum (Figure 4-64d) and the other is rich in nickel (Figure 4-64e). These may be the $\gamma$ and $\delta$ phases. As indicated Figure 4-64a, the $\gamma$ and $\delta$ phase formed a lamellar structure around pure molybdenum particles.

### 4.3.5. SEM Microstructure of Ni-Mo-Al Alloys Solution Treated and Aged at 650°C for 100 Hours

The OLM microstructure (Figure 4-25) of the $Ni_4Mo$ alloy showed that the $\alpha$ phase has transformed to a domain structure of $\beta$ on aging at 650°C for 100 hours. There was some grain boundary migration, which in stoichiometric $Ni_4Mo$ alloys is associated

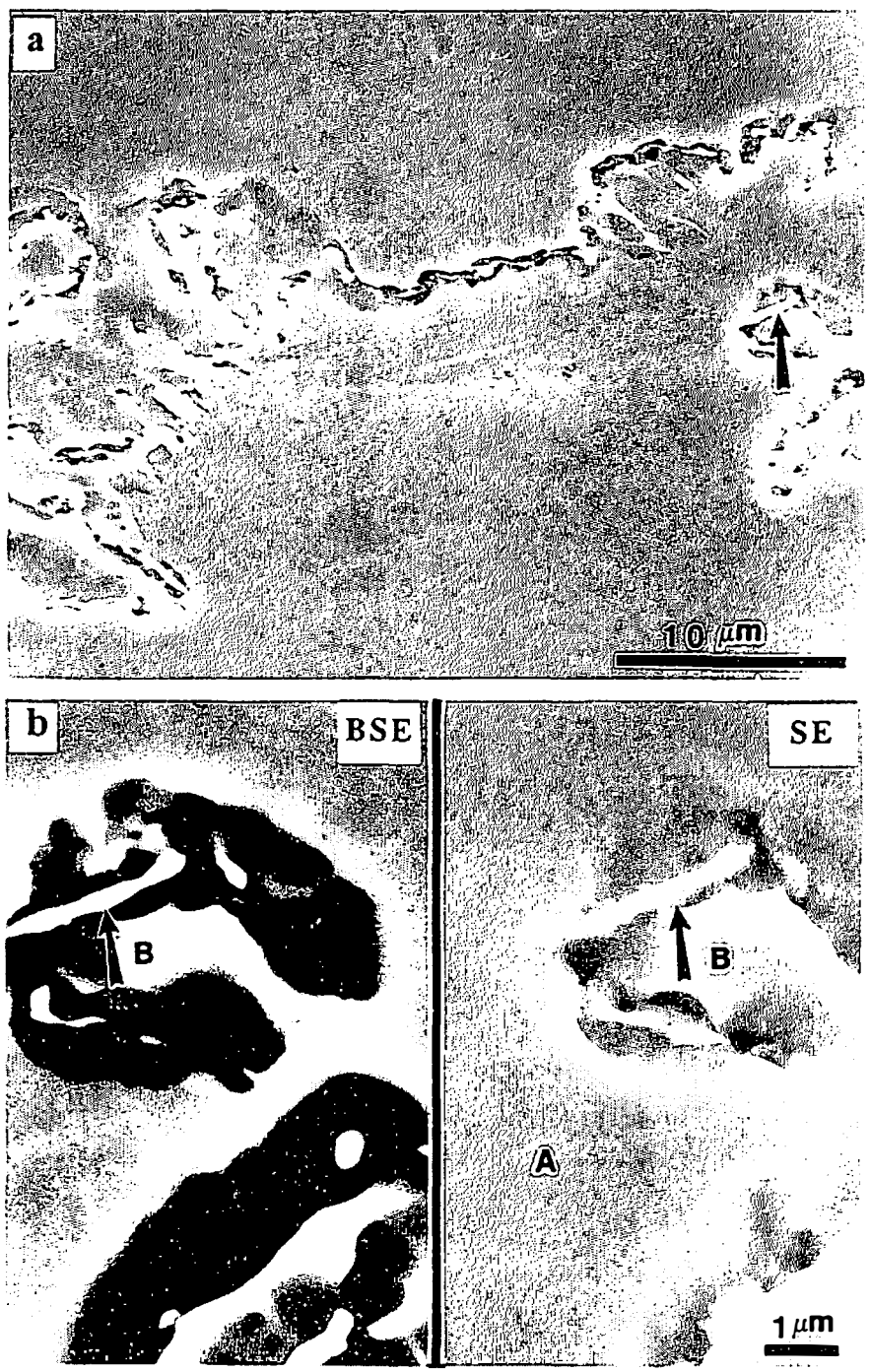



Figure 4-63. SEM microstructure (SE) of 7 at.% Al alloy aged at 600°C for 100 hours showing (a) grain boundary migration and secondary phase formation along grain boundaries, (b) high magnification of secondary phase, (c) EDS analysis from matrix, (d) EDS analysis from striation line.

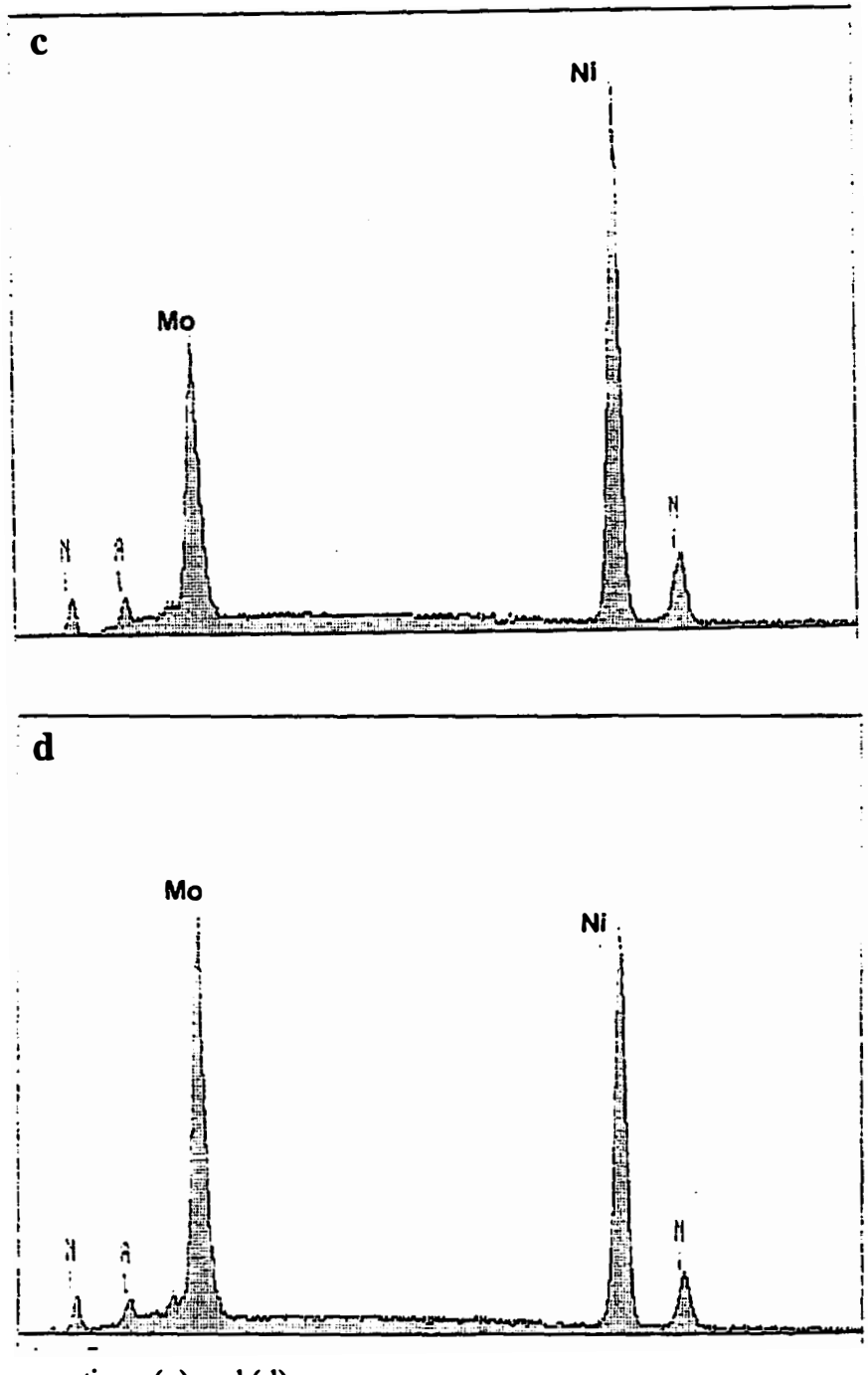



Figure 4-63. continue (c) and (d).

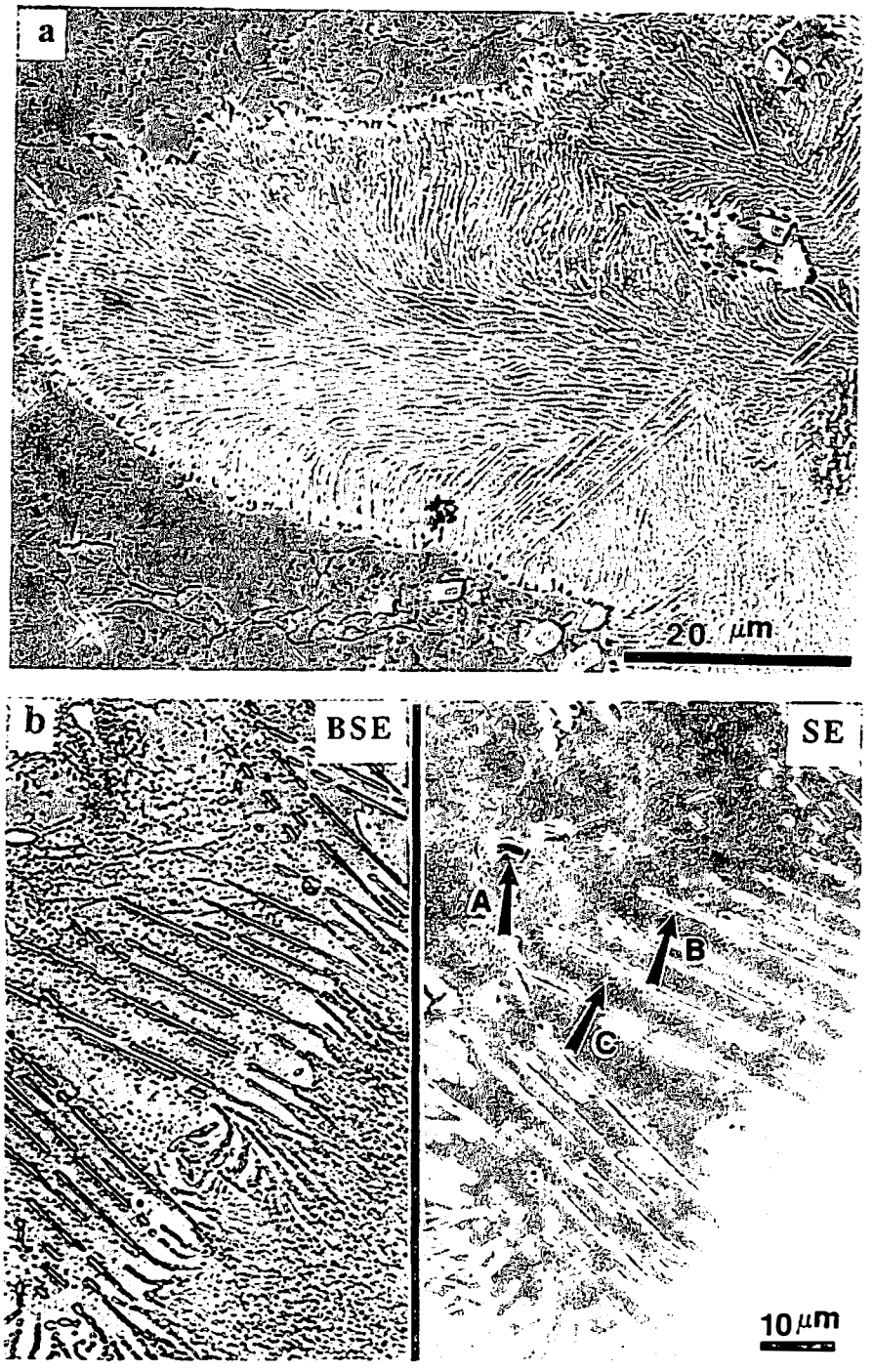



Figure 4-64. SEM microstructure (SE) of 9 at.% Al alloy solution treated at 1280°C for 50 hours and aged at 600 °C for 100 hours showing (a) lamellar structure with precipitates, (b) high magnification of lamellar structure, (c) EDS analysis from particles, (d) EDS analysis from bright striation line, (e) EDS analysis from dark striation line.

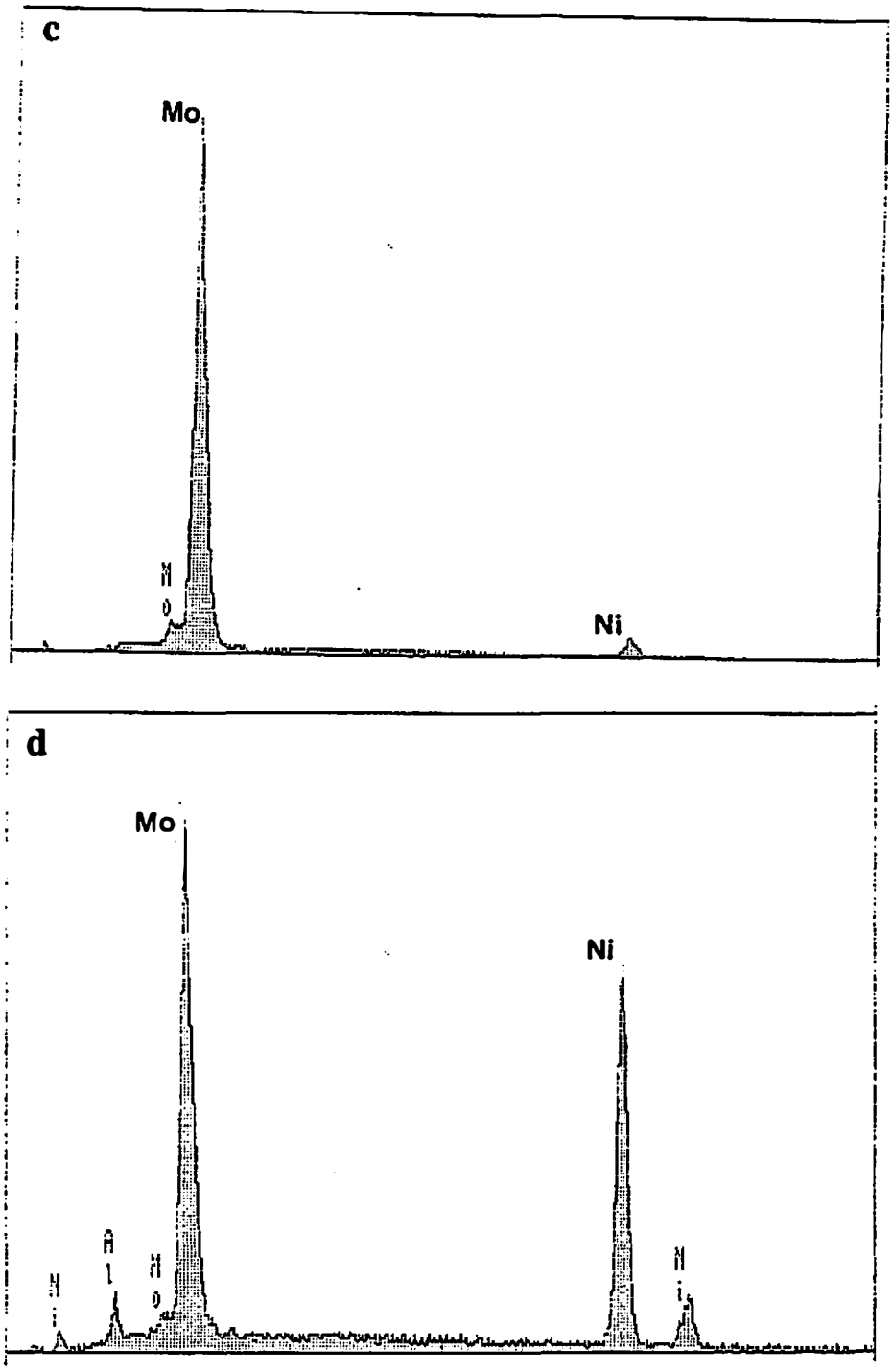



Figure 4-64. continue (c) and (d).

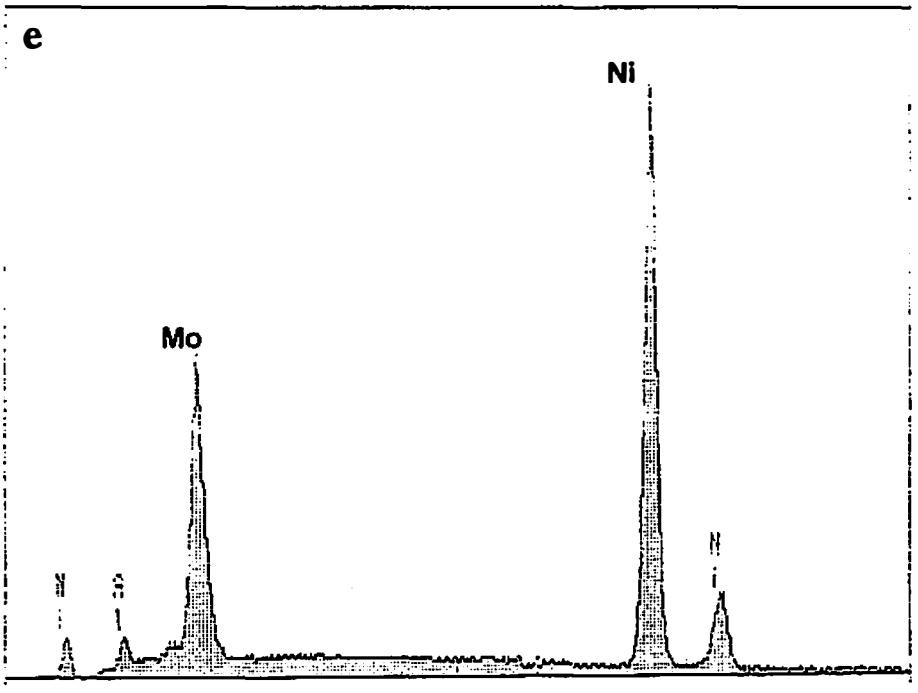



Figure 4-64. continue (e).

with domain coarsening [51, 72, 73, 76, 77]. Figure 4-65a shows a region of boundary migration, and there are two phases, lamellar structure present. EDS analyses from the regions noted are in Figure 4-65, b to d. The fine plates or rods (A) are relatively rich in molybdenum, and are taken to be the $\gamma$ phase. The phase in between (C) (EDS in Figure 4-65d) is the same as the $\beta$ matrix (B) (EDS in Figure 4-65c) and is taken to be $\beta$. Thus the reaction at the grain boundary is discontinuous precipitation of $\gamma$ from $\beta$ associated with the boundaries migration to produce a lamellar structure of $\beta$ and $\gamma$. This indicates that the composition of this binary $Ni_4Mo$ alloy was slightly on the molybdenum-rich side of 20 at.% Mo, placing the alloy in this two phase region at equilibrium.

The 2 at.% Al alloy appeared to be single phase (see Figure 4-26). The 5 at.% Al alloy had a lamellar structure forming from the grain boundaries (Figure 4-27). The 7 at.% Al alloy showed the lamellar structure forming along the grain boundaries (Figure 4-66, a and b). However, the structure is too fine for meaningful EDS analysis. The matrix showed no Widmanstatten etching structure, so it has not transformed to $\beta$ phase. The structure of this alloy is described in more detail in the TEM section.

### 4.3.6. SEM Microstructure of Ni-Mo-Al Alloys with a Solution Treated and Aged at 700°C for 100 Hours.

The 2 at.% Al alloy remained single phase after aging for 100 hours at 700°C (Figure 4-30) (see the TEM section). In the 5 at.% Al alloy the single phase transformed to a lamellar structure (Figure 4-31). In the 7 at.% Al alloy, the lamellar structure has only partially formed. No SEM observations were made of these samples.

The 9 at.% Al alloy sample showed signs of residual dendritic segregation (Figure 4-33), with a rather heterogeneous structure present. There was a fine lamellar structure, which in areas was converting to a coarse lamellar structure (Figure 4-67a). However, in

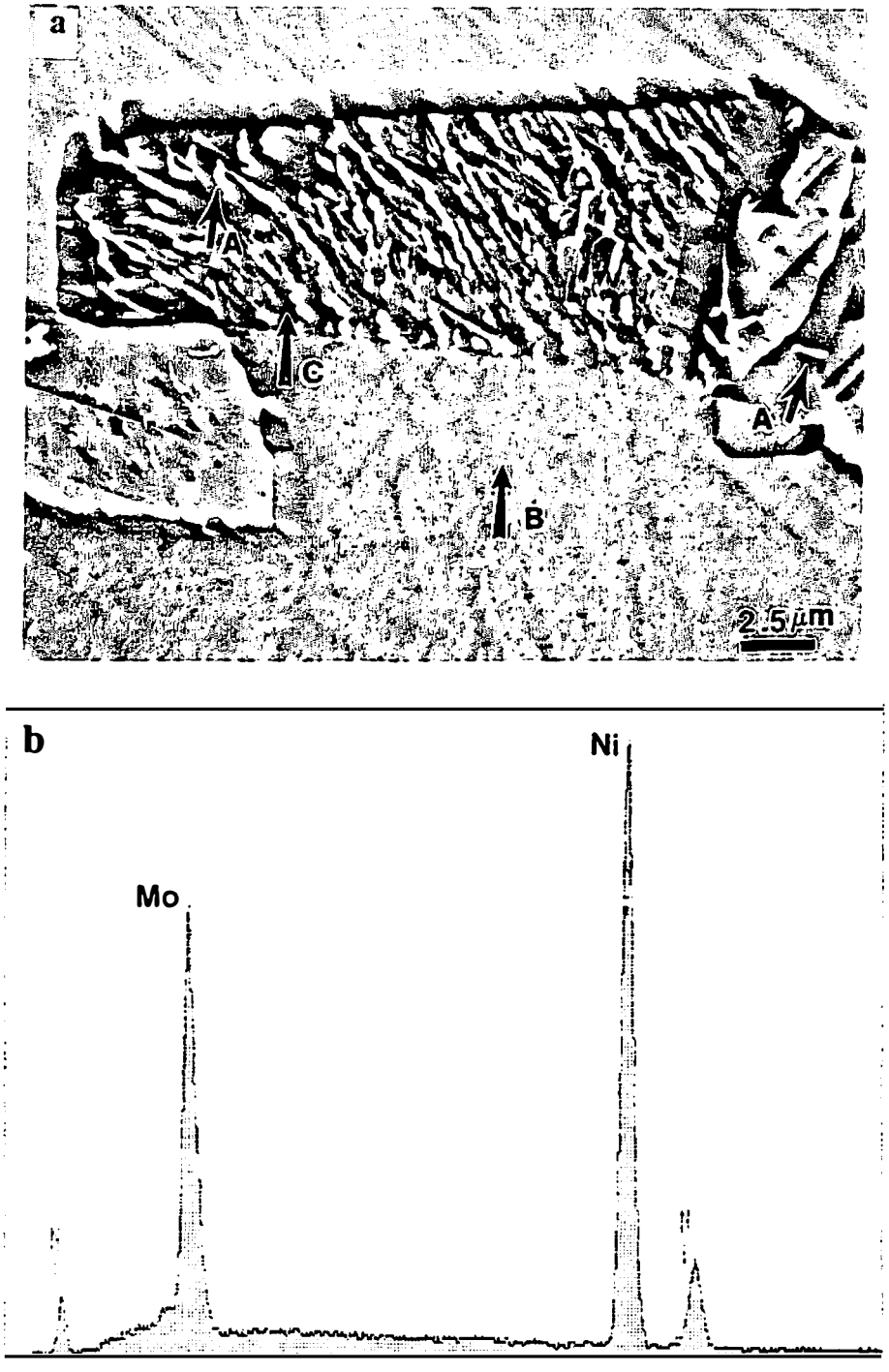



Figure 4-65. (a)SEM microstructure (BSE) of $Ni_4Mo$ solution treated at 1280°C for 50 hours and aged at 650°C for 100 hours showing β domain phase along the grain boundaries in $Ni_4Mo$ alloy, (b) EDS analysis from particles in domain region, (c) EDS analysis from matrix, (d) EDS analysis from around particles region.

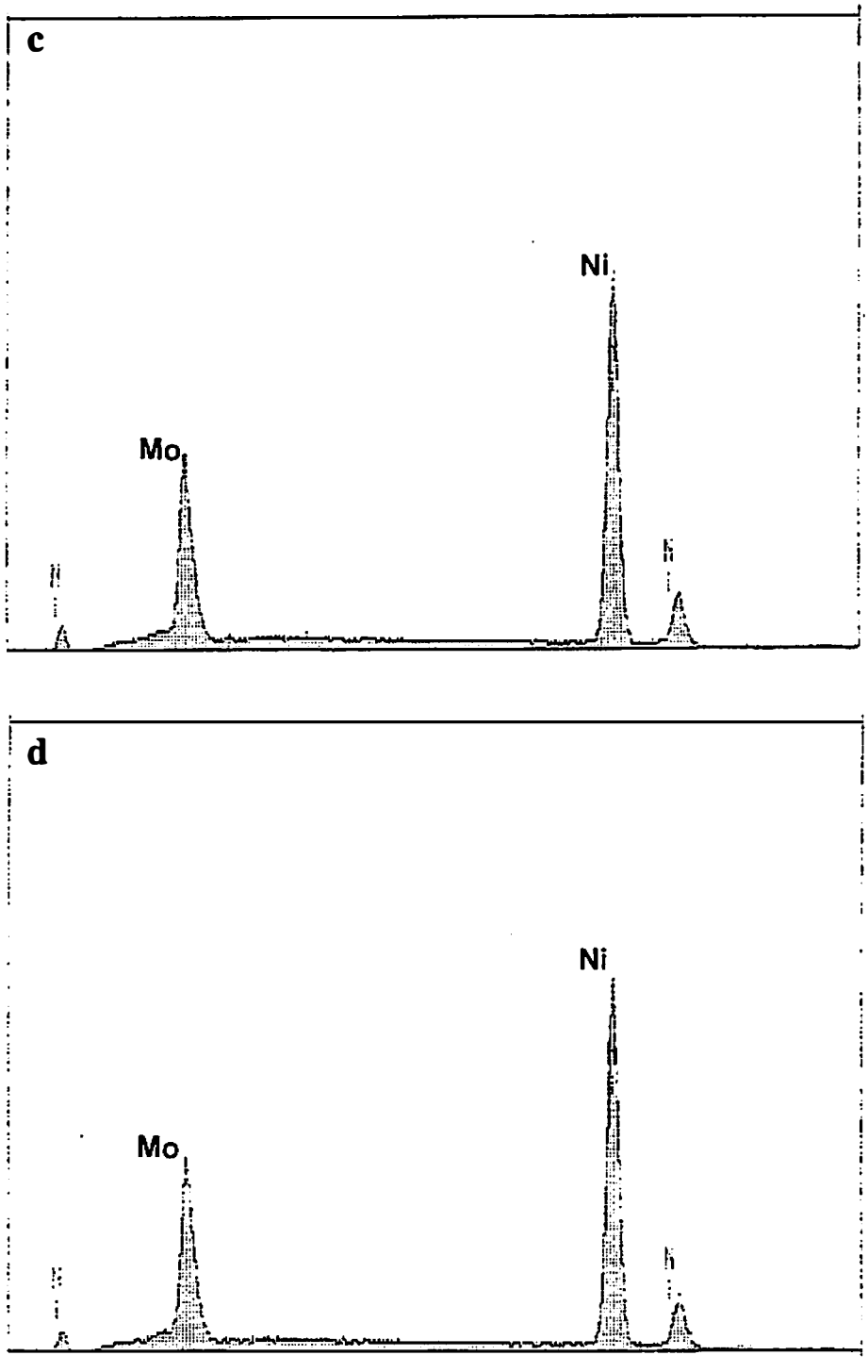



Figure 4-65. continue (c) and (d).

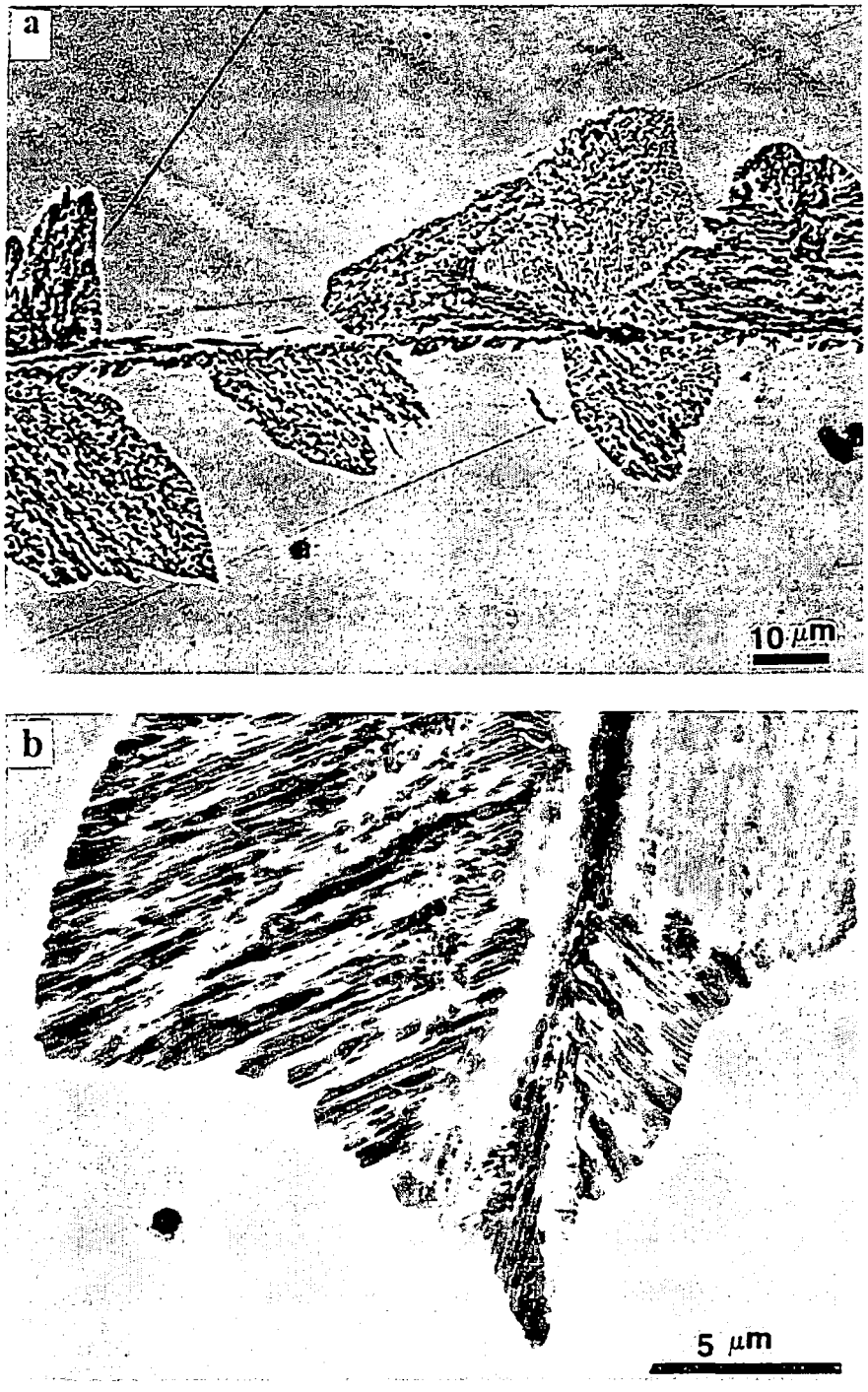



Figure 4-66. SEM microstructure of 7 at.% Al alloy solution treated at 1280°C for 50 hours and aged at 650°C for 100 hours showing (a) secondary phase formation along the grain boundaries, (b) high magnification of lamellar structure.

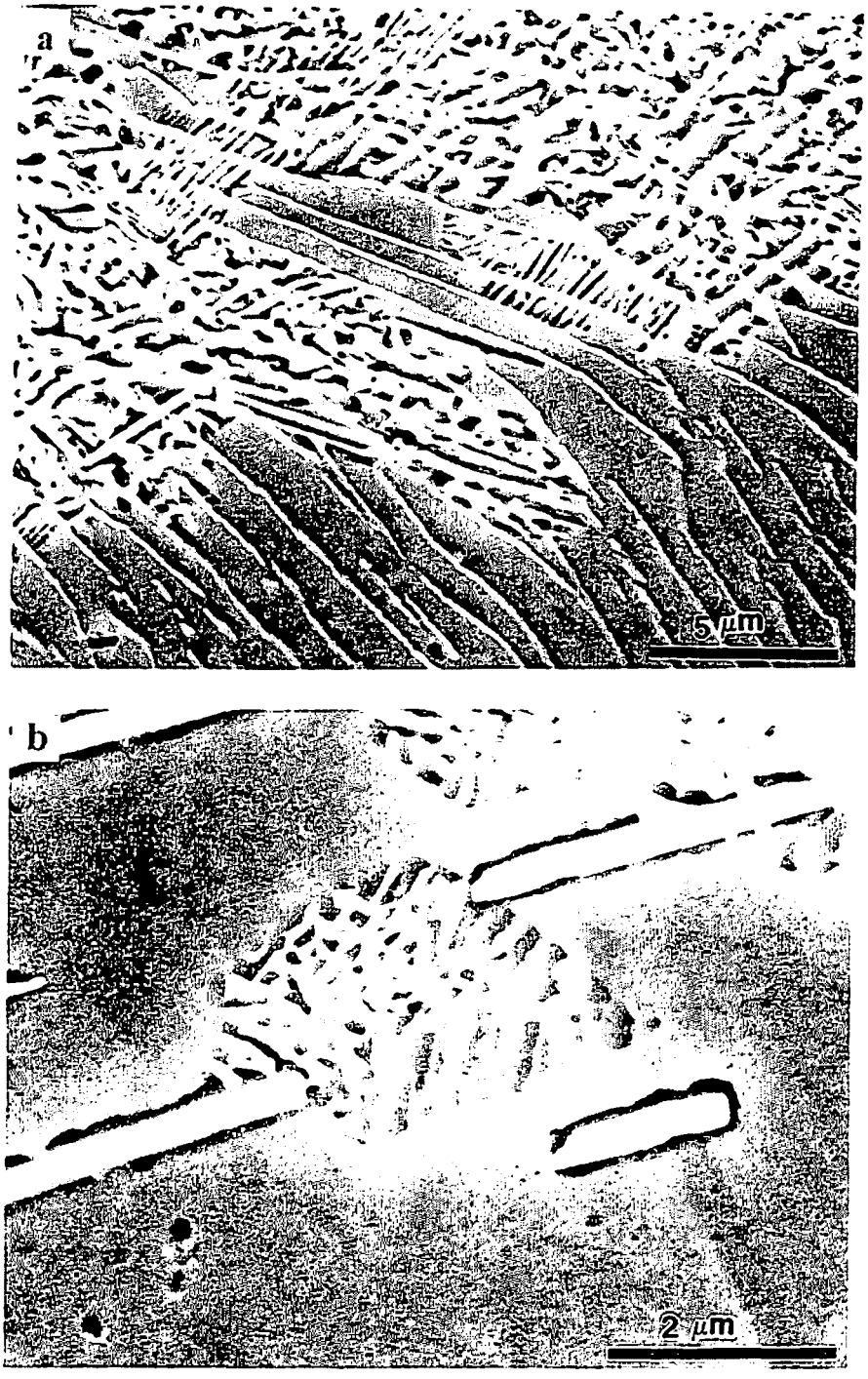



Figure 4-67. SEM microstructure (SE) of 9 at.% Al alloy solution treated at 1280°C for 50 hours and aged at 700°C for 100 hours showing (a) coarsen lamellar structure, (b) and (c) high magnification of lamellar structure.

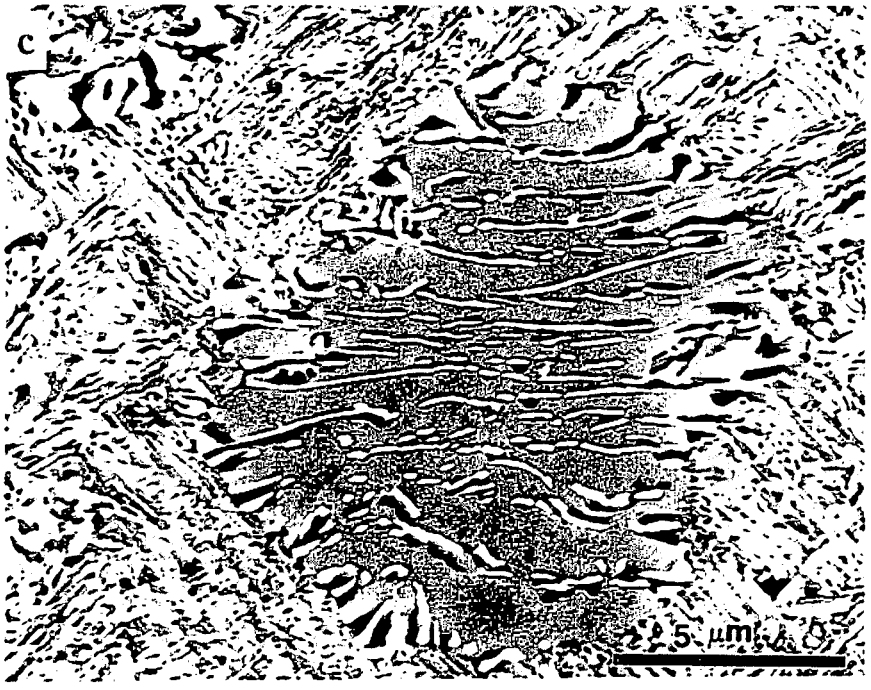



Figure 4-67. continue (c).

other areas it appears that the fine lamellar structure is consuming the coarse lamellar structure (Figure 4-67, b and c).

### 4.3.7. SEM Microstructure of Ni-Mo-Al Alloys a Solution Treated and Aged at 750°C for 10, 50, and 100 Hours

After aging for 100 hours at 750°C, the $Ni_4Mo$ alloy shows grain boundary migration (Figures 4-68 and 4-69a), and secondary phase formed in the β domain region. Figure 4-69 showed a well-developed Widmanstatten pattern of β domains. In the region marked A the boundary is moving to the right, but the domain pattern appears about the same as in the matrix. In the up peregion marked B the boundary is moving to the left, and a second phase is present. This is probably discontinuous precipitation of γ as found in the $Ni_4Mo$ alloy on aging at 650°C (Figure 4-65a).

In the 2 at.% Al alloy, OLM indicated a single phase after aging for 10 hours, but there appeared to be some fine structure along the grain boundaries (Figure 4-35). After 50 hours aging , a clear boundary structure had formed, and there were fine precipitates in the matrix (Figure 4-39). Figure 4-70a shows the grain boundary structure, and Figure 4-70b shows the precipitates. Aging for 100 hours produced more of the precipitates within the grains (Figure 4-43), as shown in Figure 4-71a. These particles are very fine for useful EDS, but Figure 4-71b shows an analysis from the grain boundary particle noted by the arrow in Figure 4-71a. It is rich in molybdenum. This is the unstable $Ni_2Mo$ phase (see TEM section).

In the 5 at.% Al alloy, a lamellar structure started to form upon aging for 50 hours and completely consumed the matrix after 100 hours. The structure formed is shown in Figure 4-72. There appears to be grain boundary coarsening occurring. No EDS analyses were obtained from this sample.




Figure 4-68. SEM microstructure (SE) of $Ni_4Mo$ alloy solution treated at 1280°C for 50 hours and aged at 750°C for 100 hours showing grain boundary migration and secondary phase formation.

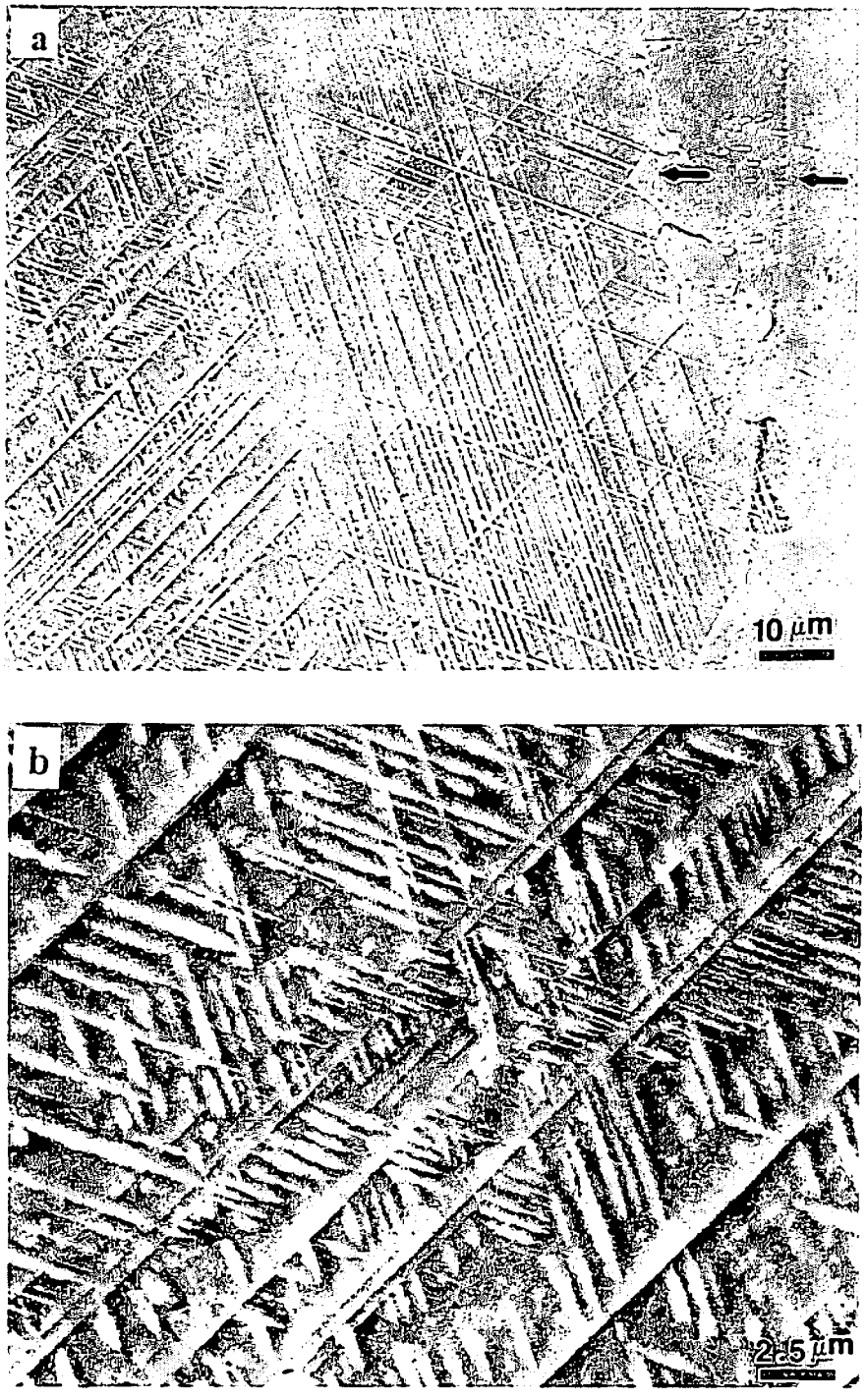



Figure 4-69. SEM microstructure (SE) of $Ni_4Mo$ alloy solution treated at 1280°C for 50 hours and aged at 750°C for 100 hours showing (a) Widmanstatten pattern β with grain boundaries migration, (b) high magnification of Widmanstatten pattern β phase.

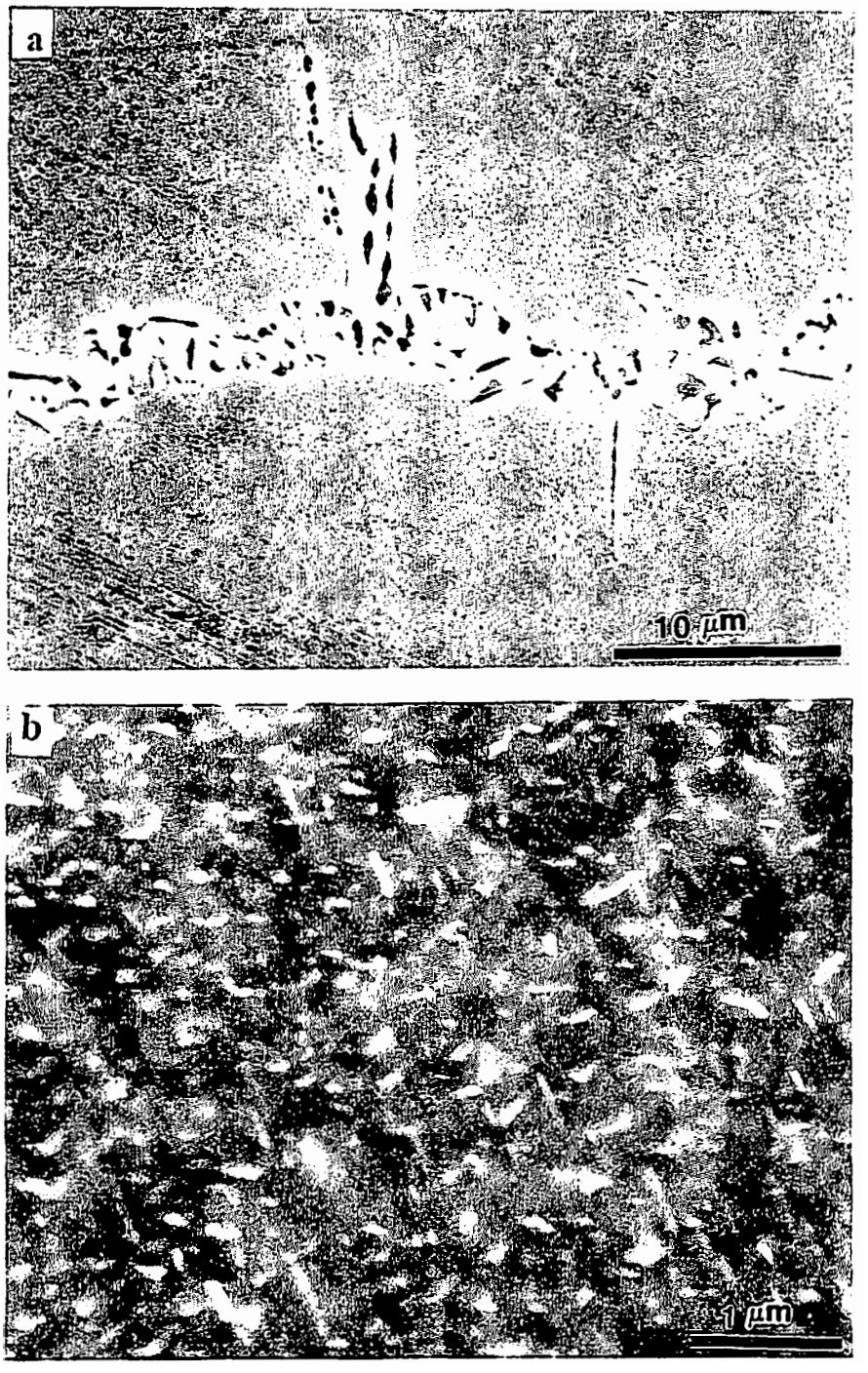



Figure 4-70. SEM microstructure (SE) of 2 at.% Al alloy solution treated at 1280°C for 50 hours and aged at 750°C for 50 hours showing (a) coarsen structure along grain boundaries, (b) precipitates in matrix.

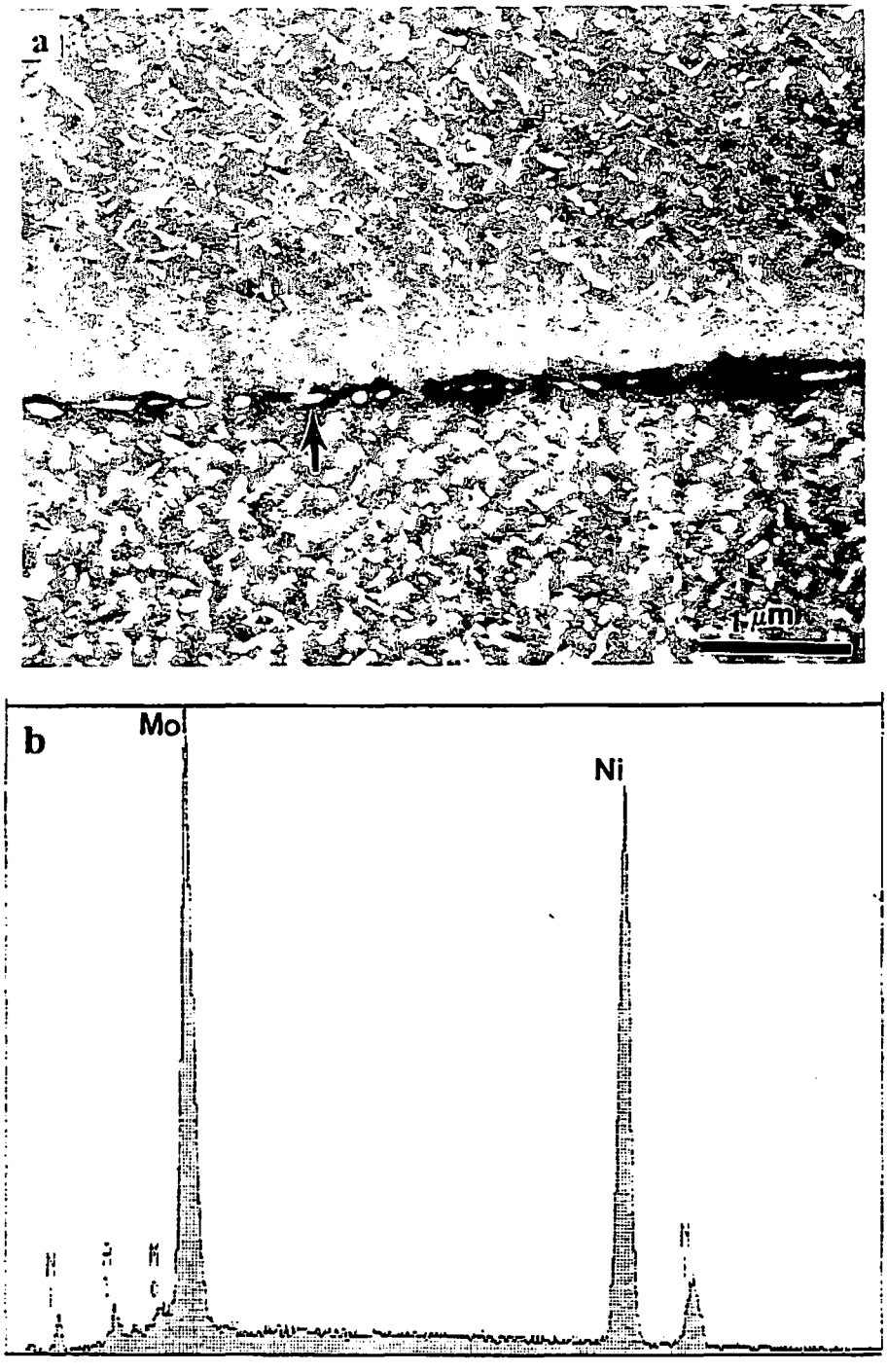



Figure 4-71. (a) SEM microstructure (SE) of 2 at.% Al alloy solution treated at 1280°C for 50 hours and aged at 750°C for 100 hours showing precipitates in matrix, (b) EDS analysis from particles along grain boundaries.

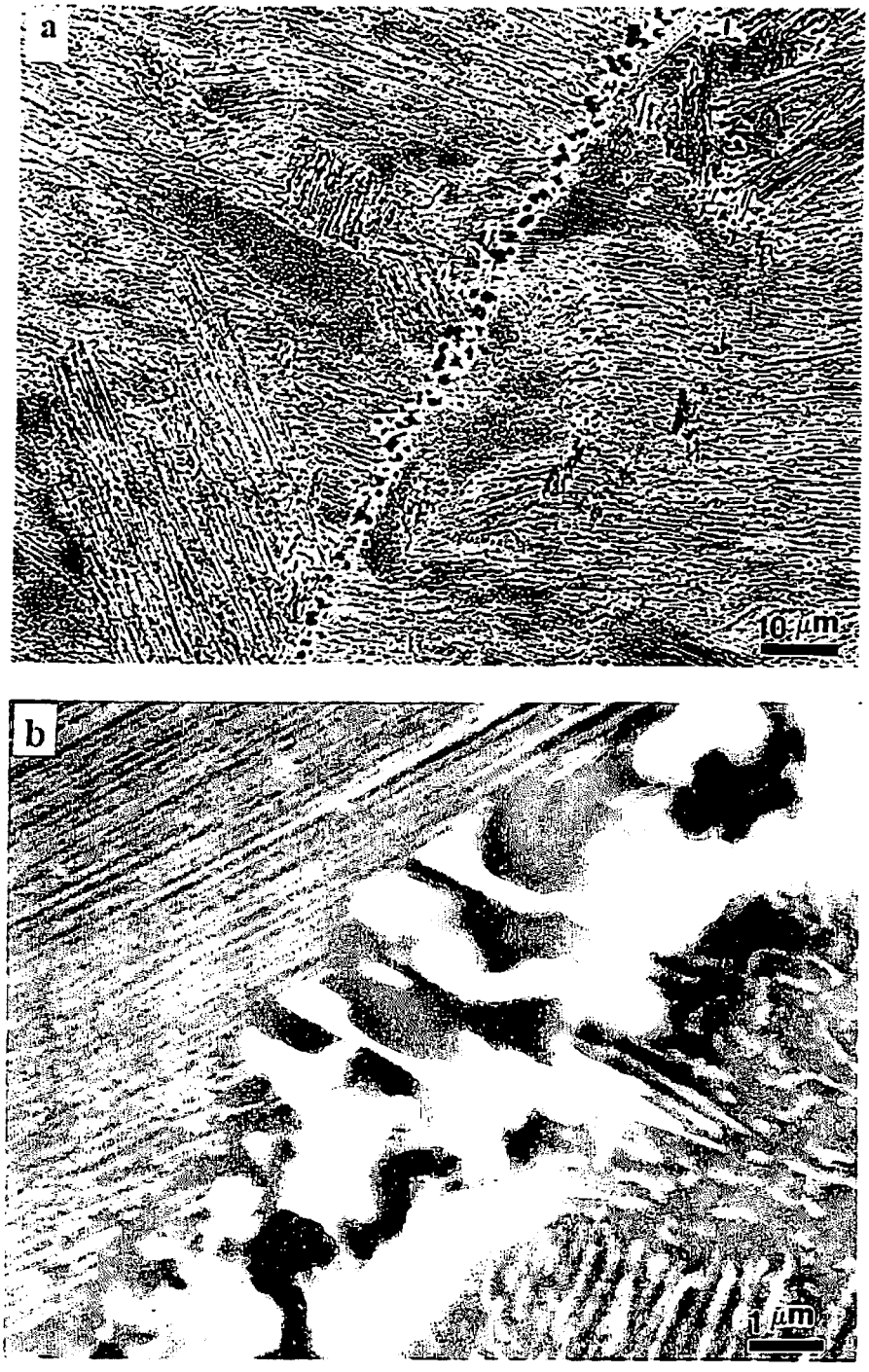



Figure 4-72. SEM microstructure (SE) of 5 at.% Al alloy solution treated at 1280°C for 50 hours and aged at 750°C for 100 hours showing (a) coarsen structure along grain boundaries with lamellar structure, (b) high magnification of coarse grain boundary structure.

The 7 at.% Al alloy had considerable lamellar structure forming from the grain boundaries after aging for 100 hours, and this is shown in Figure 4-73. A similar lamellar structure was present in the 9 at.% Al alloy after aging from 100 hours. These structures are too fine for useful EDS analyses.

### 4.3.8. SEM Microstructure of Ni-Mo-Al Alloys with a Solution Treated and Aged at 850°C for 100 Hours

The 2 at.% Al alloy, after aging for 100 hours at 850°C, showed in OLM three types of structure: a fine structure of thin parallel plates, coarse parallel plates and a lamellar structure (Figure 4-48). The structure of the fine plates is shown in Figure 4-74. The plates appear to have nucleated closely together from a grain boundary and grown along a common crystallographic plane into the matrix. In the region shown in Figure 4-74a, these plates have crossed another boundary (arrow), but have retained their orientation. On this boundary are rounded particles (Figure 4-74b), and EDS of them is shown in Figure 4-74c. They are molybdenum-rich and may be the $\delta$ phase. Figure 4-74d shows a region in the 2 at.% Al alloy which has the lamellar structure. Note that the sides of these plates are not parallel to the thin plates adjacent to them. No EDS analysis was obtained from the lamellar structure.

Aging the 5 at.% Al alloy for 100 hours produced a structure of fine precipitates (Figure 4-49). This is shown in Figure 4-75. The round particles (C) along the grain boundary are molybdenum-rich (Figure 4-75e) and are taken to be $\delta$ phase. The needles which did not etch out (A in Figure 4-75b) had a nickel to molybdenum ratio of 1.4 (Figure 4-75c), and are taken to be the $\gamma$ phase. The matrix had a ratio of 2.0, indicating that it is the $\alpha$ phase (see TEM section).

The microstructure of the 7 at.% Al alloy (Figure 4-50) had converted to a finer

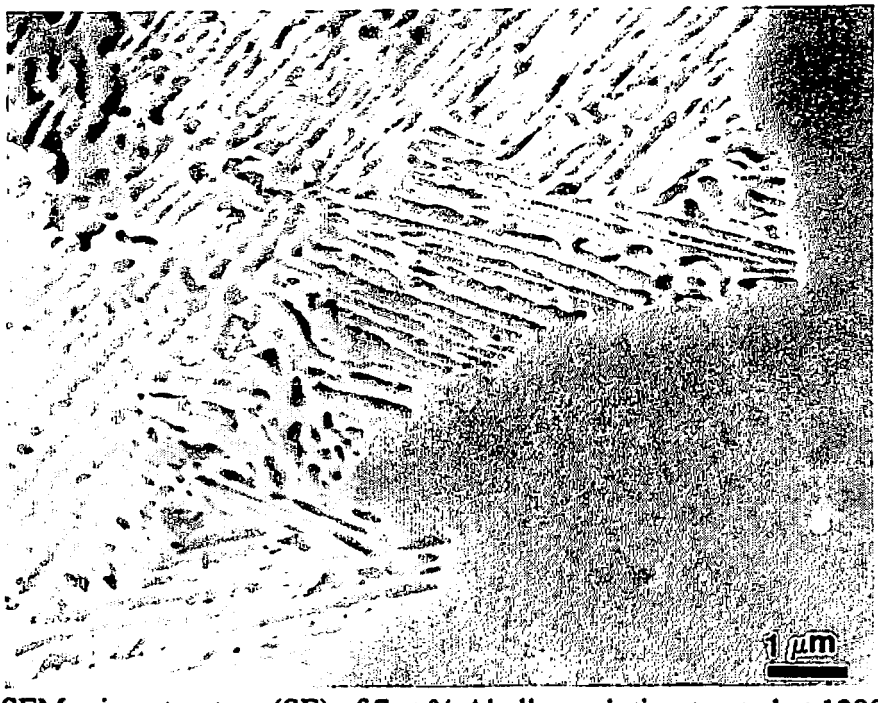



Figure 4-73. SEM microstructure (SE) of 7 at.% Al alloy solution treated at 1280°C for 50 hours and aged at 750°C for 100 hours showing lamellar structure.

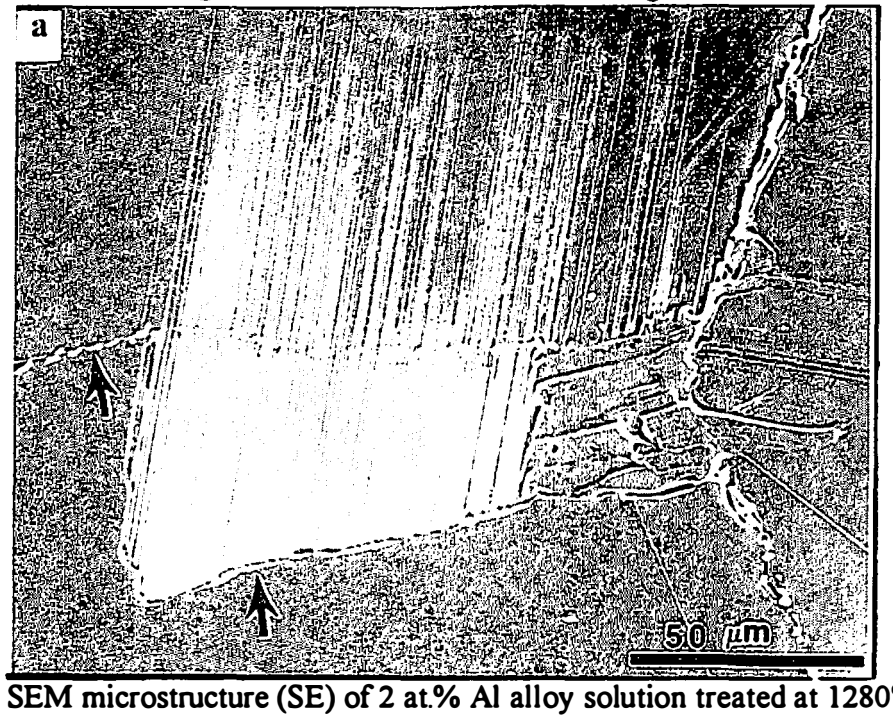



Figure 4-74. SEM microstructure (SE) of 2 at.% Al alloy solution treated at 1280°C for 50 hours and aged at 850°C for 100 hours showing (a) striation line structure, (b) the striation lines across particles, (c) EDS analysis from particles, (d) coarse lamellar structure.

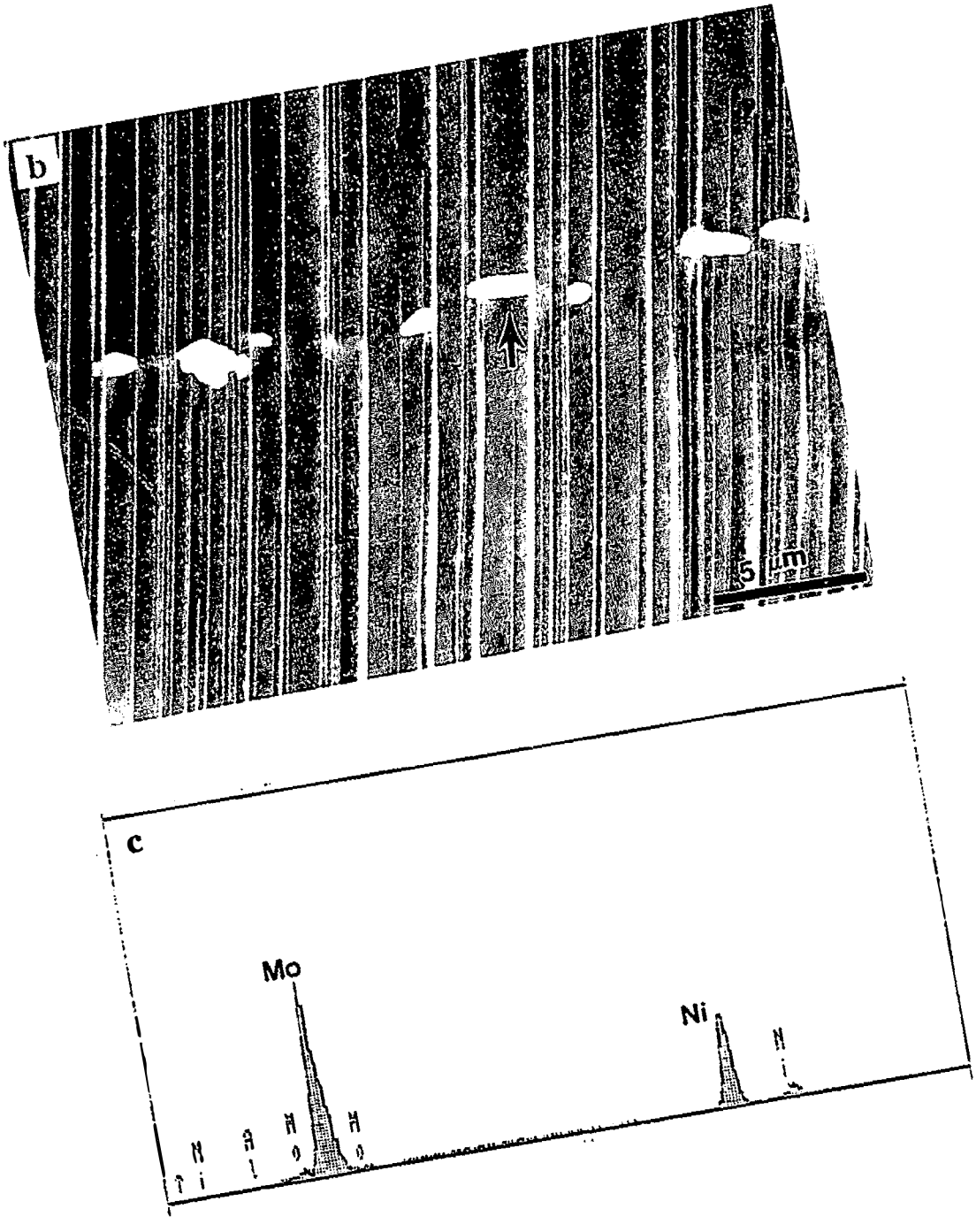



Figure 4-74. continue (b) and (c).

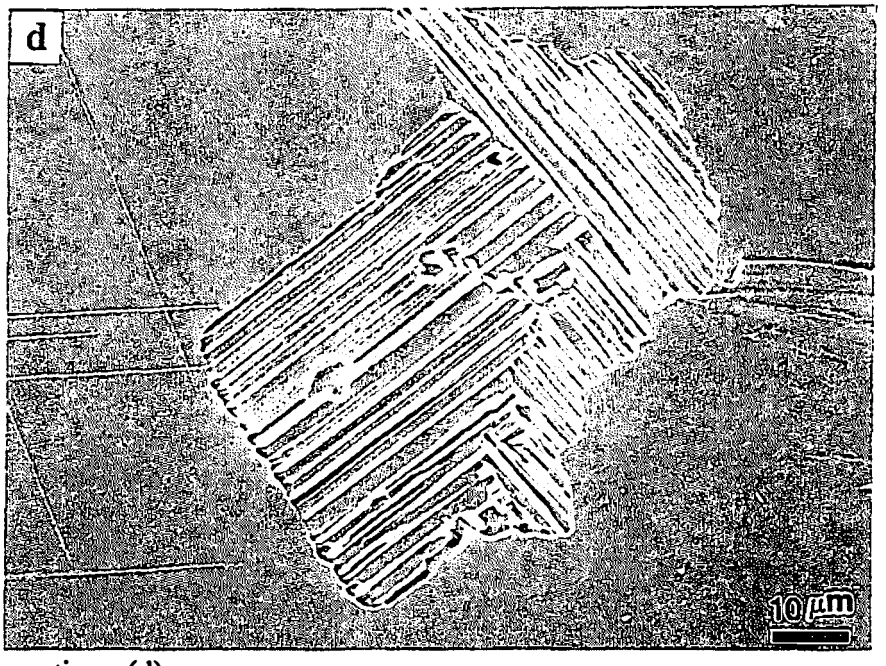



Figure 4-74. continue (d).




Figure 4-75. SEM microstructure (SE) of 5 at.% Al alloy solution treated at 1280°C for 50 hours and aged at 850°C for 100 hours showing (a) needle-like structure, (b) high magnification of needle-like structure, (c) EDS analysis from lath, (d) EDS analysis from matrix, (e) EDS analysis from particles along grain boundaries.



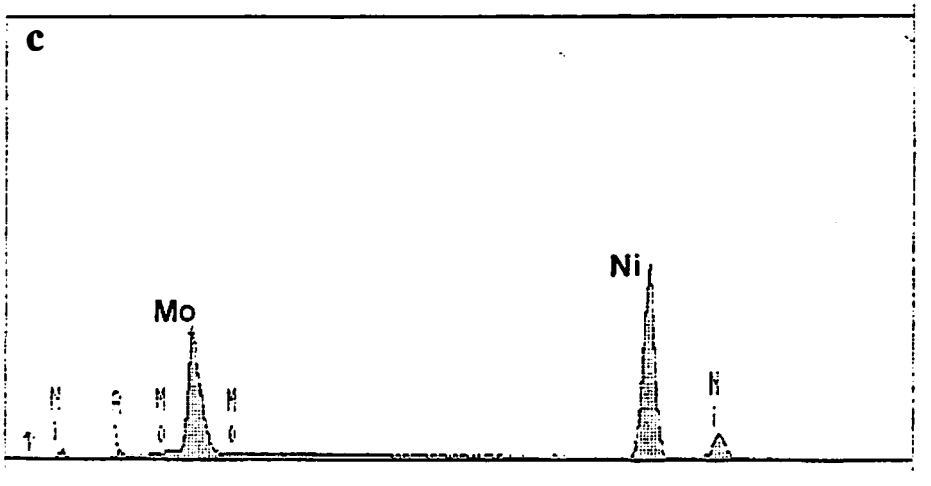




Figure 4-75. continue (b) and (c).

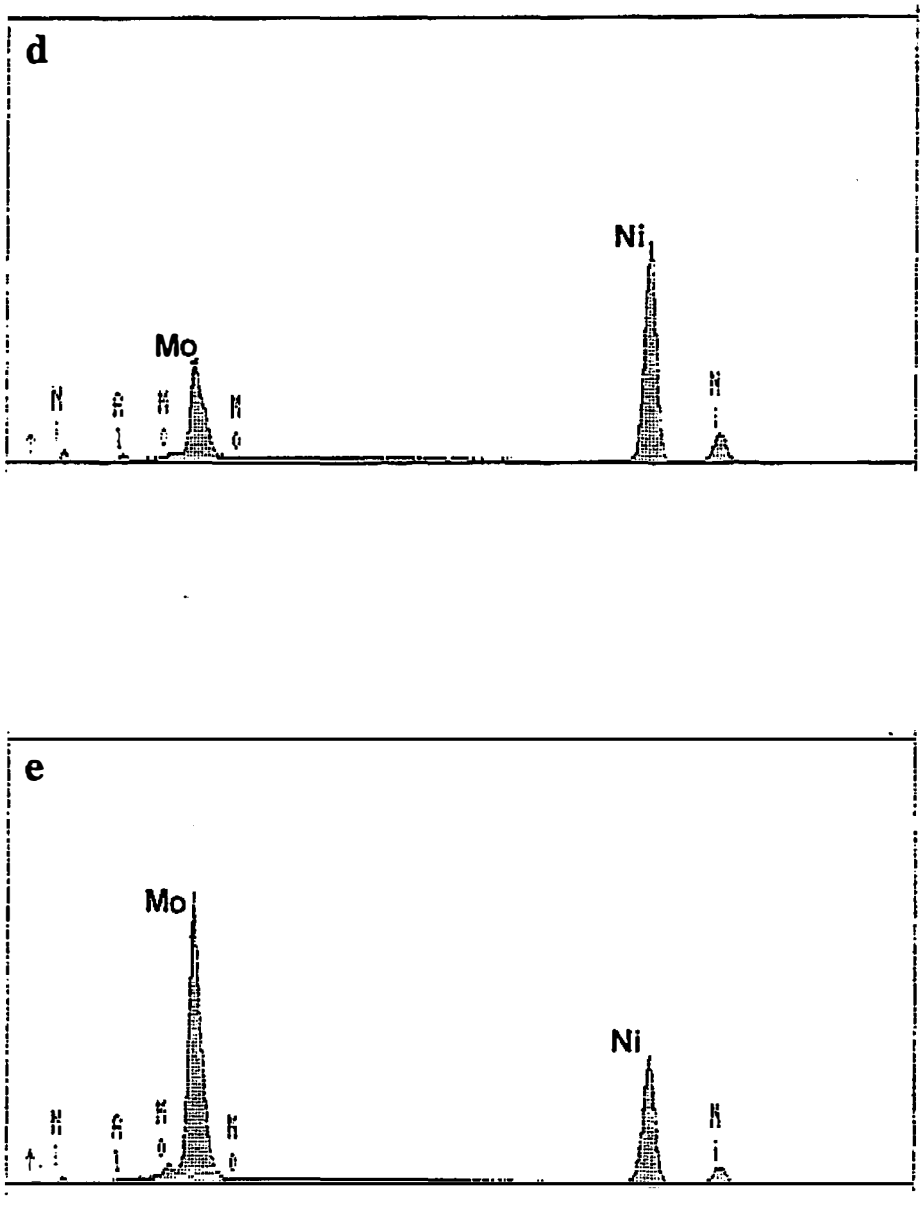



Figure 4-75. continue (d) and (e).

precipitates structure than did the 5 at.% Al alloy. This is shown in Figure 4-76. the structure is assumed to be $\delta$ and $\gamma$ in $\alpha$ phase.

### 4.3.9. SEM Microstructure of Ni-Mo-Al Alloys with a Solution Treated and Aged at 950°C for 100 Hours

The 2 at.% Al alloy showed no apparent transformation after aging for 100 hours at 950°C except for an indication of precipitation along the grain boundaries (Figure 4-52). This is shown in Figure 4-77a. The EDS analysis of the rounded grain boundary particles is shown in Figure 4-77b. These particles are Mo-rich and are taken to be the $\delta$ phase.

The 5 at.% Al alloy had converted completely to a structure of fine precipitates (Figure 4-53), and is shown in Figure 4-78a. EDS analysis (Figure 4-78b) from the grain boundaries particles show that they are molybdenum-rich and are taken to be the $\delta$ phase. The 7 at.% Al alloy showed a similar but fine structure (Figure 4-54), as shown in Figure 4-79, a and b. The larger grain boundary particles (A) are rich in Mo (Figure 4-79c), and are taken to be the $\delta$ phase. An EDS analysis from the region (B) of the two phase matrix is shown in Figure 4-79d, where it is seen to be nickel-rich. However, the other phase had etched out so no EDS analysis should be obtained. To circumvent this problem, the same sample was examined in the as-polished condition using BSE (Figure 4-80a). The dark areas are not etched out, but are a phase lower in molybdenum than the lighter particles. EDS analyses from the three regions noted are Figure 4-80b, c and d. The dark particles are very rich in nickel and contain a prominent amount of aluminum. Thus this phase is taken to be the $Ni_3(Al, Mo)$ $\gamma'$ phase. The matrix is richer in molybdenum., but still nickel-rich, and is taken to be $\gamma$ phase. The light particles is molybdenum rich and it is taken to be the $\delta$ phase.

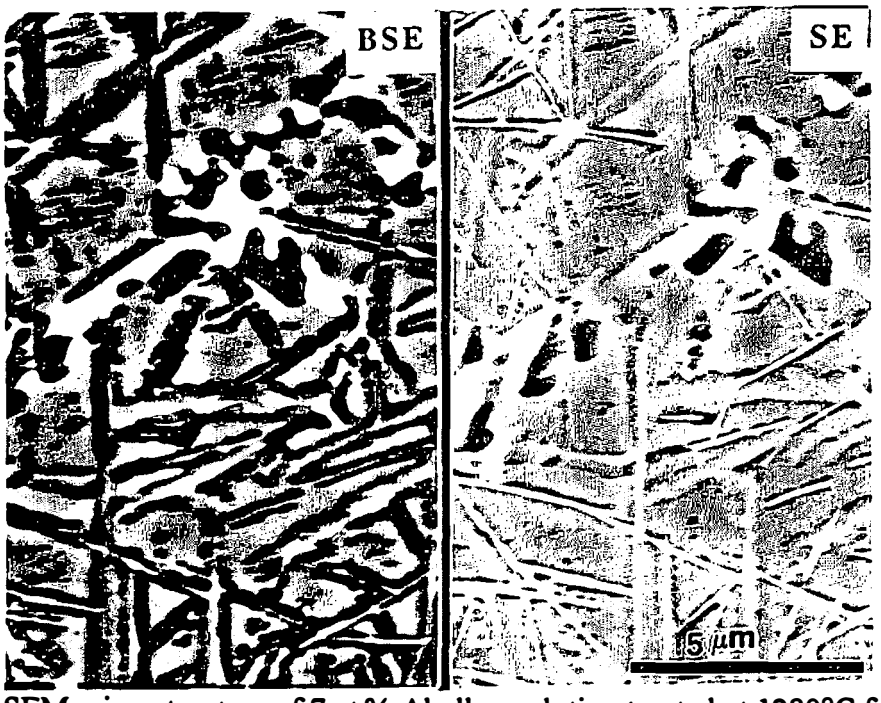



Figure 4-76. SEM microst cture of 7 at.% Al alloy solution treated at 1280°C for 50 hours and aged at 850°C for 100 hours showing particles along grain boundaries and needle-like structure.

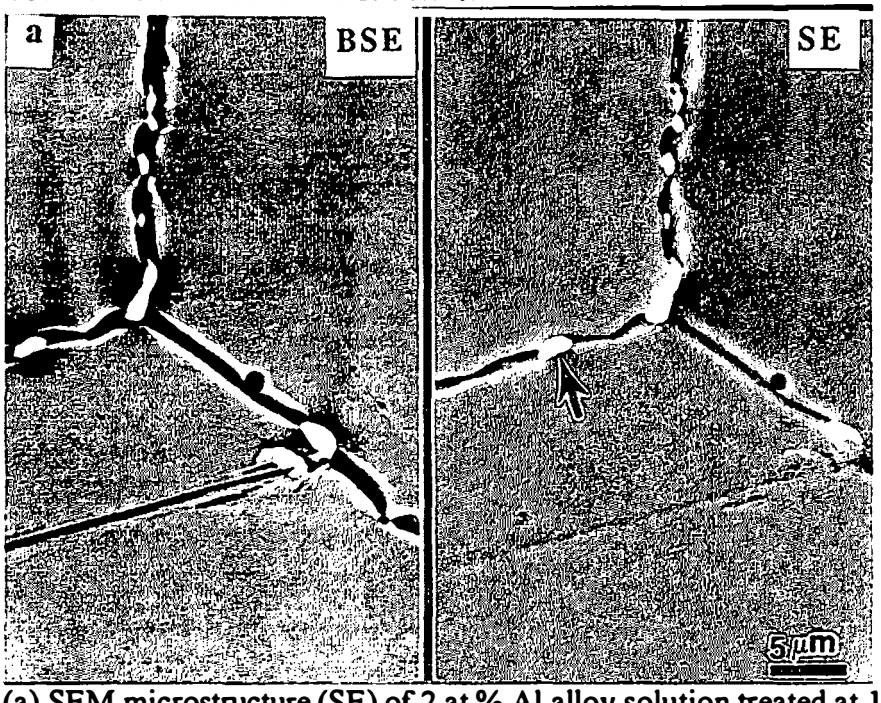



Figure 4-77. (a) SEM microstructure (SE) of 2 at.% Al alloy solution treated at 1280°C for 50 hours and aged at 950°C for 100 hours showing particles along grain boundaries, (b) EDS analysis from particles along grain boundaries.

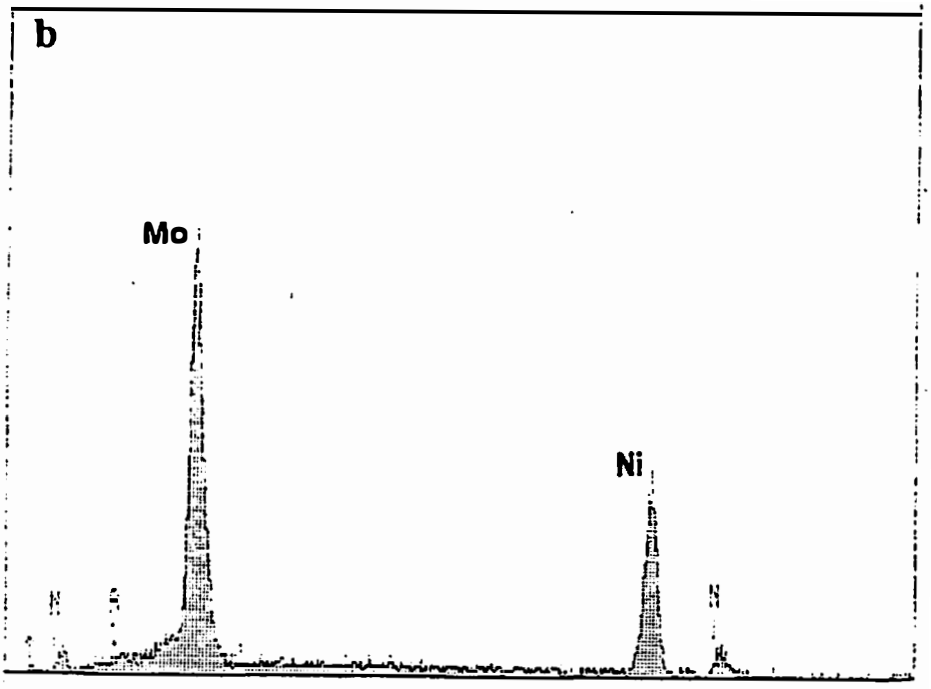



Figure 4-77. continue (b).

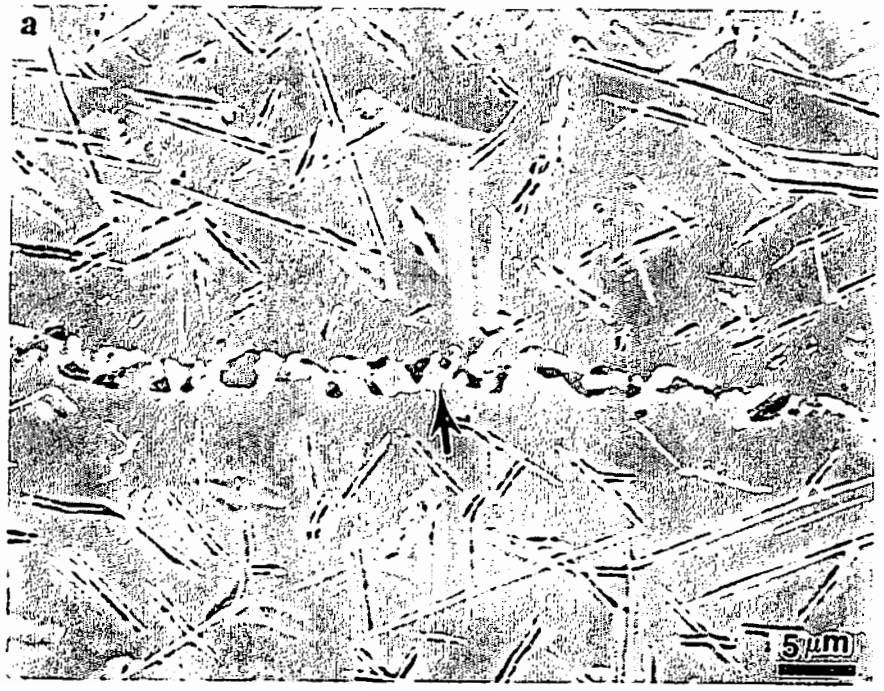



Figure 4-78. (a) SEM microstructure (SE) 5 at.% Al alloy solution treated at 1280°C for 50 hours and aged at 950°C for 100 hours showing particles along grain boundaries aand needle-like structure, (b) EDS analysis from particles along grain boundaries.

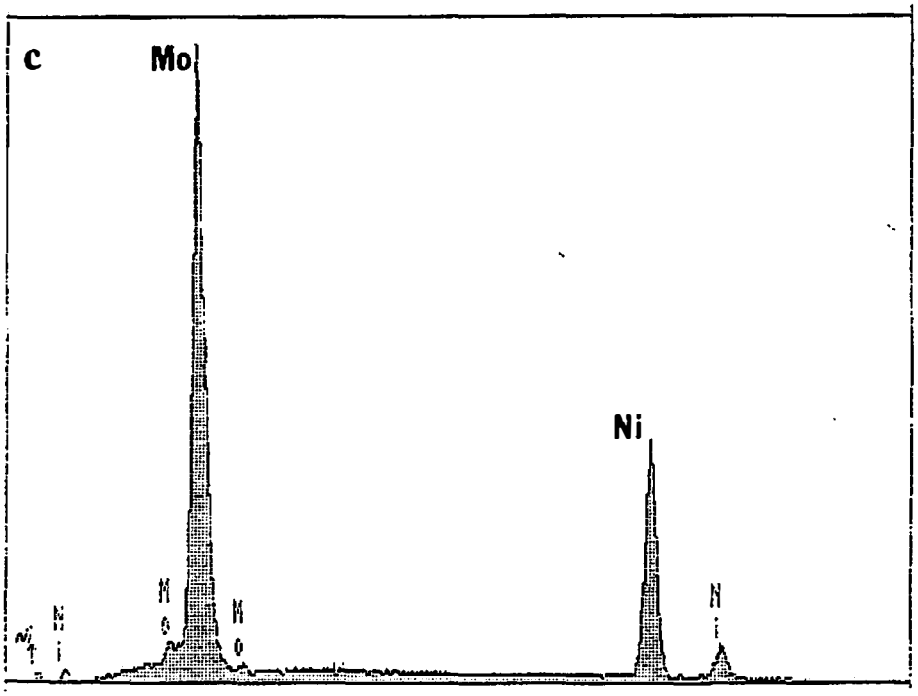



Figure 4-78. continue (b).

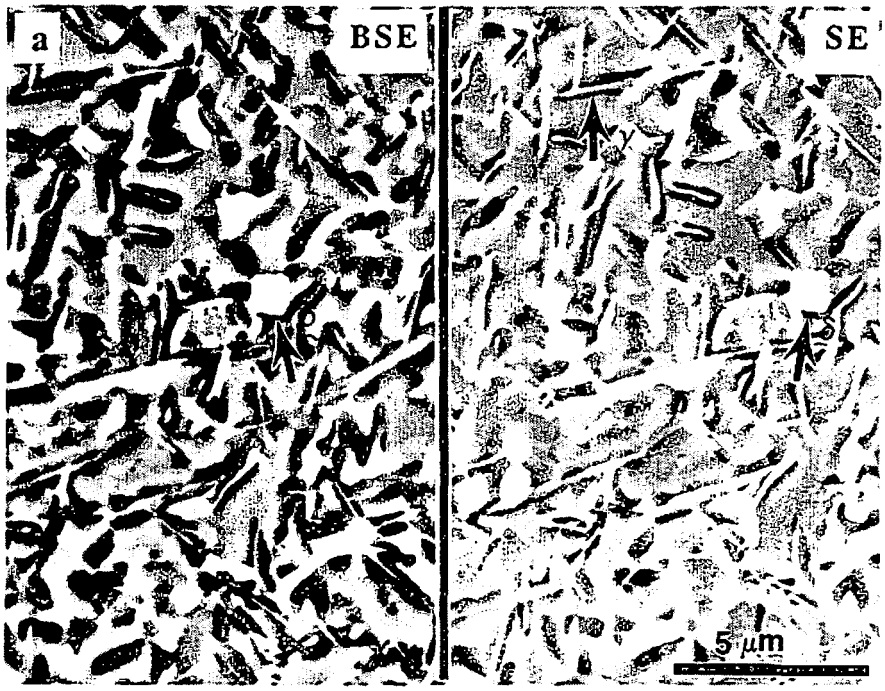



Figure 4-79. SEM microstructure of 7 at.% Al alloy solution treated at 1280°C for 50 hours and aged at 950°C for 100 hours showing particles and needle-like structure, (b) high magnification of particles along grain boundaries, (c) EDS analysis from particles along grain boundaries, (d) EDS analysis from matrix.

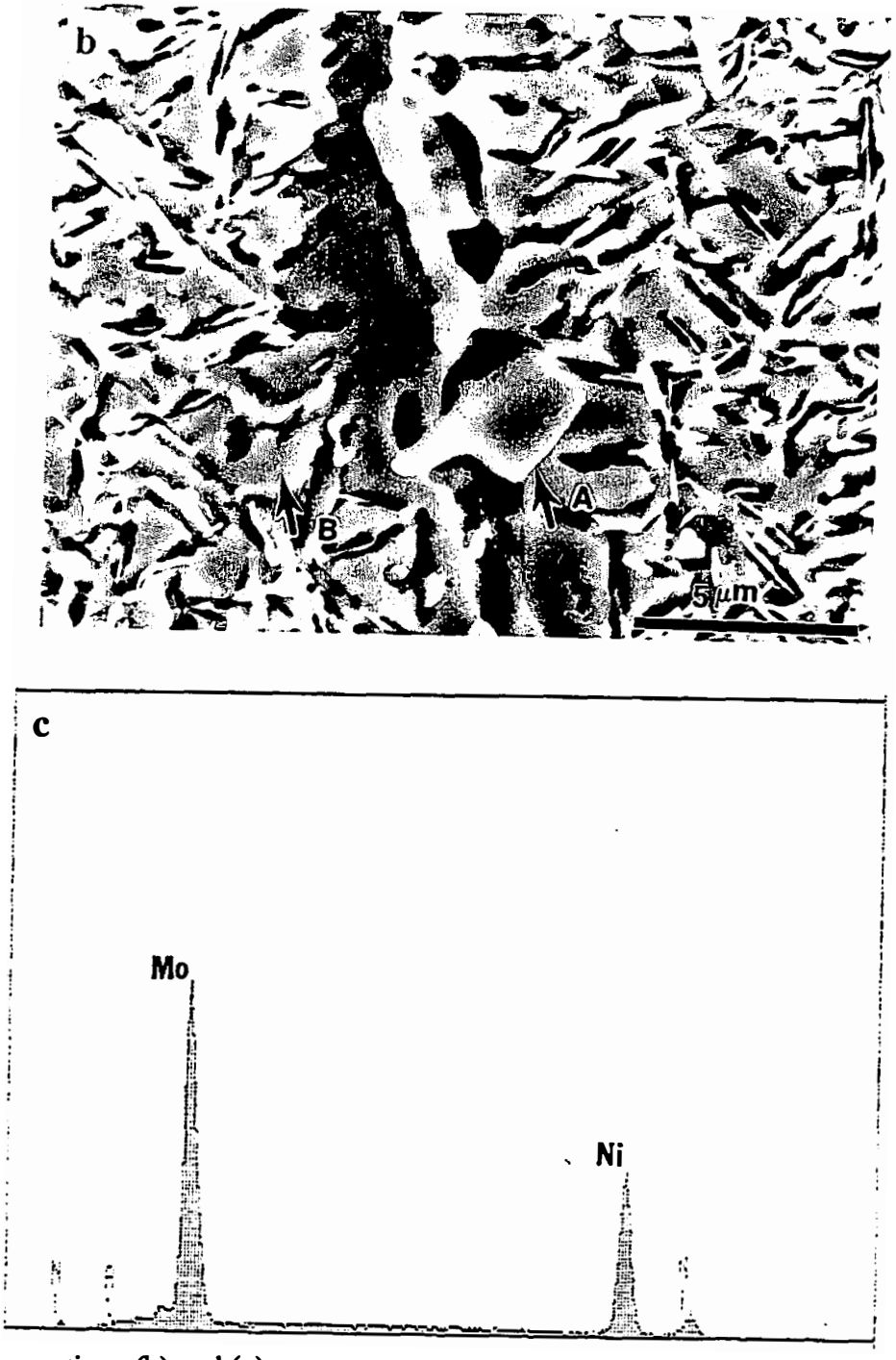



Figure 4-79. continue (b) and (c).

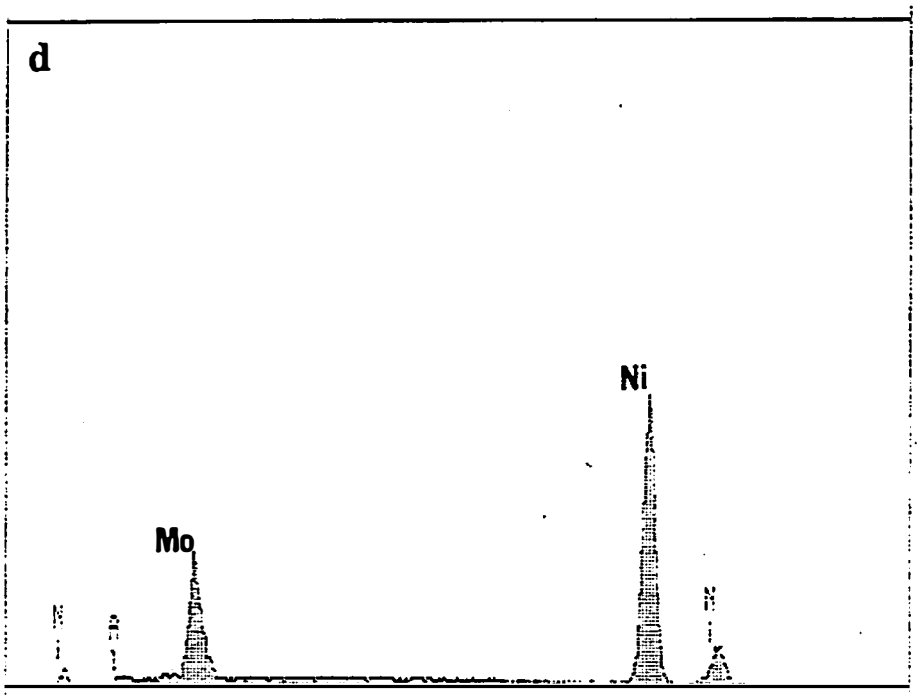



Figure 4-79. continue (d).




Figure 4-80. SEM microstructure (BSE) of 7 at.% Al alloy solution treated at 1280°C for 50 hours and aged at 950°C for 100 hours showing sample in the as-polished condition, (b) EDS analysis from dark area, (c) EDS analysis from matrix, (d) EDS analysis from bright area.

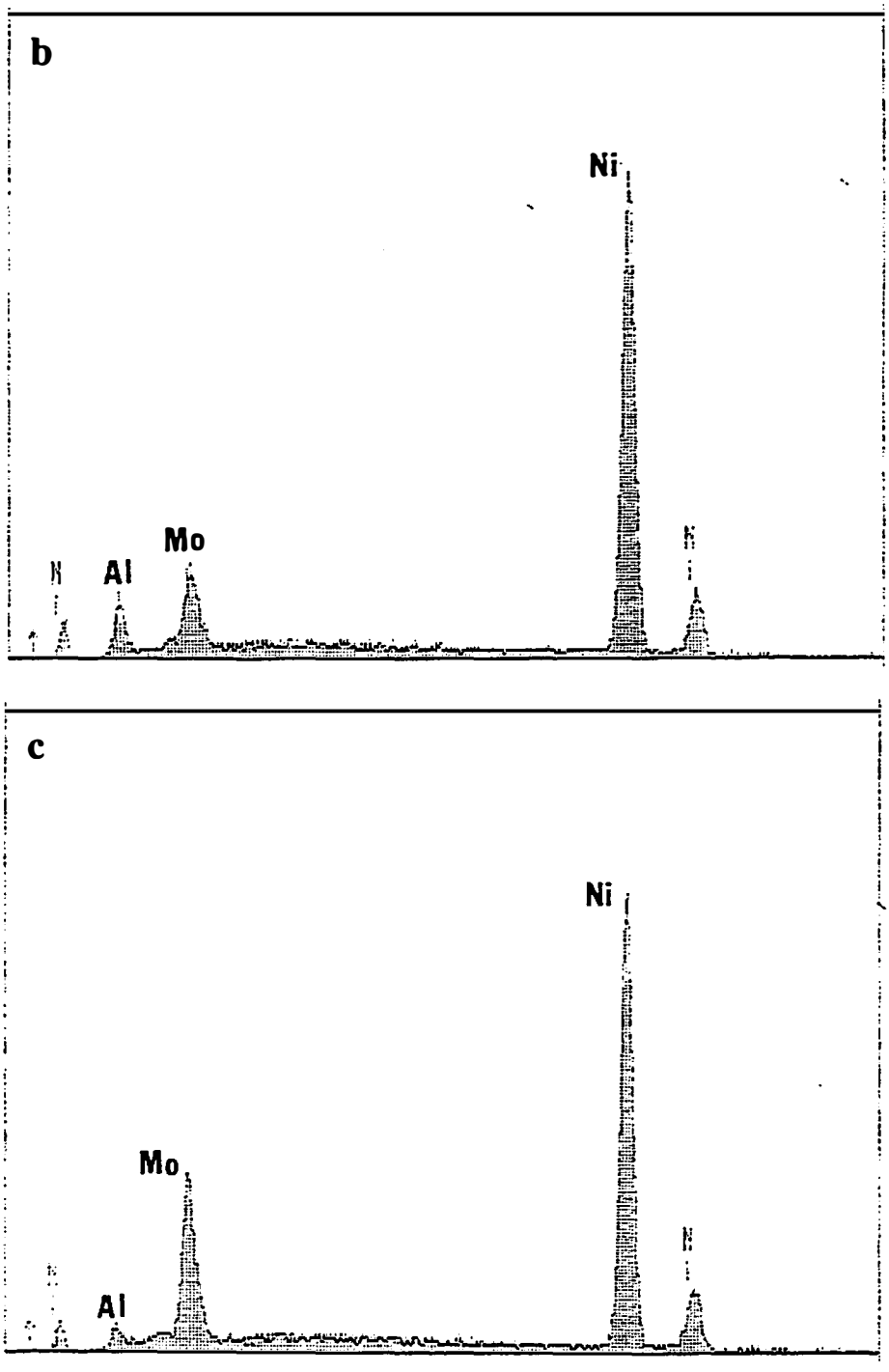



Figure 4-80. continue (b) and (c).

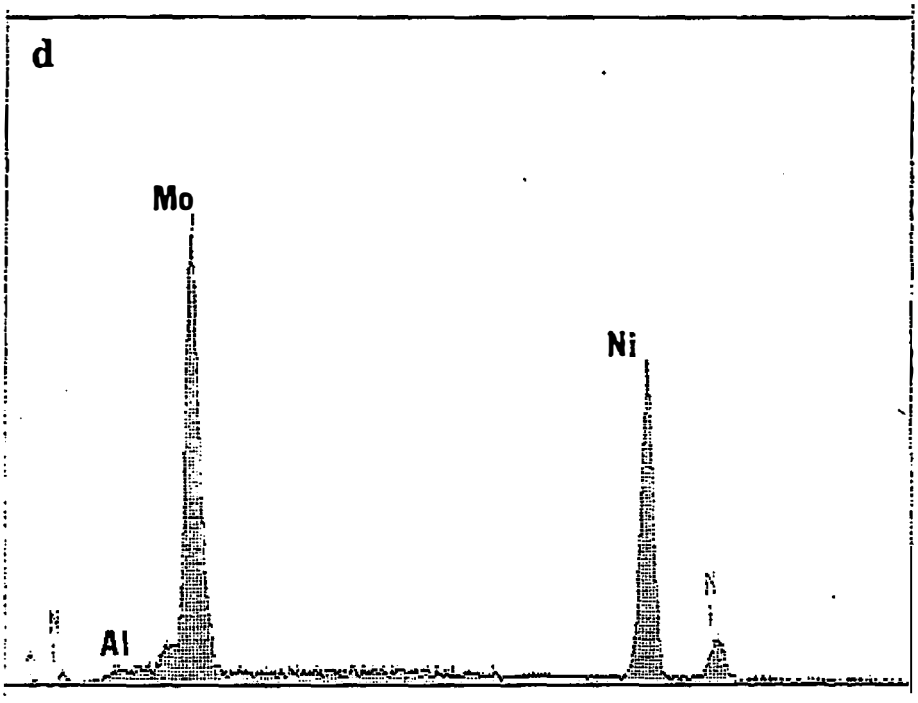



Figure 4-80. continue (d).

### 4.3.10. Summary of SEM Observations

The conclusions about the microstructure based on the SEM observation and EDS analyses are summarized in Table 4-2. Note that this is an update of the information in Table 4-1 which was based only on the OLM observations.

## 4.4. Fracture Surface Topology Investigation

The underlying motivation for this research was to search for alloying additions which would allow strengthening by aging yet retain ductility. In the binary $Ni_4Mo$ base alloy, and the commercial Hastelloy B2 alloy based on it, if the $\beta$ phase forms, the alloy becomes brittle, fracturing along the former $\alpha$ grain boundaries. This embrittlement problem is also present if other phases form during aging.

In the general range of 750°C, the decomposition of $\alpha$ occurs most rapidly, and 100 hours is sufficient to impart embrittlement in the binary $Ni_4Mo$ alloy. Thus, the fractographic examination was centered on the alloys which had been aged at 750°C for 100 hours.

Recall that the fractographic study involved metallographically polishing and etching a small specimen, then placing it in a three-point bending apparatus to place the etched surface in tension (see Section 3). The surface was bent until cracks initiated, then they were bent further, and the same cracks examined to see along what microstructural features they were advancing. With sufficient bending, the cracks opened up so that along their edge the microstructural features and the fractographic features could be simultaneously examined.

Table 4-2. SEM examination of phase transformation of alloys in all aging condition

| | $Ni_4Mo$ | 2 at.% Al alloy | 5 at.% Al alloy | 7 at.% Al alloy | 9 at.% Al alloy |
|---|---|---|---|---|---|
| 1250°C, 50 hr. | α phase | single phase | single phase | single phase | Mo-rich particles and matrix |
| 600°C, 100 hr. | - | single phase | single phase | δ phase nucleated along grain boundaries | Mo-rich particles, δ and α/γ (?) phase |
| 650°C, 100 hr. | γ particles and β phase | intergranular cracking | lamellar structure, intergranular cracking and matrix | lamellar structure nucleated along grain boundaries | - |
| 700°C, 100 hr. | - | single phase | lamellar structure | lamellar structure and matrix | coarse lamellar structure and fine lamellar structure |
| 750°C, 10 hr. | - | α phase | lamellar structure and matrix | lamellar structure and matrix | - |

| | | | | | |
|---|---|---|---|---|---|
| 750°C, 50 hr. | - | coarsened structure along grain boundaries and precipitates in matrix | lamellar structure | lamellar structure and matrix | - |
| 750°C, 100 hr. | β | precipitates in matrix | lamellar structure | lamellar structure and matrix | lamellar structure and matrix |
| 850°C, 100 hr. | - | fine and coarse lamellar structure and Widmanstatten structure | δ particles along grain boundaries and needle-like γ phase in α | δ particles along grain boundaries and needle-like γ phase in α | - |
| 950°C, 100 hr. | - | Mo particles and α phase | δ particles along grain boundaries and needle-like γ phase in α | δ particles and γ' along grain boundaries and needle-like γ phase and δ particles in matrix | |

### 4.4.1. Fracture Surface Examination of $Ni_4Mo$ Alloy

None of the alloys in the solution heat treated condition cracked during bending, and all showed good ductility.

Figure 4-81 shows the surface of the $Ni_4Mo$ alloy sample, where several grain boundaries have separated. It is important to note that inside each grain the structure is made up of former $\alpha$ high angle boundaries across which there is a crystallographic mismatch and these former $\alpha$ boundaries are the ones along which separation occurs. For the heat treatment used, it was shown previously (see Figures 4-7, 4-57) that some boundary migration has occurred. A region is shown in Figure 4-82, and here the $\gamma$ phase (see EDS in Figure 4-83) has formed by discontinuous precipitation associated with boundary migration. It is along this high angle boundary that interface separation has occurred.

Figure 4-84 shows another region of boundary migration, but no precipitation has occurred. This is probably domain coarsening accompanying the boundary migration, since the Widmanstatten pattern associated with the formation of a fine domain structure does not extend into the migrated area. Clearly cracking has occurred along the migrated high angle boundary.

Figure 4-85 shows a region of the fracture surface after the sample was broken into two pieces. The microstructure is to the right, and the fracture surface to the left. The fracture surface is rough, indicating that at this location fracture has occurred along a migrated boundary. The discrete particles seen also indicate that this a region in which the $\gamma$ has formed, and that these particles are $\gamma$. That is ,this region of the fracture surface is like the one shown in Figure 4-82.

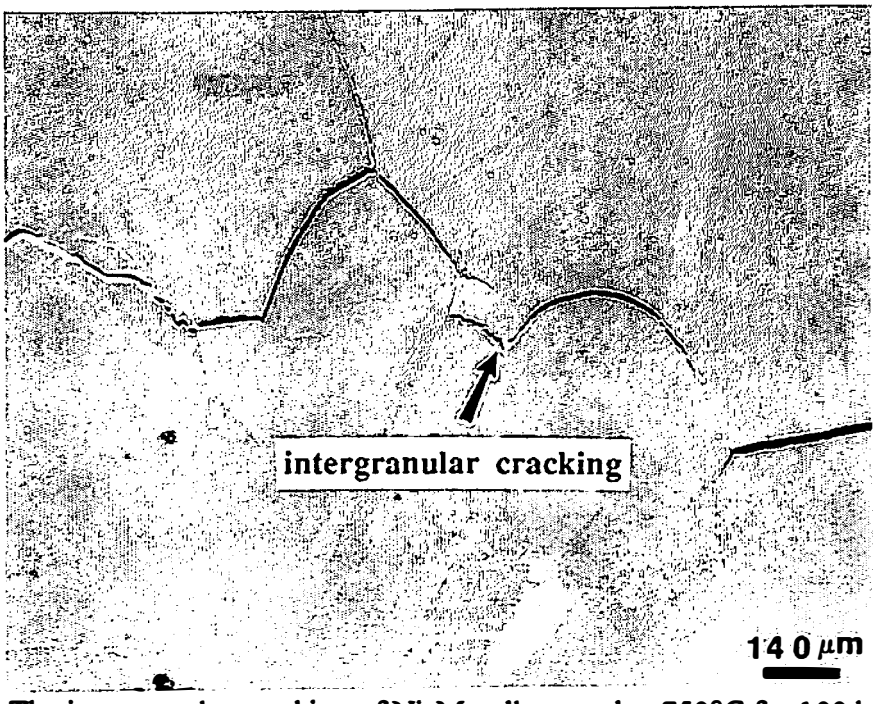



Figure 4-81. The intergranular cracking of $Ni_4Mo$ alloy aged at 750°C for 100 hours.

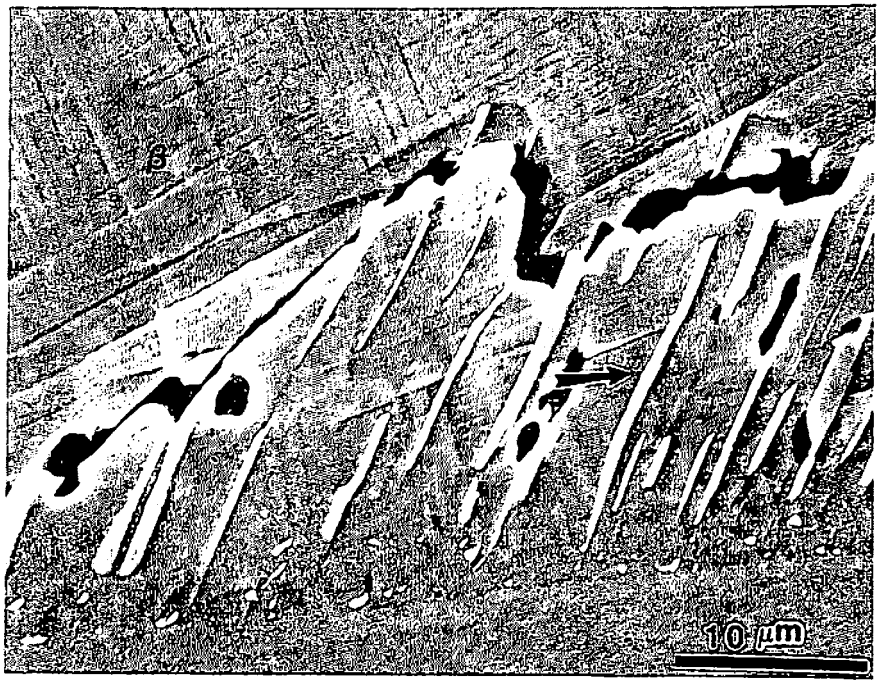



Figure 4-82. Interface cracking between coarsened β structure and Widmanstatten pattern β structure in $Ni_4Mo$ alloy aged at 750°C for 100 hours. The arrow indicated γ phase.

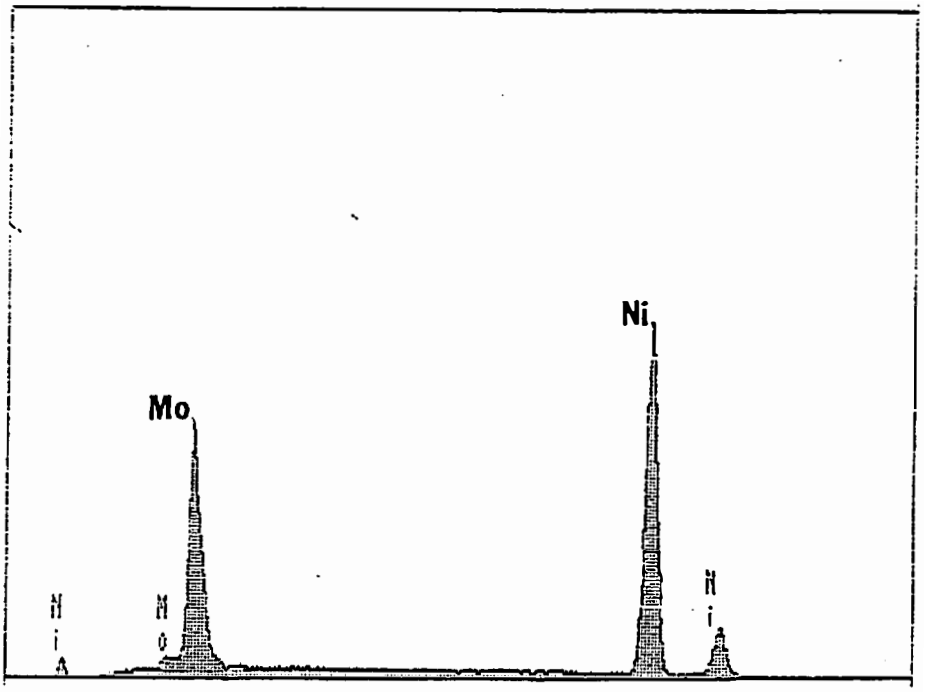



Figure 4-83. The EDS analysis from the bright lath in coarsened β region in $Ni_4Mo$ alloy (see arrow in Figure 4-82).

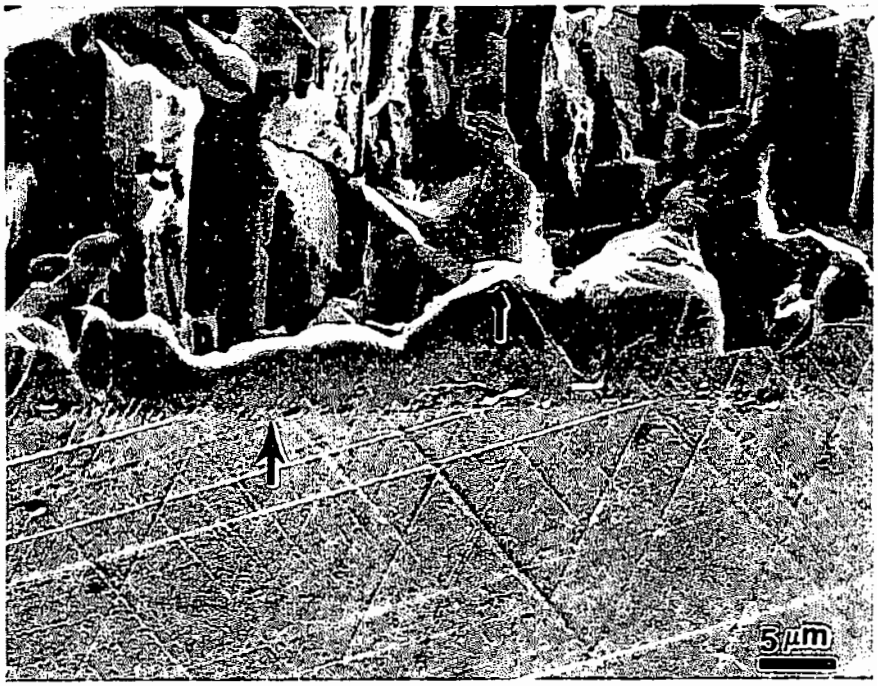



Figure 4-84. The cleavage morphology at grain boundaries between coarsened β and Widmanstatten pattern β structure in $Ni_4Mo$ alloy.

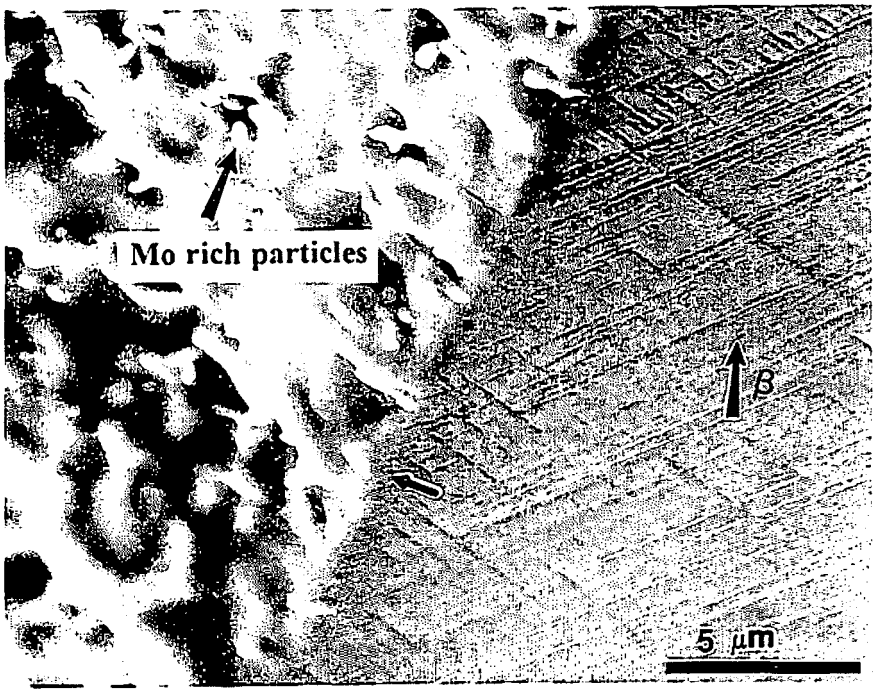



Figure 4-85. Molybdenum particles segregated along grain boundaries in $Ni_4Mo$ alloy.

### 4.4.2. Fracture Surface Examination of 2 at.% Al Alloy

The 2 at.% Al alloy contained some fine precipitates in the grains, and a thin band of a denuded structure along the grain boundaries (Figures 4-43 and 4-70a). The grain boundaries and matrix particles were identified as probably the δ phase. Figure 4-86 shows extensive intergranular fracture along the grain boundaries. The matrix did not show an etched Widmanstatten structure, so β was not present. Figure 4-87 shows a region of the fracture surface. The particles (see arrow) are rich in molybdenum (see EDS analysis in Figure 4-88), and are taken to be the δ phase. There appear to be dimples associated with these particles indicating some local ductility referred to Figure 4-89. The exact topography of the fracture surface in between these dimples is not clear, but is not particularly smooth.

### 4.4.3. Fracture Surface Examination of 5 at.% Al Alloy

The microstructure of the 5 at.% Al alloy after aging for 100 hours at 750°C consisted of a lamellar structure and a coarser globular structure along the grain boundaries (Figure 4-72a). The surface of the bent sample is shown in Figure 4-90, where it is seen that cracking has occurred along the original grain boundary regions. Figures 4-91 and 4-92 show the edge of the fractured surface, with the lamellar microstructure adjacent to it. Fracture is occurring by interphase separation, and the crack advances by a series of ledges between and across the phase (Figure 4-93). The fracture surface is shown at high magnification in Figure 4-94, but the fracture surface is still not clear.

### 4.4.4. Fracture Surface Investigation of 7 at.% Al Alloy

After aging for 100 hours at 750°C, the microstructure of the 7 at.% Al alloy has considerable lamellar structure along the grain boundaries (Figures 4-45 and 4-73). The

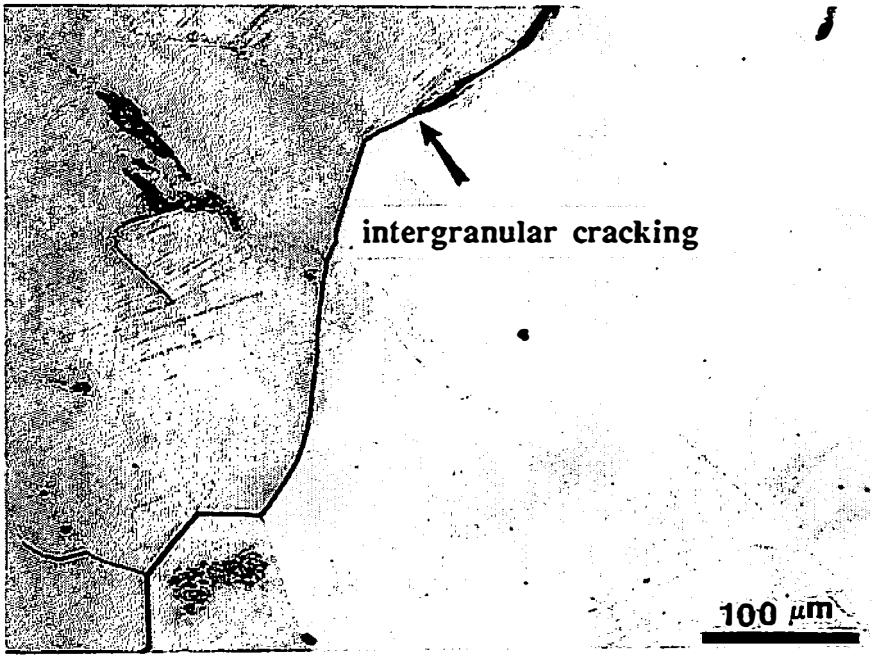



Figure 4-86. Intergranular cracking in 2 at.% Al alloy aged at 750°C for 100 hours.

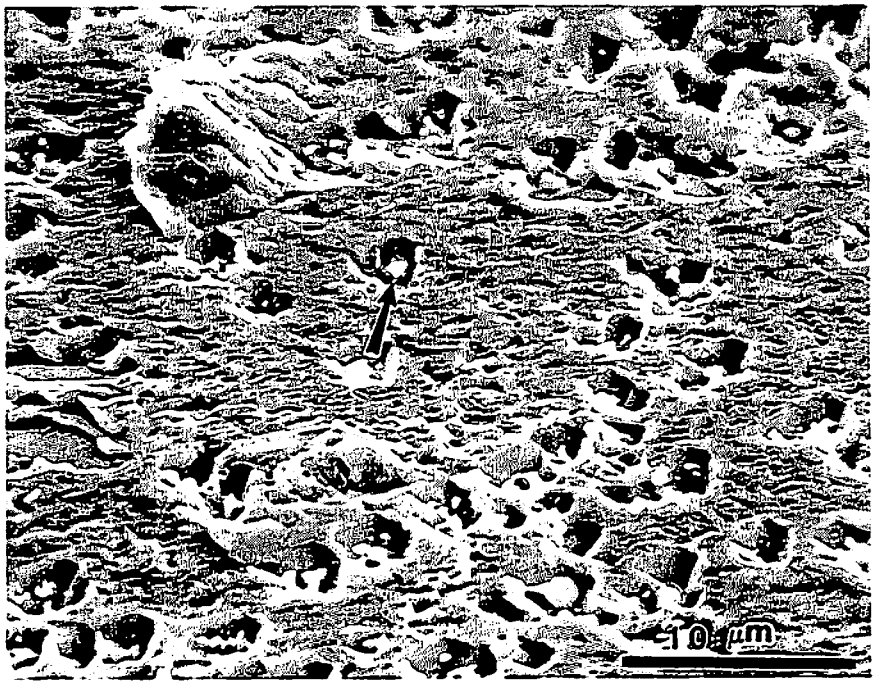



Figure 4-87. Fracture morphology of 2 at.% Al alloy aged at 750°C for 100 hours.

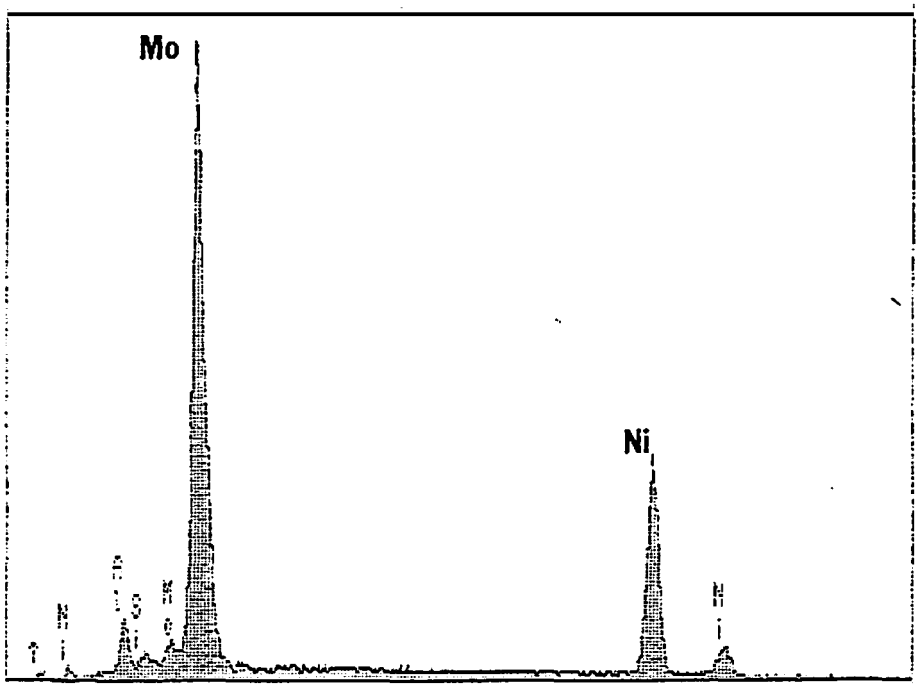



Figure 4-88. The EDS analysis from particles in 2 at.% Al alloy (see arrow in Figure 4-87).

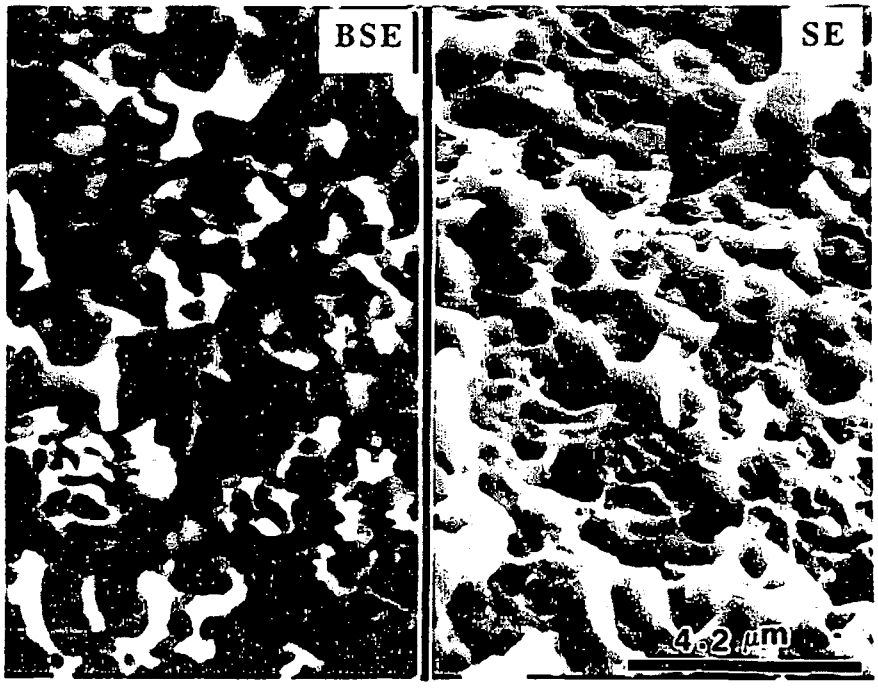



Figure 4-89. Intergranular dimple morphology of 2 at.% Al alloy aged at 750°C for 100 hours.

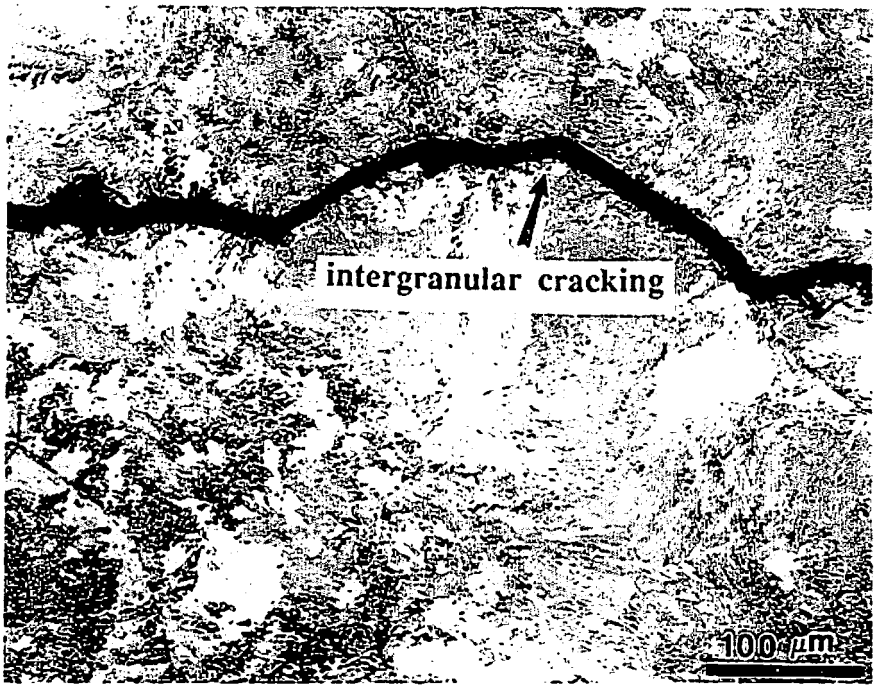



Figure 4-90. Intergranular cracking in 5 at.% Al alloy aged at 750°C for 100 hours.

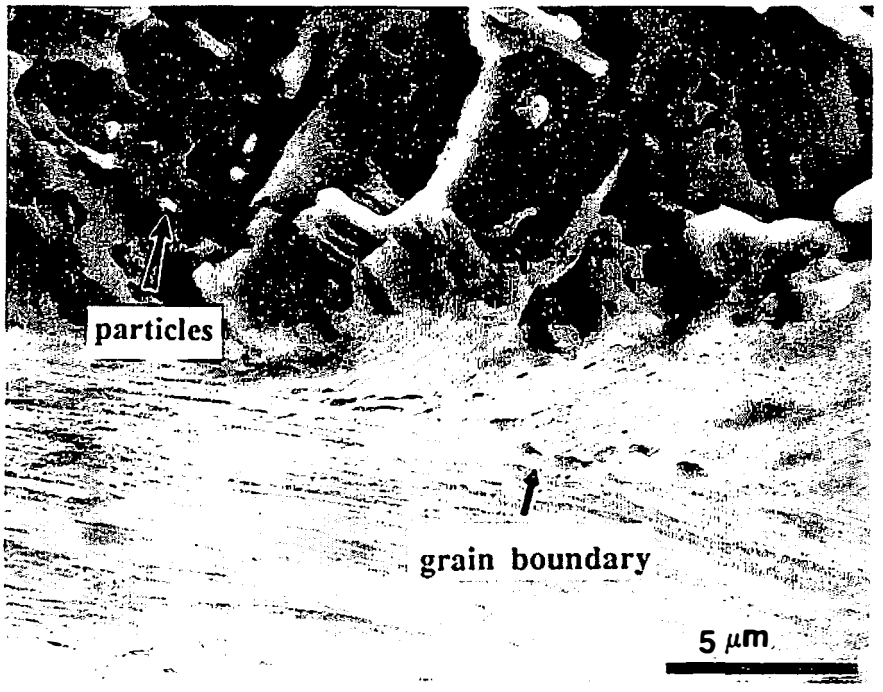



Figure 4-91. The fracture surface of 5 at.% Al alloy aged at 750°C for 100 hours.

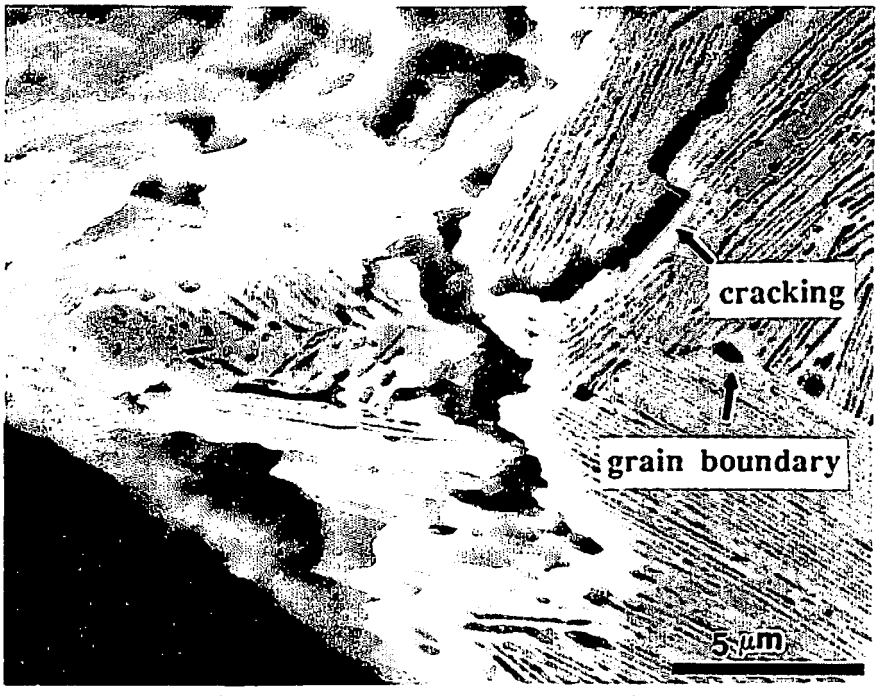



Figure 4-92. Secondary cracking along the lamellar plates and interface between lamellar structure and coarsened structure.

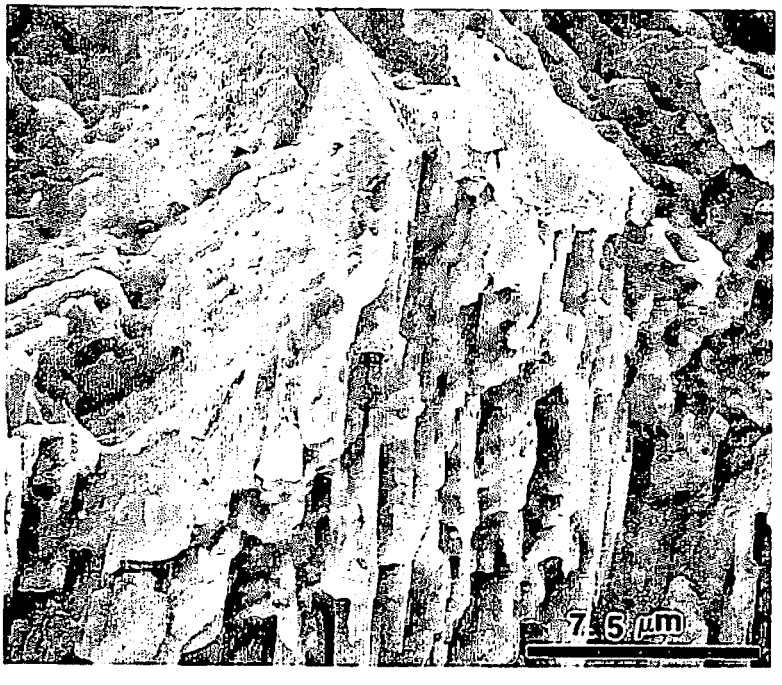



Figure 4-93. The fracture surface of 5 at.% Al alloy aged at 750°C for 100 hours.

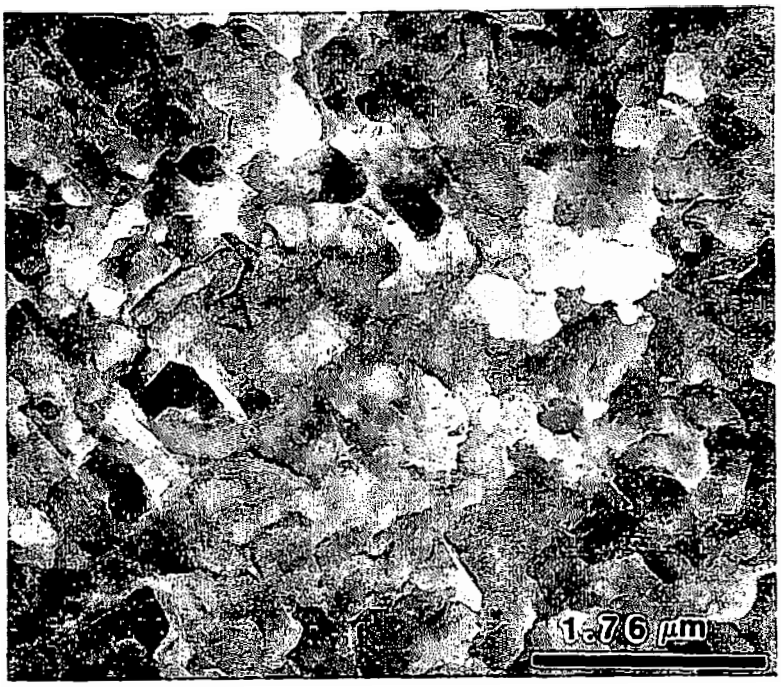



Figure 4-94. The fracture surface of 5 at.% Al alloy aged at 750°C for 100 hours.

bent surface is shown in Figure 4-95, where it is seen that cracking occurred in the region of original grain boundaries, but there was also transgranular cracking. Figure 4-96 shows that the cracks propagated by interphase separation and by cleavage across the phases. Along the original grain boundaries in some regions there is a slightly coarse structure, and fracture occurred by interphase separation in these regions (Figure 4-97). In the region of the untransformed matrix, extensive slip was observed on the etched surface (Figure 4-96 and 4-98), showing that these regions were ductile. Here the fracture surface appeared to be dimpled.

### 4.4.5. Fracture Surface Investigation of 9 at.% Al Alloy

The microstructure of the 9 at.% Al alloy showed a lamellar structure along the grain boundaries and in the grains. Figure 4-99a shows the microstructure and it is seen that cracking has occurred along the regions of the original grain boundaries. Cracking has also occurred in the lamellar structure within the grains (Figure 4-99b). Figures 4-100 and 4-101 show the fracture surface. EDS analyses are given in Figure 4-102, and 4-103. The light areas are mokybdenum-rich and dark areas nickel-rich. The bright area are probably the $\delta$. The dark area could be the $\gamma'$, as some aluminum is present. It is clear that fracture has occurred by interphase separation.

### 4.4.6. Comments about Fractography and Fracture

It is clear that when $\beta$ is present, the alloys are brittle with fracture occurring along the high angle, former $\alpha$ boundaries, whether migrated or not. When a multiphase structure forms, the alloys are brittle because of weak interphase bonding. Also the inability of the ordered phases to slip make them intrinsically brittle.

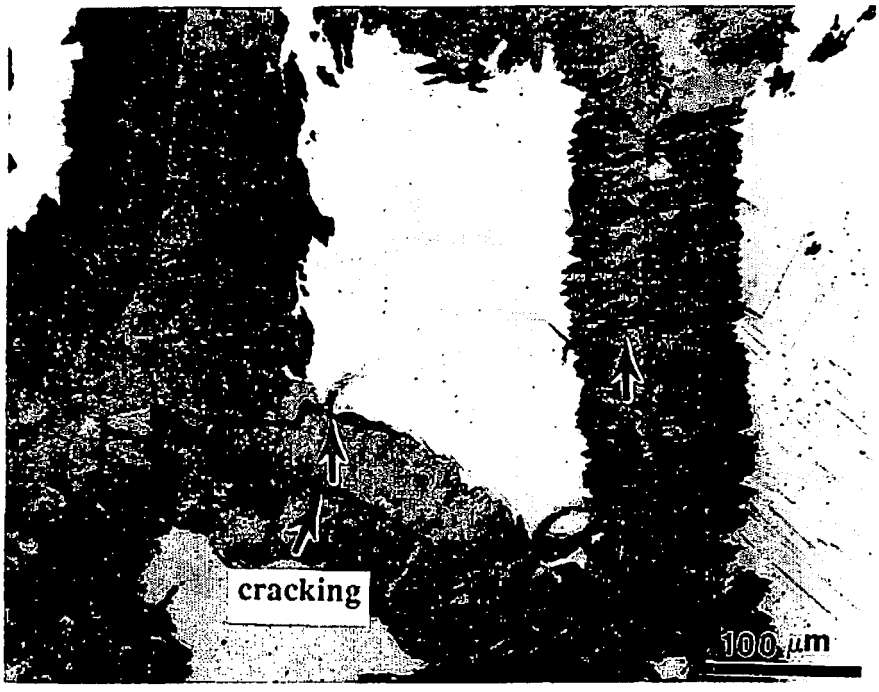



Figure 4-95. Intergranular and transgranular cracking in 7 at.% Al alloy aged at 750°C for 100 hours.

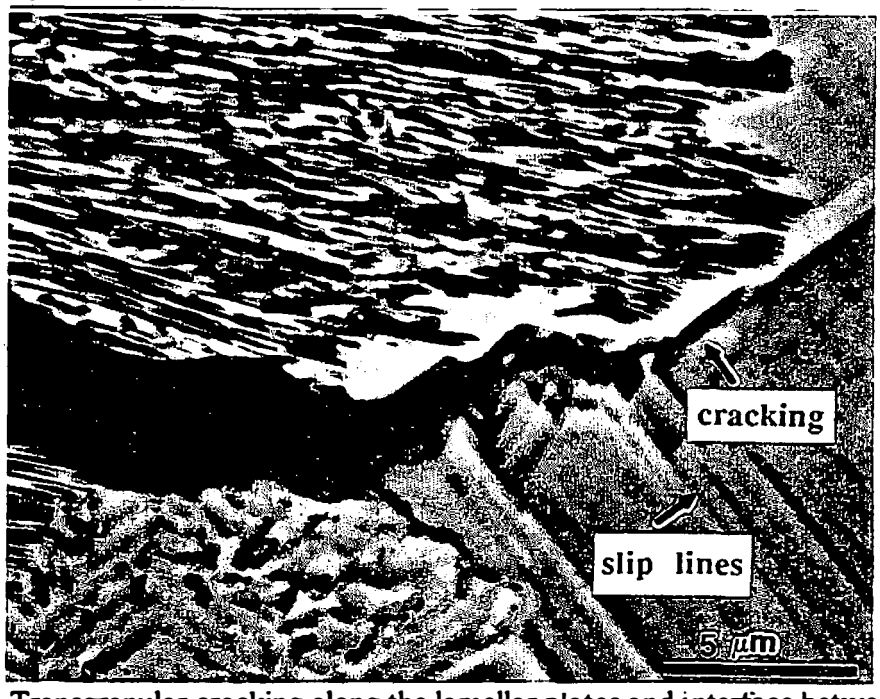



Figure 4-96. Transgranular cracking along the lamellar plates and interface between lamellar structure and matrix in 7 at.% Al alloy.

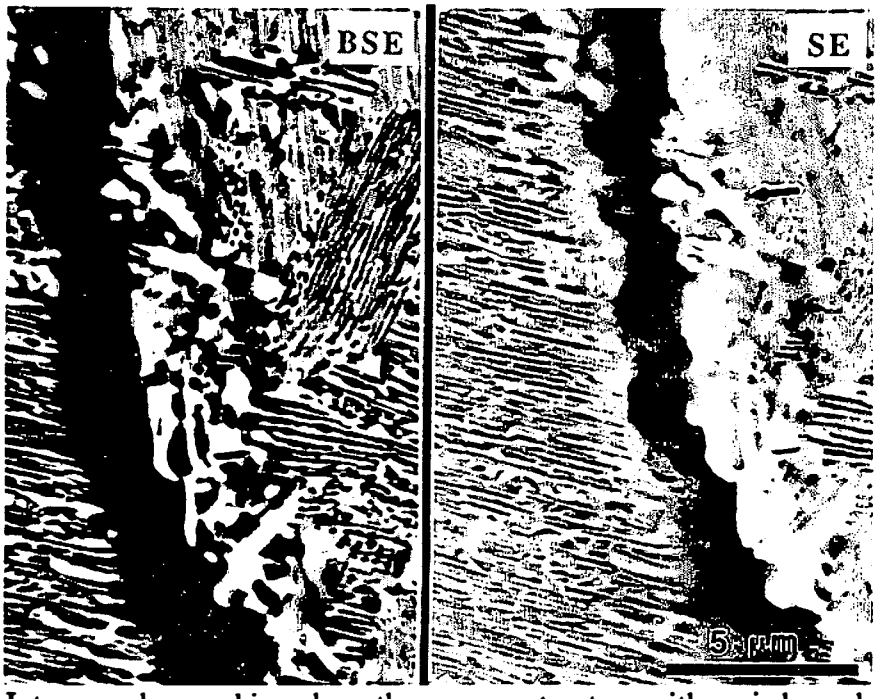



Figure 4-97 Intergranular cracking along the coarsen structure with grain boundaries in 7 at.% Al alloy.

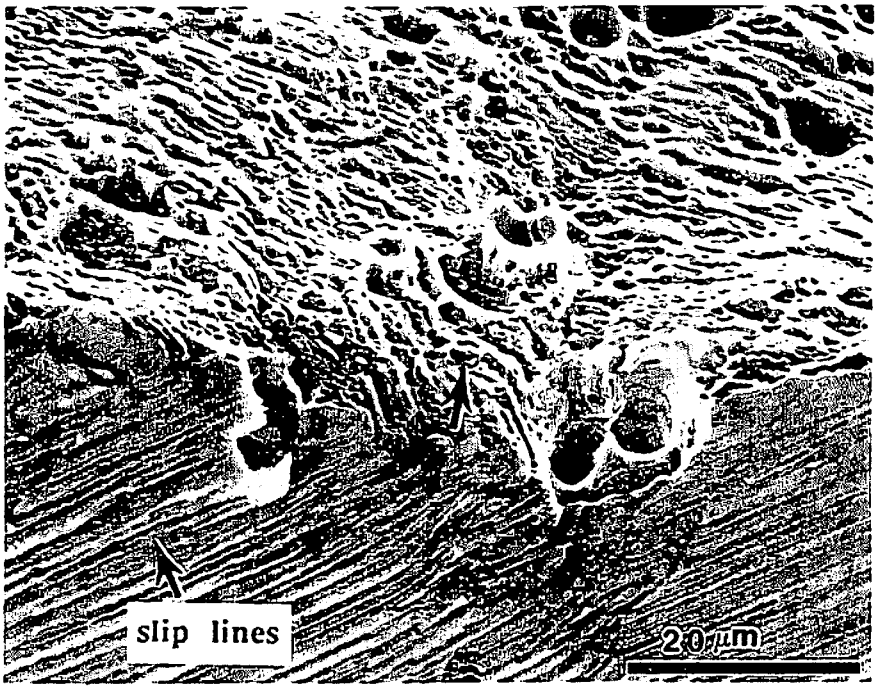



Figure 4-98. Dimple fracture morphology in matrix in 7 at.% Al alloy.

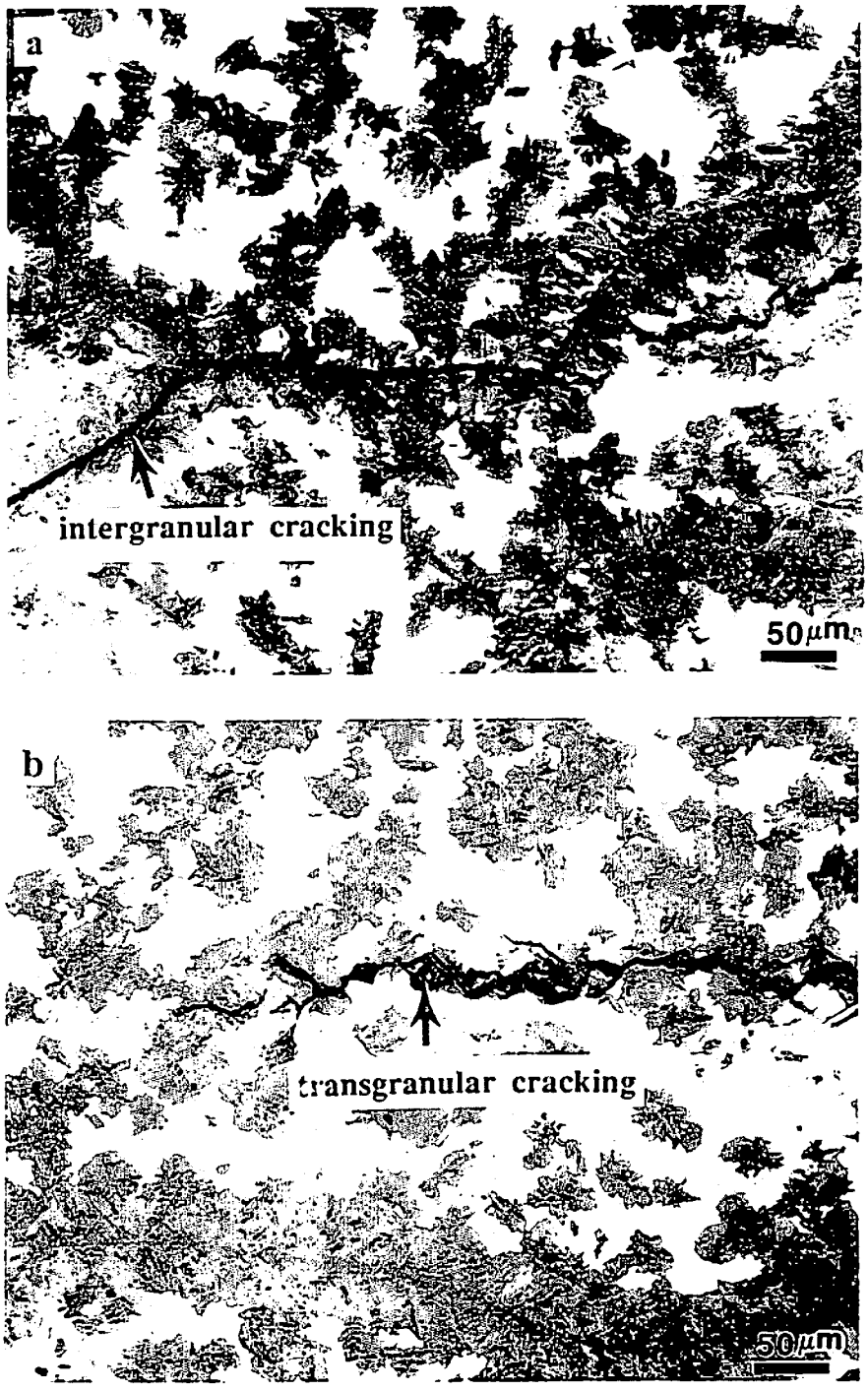



Figure 4-99. (a) Intergranular cracking , (b) Transgranular cracking in 9 at.% Al alloy aged at 750°C for 100 hours.




Figure 4-100. The fracture morphology (SE) of 9 at.% Al alloy aged at 750°C for 100 hours.




Figure 4-101. Backscattered electron image of 9 at.% Al alloy aged at 750°C for 100 hours.

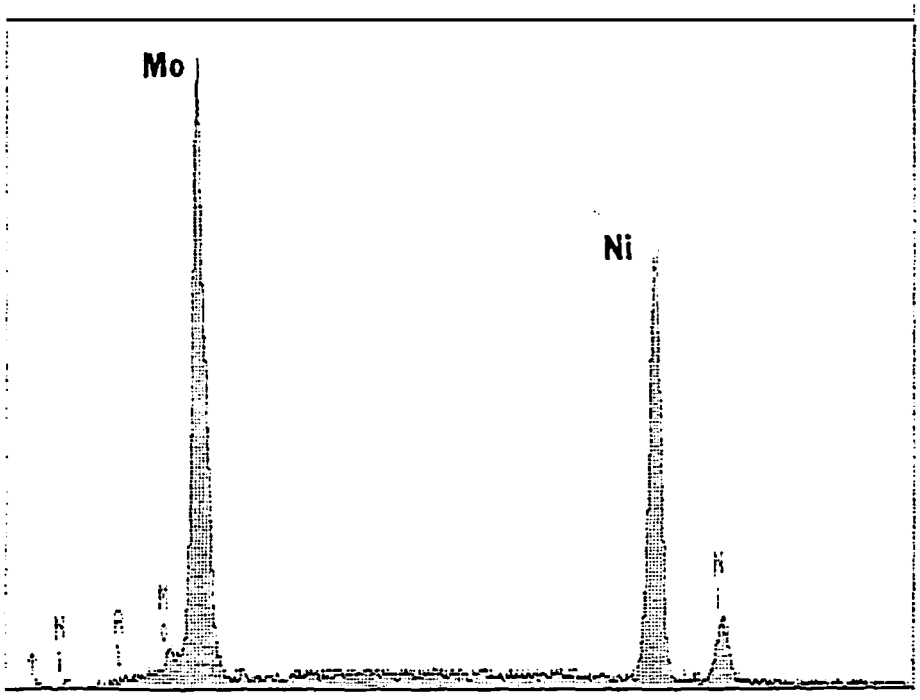



Figure 4-102. The EDS analysis from bright area, molybdenum-rich plates (see arrow A in Figure 4-101).

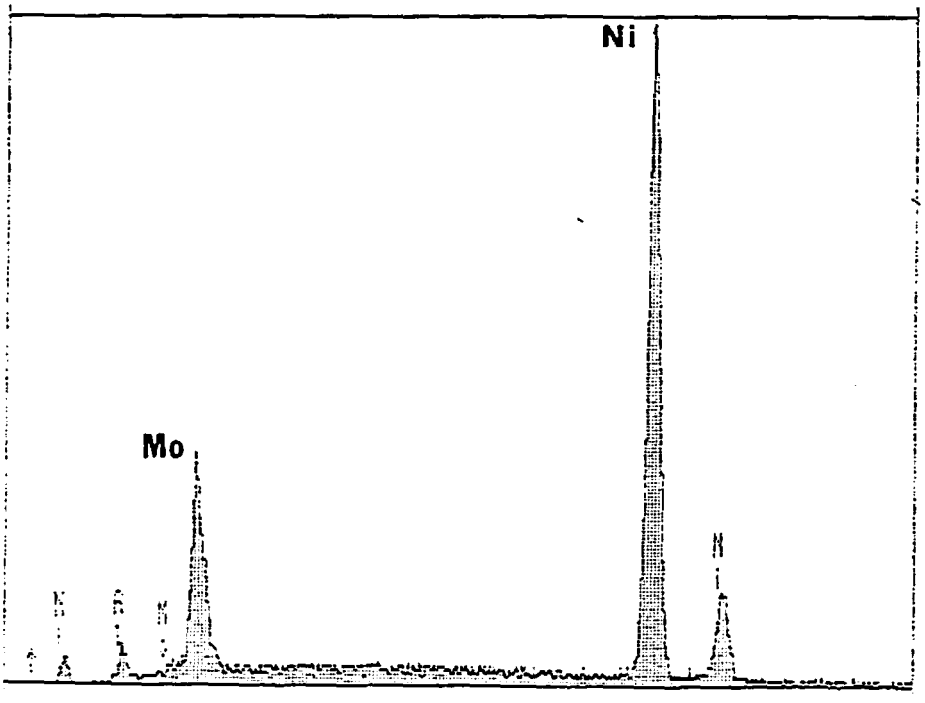



Figure 4-103. The EDS analysis from dark area, nickel-rich plates (see arrow B in Figure 4-101).

## 4.5. Transmission Electron Microscope (TEM) Microstructure and Electron Diffraction Pattern Analysis

In this section the TEM observation are presented and analyzed. The format in the previous sections detailing the OLM and SEM observations is followed. In addition, at the end of this chapter some observations of aged samples of the commercial alloy Hastelloy B2 are also given.

The SEM observations described in the previous section allowed resolution of the finer details than did the OLM observations. Also, the EDS analyses, even though qualitative, provided clues to the identity of the phases. However, in many cases there was sufficient uncertainty in interpreting the spectra to prevent rigorously establishing what the phase was. Also in many cases the structure was too fine for meaningful EDS analyses. To make positive identification, transmission electron microscopy was used where electron diffraction patterns could be obtained and analyzed, and in some cases quantitative EDS analysis could be obtained from the crystals. Thus not only could the finer details be resolved, their crystal structure and chemistry could be determined, and hence the phase identified.

In the Ni-Mo system, the high temperature equilibrium phase is $\alpha$, a face-centered cubic solid solution of molybdenum in nickel. However, the atom arrangements are not random, but the structure has short-range order (SRO). There are three intermetallic compounds: $\beta$ ($Ni_4Mo$); $\gamma$ ($Ni_3Mo$); $\delta$ (NiMo) (Figure 2-1). In addition, during the decomposition of $\alpha$ upon aging, two metastable phases have been found: the compound $Ni_2Mo$ ($Pt_2Mo$ prototype) and a compound with the $DO_{22}$ structure having $Ni_3Mo$ stoichometry. In the nickel-rich Ni-Mo-Al alloys, all these phases may form. In

addition, pure molybdenum may be present, and in the more aluminum-rich alloys, the γ' ($Ni_3Al$) may form where it will contain some molybdenum.

In this research, the identification of the phases by analyzing electron diffraction pattern has relied on obtaining patterns of specific orientation for which the patterns are already known for the phases. Especially convenient are the [001] and the [112] zone patterns, and they are shown in Figures 4-104 and 4-105. These patterns include multiple domain orientations and double diffraction. Some of the combined patterns are shown in Figure 4-106 [74, 75]. It was pointed out above that the α phase is SRO, which is responsible for weak spots at the locations shown in Figure 4-104 (a). All of these crystal structures can be characterized be the relative location of the nickel and molybdenum atoms on the face-centered cubic (FCC) lattice. Thus in the schematic electron diffraction patterns these common spots are referred to as the fundamental spots.

Another important point to remember is that a limitation of TEM observations is the very small area of the sample intrinsically being examined. In microstructures containing a heterogeneous structure, such as a lamellar structure in a single phase matrix, it may be difficult to prepare TEM samples which allow suitable thinning of all regions. That is, it may be that only the single phase region thins. Thus for the mixed microstructures which were examined in the OLM and SEM sections, it will be made clear what region are being examined in TEM.

### 4.5.1. TEM Microstructural Evaluation of Ni-Mo-Al Alloy After Solution Treated at 1250°C

a) $Ni_4Mo$ Alloy

The TEM microstructure of the $Ni_4Mo$ alloy after solution heat treated at 1250°C

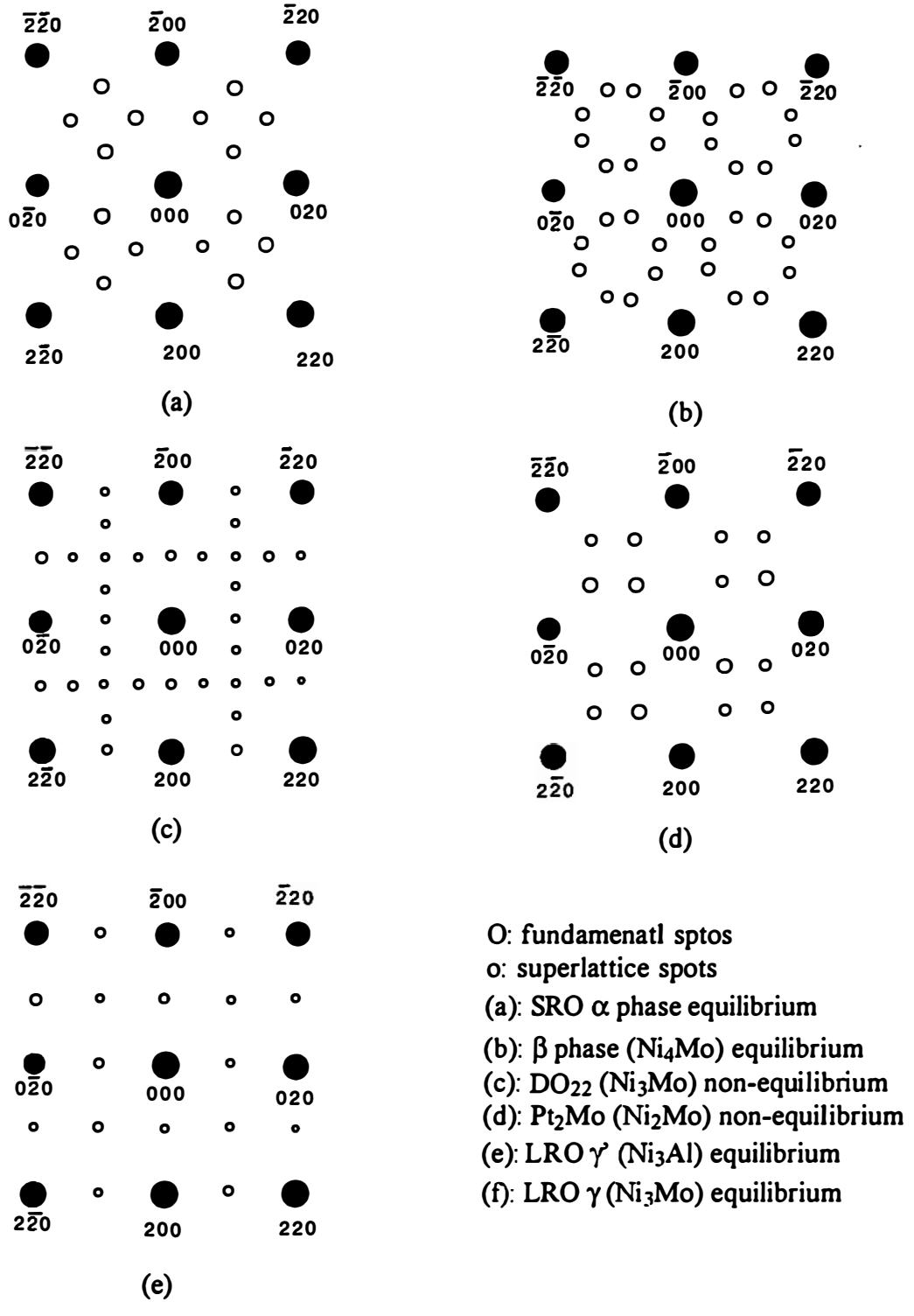
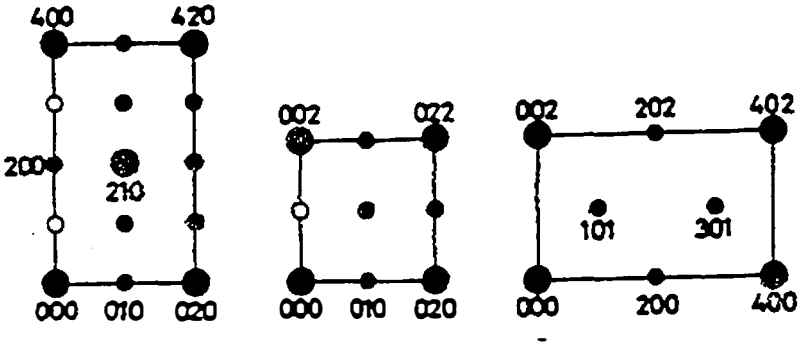



Figure 4-104. a) Schematic the [001] zone electron diffraction pattern for α, β, $DO_{22}$, $Ni_2Mo$, and γ' structure, b) diffraction pattern for γ phase.




Reciprocal lattice section of fully ordered $Ni_3Mo$. a) (001), (100) and (010) sections;

Ref. E. Ruedl and S. Amelinckx, " The Substructure of $Ni_3Mo$ due to Ordering," Mat. Res. Bull., 4:361-368 (1969).

Figure 4-104. continue (b).

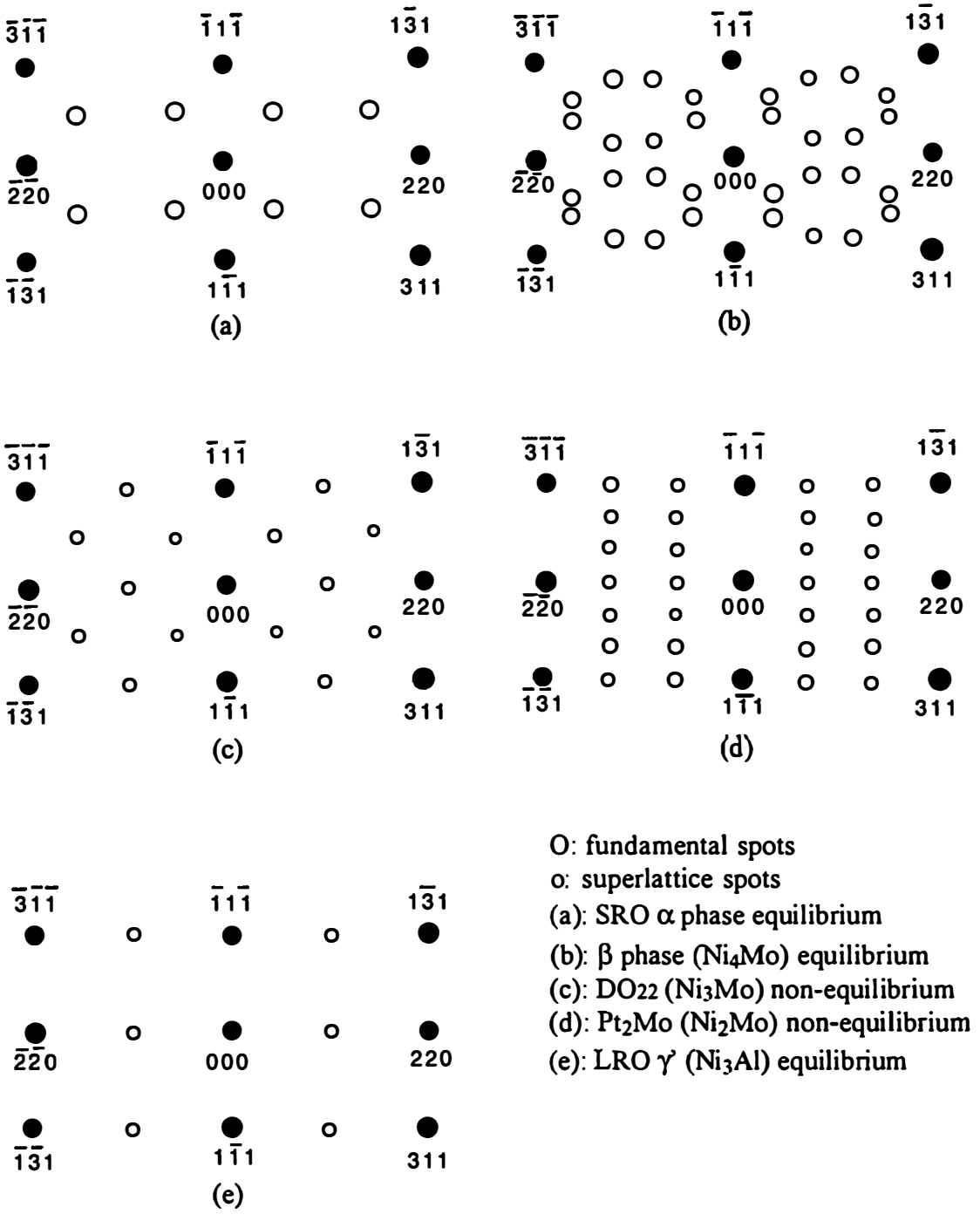



Figure 4-105. Schematic the [112] zone axis electron diffraction pattern for α, β, $DO_{22}$, $Ni_2Mo$, and γ' structure.

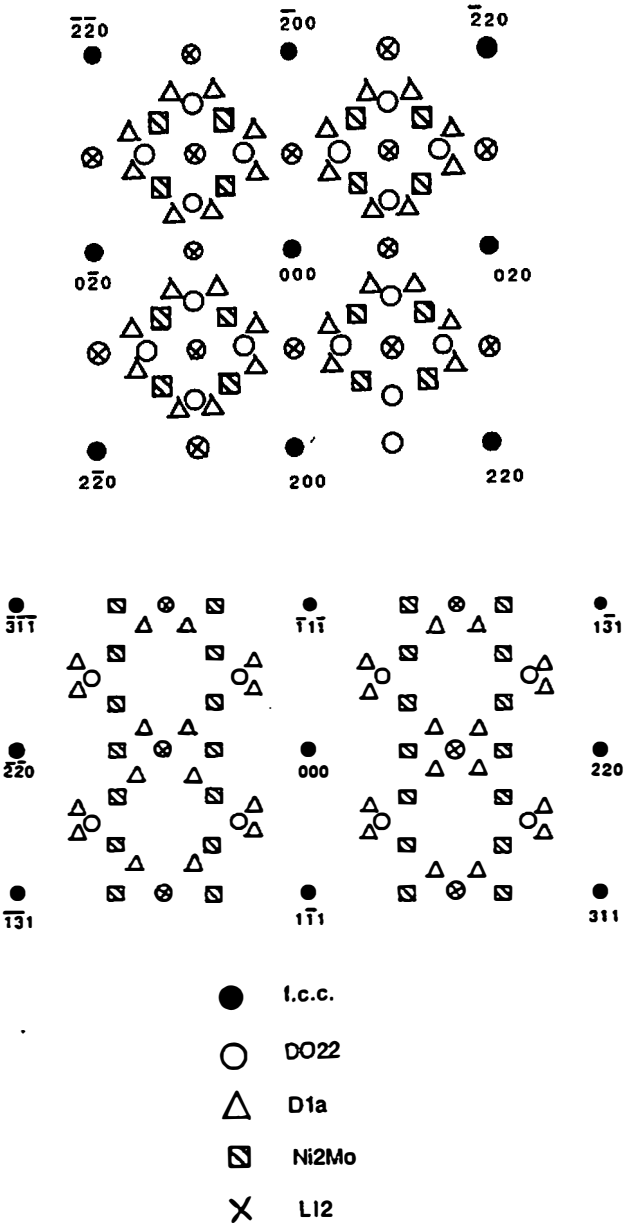



Figure 4-106. Schematic diffraction patterns showing the location of maxima for the f.c.c. fundamental lattice and the β, $DO_{22}$, $Ni_2Mo$ and γ' superlattices. (a) [001] zone, (b) [112] zone.

Ref. Martin and Williams, Long Range Order in Ni3Mo Based Ternary Alloys-I Isothermal Aging Response, Acta Metall., Vol. 32, 1984.

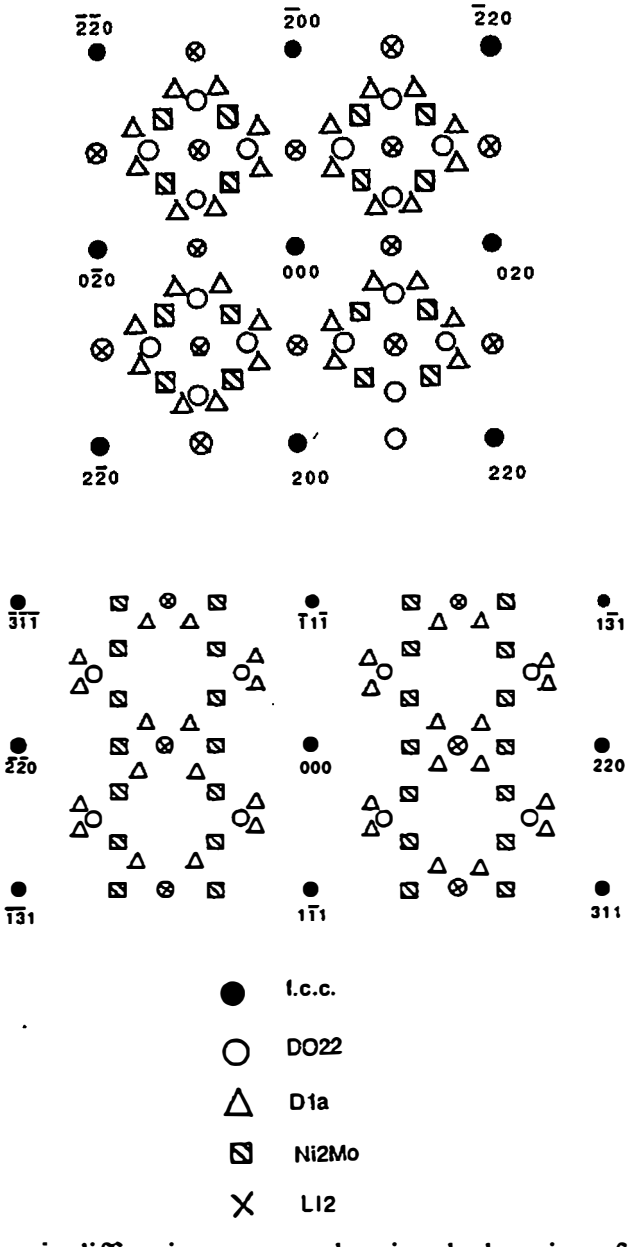



Figure 4-106. Schematic diffraction patterns showing the location of maxima for the f.c.c. fundamental lattice and the β, $DO_{22}$, $Ni_2Mo$ and γ' superlattices. (a) [001] zone, (b) [112] zone.

Ref. Martin and Williams, Long Range Order in $Ni_3Mo$ Based Ternary Alloys-I Isothermal Aging Response, Acta Metall., Vol. 32, 1984.

for 50 hours is presented in Figure 4-107a. There is a relatively high density of dislocation pile-ups adjacent to the grain boundary. The electron diffraction patterns (Figure 4-107, b and c) contains weak spots (arrow), which is characteristic of the SRO structure as shown in the [001] zone (Figure 4-104a) and in the [112] zone diffraction pattern in Figure 4-104b. Hence, a fully SRO $\alpha$ phase was obtained after a solution treatment and quenching from 1250°C.

b) 2 at.% Al Alloy

Figure 4-108a shows the TEM microstructure in the 2 at.% Al alloy. The microstructure shows a fine contrast structure, dislocations and intrinsic stacking faults. However, the [001] zone electron diffraction pattern (Figure 4-108b) shows the intensity maxima at SRO $\alpha$ spots with faint intensity at $DO_{22}$ position spots (Figure 4-104c). Thus the quenched structure is not single phase $\alpha$, but also contains the non-equilibrium $DO_{22}$ phase. Thus there was concern that the cooling rate during quenching the sample while breaking the quartz tube was not sufficient to retain only the $\alpha$ phase. In order to confirm that the $DO_{22}$ phase formed during quenching, an unprotected (not encapsulated in a quartz tube) sample of the 2 at.% Al alloy was heated in air to 1250°C for 20 minutes, than rapidly quenched directly in water. The diffraction pattern in Figure 4-109a shows only SRO $\alpha$ spots; there is no evidence of the $DO_{22}$ structure.

The important point here is that is some alloys the quenched structure, which is the starting structure for the aging treatments, may contain both SRO $\alpha$ and $DO_{22}$ phase. This could not be determined form the OLM and SEM observations, where the microstructure appeared to be single phase $\alpha$ and in some cases was referred to as such.

Hardness of 2 at.% Al alloy increased slightly compared to $Ni_4Mo$ alloy, that is, the hardness of the $DO_{22}$ and SRO $\alpha$ structure is greater than that of SRO $\alpha$ structure.

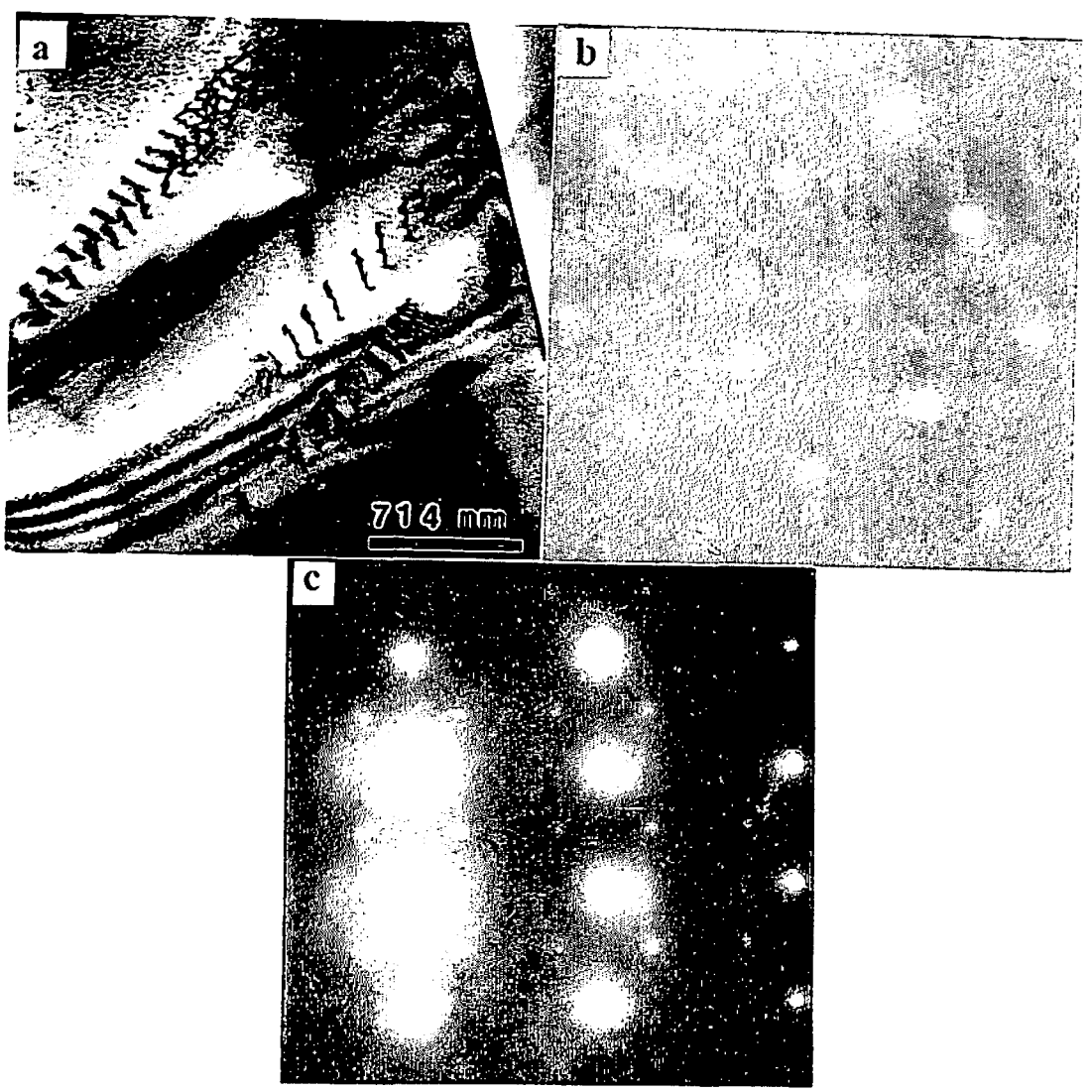



Figure 4-107. TEM microstructure of $Ni_4Mo$ alloy solution treated at 1250°C for 50 hours. a) SRO α phase with dislocations pile-ups at grain boundary. b) corresponding [001] zone diffraction pattern, c) [112] zone.

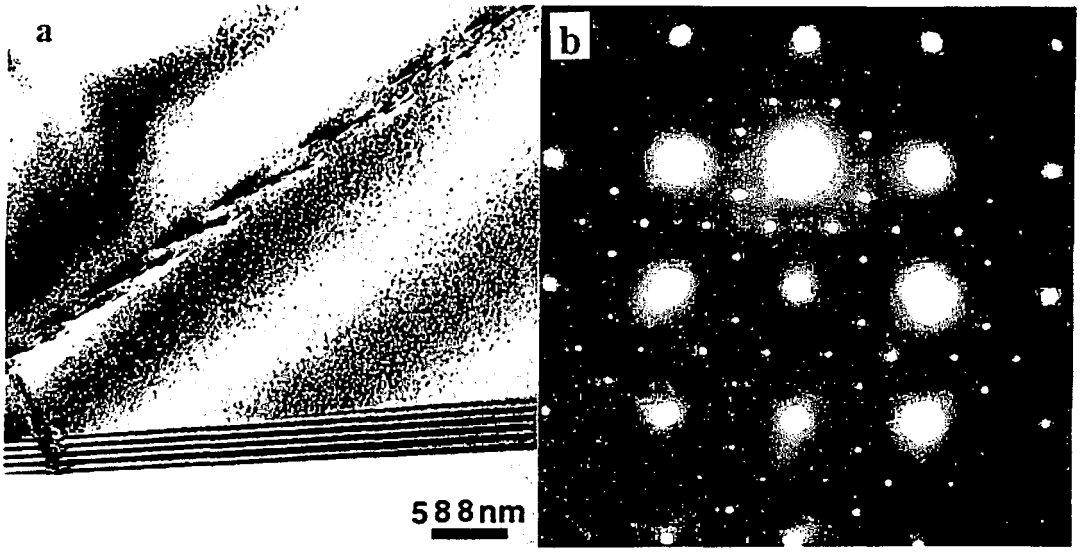



Figure 4-108. TEM microstructure of 2 at.% Al alloy solution treated at 1250°C for 50 hours. a) $DO_{22}$ precipitates in SRO $\alpha$ phase matrix and dislocations pile-ups at grain boundary with stacking faults. b) corresponding [001] zone diffraction pattern.

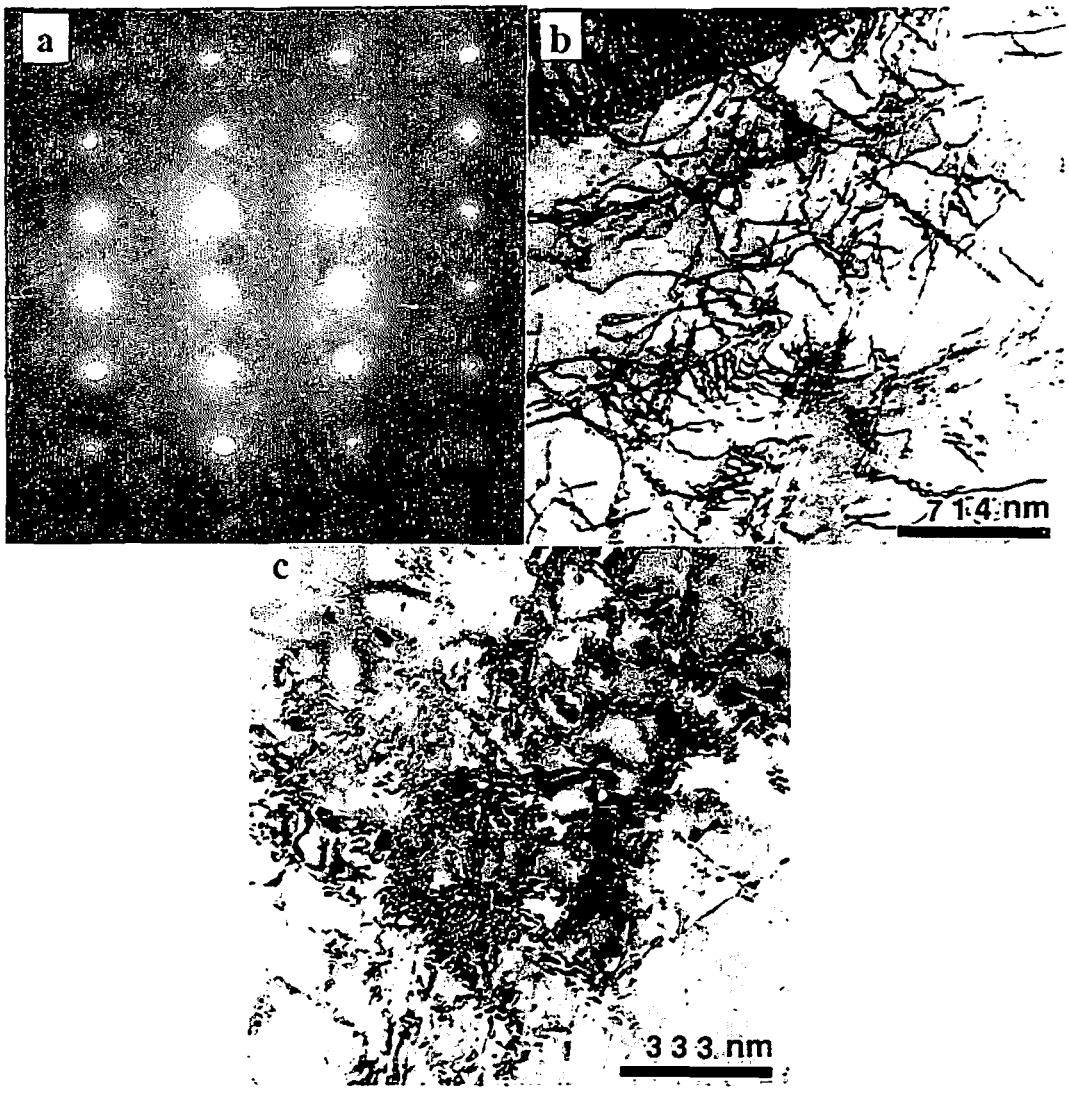



Figure 4-109. TEM microstructure of 2 at.% Al alloy solution treated at 1250°C for 20 minutes. a) [112] zone diffraction pattern showing SRO α superlattice spots. b) and c) SRO α phase and dense dislocations.

c) 5 at.% Al Alloy

In 5 at.% Al alloy, the [112] zone electron diffraction pattern shows intensity maxima at {1 1/2 0}, {100}, and {110} positions (Figure 4-110a) of the $DO_{22}$ structure. The SRO $\alpha$ spots overlaps the $DO_{22}$ spots in the [112] zone diffraction pattern. From the [112] zone diffraction pattern, it is not clear that SRO $\alpha$ is present or not. However, the $DO_{22}$ phase is present. The $DO_{22}$ phase formation may be due to slow cooling or the aluminum enhanced the rate of formation of the $DO_{22}$ phase. The $DO_{22}$ domain structure and intrinsic stacking faults is shown in Figure 4-110b.

d) 7 at.% Al Alloy

In the 7 at.% Al alloy, the [001] and [112] diffraction patterns (Figure 4-111, a and b) show spots for the $DO_{22}$ phase and the $Ni_2Mo$ phase. There are no SRO $\alpha$ spots. Thus upon quenching the $\alpha$ phase decomposed to a fine structure of these two phases (Figure 4-111c). The OLM and SEM microstructure showed what appeared to be only a single phase. The hardness increased considerably in comparison to that of the SRO $\alpha$ phase in the $Ni_4Mo$ alloy and the 2 at.% Al alloy (Figure 4-1).

e) 9 at.% Al Alloy

In the 9 at.% Al alloy, the [112] electron diffraction pattern (Figure 4-112a) had spots at the $Ni_2Mo$ and $DO_{22}$ positions, but not SRO $\alpha$ spots. Thus, the microstructure (Figure 4-112, b and c) consists of a fine mixture of domains of these two phases. Note that the structure is coarse in the 9 at.% Al alloy than in the 7 at.% Al alloy (Figure 4-111c), but the hardness was somewhat higher than for the 7 at.% Al alloy (Figure 4-1).

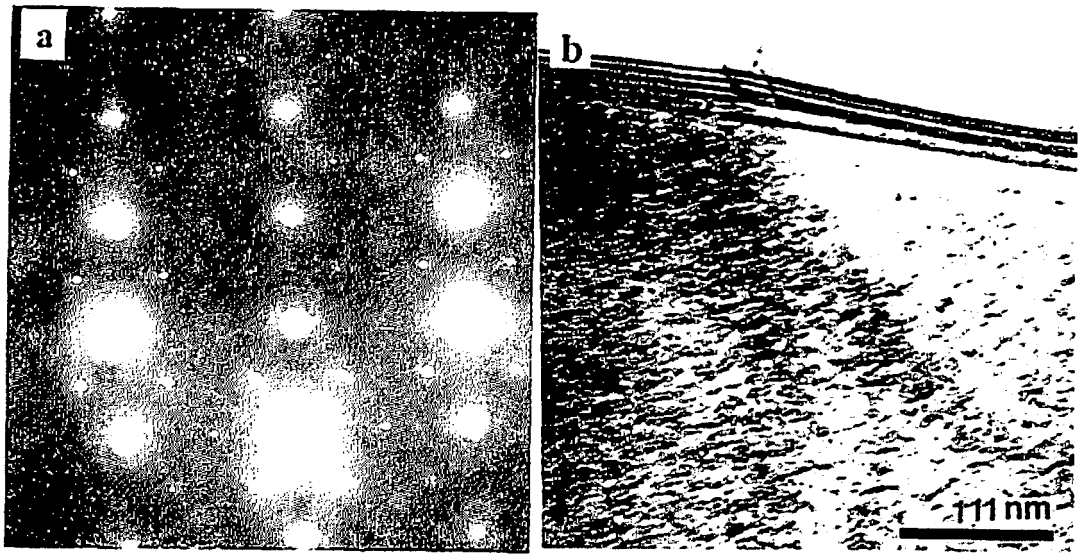



Figure 4-110. TEM microstructure of 5 at.% Al alloy solution treatment at 1250°C for 50 hours. a) the [112] zone diffraction pattern showing $DO_{22}$ superlattice spots. b) corresponding microstructure and stacking faults.

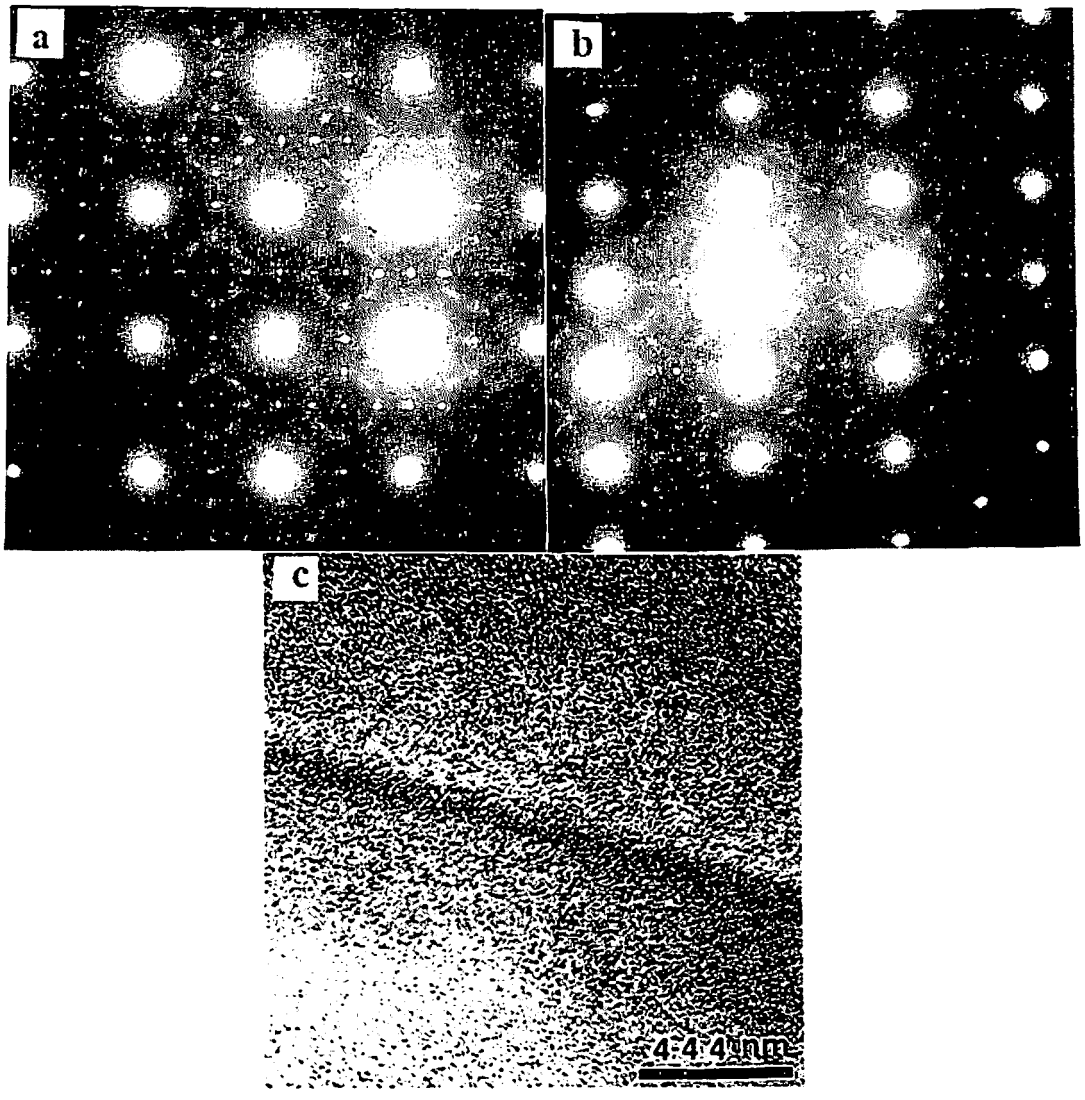



Figure 4-111. TEM microstructure of 7 at.% Al alloy solution treated at 1250°C for 50 hours. a) and b) [001] and [112] zone diffraction pattern showing $DO_{22}$ and $Ni_2Mo$ superlattice spots. c) corresponding microstructure of uniform $DO_{22}$ and $Ni_2Mo$ phases at [112] zone.

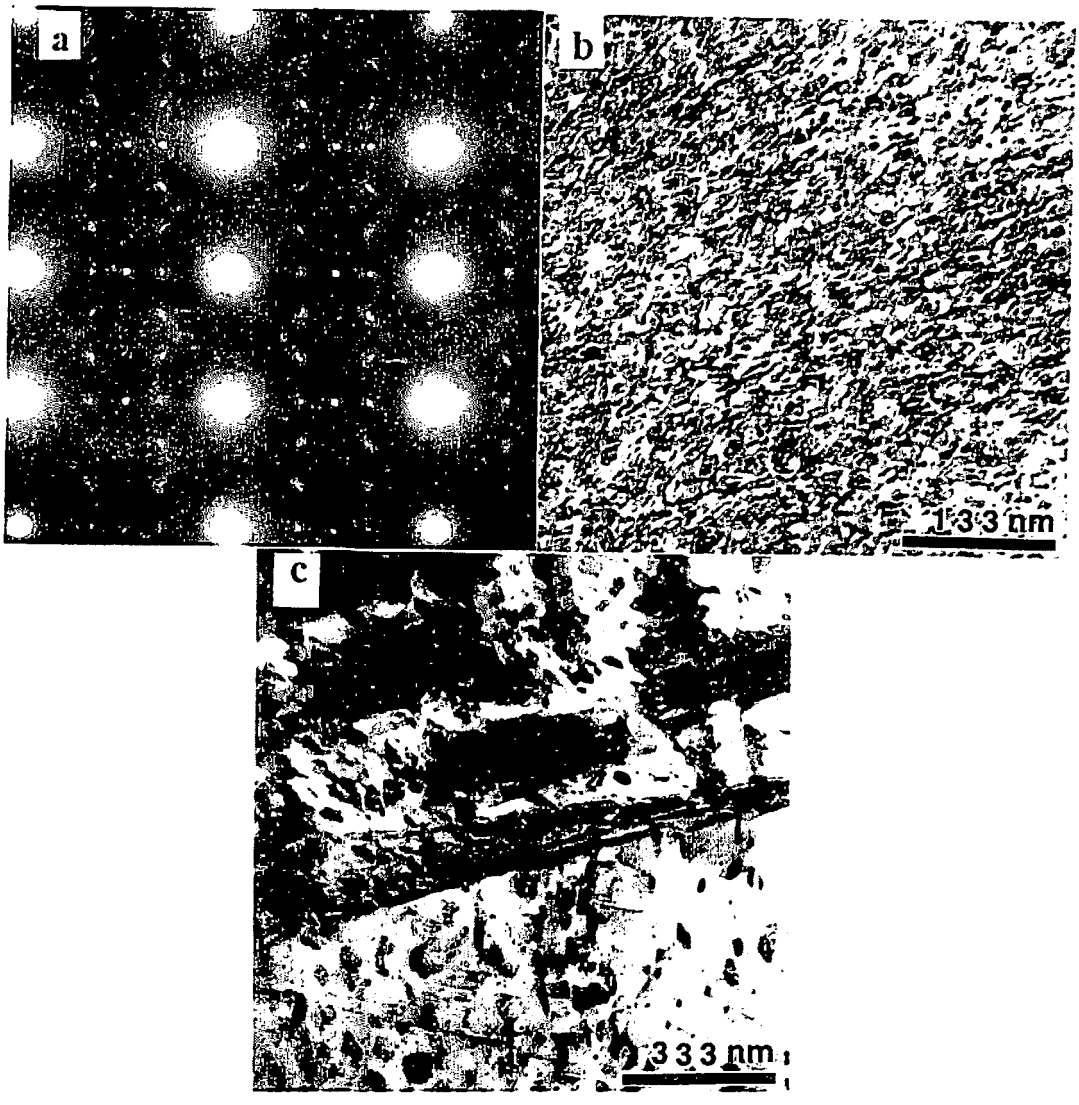



Figure 4-112. TEM microstructure of 9 at.% Al alloy solution treated at 1250°C for 50 hours. a) [112] zone diffraction pattern showing $DO_{22}$ and $Ni_2Mo$ superlattice spots, b) corresponding microstructure, c) particles and stacking faults in matrix.

f) Summary

The structure present after the solution heat treatment of 50 hours at 1250°C, followed by water quenching (by breaking the quartz tubes), is summarized in Table 4-3. The evidence is that the restricted cooling upon breaking the quartz tube prevented the retention of all SRO α. As the aluminum content increased, the kinetics of the decomposition of SRO α to the $DO_{22}$, and then a mixture of the $DO_{22}$ and $Ni_2Mo$ phases, was etchanced. Note that these domain structure are the precursor structure for the aging treatments.

Figure 4-1 shows that the hardness of the $Ni_4Mo$ alloy and the 2 and 5 at.% Al alloy are about the same. There is a marked increase in hardness upon the addition of 7 and 9 at.% Al, which coincides with the appearance of the fine domain structure containing both the $DO_{22}$ and the $Ni_2Mo$ phase, although the domain structure for the 9 at.% Al alloy is more coarse than that in the 5 at.% Al alloy.

Table 4-3. The microstructure of Ni-Mo-Al alloys after solution heat treated (1250°C, 50 hours) and water quenched

| | $Ni_4Mo$ | 2 at.% Al | 5 at.% Al | 7 at.% Al | 9 at.% Al |
|---|---|---|---|---|---|
| as-quenched | SRO α | SRO α + $DO_{22}$ | SRO α ? + $DO_{22}$ | $DO_{22}$ + $Ni_2Mo$ | $DO_{22}$+ $Ni_2Mo$ |

## 4.5.2. TEM Microstructural Evaluation of Ni-Mo-Al Alloys After Solution Treated at 1280°C and Aged at 600°C for 100 Hours

a) 2 at.% Al Alloy

Figures 4-113, a and b give the [001] and [112] zone electron diffraction patterns which shows SRO α and β superlattice spots at a intermediate transformation step of

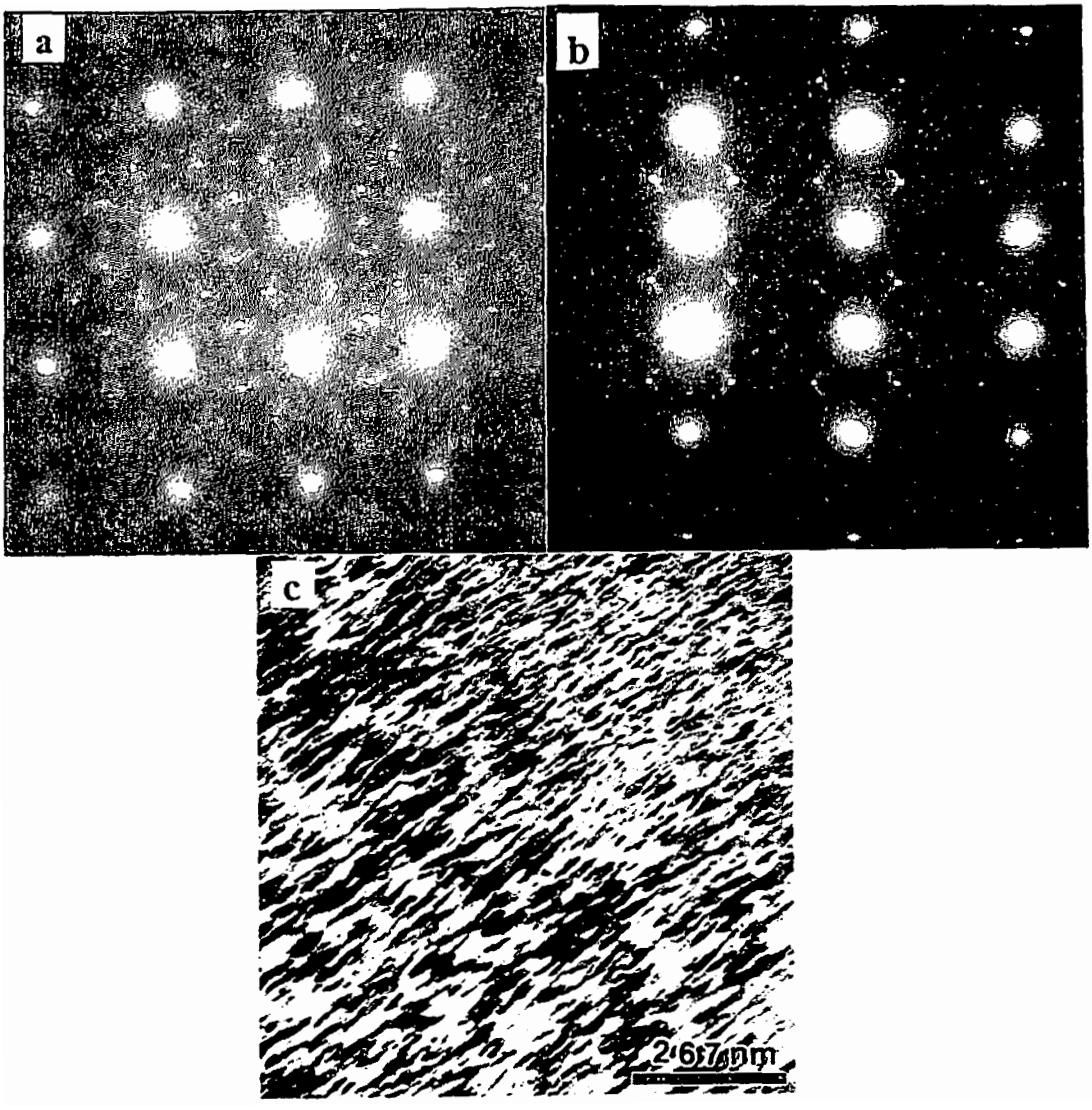



Figure 4-113. TEM microstructure of 2 at.% Al alloy aging at 600°C for 100 hours. a) [001] zone diffraction pattern showing SRO α, LRO β and $DO_{22}$ superlattice spots, b) [112] zone diffraction pattern showing SRO α, LRO β and $DO_{22}$ superlattice spots, c) corresponding microstructure of the [112] zone diffraction pattern.

SRO α to LRO β. Also the $DO_{22}$ diffraction spots are present. The intensity of the SRO reflections remains stronger than that of $DO_{22}$ and β. Diffuse streaking in the {4 2 0} direction is seen to extend between β and $DO_{22}$ superlattice positions. Thus, the microstructure corresponds to a fine structure of the α, β and $DO_{22}$ phases.

b) 5 at.% Al Alloy

Figure 4-114a shows the microstructure of 5 at.% Al alloy after aging for 100 hours at 600°C. There is a fine structure. Figure 4-114b shows the [001] zone diffraction pattern. There is clear evidence of the presence of the $DO_{22}$ phase. No SRO α or β were observed.

c) 7 at.% Al Alloy

In 7 at.% Al alloy, after aging at 600°C for 100 hours, the [112] zone diffraction pattern shows intensity maxima at $DO_{22}$ and $Ni_2Mo$ positions (Figure 4-115a). The fine microstructure contains two phases of $DO_{22}$ and $Ni_2Mo$ as shown in Figure 4-115b.

d) 9 at.% Al Alloy

After aging at 600°C for 100 hours, the microstructure in 9 at.% Al alloy formed a fine structure (Figure 4-116a). The [112] zone selected area diffraction pattern shows $DO_{22}$ and $Ni_2Mo$ superlattice spots (Figure 4-116b). The 2, 5, and 7 at.% Al alloy had no other phases than the fine structure revealed by TEM, as shown in the OLM in Figure 4-21 to 4-23. However, the 9 at.% Al alloy had begun to form a lamellar structure (Figure 4-24) It is clear, though, that the local region of the TEM observations (Figure 4-116) was in the matrix.

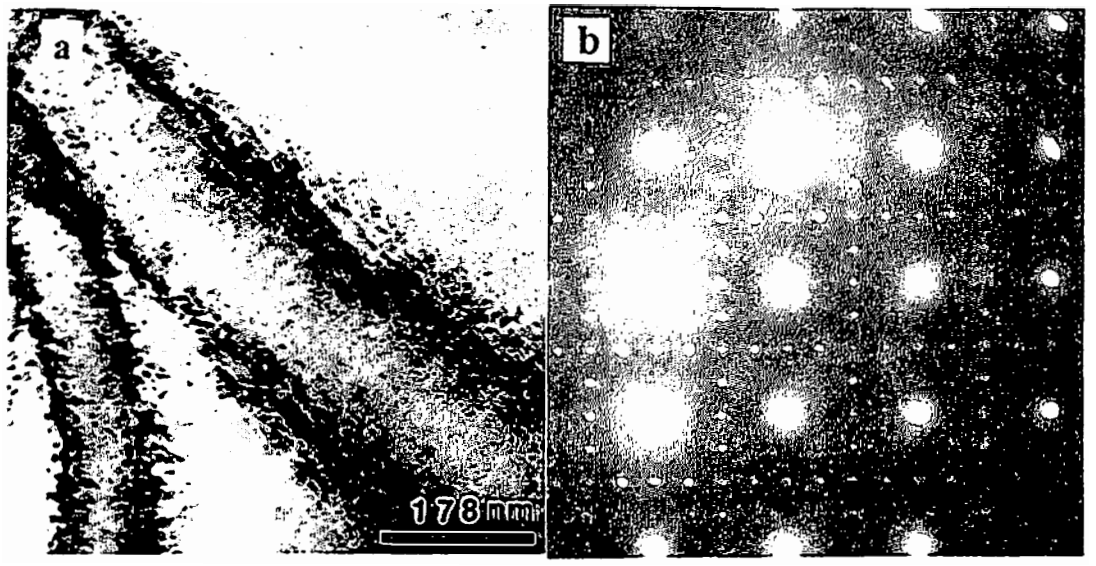



Figure 4-114. TEM microstructure of 5 at.% Al alloy aged at 600°C for 100 hours, a) $DO_{22}$ phase, b) corresponding [001] zone diffraction pattern.

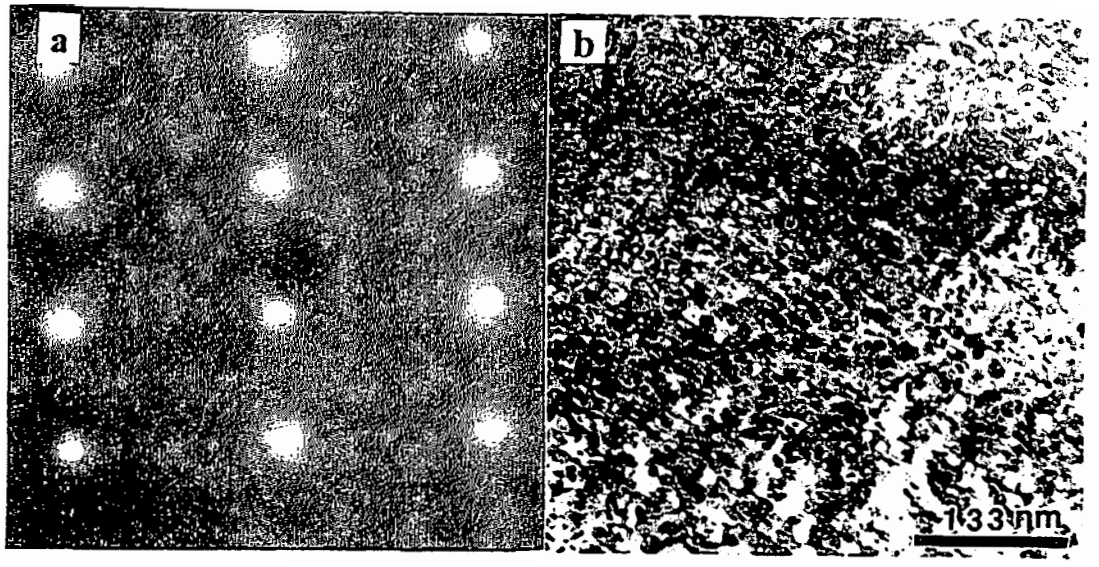



Figure 4-115. TEM microstructure of 7 at.% Al alloy aged at 600°C for 100 hours, a) [112] zone diffraction pattern showing $DO_{22}$ and $Ni_2Mo$ superlattice spots, b) corresponding microstructure of $DO_{22}$ and $Ni_2Mo$ phases.

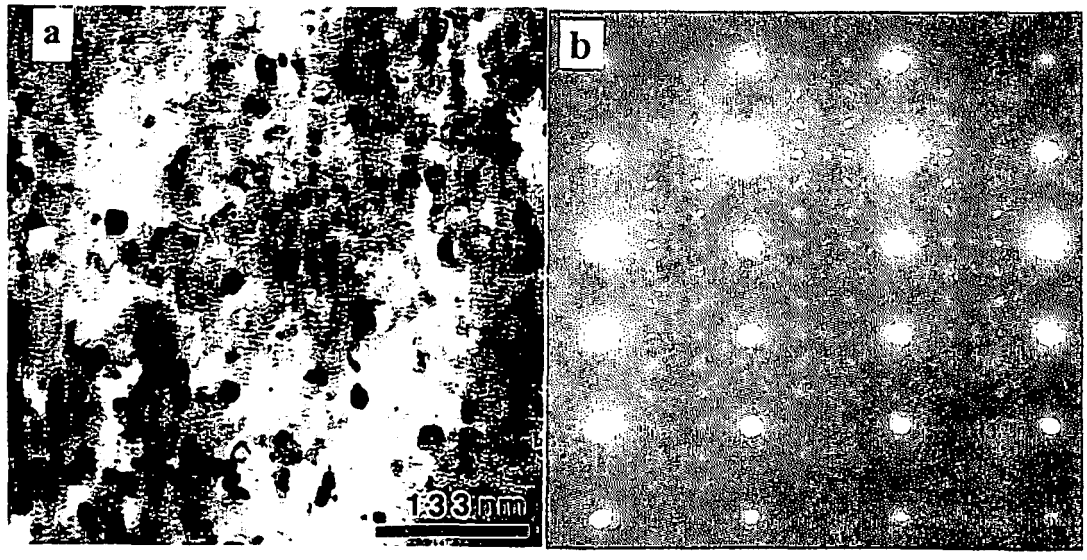



Figure 4-116. TEM microstructure of 9 at.% Al alloy aged at 600°C for 100 hours, a) microstructure of $DO_{22}$ and $Ni_2Mo$ phases, b) corresponding [112] zone diffraction pattern.

e) Summary

The structures present after aging at 600 °C for 100 hours are summarized in Table 4-4. The 2 at.% Al alloy has begun to from the β phase, but both α and $DO_{22}$ are still present. In the 5, 7, and 9 at.% Al alloys, the same structure is present as in the as-quenched condition. In all cases, the structure has not coarsened appreciably.

Table 4-4. The microstructure of Ni-Mo-Al alloys aged at 600°C.

| | $Ni_4Mo$ | 2 at.% Al | 5 at.% Al | 7 at.% Al | 9 at.% Al |
|---|---|---|---|---|---|
| as-quenched | SRO α | SRO α + $DO_{22}$ | SRO a ? + $DO_{22}$ | $DO_{22}$ + $Ni_2Mo$ | $DO_{22}$ + $Ni_2Mo$ |
| aged at 600°C | – | α + β + $DO_{22}$ | $DO_{22}$ | $DO_{22}$ + $Ni_2Mo$ (matrix) | $DO_{22}$ + $Ni_2Mo$ (matrix) |

4.5.3. TEM Microstructural Evaluation of Ni-Mo-Al Alloys After Solution Treated at 1280°C and Aged at 650°C for 100 Hours

a) $Ni_4Mo$ Alloy

The microstructure of the $Ni_4Mo$ alloy after aging at 650°C consisted entirely of fine β domains (Figure 4-117). This structure is in general agreement with other research on the binary alloy [76-80]. A considerable hardness increase accompanied the formation of the β structure (Figure 4-1).

b) 2 at.% Al Alloy

In OLM, the microstructure if the 2 at.% Al alloy appeared single phase (Figure 4-26). Figure 4-118 shows a microstructure of fine domains, and the diffraction pattern

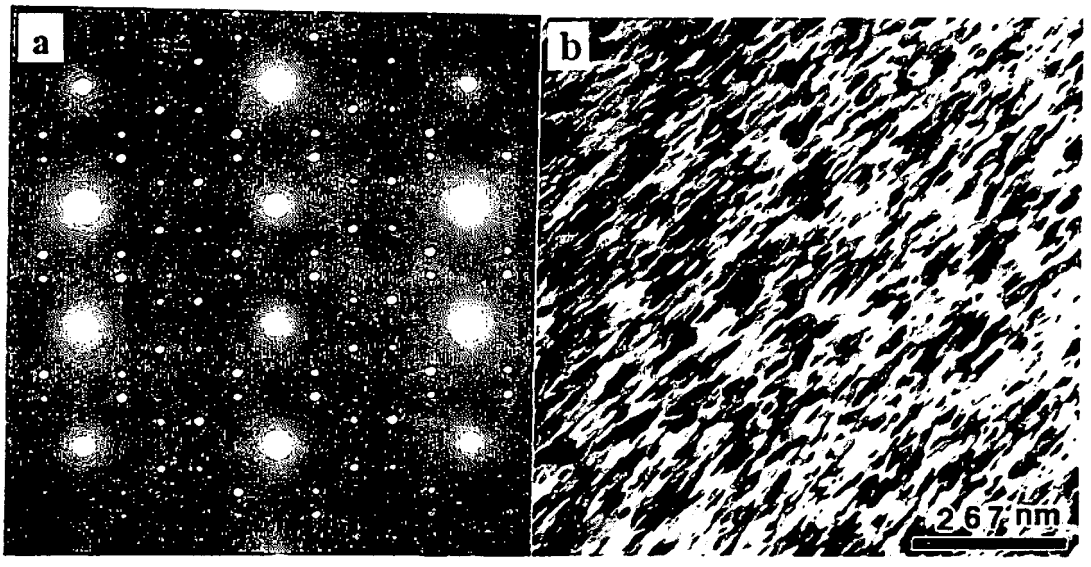



Figure 4-117. TEM microstructure of $Ni_4Mo$ alloy aged 650°C for 100 hours, a) [112] zone diffraction pattern showing β superlattice spots, b) corresponding microstructure of β phase.

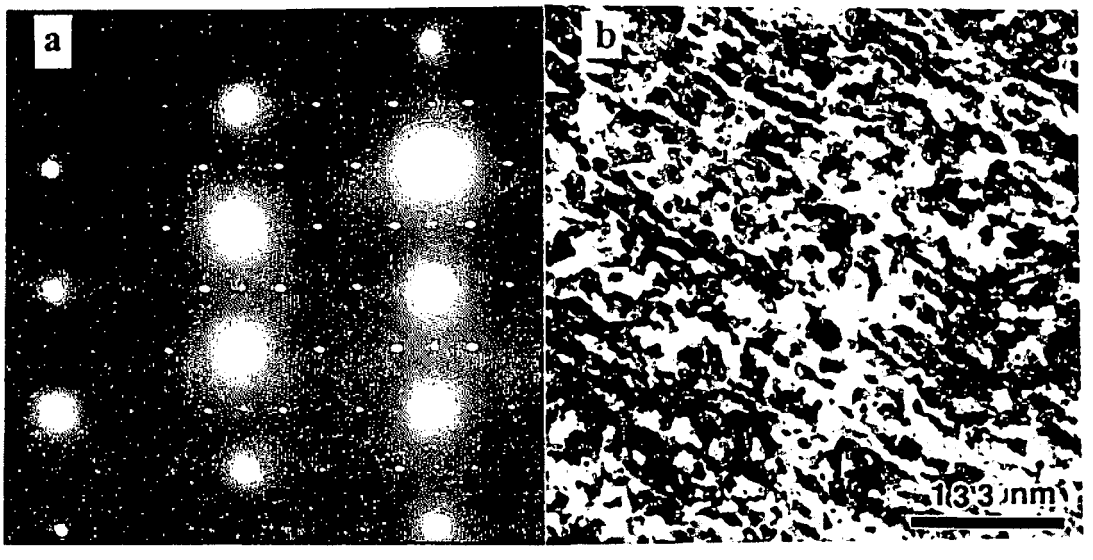



Figure 4-118. TEM microstructure of 2 at.% Al alloy aged at 650°C for 100 hours, a) diffraction pattern at the [321] zone, b) corresponding microstructure of $DO_{22}$ and α phases.

shows LRO spots. However, the pattern was not indexed. The hardness increased from the as-quenched value (Figure 4-3).

c) 5 at.% Al Alloy

The 5 at.% Al alloy had formed a considerable amount of a lamellar structure (Figure 4-27) in the matrix. Figure 4-119b shows a fine domain structure of the matrix, and the electron diffraction pattern from this region shows $DO_{22}$ and $Ni_2Mo$ (weak) spots (see arrow). Figure 4-119c shows the microstructure of the lamellar structure, but its identification is discussed later.

d) 7 at.% Al Alloy

The microstructure of the 7 at.% Al alloy showed mostly an apparent single phase matrix, with some grain boundary lamellar structure (Figure 4-28). Figure 4-120b shows that the matrix consists of fine domains, and the diffraction pattern identifies these as the $DO_{22}$ and $Ni_2Mo$ phases. Figure 4-120c shows the lamellar structure, and the associated diffraction pattern is in Figure 4-120d. The identification of this lamellar structure is discussed later.

e) Summary

Table 4-5 summarizes the structures after aging 650°C. In the 5 at.% Al alloy, in the matrix the initial $DO_{22}$ structure has formed some $Ni_2Mo$, and a lamellar structure also formed. In the 7 at.% Al alloy, the matrix still contained only the $DO_{22}$ and $Ni_2Mo$ phases, and a lamellar structure formed. The hardness is about the same for the 2 at.% Al alloy, but increases considerably for the 5 and 7 at.% Al alloys (Figure 4-3), which corresponds to the appearance of the lamellar structure.

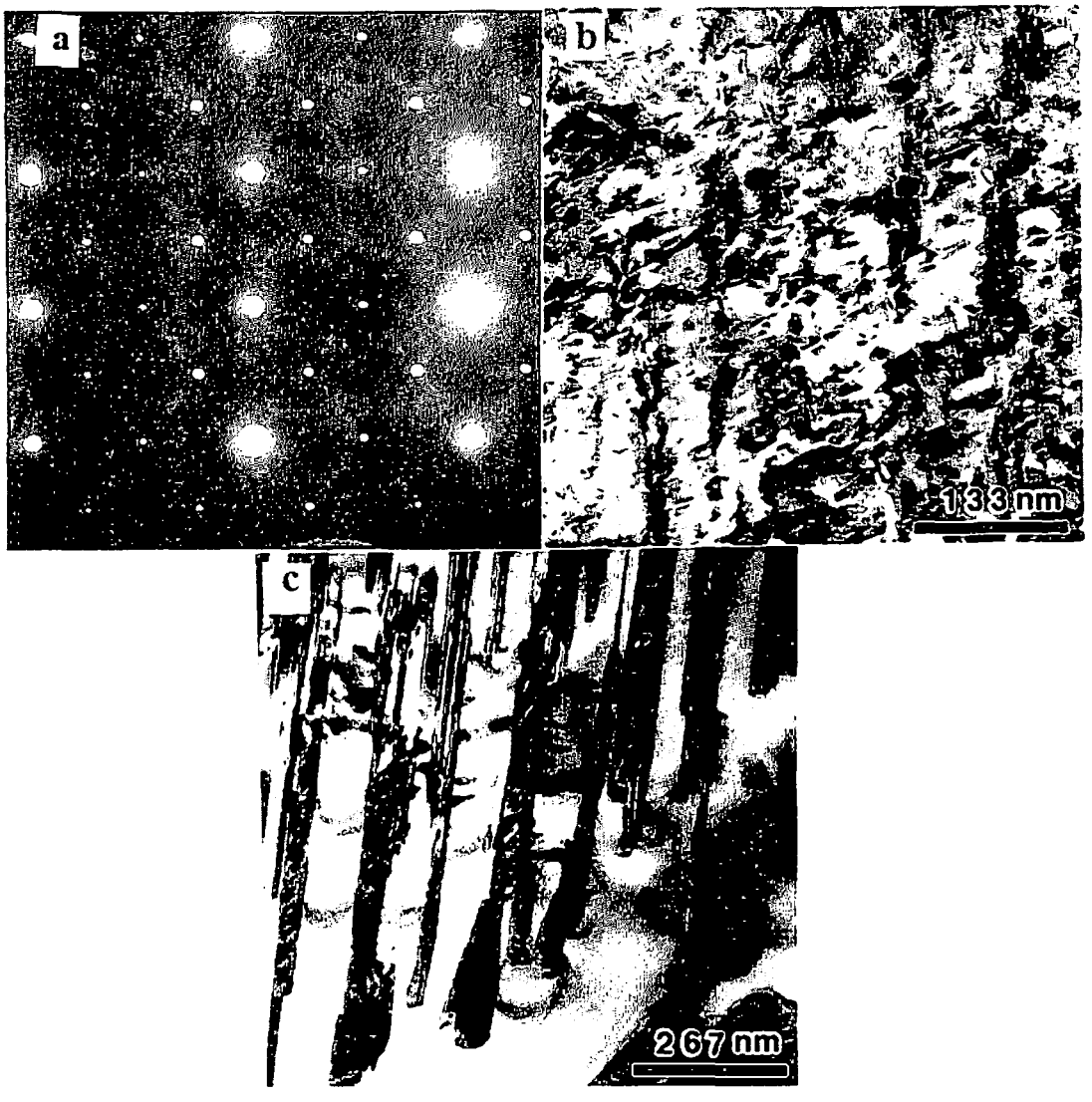



Figure 4-119. TEM microstructure of 5 at.% Al alloy aged at 650°C for 100 hours, a) [112] zone diffraction pattern showing strong intensity $DO_{22}$, and weak intensity $Ni_2Mo$, b) corresponding microstructure of $DO_{22}$ and $Ni_2Mo$ phases, c) lamellar structure.

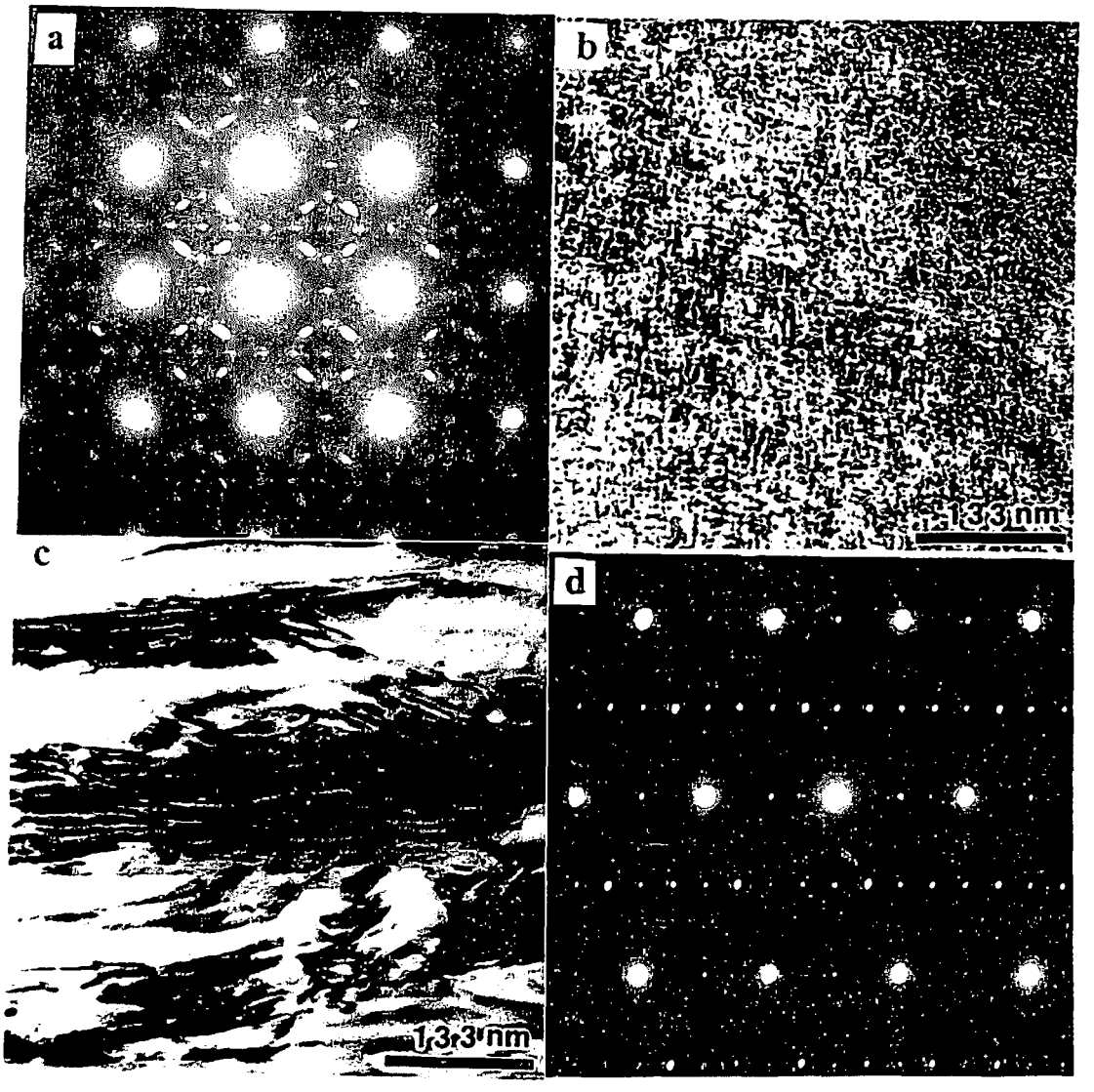



Figure 4-120. TEM microstructure of 7 at.% Al alloy aged 650°C for 100 hours, a) [001] zone diffraction pattern showing $DO_{22}$ and $Ni_2Mo$ superlattice spots, b) corresponding microstructure of $DO_{22}$ and $Ni_2Mo$ phases, c) lamellar structure, d) the diffraction pattern at c) region.

Table 4-5. The microstructure of Ni-Mo-Al alloys aged at 650°C.

| | $Ni_4Mo$ | 2 at.% Al | 5 at.% Al | 7 at.% Al | 9 at.% Al |
|---|---|---|---|---|---|
| as-quenched | SRO α | SRO α + $DO_{22}$ | SRO a ? + $DO_{22}$ | $DO_{22}$ + $Ni_2Mo$ | $DO_{22}$ + $Ni_2Mo$ |
| aged at 650°C | β | SRO α + $DO_{22}$ (?) | $DO_{22}$ + $Ni_2Mo$ (matrix), lamellar structure | $DO_{22}$ + $Ni_2Mo$ (matrix), lamellar structure | - |

4.5.4. TEM Microstructural Evaluation of Ni-Mo-Al Alloys After Solution Treated at 1280°C and Aged at 750°C for 10 Hours

a) $Ni_4Mo$ Alloy

After aging for 10 hours at 750°C, the $Ni_4Mo$ alloy transformed completely to a structure of fine β domain (Figure 4-121). No other phases were present. The hardness approximately doubled (Figure 4-4) in comparison to the as-quenched condition.

b) 2 at.% Al Alloy

After aging for 10 hours at 750°C, the 2 at.% Al alloy showed a single phase (Figure 4-35). It had a fine structure which appears to be domains (Figure 4-122b), but the diffraction pattern (Figure 4-122a) from this region showed only SRO α spots. However, in the solution heat treatment condition, this alloy showed both α and the $DO_{22}$ phase (Table 4-3). Aging for 10 hours did not appreciable change the hardness.

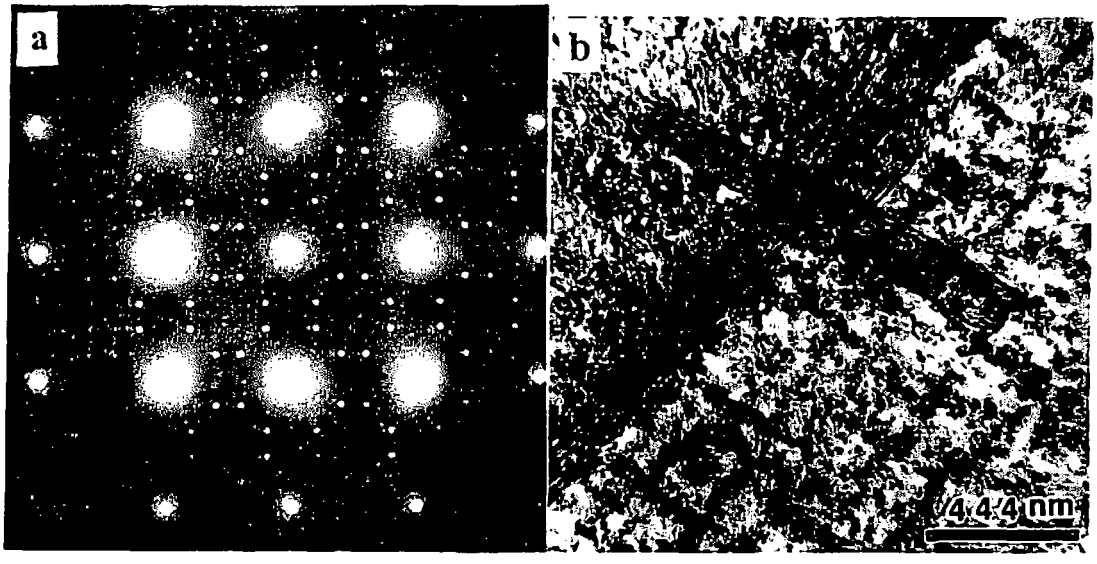



Figure 4-121. TEM microstructure of $Ni_4Mo$ alloy aged at 750°C for 10 hours, a) [001] diffraction pattern showing β superlattice spots, b) β domain and stacking faults.

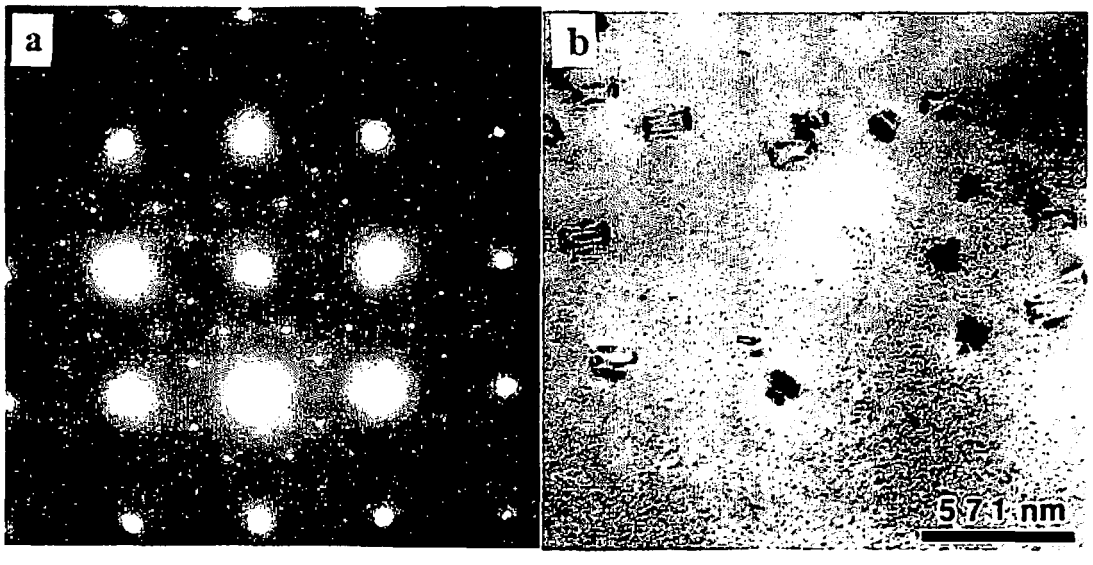



Figure 4-122. TEM microstructure of 2 at.% Al alloy aged at 750°C for 10 hours, a) [001] zone diffraction pattern showing SRO α superlattice spots, b) SRO α phase.

c) 5 at.% Al Alloy

The microstructure of the 5 at.% Al alloy after aging for 10 hours was mainly the matrix with a lamellar structure forming along the grain boundaries (Figure 4-36). Figure 4-123a shows the lamellar structure. The diffraction pattern (Figure 4-123b) is indexed in Figure 4-123c, showing that one set of lathes is the equilibrium $\gamma$ ($Ni_3Mo$) phase. The other is $\gamma'$ phase. This is discussed later. There was a marked increased in hardness after aging for 10 hours.

d) Summary

The microstructure after aging for 10 hours at 750°C are summarized in Table 4-6.

Table 4-6 The microstructure of Ni-Mo-Al alloys aged at 750°C for 10 hours.

| | $Ni_4Mo$ | 2 at.% Al | 5 at.% Al | 7 at.% Al | 9 at.% Al |
|---|---|---|---|---|---|
| as-quenched | SRO $\alpha$ | SRO $\alpha$ + $DO_{22}$ | SRO a ? + $DO_{22}$ | $DO_{22}$ + $Ni_2Mo$ | $DO_{22}$ + $Ni_2Mo$ |
| aged at 750°C for 10 hours | $\beta$ | SRO $\alpha$ | lamellar structure ($\gamma$ + $\gamma'$) | - | - |

4.5.5. TEM Microstructural Evaluation of Ni-Mo-Al Alloys After Solution Treated at 1280°C and Aged at 750°C for 50 Hours

a) $Ni_4Mo$ Alloy

In the $Ni_4Mo$ alloy, after 50 hours at 750°C , the structure was $\beta$ domains (Figure 4-124a), which had coarsened somewhat compared to 10 hours aging (Figure 4-121).

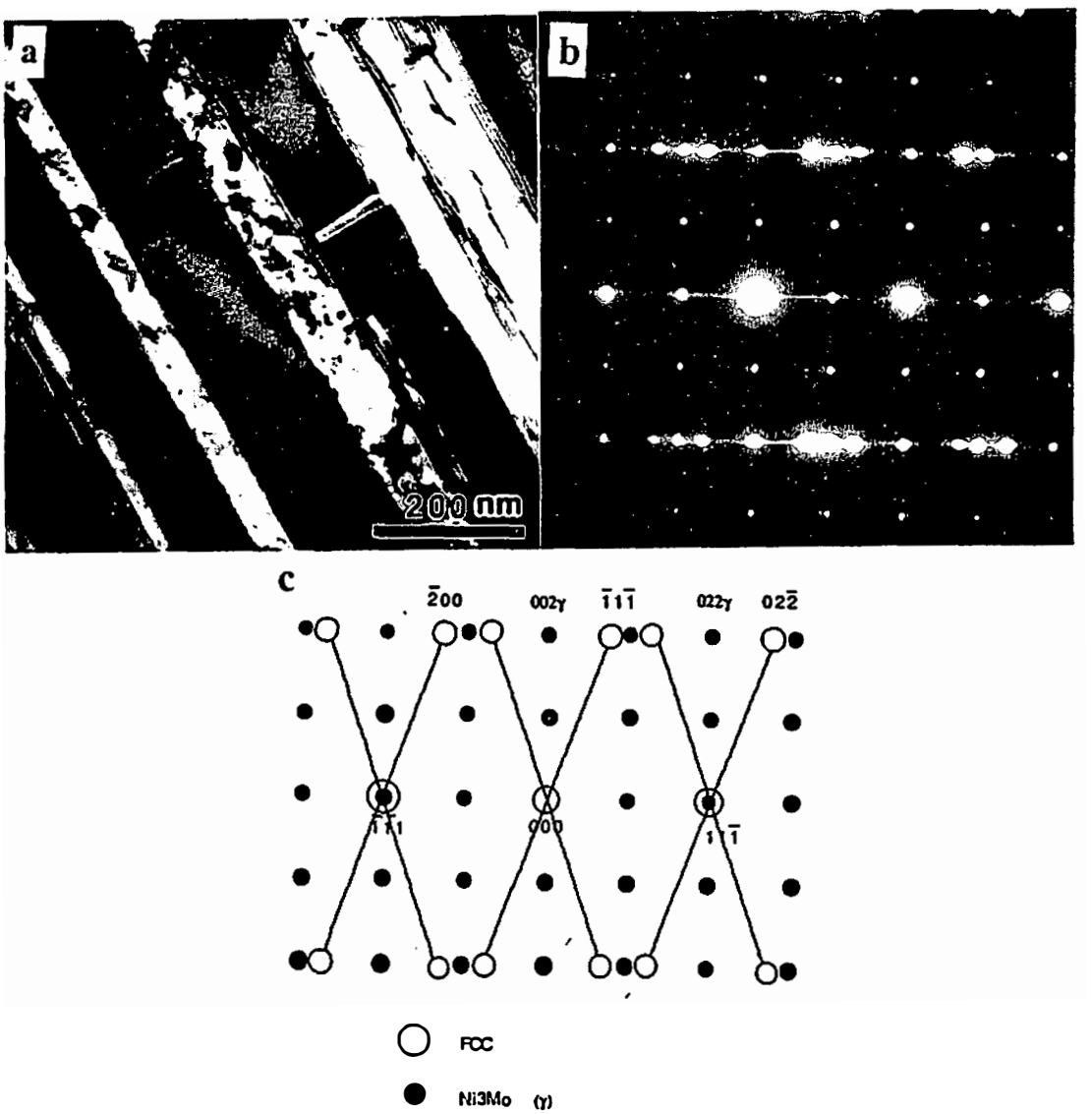



Figure 4-123. TEM microstructure of 5 at.% Al alloy aged at 750°C for 10 hours, a) lamellar structure, b) diffraction pattern [100]γ // [011]fcc, c) schematic diagram of diffraction pattern [100]γ//[011]fcc.

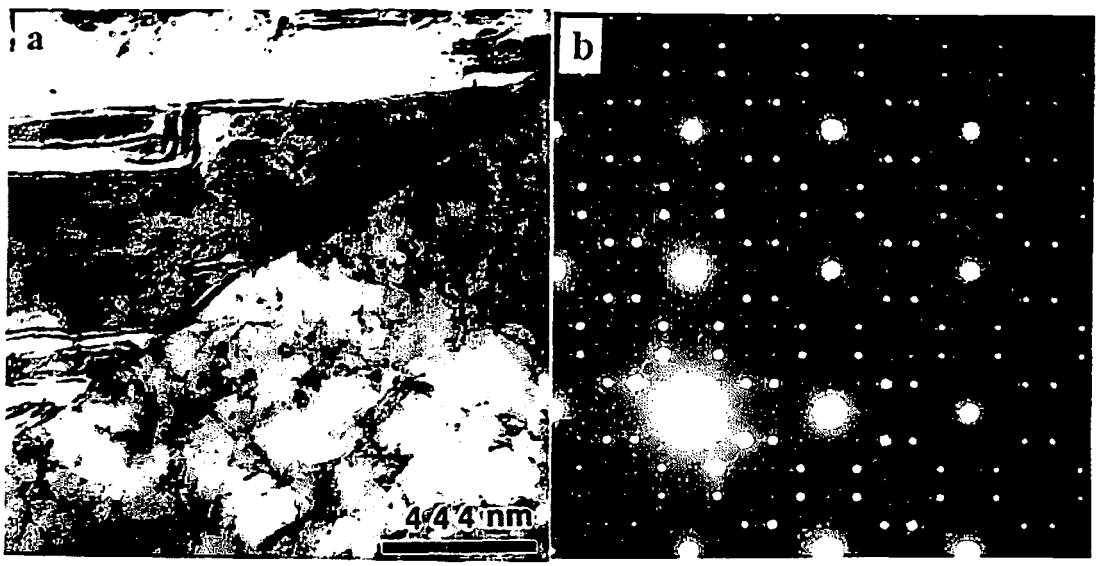



Figure 4-124. TEM microstructure in $Ni_4Mo$ alloy aged at 750°C for 50 hours, a) β phase and stacking faults, b) [001] zone diffraction pattern showing β superlattice spots.

Striations which are probably stacking faults had formed, perhaps associated with stress relief as the domains grew [81]. The weak spots also shown in Figure 4-124b were not indexed.

b). 2 at.% Al Alloy

After aging for 50 hours, the 2 at.% Al alloy still showed primarily untransformed matrix, with a small amount of a lamellar structure in the grain boundaries (Figure 4-39). The matrix structure consisted of domains, with some stacking faults present (Figure 4-125a). The [111] zone diffraction pattern probably shows the $DO_{22}$ structure. The hardness was essentially the same as that after aging for 10 hours (Figure 4-4).

c) 5 at.% Al Alloy

The microstructure of the 5 at.% Al alloy after aging for 50 hours consisted entirely of a lamellar structure (Figure 4-40). The lamellar structure is shown in Figure 4-126. No diffraction pattern is available. The hardness increased somewhat over that for aging 10 hours.

d) 7 at.% Al Alloy

The microstructure of the 7 at.% Al alloy consisted of a considerable amount of a lamellar structure formed along the grain boundaries and the matrix (Figure 4-41). Figure 4-127b shows the fine structure of the matrix. It consists of fine domains of the $DO_{22}$ and $Ni_2Mo$ phases (Figure 4-127a).

e) Summary

The microstructure after aging for 50 hours at 750°C is summarized in Table 4-7.

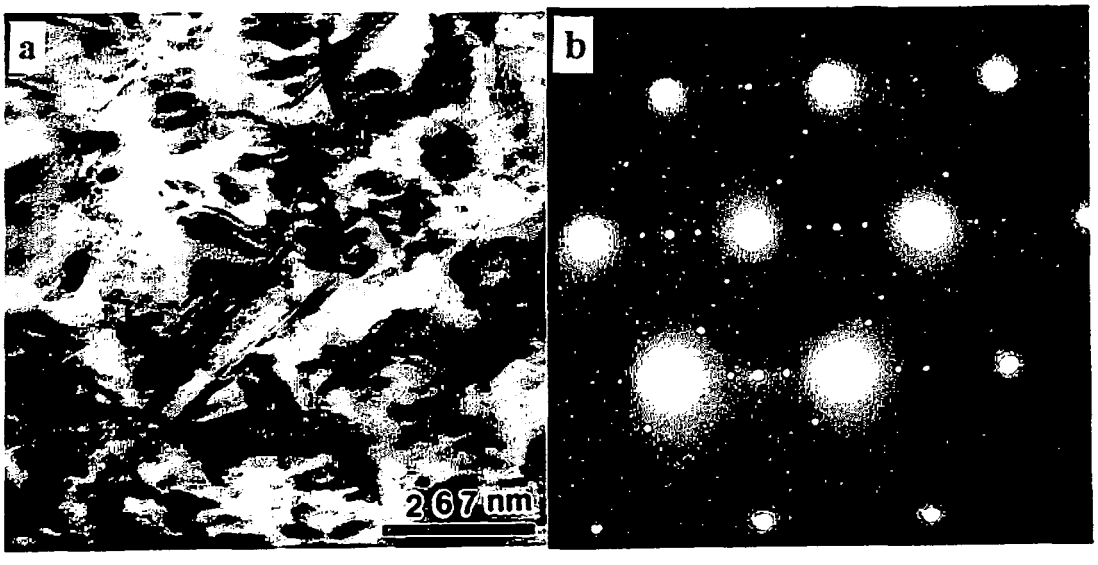



Figure 4-125. TEM microstructure of 2 at.% Al alloy aged at 750°C for 50 hours, a) stacking faults and precipitates, b) [111] zone diffraction pattern showing $DO_{22}$ superlattice spots.

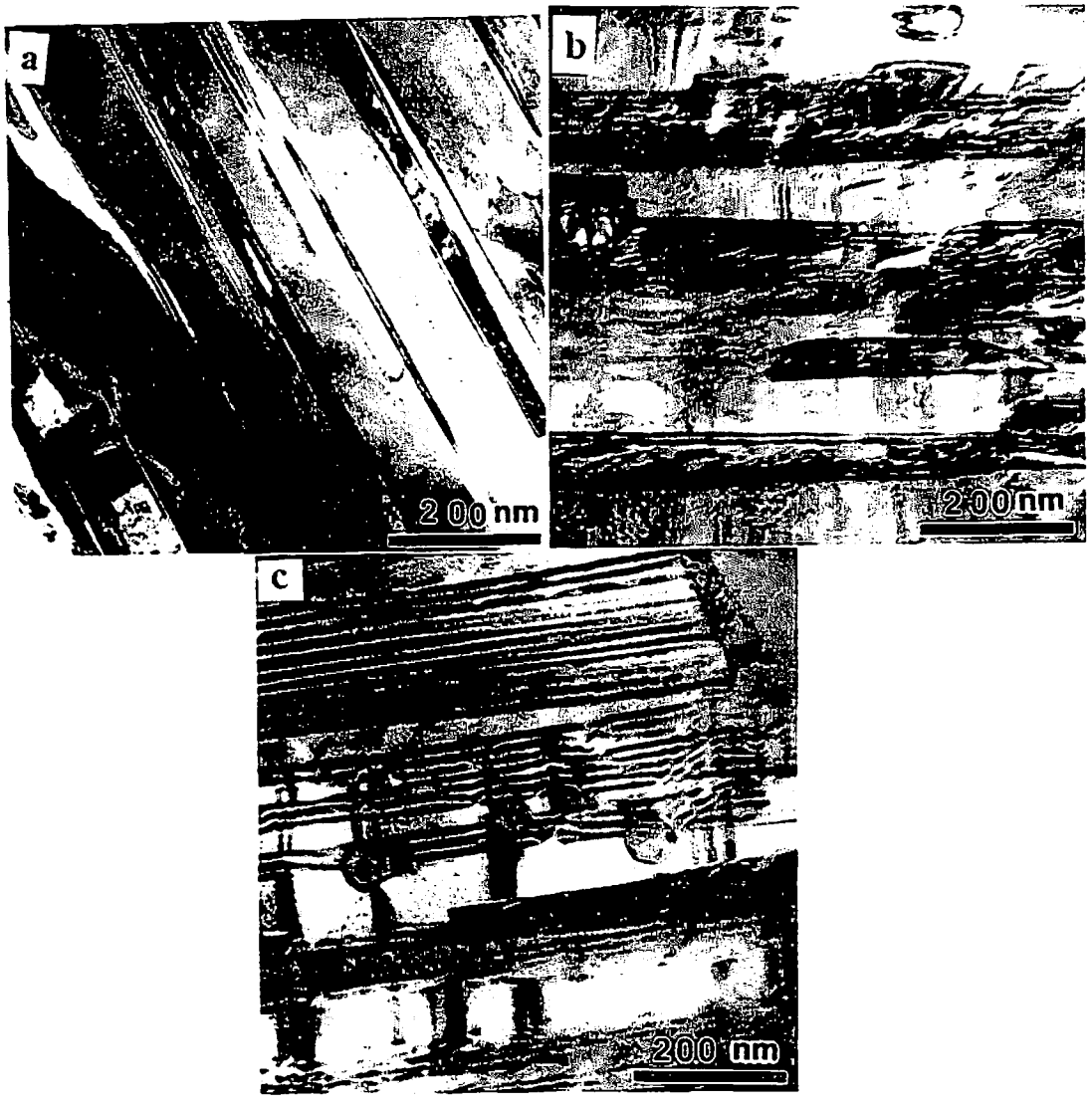



Figure 4-126. TEM microstructure of 5 at.% Al alloy aged at 750°C for 50 hours, a) and b) lamellar structure, c) stacking faults and particles.

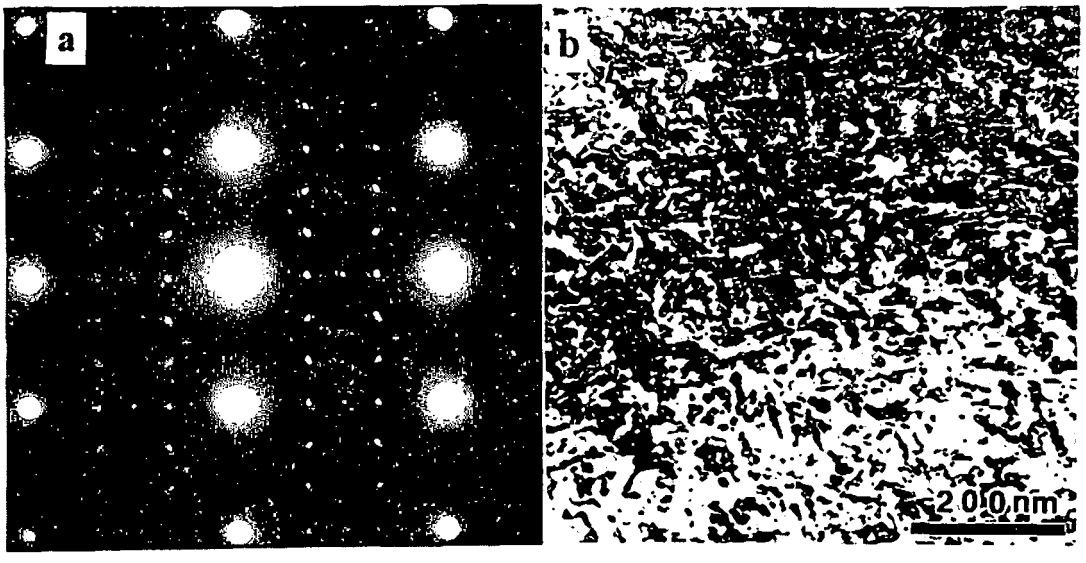



Figure 4-127. TEM microstructure of 7 at.% Al alloy aged at 750°C for 50 hours, a) [112] zone diffraction pattern showing $DO_{22}$ and $Ni_2Mo$ superlattice spots, b) the microstructure of $DO_{22}$ and $Ni_2Mo$ phases

Table 4-7 The microstructure of Ni-Mo-Al alloys aged at 750°C for 50 hours.

| | $Ni_4Mo$ | 2 at.% Al | 5 at.% Al | 7 at.% Al | 9 at.% Al |
|---|---|---|---|---|---|
| as-quenched | SRO α | SRO α + $DO_{22}$ | SRO a ? + $DO_{22}$ | $DO_{22}$ + $Ni_2Mo$ | $DO_{22}$ + $Ni_2Mo$ |
| aged at 750°C for 50 hours | β | $DO_{22}$ + ? | lamellar structure (γ + γ') | $DO_{22}$ + $Ni_2Mo$ (matrix) | - |

4.5.6. TEM Microstructural Evaluation of Ni-Mo-Al Alloys After Solution Treated at 1280°C and Aged at 750°C for 100 Hours

a) $Ni_4Mo$ Alloy

After aging for 100 hours at 750°C, the β domains have coarsened somewhat (Figure 4-128b). The hardness was the same as that after aging 50 hours (Figure 4-4). In addition to the β spots, the electron diffraction pattern (Figure 4-128a) showed weak spots consistent with the presence of the metastable $Ni_2Mo$ phase. This phase may be the dark area marked by the arrow. There were some weak unidentified spots.

b) 2 at.% Al Alloy

The 2 at.% Al alloy showed a rather uniform structure of fine precipitates in OLM (Figure 4-43). The fine structure is shown in Figure 4-129b. The electron diffraction pattern from this area shows that the structure consists of domains of β, $DO_{22}$ and $Ni_2Mo$. The hardness is about the same as that after aging 50 hours (Figure 4-5).

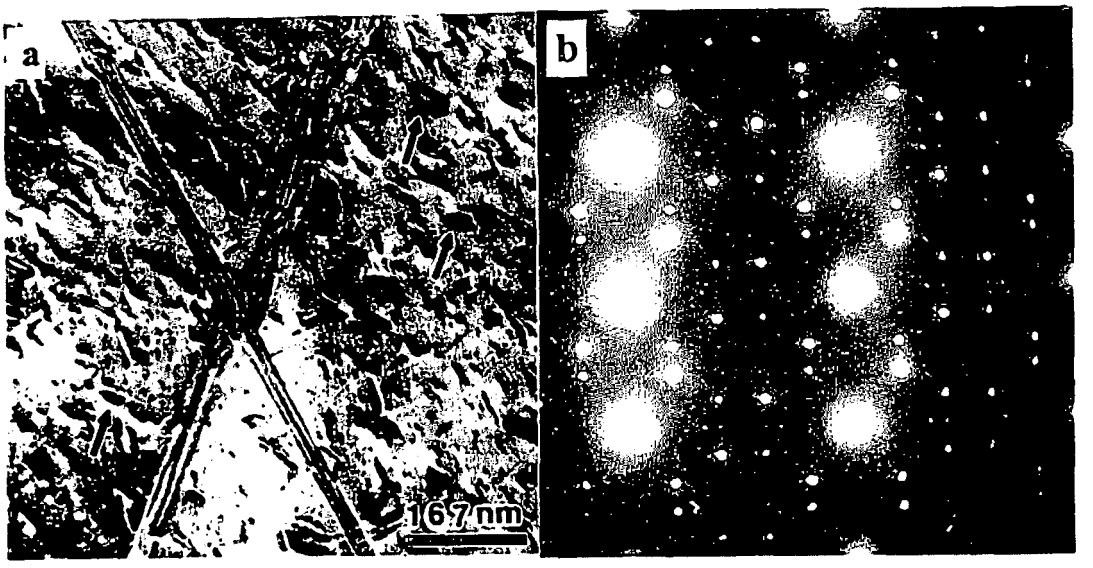



Figure 4-128. TEM microstructure of $Ni_4Mo$ alloy aged at 750°C for 100 hours, a) the microstructure of β and $Ni_2Mo$ phases, b) [112] zone diffraction pattern showing β and $Ni_2Mo$ superlattice spots.

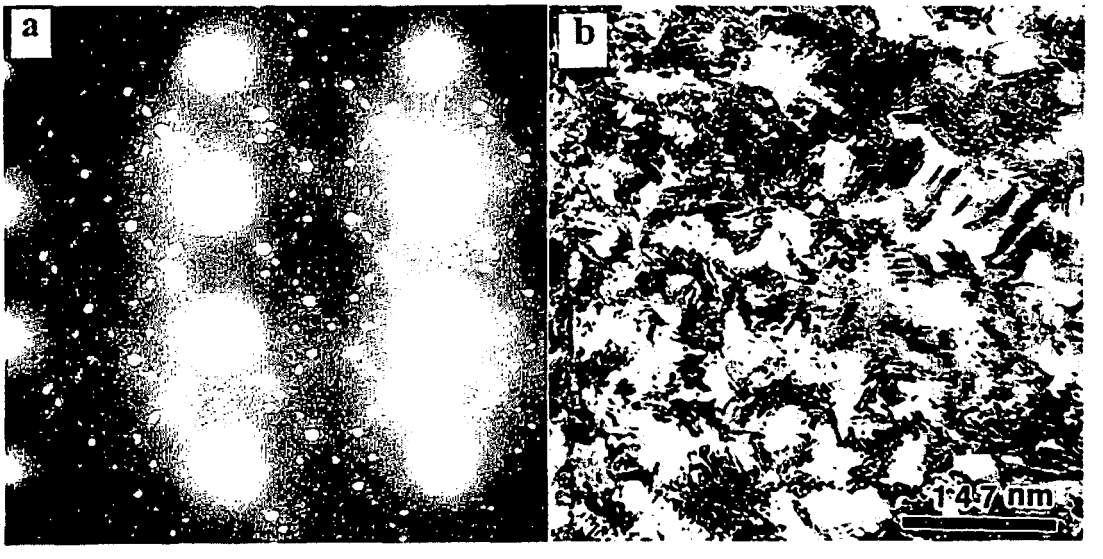



Figure 4-129. TEM microstructure of 2 at.% Al alloy aged at 750°C for 100 hours, a) [112] zone diffraction pattern showing β, $DO_{22}$ and $Ni_2Mo$ superlattice spots, b) the microstructure of β, $DO_{22}$ and $Ni_2Mo$ phases.

c) 5 at.% Al Alloy

The 5 at.% Al alloy had transformed completely to a lamellar and somewhat spheroidized structure after aging for 100 hours at 750°C (Figures 4-44 and 4-72). The lamellar structure is shown in Figure 4-130a. The diffraction pattern form this area is shown in Figure 4-130b. Most of the spots can be accounted for by the γ phase. EDS analyses from the area A, B, C and D are in Figure 4-130, f to i. Chemical composition derived from these spectra are shown in Table 4-8.

Table 4-8. Chemical composition of lamellar structure in Figure 4-130

| | Al (K) | | Ni (K) | | Mo (K) | | phase |
|---|---|---|---|---|---|---|---|
| | wt.% | at.% | wt.% | at.% | wt.% | at.% | |
| lath A | 6.2 | 13.3 | 78.3 | 77.3 | 15.5 | 9.4 | γ' $Ni_3(Al,Mo)$ |
| lath B | 1.0 | 2.5 | 63.5 | 72.7 | 35.5 | 24.8 | γ $Ni_3Mo$ |
| lath C | 5.6 | 12.0 | 82.4 | 80.8 | 12.0 | 7.2 | γ' $Ni_3(Al,Mo)$ |
| lath D | 0.9 | 2.2 | 70.8 | 78.5 | 28.3 | 19.3 | γ $Ni_3Mo$ |
| lath E | 5.5 | 11.8 | 78.4 | 78.3 | 16.1 | 9.9 | γ' $Ni_3(Al,Mo)$ |
| lath F | 0.3 | 0.7 | 69.1 | 78.1 | 30.6 | 21.2 | γ $Ni_3Mo$ |

The laths B and D have a very low aluminum content and have about the right nickel to molybdenum ratio to be the $Ni_3Mo$ γ phase. The prominent diffraction spots in Figure 4-130b are consistent with the known pattern of γ shown in Figure 4-130a. Thus the dark laths in Figure 4-130a are the γ phase. The bright laths A and C have a high aluminum content, and the ratio of nickel to the sum of molybdenum and aluminum is about right for the γ' $Ni_3(Al,Mo)$ phase. The diffraction spots from the γ' probably coincide with some of those of γ, but also could account for the weak spots not accounted

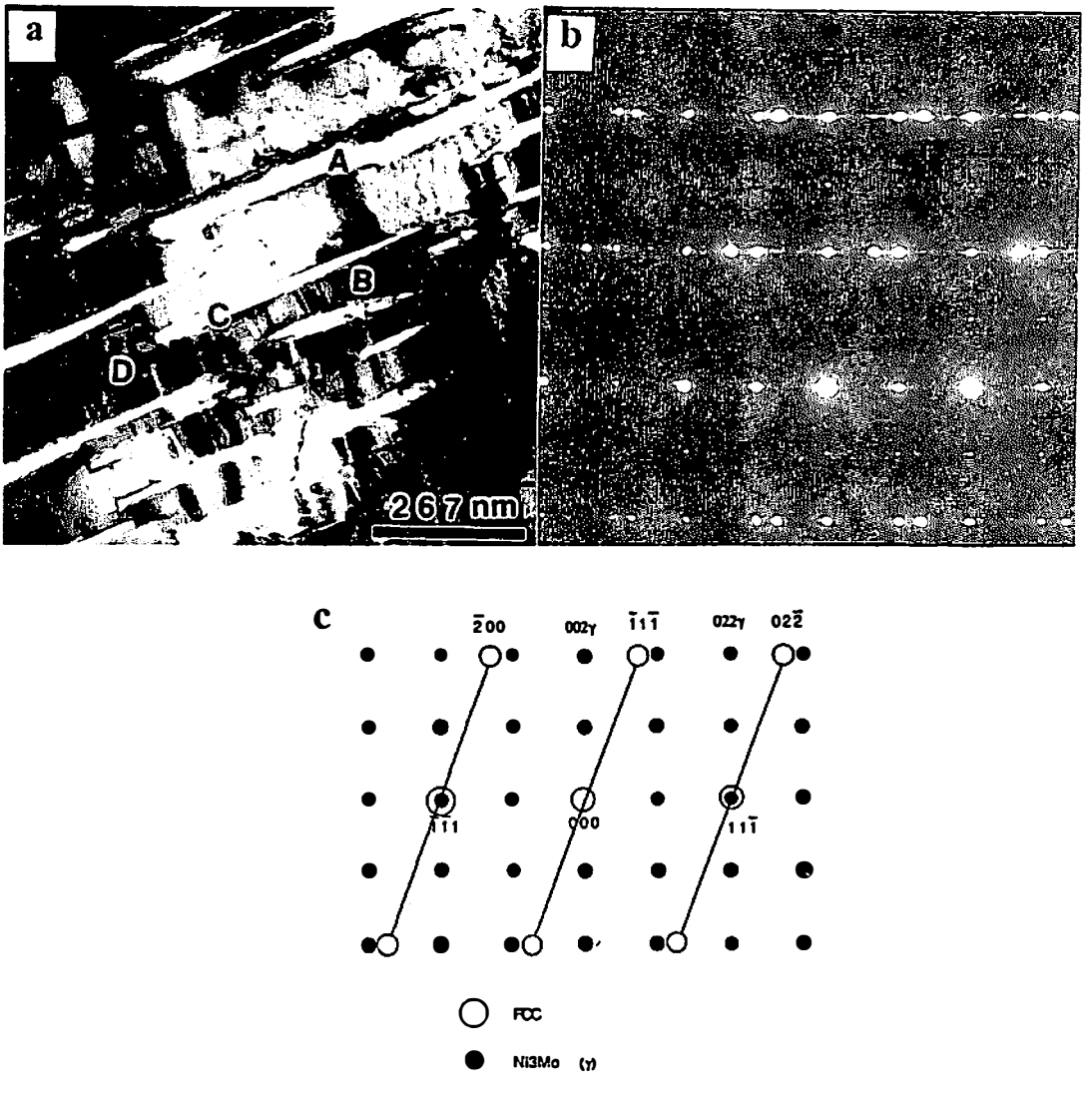
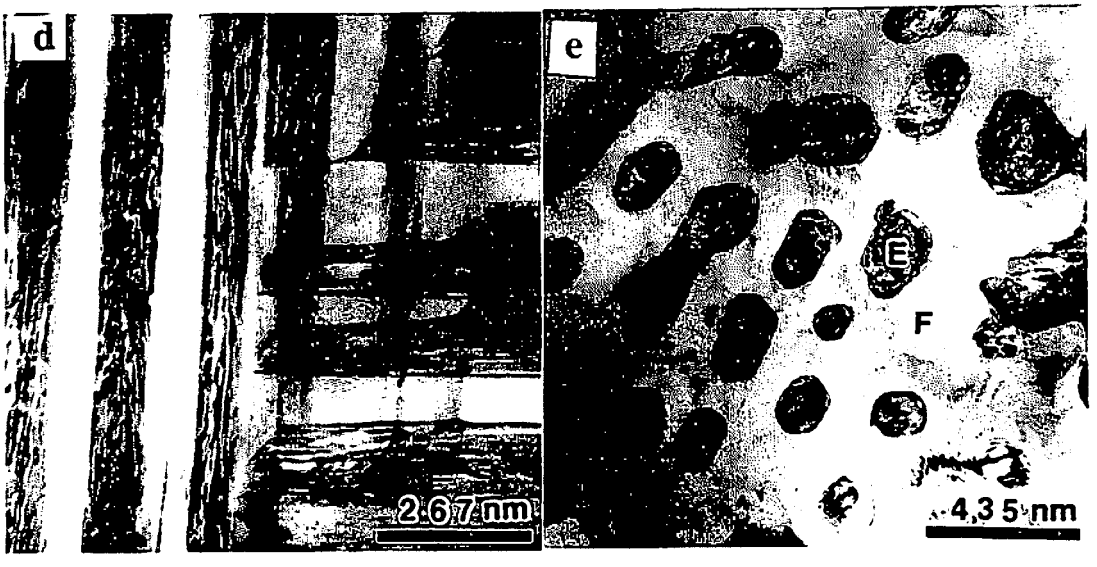



Figure 4-130. TEM microstructure of 5 at.% Al alloy aged at 750°C for 100 hours, a) lamellar structure of γ and γ' phases, b) corresponding diffraction pattern, c) schematic diagram of diffraction pattern, d) lamellar structure, d) Ni-rich particles.



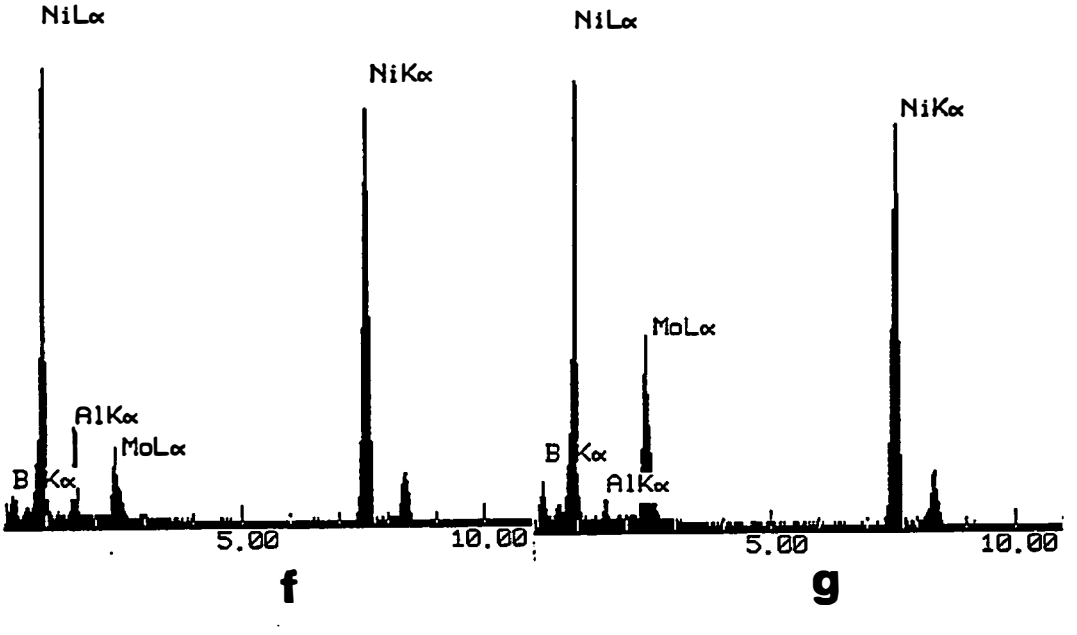




Figure 4-130. EDS analysis result from lamellar structure, f) A, g) B, h) C, i) D, j) E, k) F.

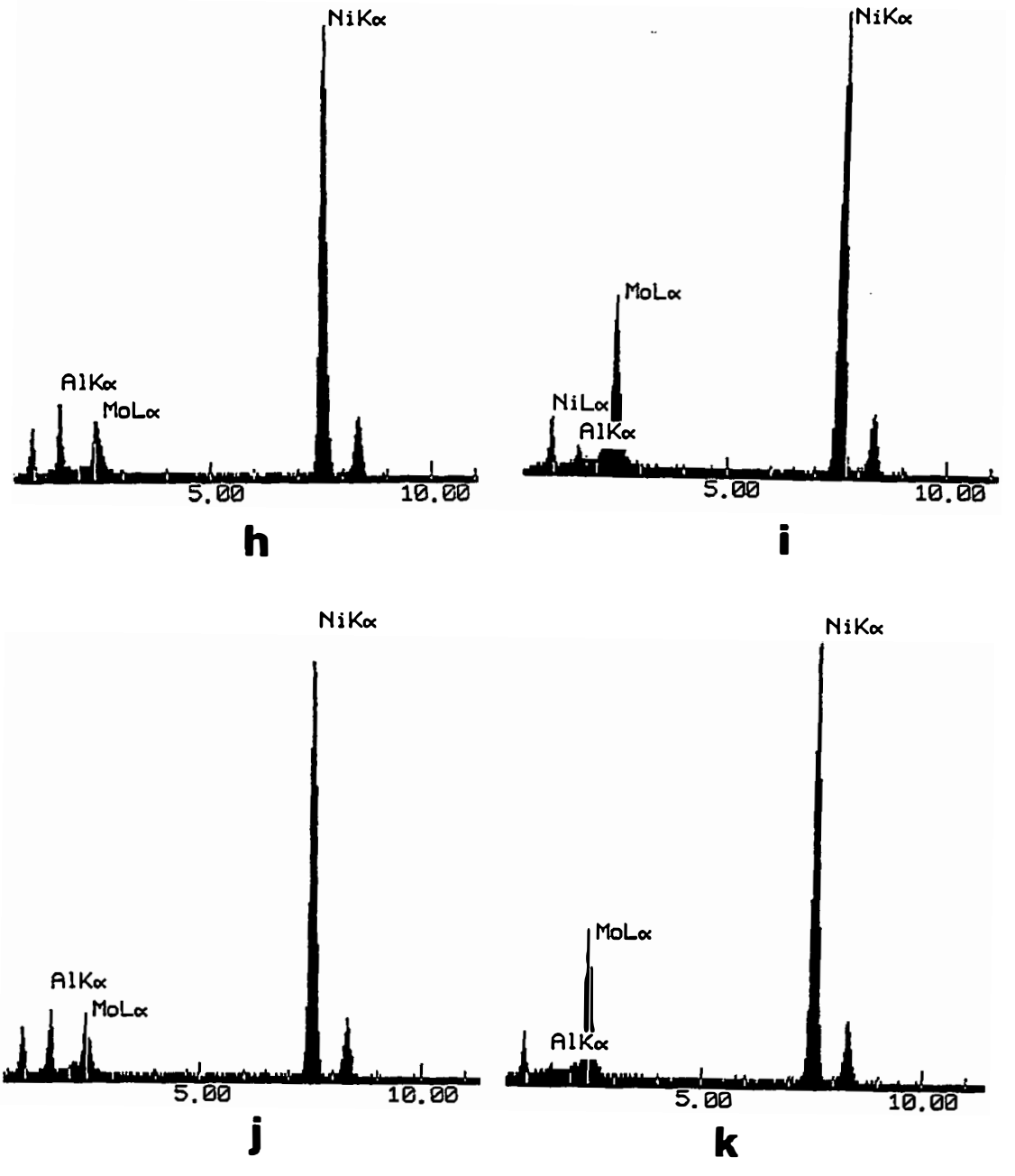



Figure 4-130. continue (h), (i), (j) and (k).

for by the γ. The particles in Figure 4-130e could be rods viewed on end. The chemical composition derived from the EDS spectra (Figure 4-130, j and k) indicate that these two particles are γ and γ'. The result is in general agreement with other researcher in ternary alloys [82 to 87].

d) 7 at.% Al Alloy

After aging for 100 hours at 750°C, the 7 at.% Al alloy consisted of lamellar structure which had formed along the grain boundaries and an untransformed matrix (Figure 4-45). Some of the lamellar structure along grain boundary was changing to a coarse lamellar structure. The matrix consisted of a very fine tweed structure (Figure 4-131a) which the electron diffraction pattern showed consists of the $Ni_2Mo$, γ' and $DO_{22}$ phases. The lamellar structure is shown in Figure 4-131b, and according to the analysis above for the 5 at.% al alloy, it consists of the γ and γ' phases. The hardness after aging for 100 hours was about the same as the after 50 hours. (Figure 4-4).

d) 9 at.% Al Alloy

The 9 at.% Al alloy had transformed to about half a lamellar structure in the matrix after aging for 100 hours at 750°C (Figure 4-46). The matrix had a tweed structure (Figure 4-132b); the diffraction pattern from it is shown in Figure 4-132a. It was not indexed, so that structure is unknown. The EDS analyses from the laths A and B and matrix C are shown in Figure 4-132, e to g. The laths are composed of γ and γ' phase. However, the 7 at.% Al alloy had a similar tweed matrix structure (Figure 4-131a), and the electron diffraction pattern indicated that the tweed structure consisted of $Ni_2Mo$, $DO_{22}$ and γ'. The hardness of this alloy was about the as that of the 5 and 7 at.% Al alloys (Figure 4-3).

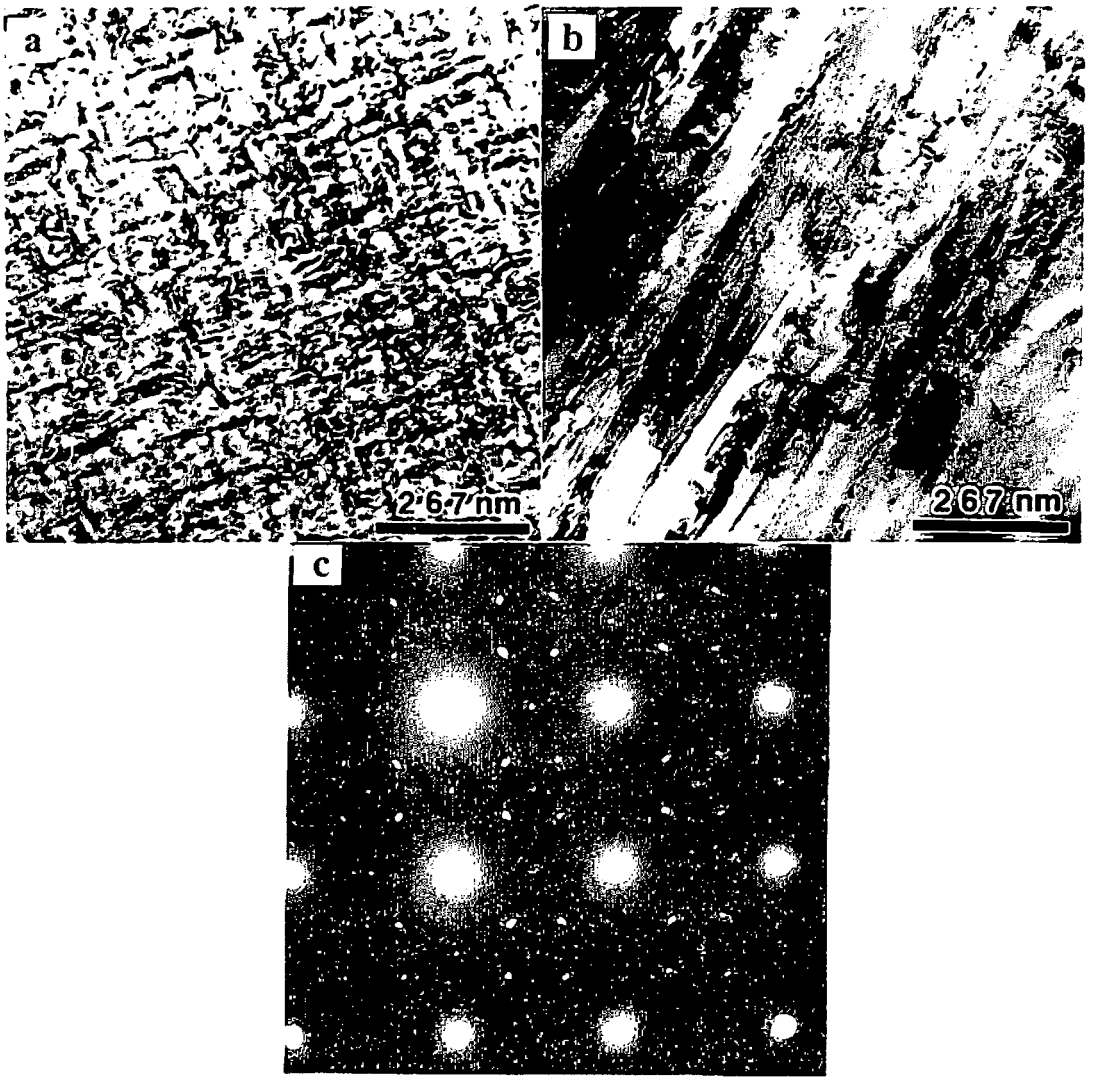



Figure 4-131. TEM microstructure of 7 at.% Al alloy aged at 750°C for 100 hours, a) tweed structure, b) lamellar structure, c) [001] zone diffraction pattern corresponding tweed microstructure showing strong intensity $Ni_2Mo$ and $\gamma'$ and weak intensity $DO_{22}$ superlattice spots.

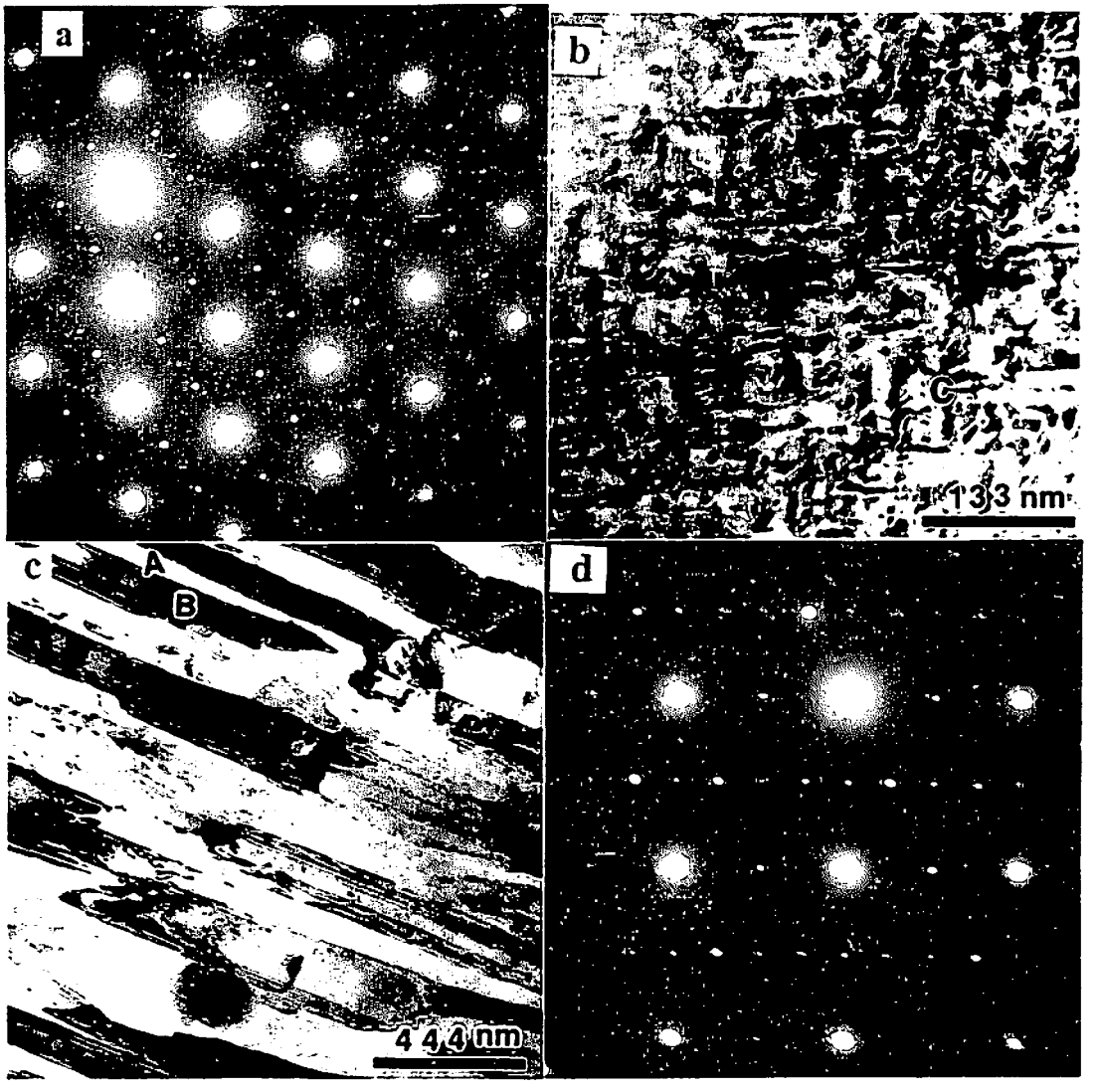



Figure 4-132. TEM microstructure of 9 at.% Al alloy aged at 750°C for 100 hours, a) [111] zone diffraction pattern showing $DO_{22}$ superlattice spots, b) corresponding microstructure of tweed structure, c) lamellar structure, d) corresponding [001] zone diffraction pattern.

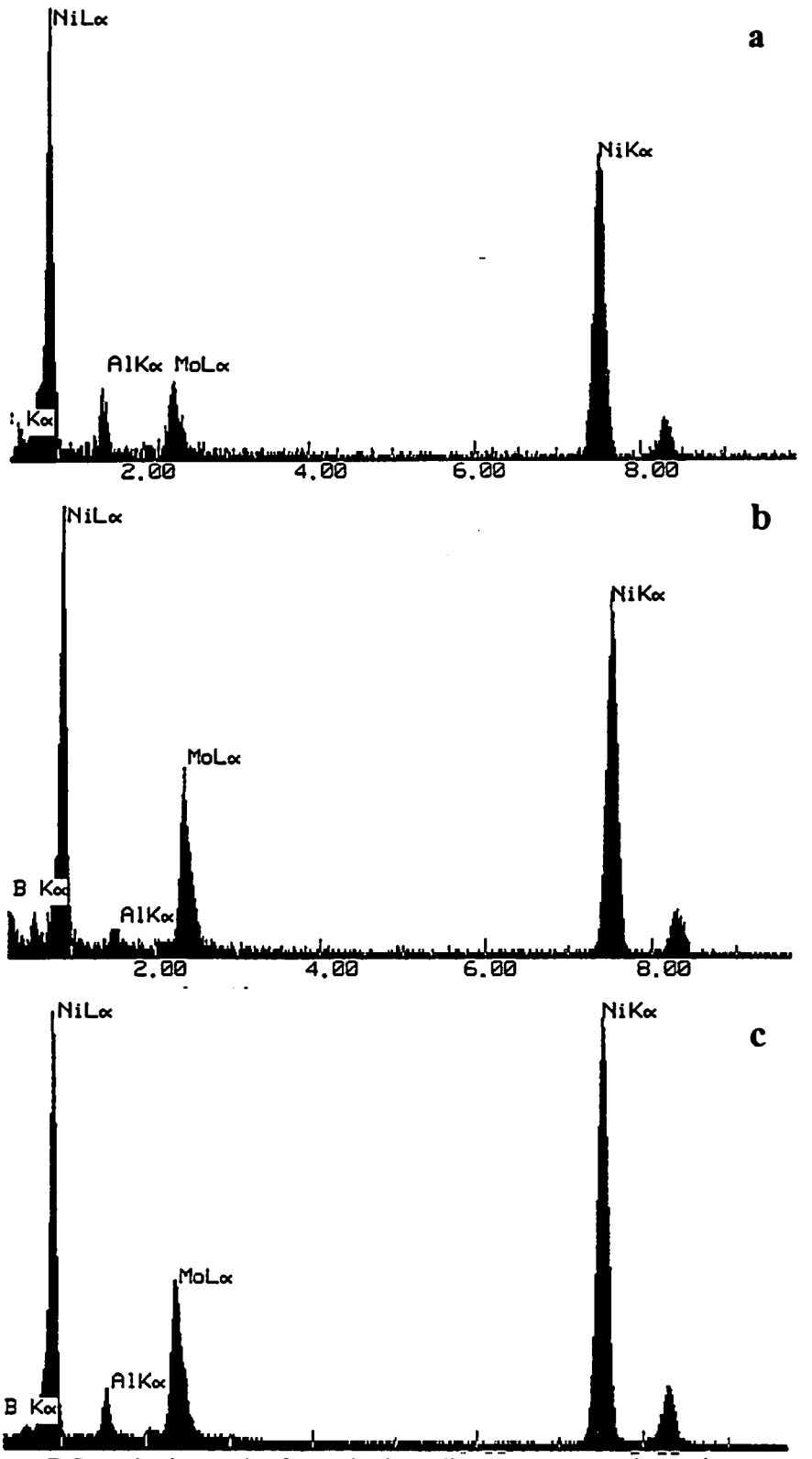



Figure 4-132. EDS analysis results from the lamellar structure and matrix.

e) Summary

The microstructure in $Ni_4Mo$ and Ni-Mo-Al alloys after aging for 100 hours at 750°C is summarized in Table 4-9.

Table 4-9. The microstructure of Ni-Mo-Al alloys aged at 750°C for 100 hours.

| | $Ni_4Mo$ | 2 at.% Al | 5 at.% Al | 7 at.% Al | 9 at.% Al |
|---|---|---|---|---|---|
| as-quenched | SRO α | SRO a + $DO_{22}$ | SRO α ? + $DO_{22}$ | $DO_{22}$ + $Ni_2Mo$ | $DO_{22}$ + $Ni_2Mo$ |
| aged at 750°C for 100 hours | β | β + $DO_{22}$ + $Ni_2Mo$ | γ + γ' (lamellar structure) | $Ni_2Mo$ + $DO_{22}$ (matrix), γ + γ' (lamellar structure) | $Ni_2Mo$ + $DO_{22}$ (matrix), γ + γ' (lamellar structure) |

4.5.7. TEM Microstructural Evaluation in Ni-Mo-Al Alloys After Solution Treated at 1280°C and Aged at 850°C for 100 Hours

a) 2 at.% Al Alloy

After aging at 850°C for 100 hours, the 2 at.% Al alloy had a fine plate-like structure, a lamellar structure and a striated structure forming from the grain boundaries and in the grains (Figures 4-48 and 4-74). The diffraction pattern of the matrix indicates that it is the $DO_{22}$ phase (Figures 4-133, a and b). Dislocations are observed (Figure 4-133c). One of the lamellar structure is shown in figure 4-133d, but no diffraction pattern was obtained. After aging 100 hours at 850°C, the hardness decreased somewhat from the value after aging at 750°C 100 hours value (Figure 4-3).

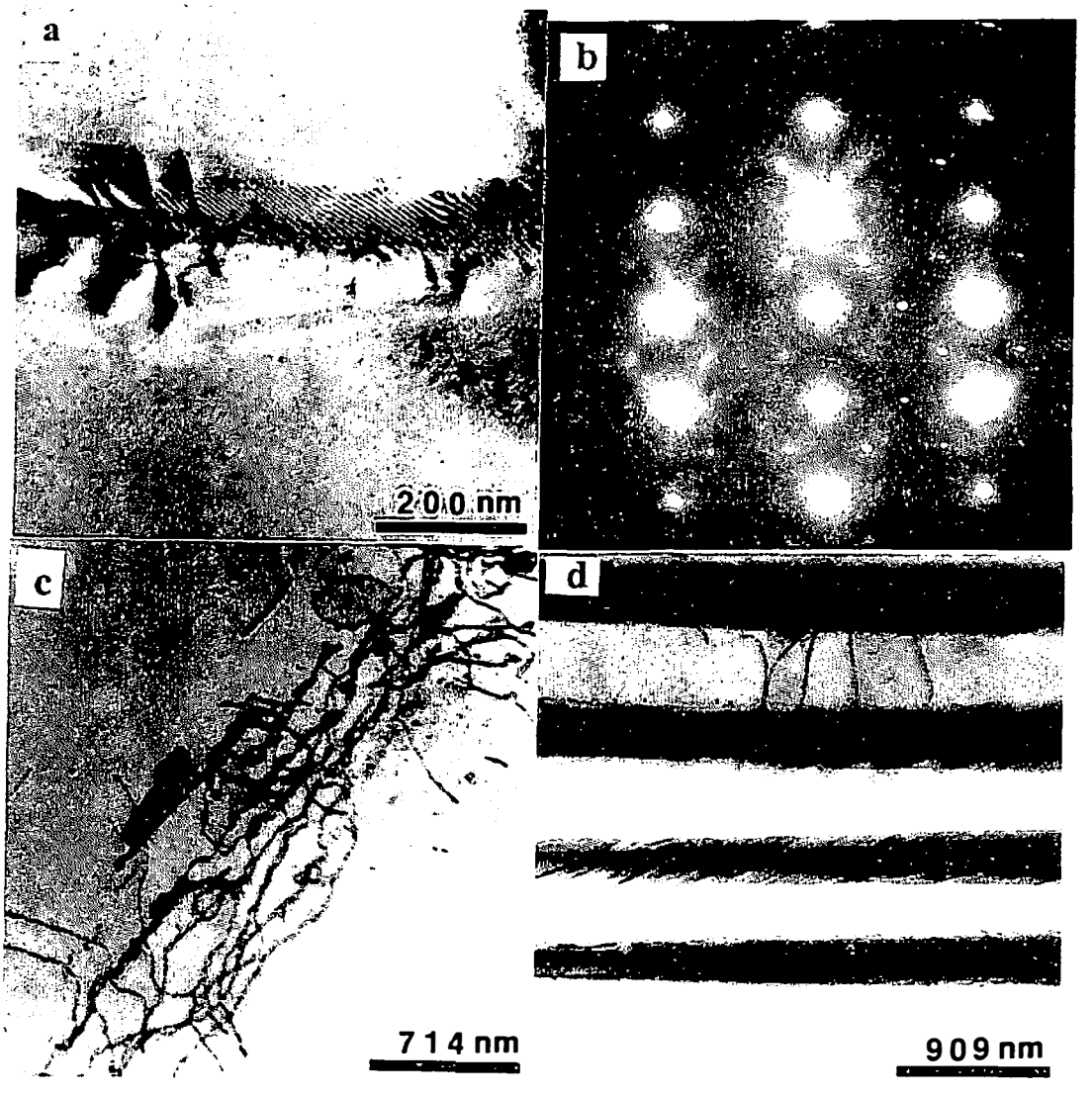



Figure 4-133. TEM microstructure of 2 at.% Al alloy aged at 850°C for 100 hours, a) microstructure of $DO_{22}$, b) [112] zone diffraction pattern showing $DO_{22}$ superlattice spots, c) dislocation, d) lamellar structure.

b) 5 at.% Al Alloy

After aging for 100 hours at 850°C, the 5 at.% Al alloy consisted entirely of needle-like precipitates (Figures 4-49 and 4-75). These are shown in Figure 4-134, and they are surrounded by dislocation. No diffraction patterns were obtained. These precipitates are the δ and γ phases. They will be discussed in 7 at.% Al alloy upon aging at 950°C. The hardness was above that of the solution heat treated condition (Figure 4-3).

c) Summary

The microstructure in Ni-Mo-Al alloys after aging at 850°C for 100 hours is summarized in Table 4-10.

Table 4-10. The microstructure of Ni-Mo-Al alloys aged at 850°C for 100 hours

| | $Ni_4Mo$ | 2 at.% Al | 5 at.% Al | 7 at.% Al | 9 at.% Al |
|---|---|---|---|---|---|
| as-quenched | SRO α | SRO α + $DO_{22}$ | SRO a ? + $DO_{22}$ | $DO_{22}$ + $Ni_2Mo$ | $DO_{22}$ + $Ni_2Mo$ |
| aged at 850°C for 100 hours | – | $DO_{22}$ (matrix), lath structure | γ + δ, α (matrix) | - | - |

4.5.8. TEM Microstructural Evaluation in Ni-Mo-Al Alloys After Solution Treated at 1280°C and Aged at 950°C for 100 Hours

a) 5 at.% Al Alloy

The microstructure of the 5 at.% Al alloy after aging for 100 hours at 950°C

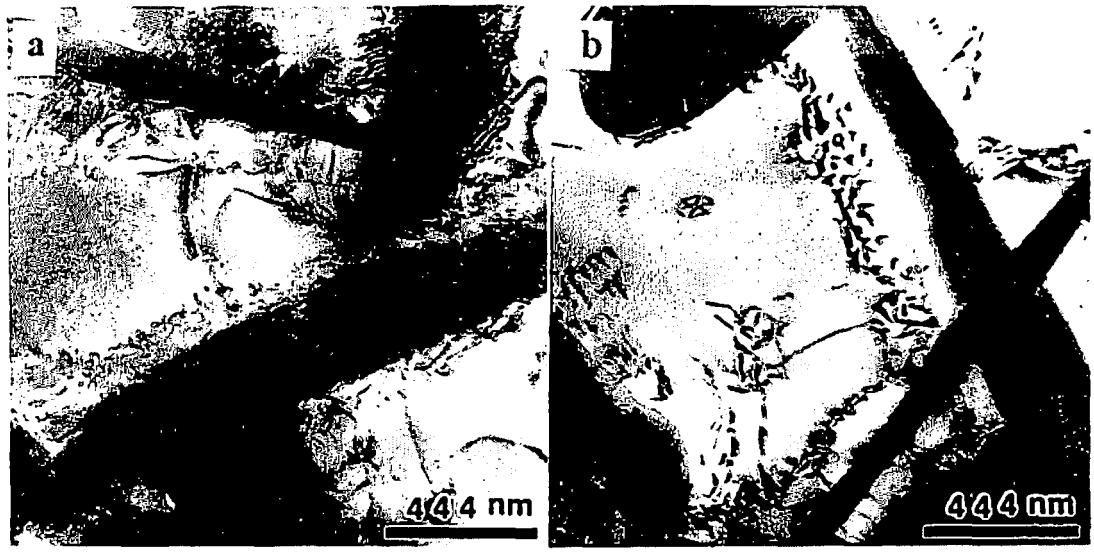



Figure 4-134. TEM microstructure of 5 at.% Al alloy aged at 850°C for 100 hours, a) and b) different shape precipitates and dislocation pile-ups at precipitates.

contained needle-like precipitates and particles (Figures 4-53 and 4-78). The particles are 5a and the corresponding diffraction pattern in Figure 4-135b. It is rather complex, and was not indexed. This structure is discussed in 7 at.% Al alloy. The hardness of this alloy was about the same as that for the solution heat treated condition (Figure 4-3).

b) 7 at.% Al Alloy

After aging for 100 hours at 950°C, the 7 at.% Al alloy also consisted of fine precipitates (Figures 4-54 and 4-79), but much finer than in the 5 at.% Al alloy. These are shown in Figure 4-136a. Note that there are dislocations around them. EDS analyses were obtained from the particles shown, and the chemical analyses are shown in Table 4-11.

Table 4-11. Chemical composition of precipitates

| location | Al | | Ni | | Mo | | phase |
|---|---|---|---|---|---|---|---|
| | wt% | at.% | wt% | at.% | wt% | at.% | |
| Matrix (A) | 2.4 | 5.6 | 69.2 | 75.4 | 28.4 | 19 | $\alpha$ |
| black (B) | 0.4 | 1.1 | 36.7 | 48.3 | 62.9 | 50.6 | $\delta$ (NiMo) |
| short rod (C) | 0.1 | 0.4 | 34.3 | 45.9 | 65.6 | 53.8 | $\delta$ (NiMo) |
| lath (D) | 2.6 | 6.4 | 59.6 | 67.5 | 37.8 | 26.2 | $\gamma$ ($Ni_3Mo$) |

Based on these data, the precipitates are identified as $\delta$ and $\gamma$. The matrix is taken to be $\alpha$. The hardness of this alloy had increased somewhat over that of the solution heat treated value (Figure 4-3).

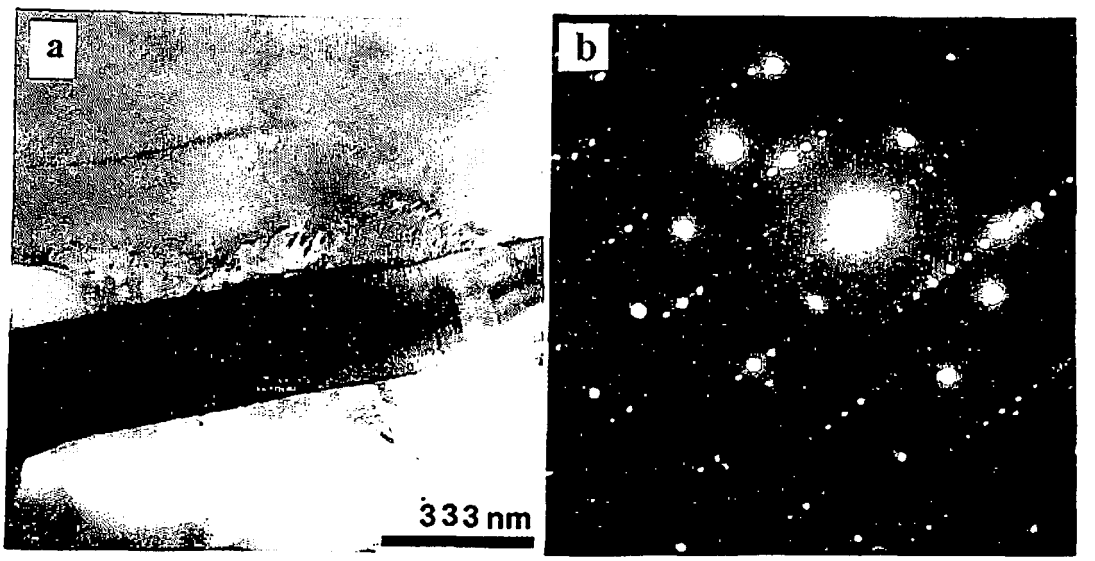



Figure 4-135. TEM microstructure of 5 at.% Al alloy aged at 950°C for 100 hours, a) lath shape precipitates and dislocations pile-ups at precipitates, b) diffraction pattern.

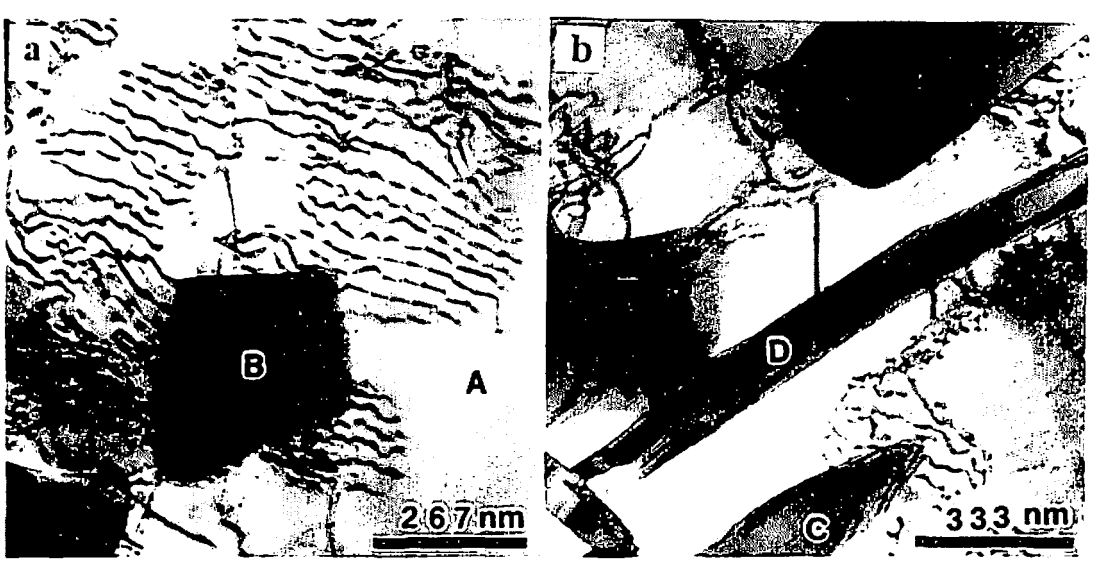



Figure 4-136. TEM microstructure of 7 at.% Al alloy aged at 950°C for 100 hours, a) and b) precipitates and dislocations, c) EDS analysis result from at A, d) B, e) D.

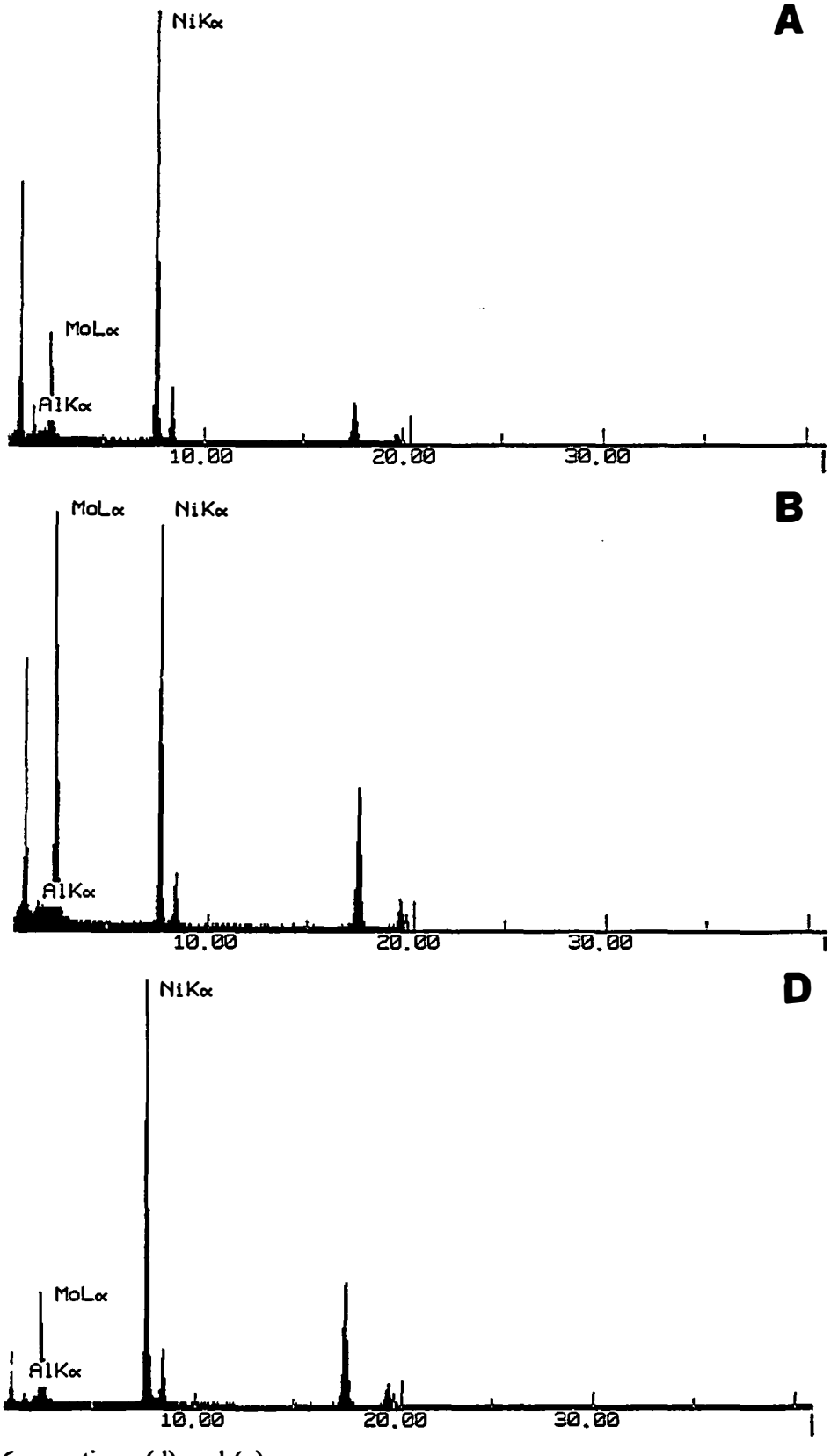



Figure 4-136. continue (d) and (e).

c) Summary

The microstructure in Ni-Mo-Al alloys after aging at 950°C for 100 hours is summarized in Table 4-12.

Table 4-12. The microstructure of Ni-Mo-Al alloys aged at 950°C

| | $Ni_4Mo$ | 2 at.% Al | 5 at.% Al | 7 at.% Al | 9 at.% Al |
|---|---|---|---|---|---|
| as-quenched | SRO α | SRO α + $DO_{22}$ | SRO a ? + $DO_{22}$ | $DO_{22}$ + $Ni_2Mo$ | $DO_{22}$ + $Ni_2Mo$ |
| aged at 950°C for 100 hours | – | - | γ, α (matrix) | γ + δ, α (matrix) | - |

4.5.9. Summary of the Phase Identification of the Ni-Mo-Al Alloys for All the Heat Treatments.

The phase identification of the Ni-Mo-Al alloys in all aging conditions based on the SEM and especially the TEM results is summarized in Table 4-13.

4.5.10. TEM Microstructural Evaluation of Aged Hastelloy B2 Alloy

In addition to the detailed examination of the Ni-Mo-Al alloys, there was the opportunity for TEM examination of some samples of the commercial alloy Hastelloy B2. This alloy is based on $Ni_4Mo$, but has additions of iron, cobalt, chromium, and manganese which may amount to about 4 wt.%. Thus the alloy has some of the transformation characteristics of the ternary Ni-Mo-Fe and Ni-Mo-Cr alloys. The SRO α phase can be retained be sufficiently rapid cooling from the α region, and this structure is ductile. Upon aging, the a transforms to β, which the well known accompanying

Table 4-13. Summary examination of phase transformation in alloys

| | $Ni_4Mo$ | 2 at.% Al alloy | 5 at.% Al alloy | 7 at.% Al alloy | 9 at.% Al alloy |
|---|---|---|---|---|---|
| 1250°C, 50 hr. | SRO α | SRO α + $DO_{22}$ | SRO α ? +$DO_{22}$ | $DO_{22}$ + $Ni_2Mo$ | $DO_{22}$ + $Ni_2Mo$, Mo-rich particles |
| 600°C, 100 hr. | - | α + β + $DO_{22}$ | $DO_{22}$ | $DO_{22}$ + $Ni_2Mo$ (matrix), δ lath | $DO_{22}$ + $Ni_2Mo$ (matrix) Mo-rich particles, δ lath |
| 650°C, 100 hr. | β (matrix), γ particles | α + $DO_{22}$ (?) | $DO_{22}$ + $Ni_2Mo$ (matrix), γ+γ' (lamellar structure) | $DO_{22}$ + $Ni_2Mo$ (matrix), γ+γ' (lamellar structure) | - |
| 750°C, 10 hr. | β | SRO α | γ+γ' ( lamellar structure), $DO_{22}$ + $Ni_2Mo$ (matrix) | γ+γ' ( lamellar structure), $DO_{22}$ + $Ni_2Mo$ (matrix) | - |
| 750°C, 50 hr. | β | $DO_{22}$ + ?, δ particles | γ+γ' ( lamellar structure) | $DO_{22}$ + $Ni_2Mo$ (matrix), γ+γ' (lamellar structure) | - |

| | | | | | |
|---|---|---|---|---|---|
| 750°C, 100 hr. | $\beta + Ni_2Mo$ | $\beta + DO_{22} +$ $Ni_2Mo$, $\delta$ particles | $\gamma + \gamma'$ ( lamellar structure) | $Ni_2Mo + DO_{22}$ (matrix), $\gamma + \gamma'$ (lamellar structure) | $Ni_2Mo + DO_{22}$ (matrix), $\gamma + \gamma'$ (lamellar structure) |
| 850°C, 100 hr. | - | $DO_{22}$ ( matrix), lath structure | $\gamma$ lath, $\alpha$ (matrix), $\delta$ particles | $\gamma$ lath, $\alpha$ (matrix), $\delta$ particles | - |
| 950°C, 100 hr. | - | Mo-rich particles, SRO $\alpha$ (matrix) | $\gamma$ lath, $\alpha$ (matrix), $\delta$ particles | $\gamma$ lath, $\alpha$ (matrix). $\delta$ particles and $\gamma'$ along the grain boundaries | - |

embrittlement. In Hastelloy B2 alloy, due to the alloying addition, other phases may form which also induce embrittlement.

The chemical composition of the alloy is given in the Table 3-5. The samples had been solution heat treated for 2 hours at 1065°C in argon, then aged from 550°C to 850°C for up to 1200 hours. The details of the fabrication and heat treatment are given by Brooks and Wang [20, 22]. Using OLM and SEM, they characterized their microstructures, determined the hardness and tensile properties, and characterized the fracture surfaces of the broken tensile samples.

### 4.5.11. TEM Microstructural Evaluation of Hastelloy B2 Alloy upon Aging at 550°C

In the solution heat treated condition, the Hastelloy B2 alloy showed only SRO $\alpha$. In the binary $Ni_4Mo$ alloy, the transition of the [001] electron diffraction pattern as the SRO $\alpha$ transforms to a domain structure of $\beta$ is shown in Figure 2-24. After aging the Hastelloy B2 alloy for 200 hours at 550°C, the diffraction pattern (Figure 4-137) shows that the transition to $\beta$ has begun. After 800°C hours, a fine domain structure is formed (Figure 4-138a). The electron diffraction pattern shows $\beta$ spots and weak spots of the metastable $DO_{22}$ phase. After 1200 hours, the structure has coarsened (Figure 4-139c). The diffraction pattern still shows that both the $\beta$ and $DO_{22}$ phases are present. This result is in general agreement with other researchers [90, 91].

### 4.5.12. TEM Microstructural Evaluation of Hastelloy B2 Alloy upon Aging at 650°C

Aging for 200 hours at 650°C produced a fine domain structure (Figure 4-140b). The electron diffraction pattern (Figure 4-140a) shows strong $\beta$ spots and the transition

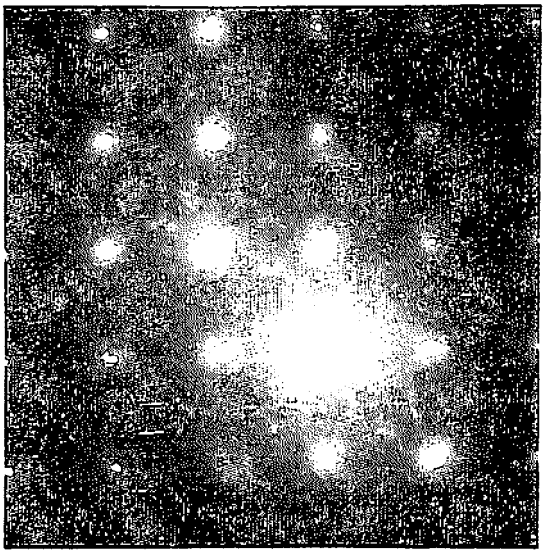


Figure 4-137. [001] zone diffraction pattern showing intermediate stage of SRO α phase transformation to β phase in Hastelloy B2 alloy aged at 550°C for 200 hours.

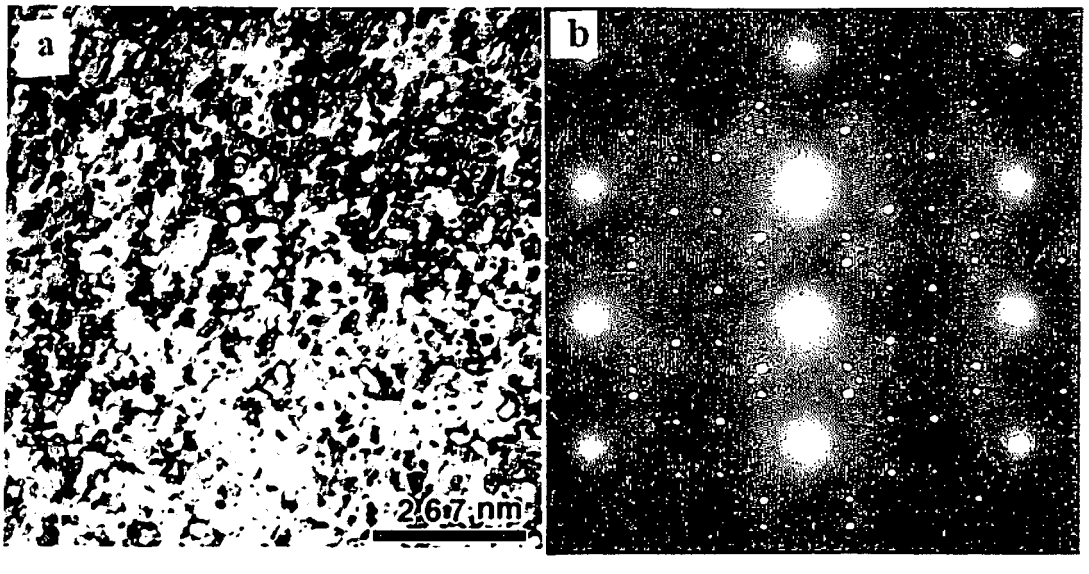



Figure 4-138. TEM microstructure of Hastelloy B2 alloy aged at 550°C for 800 hours, a) second phase precipitates in matrix, b) corresponding [112] zone diffraction pattern showing the β and $DO_{22}$ superlattice reflections.

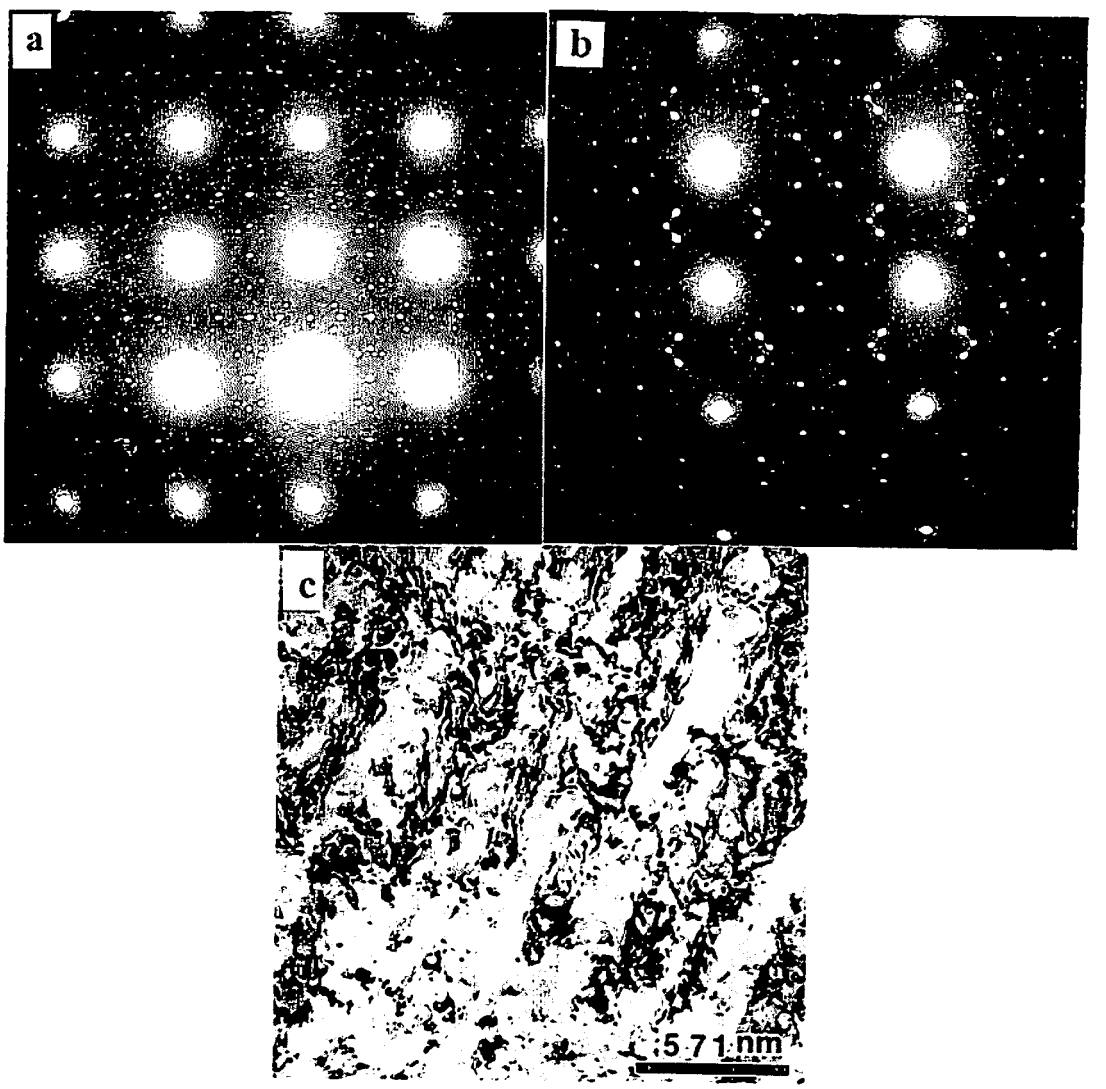



Figure 4-139. TEM microstructure of Hastelloy B2 alloy aged at 550°C for 1200 hours, a) and b) [001] and [112] zone diffraction pattern showing reflection at $DO_{22}$ and β superlattice positions, c) corresponding microstructure at [112] zone diffraction pattern showing early stage of striation of plates $DO_{22}$ phase.

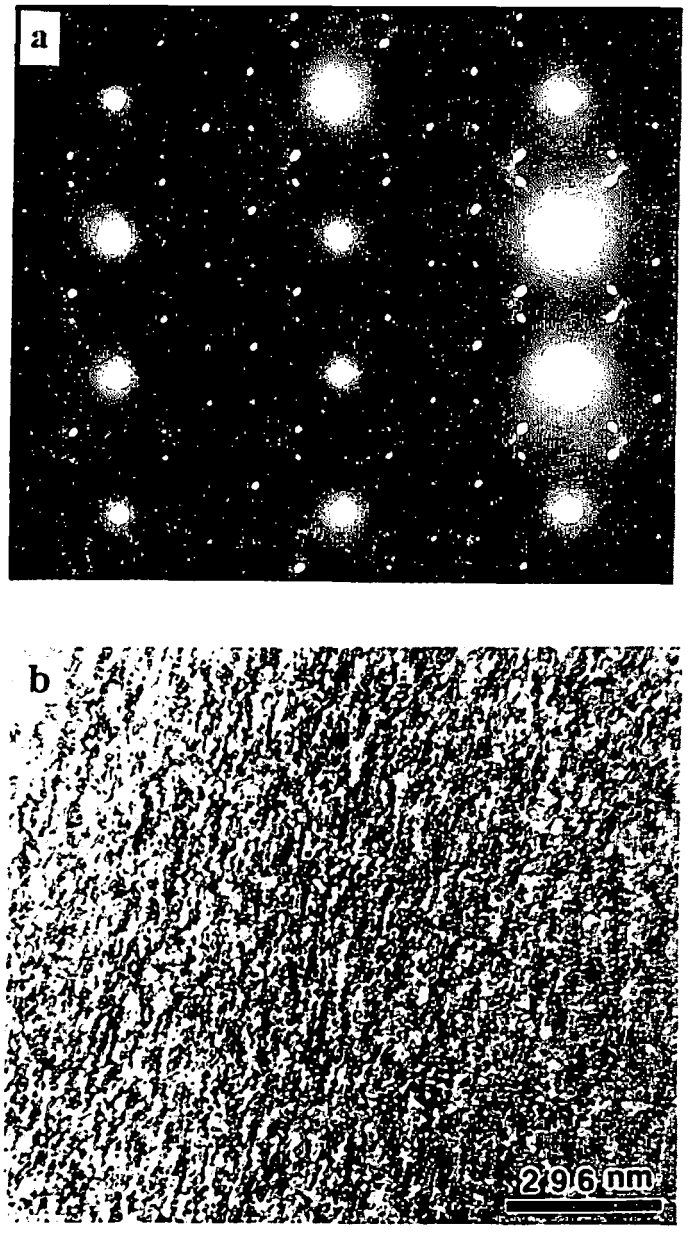



Figure 4-140. TEM microstructure of Hastelloy B2 alloy aged at 650°C for 200 hours, a) [112] zone diffraction pattern showing reflection at α and β superlattice spots, b) corresponding microstructure showing α and β phases

appearance of the SRO presence in Figure 4-137 is missing. The other spots are consistant with the DO22 phase, although some overlap with SRO α. Aging for 400 hours, did not change the microstructure nor the diffraction pattern.

Aging for 800 hours produced a similar domain structure (Figure 4-141b). The diffraction pattern (Figure 4-141a) showed only spots from β and weak $DO_{22}$ spots; no SRO α spots were present. The structure has begun to take on a lath-like appearance.

After aging for 1200 hours, the domains have coarsened and there is an indication of an aligned structure (Figure 4-142c). The electron diffraction patterns (Figure 4-142, a and b) show that the microstructure is a mixture of β and $DO_{22}$.

### 4.5.13. TEM Microstructural Evaluation of Hastelloy B2 Alloy upon Aging at 750°C

Aging at 750°C for 200 hours began to produce a lath-like structure as revealed by OLM [22]. This is shown in Figure 4-143a. The diffraction pattern shows that this structure contains β and the $DO_{22}$ phase.

After aging for 400 hours, some regions appeared to have recrystallized (Figure 4-144a). The diffraction pattern shows that only SRO α is present, but it is not clear why.

After aging for 800 hours, the structure is markedly coarsened (Figures 4-145, b and c). A [111] diffraction pattern shows superlattice spots. Note that in this orientation, superlattice spots from β will not be present in a [111] zone diffraction pattern. This pattern was not indexed so the phase were not identified.

Aging for 1200 hours formed a prominent lath-like lamellar structure in OLM [22]. This is shown in Figure 4-146a. The electron diffraction pattern in Figure 4-146b shows superlattice spots, but it was indexed, so the phases were not identified.

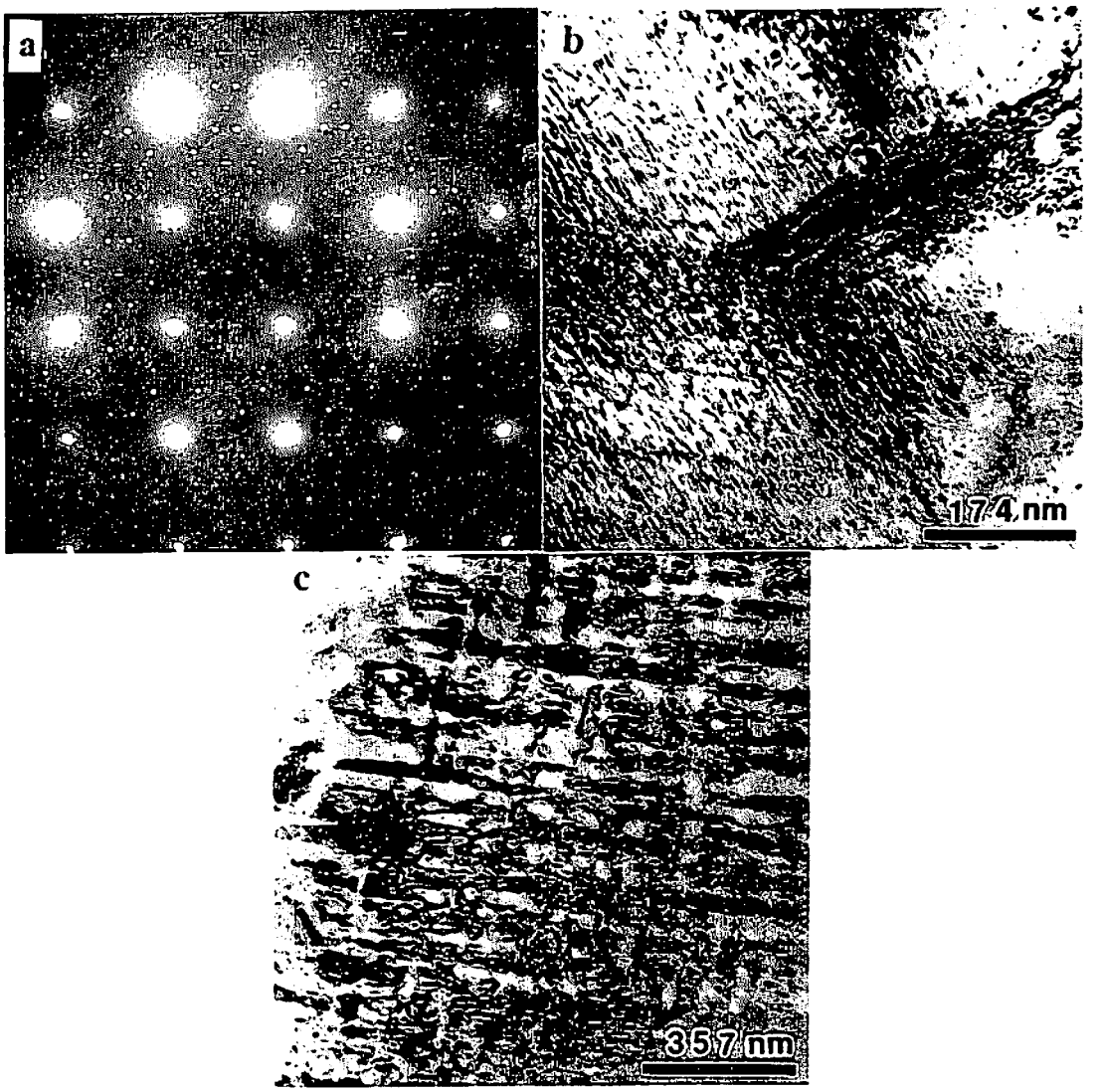



Figure 4-141. TEM microstructure of Hastelloy B2 alloy aged at 650°C for 800 hours, a) [001] zone diffraction pattern showing intensity maxima at $DO_{22}$ and β superlattice positions, b) corresponding microstructure showing $DO_{22}$ phase precipitates in β phase matrix, c) in some region, the early stage striation $DO_{22}$ phase formed.

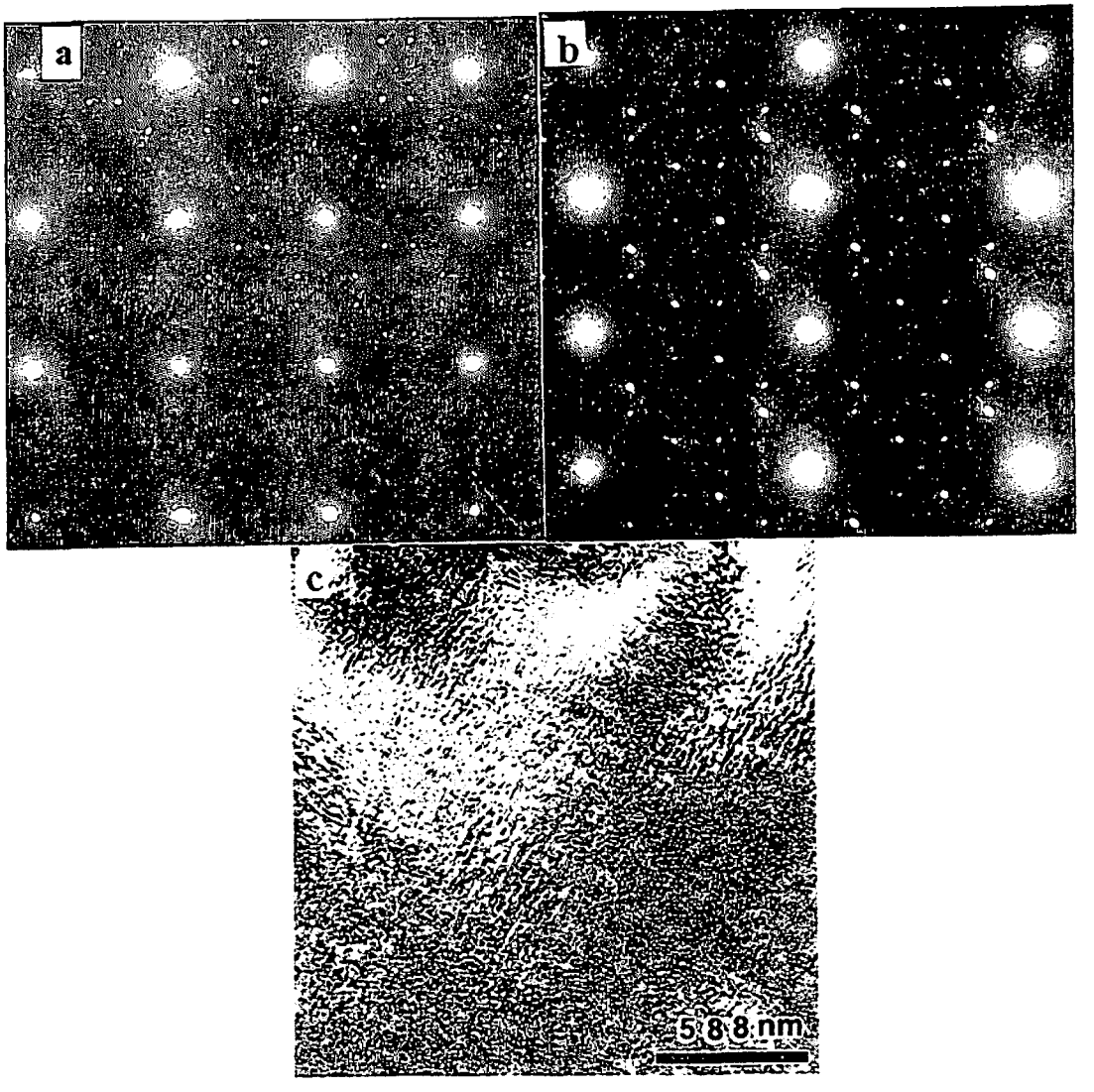



Figure 4-142. TEM microstructure of Hastelloy B2 alloy aged at 650°C for 1200 hours, a) and b) [001] and [112] zone diffraction pattern showing diffuse intensity maxima at $DO_{22}$ and β superlattice spots, c) corresponding microstructure at [112] zone showing fine $DO_{22}$ and β phase mixture.

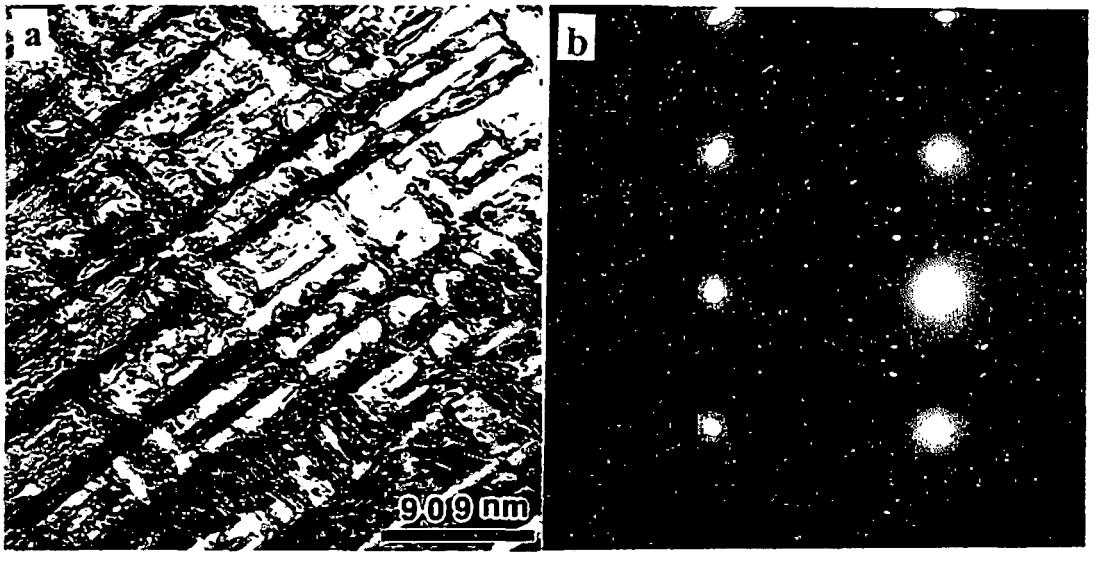



Figure 4-143. TEM microstructure of Hastelloy B2 alloy aged at 750°C for 200 hours, a) α and β phases, b) corresponding [112] zone diffraction pattern showing α and β phase.

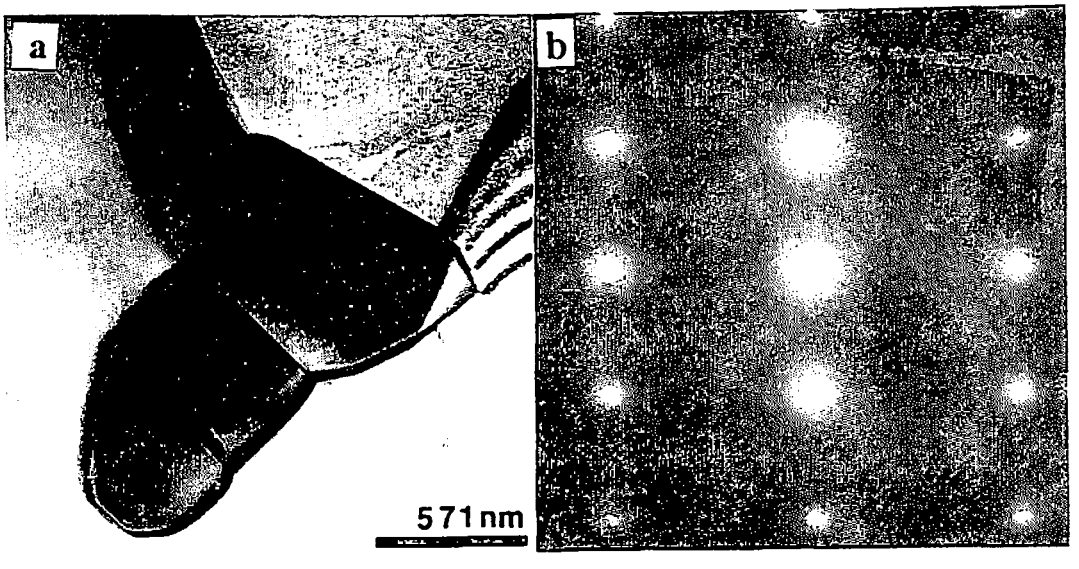



Figure 4-144. TEM microstructure of Hastelloy B2 alloy aged at 750°C for 400 hours, a) SRO α phase recrystallization at grain boundaries and caused, b) corresponding [112] zone diffraction pattern at recrystallization region showing diffuse intensity at {1 1/2 0} positions.

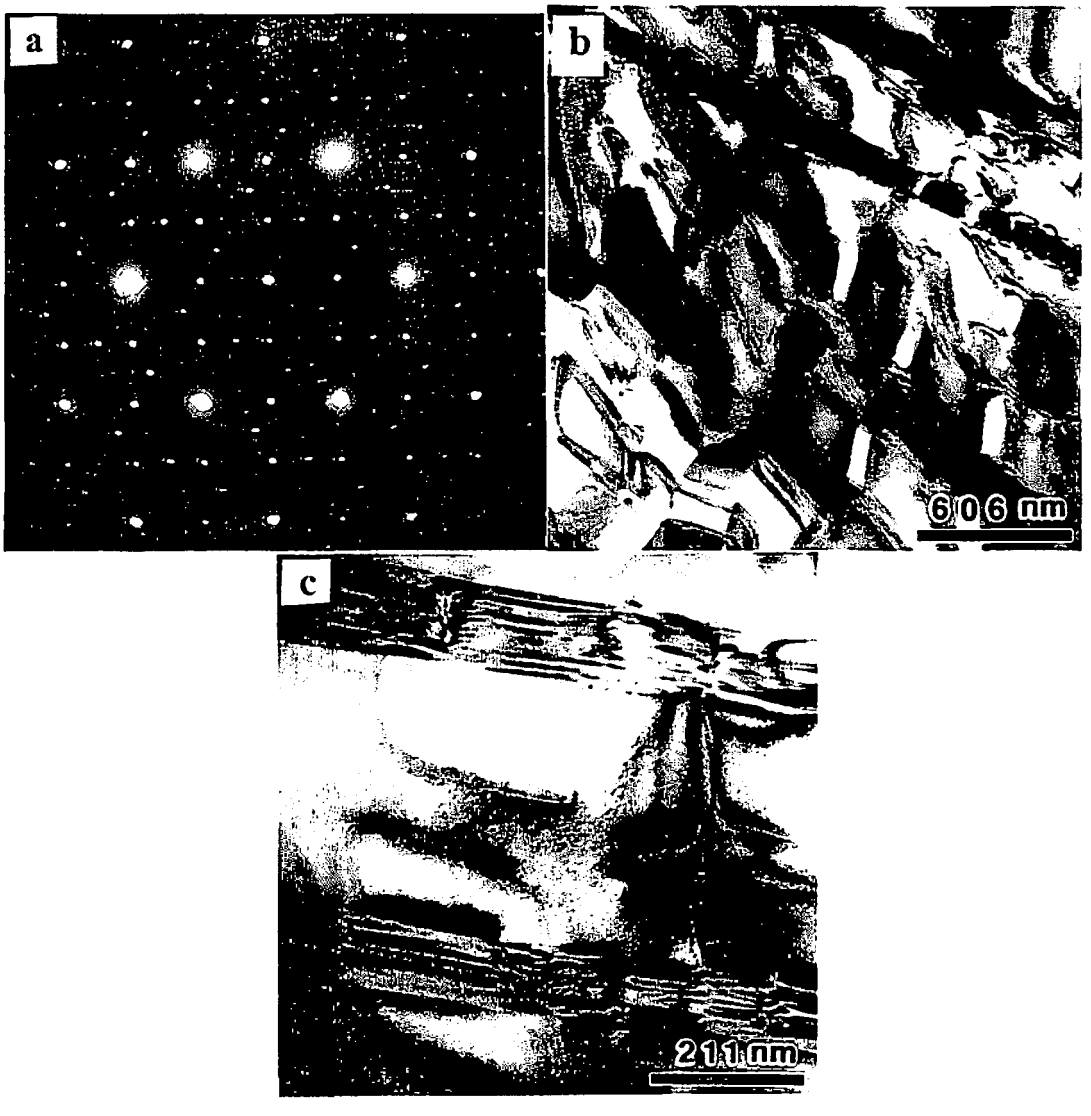



Figure 4-145. TEM microstructure of Hastelloy B2 alloy aged at 750°C for 800 hours, a) [1 1 1] zone diffraction pattern showing reflection at $DO_{22}$ superlattice positions, b) and c) coarsening $DO_{22}$ domain.

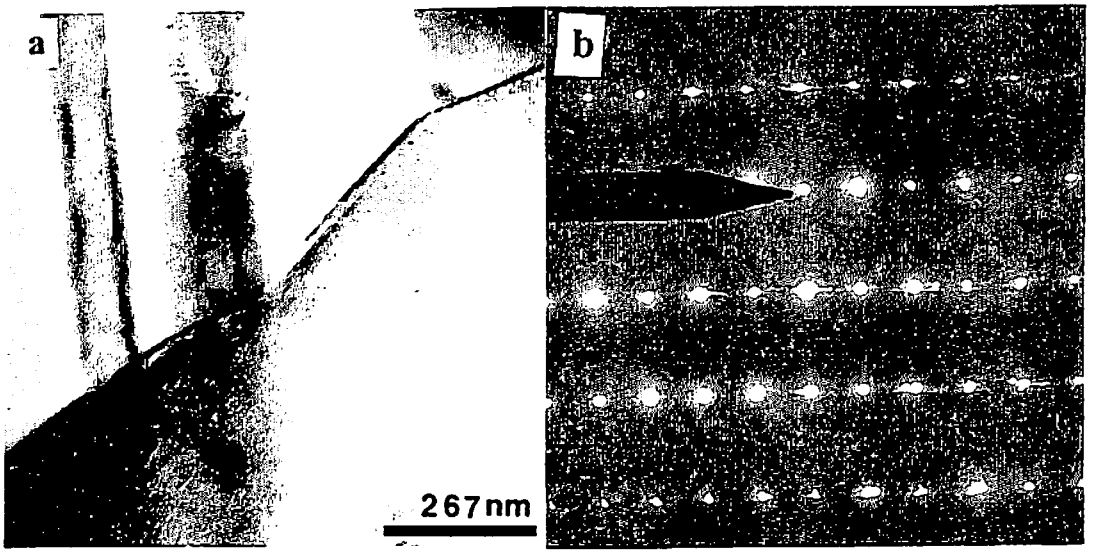



Figure 4-146. TEM microstructure of Hastelloy B2 alloy aged at 750°C for 1200 hours, a) lamellar structure form along the grain boundaries, b) corresponding diffraction pattern.

### 4.5.14. TEM Microstructural Evaluation of Hastelloy B2 Alloy upon Aging at 850°C

OLM revealed that aging for 200 hours at 850°C produced a prominent lath-like lamellar structure [22]. Only the matrix was observed in TEM microstructure (Figure 4-147). No diffraction pattern was obtained.

With increasing aging time to 400 hours, the amount of the lath-like structure increased [22]. However, the matrix (Figure 4-148b) shows no clear domains, and the diffraction pattern (Figure 4-148a) shows that the structure in only SRO $\alpha$.

After aging for 800 hours, the lath-like structure is shown in Figure 4-149a. The diffraction pattern from the A area shows the only SRO $\alpha$. No diffraction pattern form the B area was obtained.

After aging for 1200 hours, OLM shows the lath-like structure [22]. Figure 4-150a shows the SRO diffraction pattern from the matrix region. The microstructure shows only the matrix region.

### 4.5.15. Summary of Structure Formed upon Aging Hastelloy B2 Alloy

Table 4-14 summarizes the phase transformation in Hastelloy B2 alloy upon aging from 550°C to 850°C for up 1200 hours.

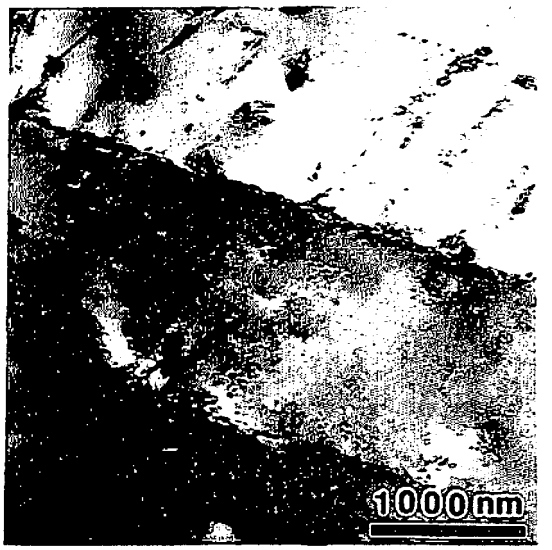



Figure 4-147. TEM microstructure of Hastelloy B2 alloy aged at 850°C for 200 hours, the dislocation loops.

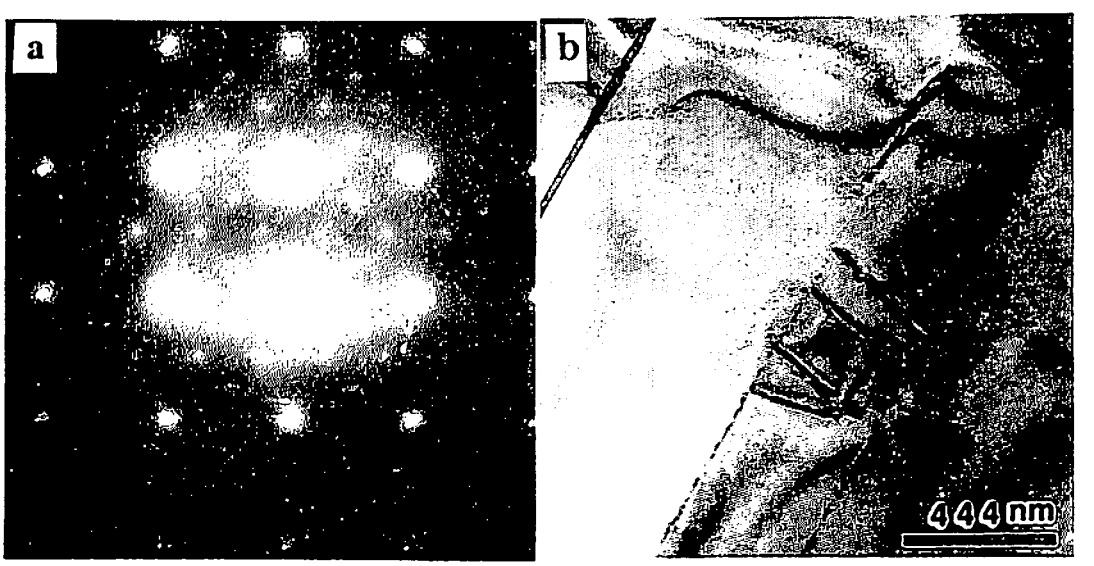



Figure 4-148. TEM microstructure of Hastelloy B2 alloy aged at 850°C for 400 hours, a) selected area diffraction pattern at [001] zone showing intensity maxima at {1 1/2 0} stops, b) corresponding microstructure showing the SRO α phase forms.

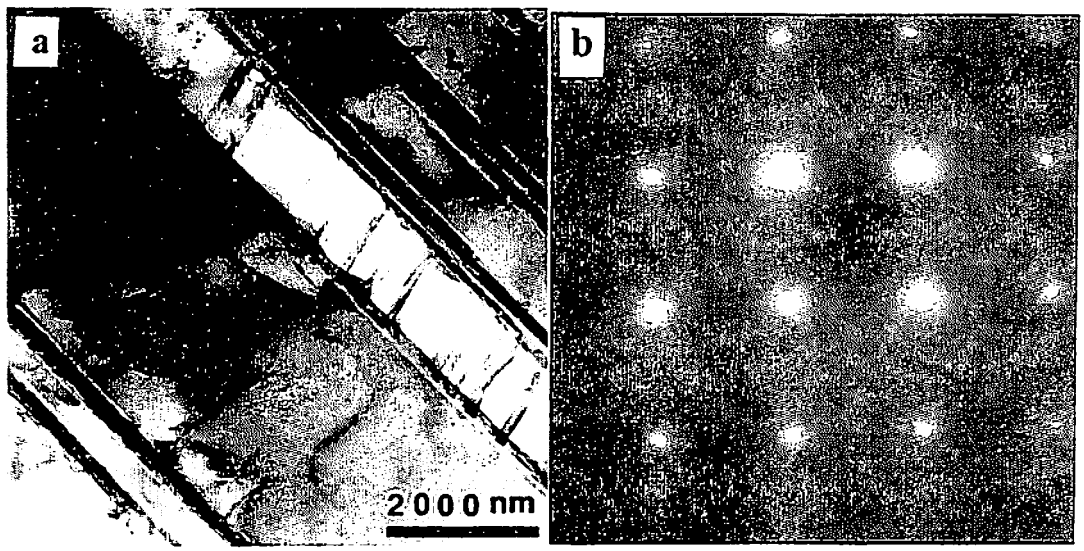



Figure 4-149. TEM microstructure of Hastelloy B2 alloy aged 850°C for 400 hours, a) the coursening lamellar structure, b) [001] zone selected area diffraction pattern showing the SRO α superlattice spots.

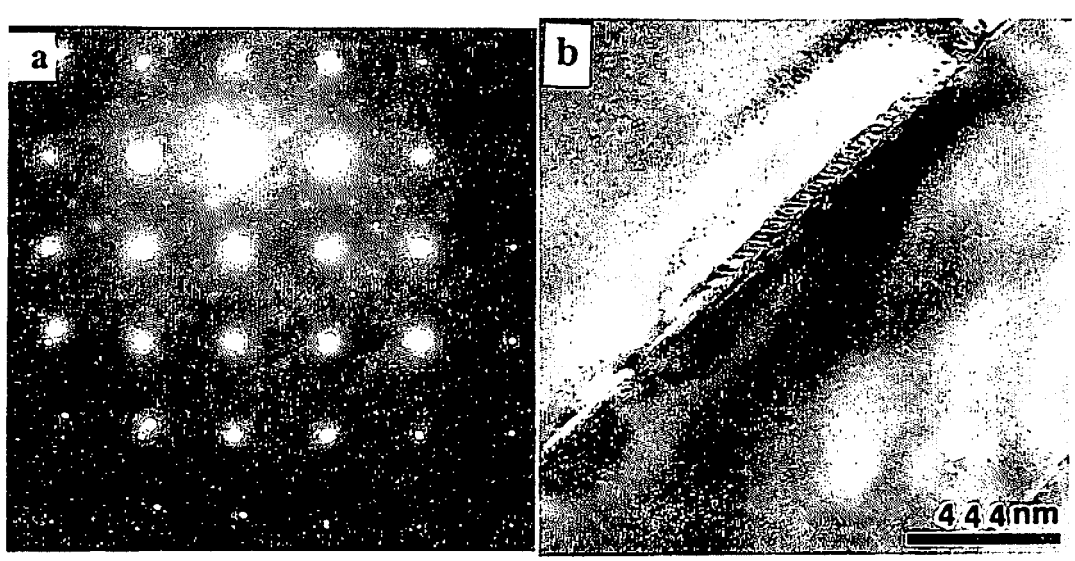



Figure 4-150. TEM microstructure of Hastelloy B2 alloy aged at 850°C for 1200 hours, a) [001] zone diffraction pattern showing diffuse intensity maxima at SRO α superlattice spots, b) corresponding microstructure showing SRO α phase and dislocation pile-ups at grain boundary.

Table 4-14 . Microstructure feature of Hastelloy B2 alloy

| | 200 hours | 400 hours | 800 hours | 1200 hours |
|---|---|---|---|---|
| 550°C | SRO $\alpha + \beta$ | SRO $\alpha + \beta$ | $\beta + DO_{22}$ | $\beta + DO_{22}$ |
| 650°C | $\beta + DO_{22}$ | $\beta + DO_{22}$ | $\beta + DO_{22}$ | $\beta + DO_{22}$ |
| 750°C | lath structure $\beta + DO_{22}$ | SRO $\alpha$ recrystallization in a few region | $DO_{22}$ + ? | lamellar structure |
| 850°C | - | SRO $\alpha$ | SRO $\alpha$ + lamellar structure | SRO $\alpha$ (matrix) |

## 4.7. **Corrosion Resistance Evaluation**

As described in the literature review, Hastelloy alloy B2 has demonstrated an unusual corrosion resistance to nonoxidizing solutions of several mineral acids, including hydrochloric, sulfuric, and phosphoric acids at elevated temperature. It is well known that aluminum alloys have good corrosion resistance in natural atmospheres [92]. The influence of aluminum on the corrosion resistance to environments depends on the presence of a thin, compact film of adherent aluminum oxide on the surface. The two factors that mostly affect a material's corrosion resistance are alloy composition and fabrication practice. Any factors which can vary the microstructural stability can affect the alloy corrosion resistance. The general corrosion behavior of Ni-Mo-Al alloys was

examined and the results are given here. Also some experimental results from $Ni_4Mo$ alloy are included for comparison purposes.

### 4.7.1. Corrosion Resistance Evaluation of $Ni_4Mo$ Alloy

$Ni_4Mo$ alloy possesses excellent corrosion resistance in a variety of nonoxidizing acid conditions, especially in a hydrochloric environment. Therefore, the general corrosion resistance and localized corrosion resistance of $Ni_4Mo$ alloy (as-received condition) has been examined by ASTM A262 Practice A, potentiodynamic anodic polarization and a modified U-bend test based on the design of the ASTM G-30 U-bend test. After aging at 750°C for 100 hours, the $Ni_4Mo$ alloy was examined by cyclic anodic polarization and polarization resistance tests.

#### (a) ASTM A262 Practice A Evaluation

After the ASTM A262 Practice A test, the oxalic electrolytic etched structure is presented in Figure 4-151. The microstructure in $Ni_4Mo$ alloy showed that $\alpha$ grain boundaries appear. The nonacceptable ditch structure was not observed. It was clearly shown that the $Ni_4Mo$ alloy passed the ASTM A262 practice A test.

#### (b) Potentiodynamic Anodic Polarization Test

According to ASTM standard G5-87 [61] and G-102 [92], the result from potentiodynamic anodic polarization test for $Ni_4Mo$ alloy is shown in Tables 4-15 and Figure 4-152. Figure 4-152 does not exhibit an anodic peak associated with the active to passive transition. In general, the results obtained agree with the results reported by Jones for Hastelloy B2 alloy conducted in deareated 1 N $H_2SO_4$ [93].

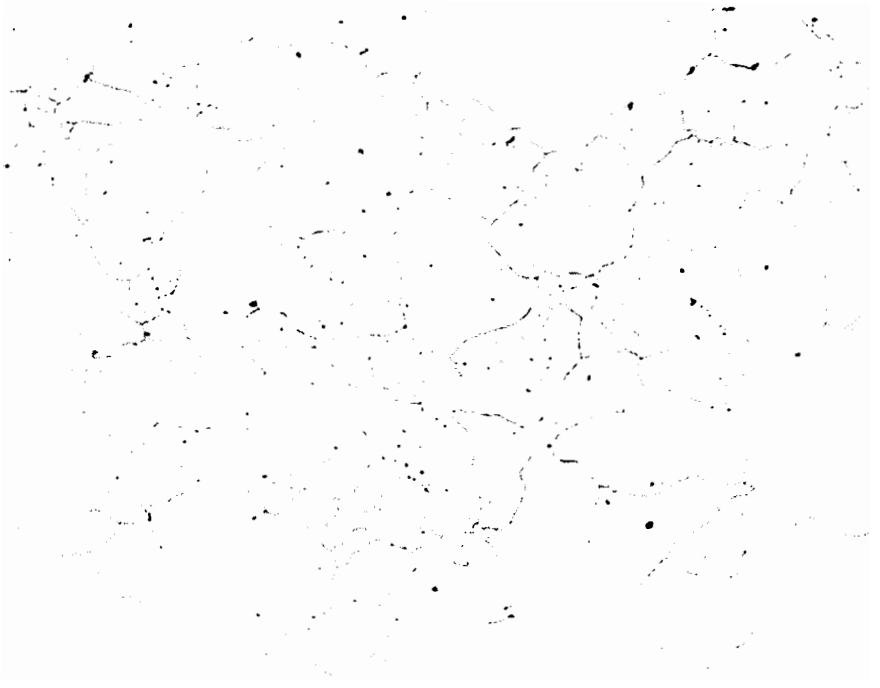


Figure 4-151. Microstructure in $Ni_4Mo$ alloy showing result of ASTM A 262 Practice A.

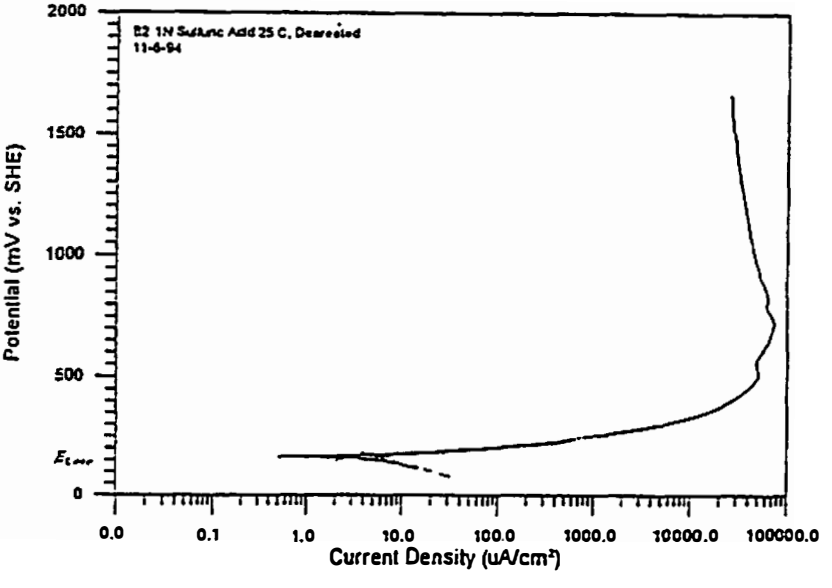



Figure 4-152 Potentiodynamic anodic polarization curve in $Ni_4Mo$ alloy (1 N $H_2SO_4$ solution in deareated condition).

Table 4-15. Anodic Polarization Parameter Measurement in $Ni_4Mo$ Alloy

| $E_{corr}$ | $i_{corr}$ | CPR (mpy) |
|---|---|---|
| +166 mV | 17.3 μA/cm$^2$ | 7.1 |

$CPR = 0.129\ (M/n)i_{corr}/9.22$

(c) Modified U-Bend Test

In order to consider the influence of stress on the stress corrosion resistance, the U-bend test was conducted (see section 3). Due to the limitation of available material, a modified U-bend test was used. However, the modified test was sufficient to evaluate the stress influence on intergranular corrosion attack. After the modified U-bend test (Figure 3-3), SEM topographic morphology of the tested surface is shown in Figure 4-153. Intergranular cracking was found in the sample.

After A262 Practice A, Potentiodynamic Anodic Polarization and Modified U-Bend test, the $Ni_4Mo$ alloy (as-received condition) showed an acceptable etch structure in the A262 practice A test and did not exhibit an anodic peak associated with active to passive transition in the potentiodynamic anodic polarization test, and showed relative corrosion good resistance (7 mpy). However, there was a notable intergranular corrosion attack tendency under the stressed condition.

4.7.2. Corrosion Resistance Evaluation of Ni-Mo-Al Alloys

The $Ni_4Mo$ alloy and the Ni-Mo-Al alloys chosen for corrosion evaluation. All samples were solution treated at 1280°C for 50 hours, water quenched, then aged at 750°C for 100 hours. The corrosion resistance was determined by using cyclic anodic polarization and polarization resistance techniques from which general corrosion resistance of samples examined can be extracted.

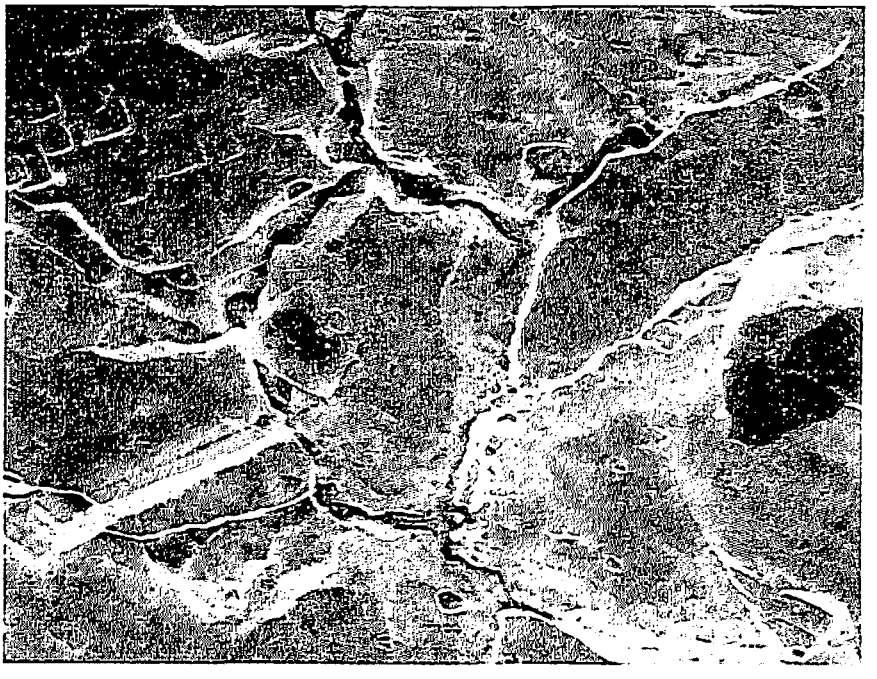


Figure 4-153. SEM microstructure in $Ni_4Mo$ alloy showing interganular cracking in U-bend test sample.

(a) Cyclic Polarization Evaluation of Ni-Mo-Al Alloys

A cyclic polarization scan can provide a qualitative view of pitting corrosion. The concept of a typical cyclic anodic polarization curve is shown in Figure 4-154. It starts at the open-circuit corrosion potential, Ecorr, then proceeds in the up-scan direction through the passive range where the material is uniformly corroding at a very low rate. At a localized-corrosion breakdown potential, $E_B$, the anodic current density increases suddenly and dramatically, an indication of pitting corrosion [94]. Many types of corrosion attack such as intergranular corrosion and crevice corrosion initiate at pits. The cyclic anodic polarization curve can give information about pitting corrosion resistance. If $E_{corr}$ is less than $E_{prot}$, there is no pitting corrosion; if $E_{corr}$ is greater than $E_{prot}$ and less than $E_B$, new pits cannot initiate but old pits can still grow; If $E_{corr}$ is greater $E_B$, pitting corrosion starts. Therefore, information about pitting behavior can be obtained from the cyclic polarization curve. The general corrosion behavior of materials can be distinguished through this approach.

The results of cyclic anodic polarization of Ni-Mo and Ni-Mo-Al alloys are shown in Figures 4-155 to 4-159. No passive film phenomenon was observed in all cyclic curves. Only Figure 4-159 shows a little hystersis loop. The $Ni_4Mo$ and Ni-Mo-Al alloys in 14% hydrochloric acid solution all showed uniform active corrosion. In general, Ni-Mo-Al alloys showed a similar corrosion resistance to $Ni_4Mo$ alloy. No corrosion pits were observed in the tested samples after cyclic polarization testing.

(b) Polarization Resistance for Ni-Mo-Al Alloys

After aging at 750°C for 100 hours, the $Ni_4Mo$ and Ni-Mo-Al alloys were examined by polarization resistance testing. The average data based on 2 to 4 independent tests for each alloy are shown in Table 4-16. As indicated, the $i_{corr}$ value are

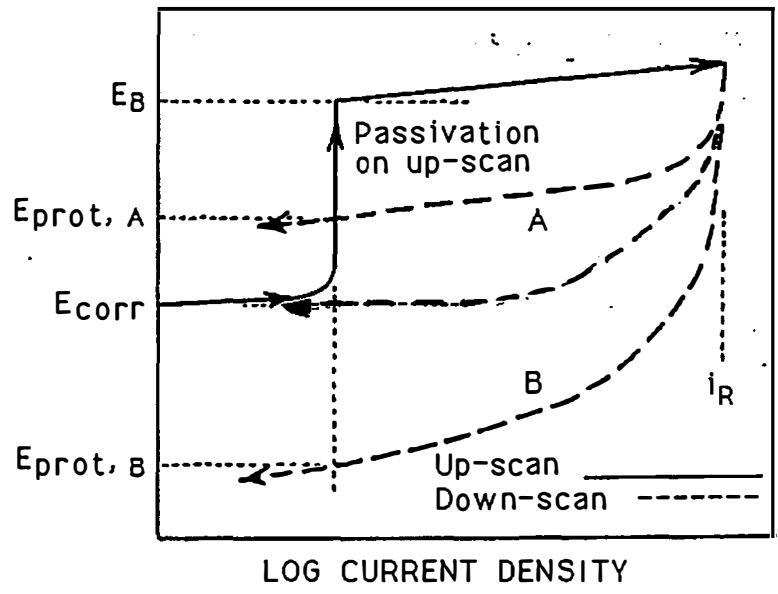



Figure 4-154. Schematic diagram of cyclic polarization curve.

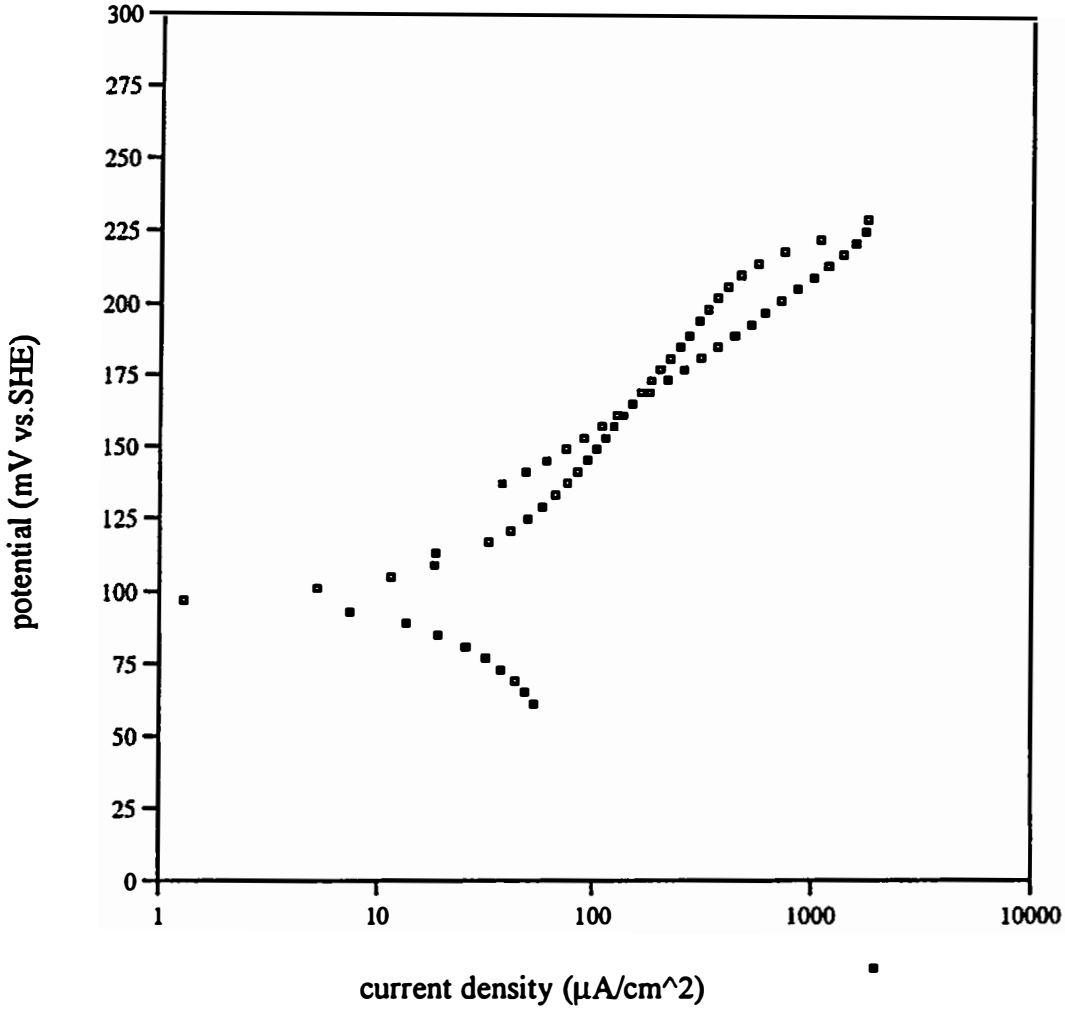



Figure 4-155. Cyclic polarization of $Ni_4Mo$ alloy in 14% hydrochloric solution after aging at 750°C for 100 hours.

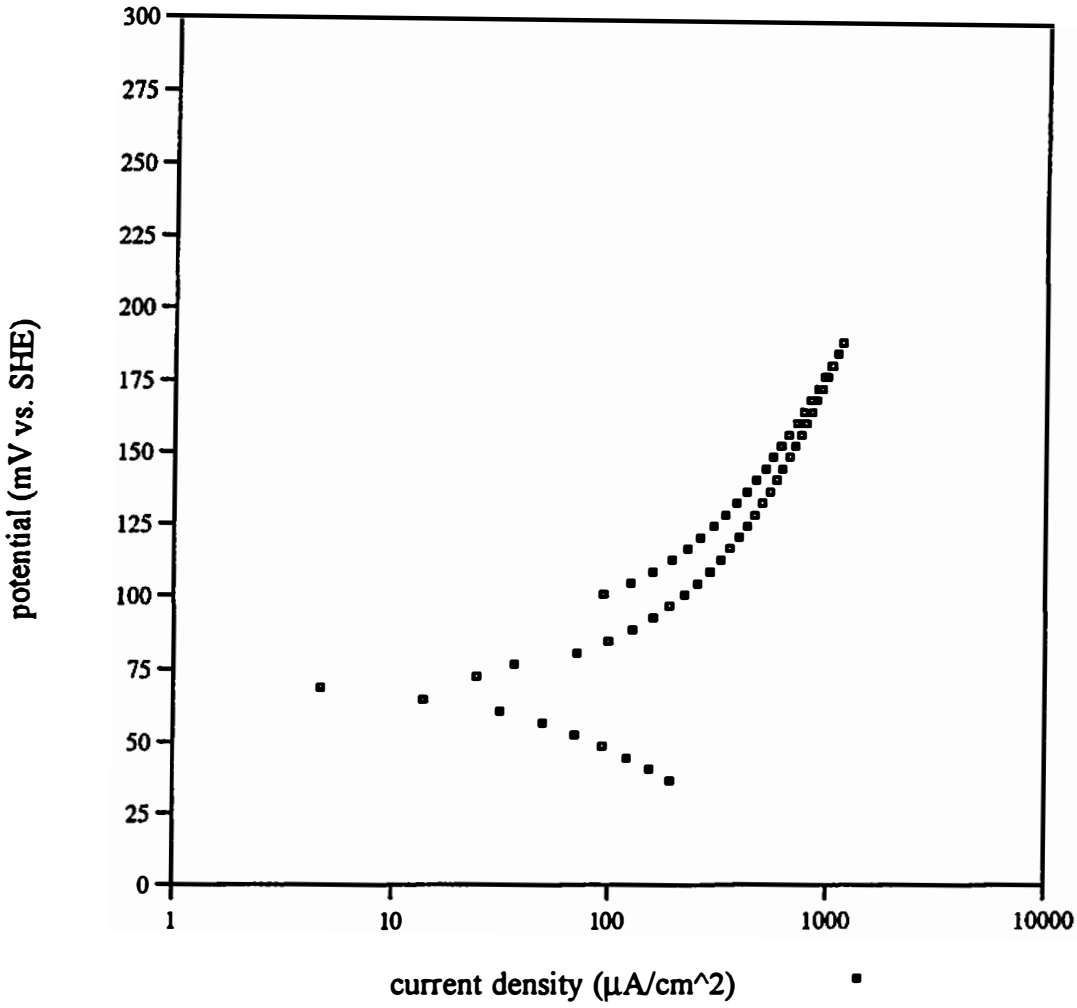



Figure 4-156. Cyclic polarization behavior of 2 at.% Al alloy in 14% hydrochloric solution after aging at 750°C for 100 hours.

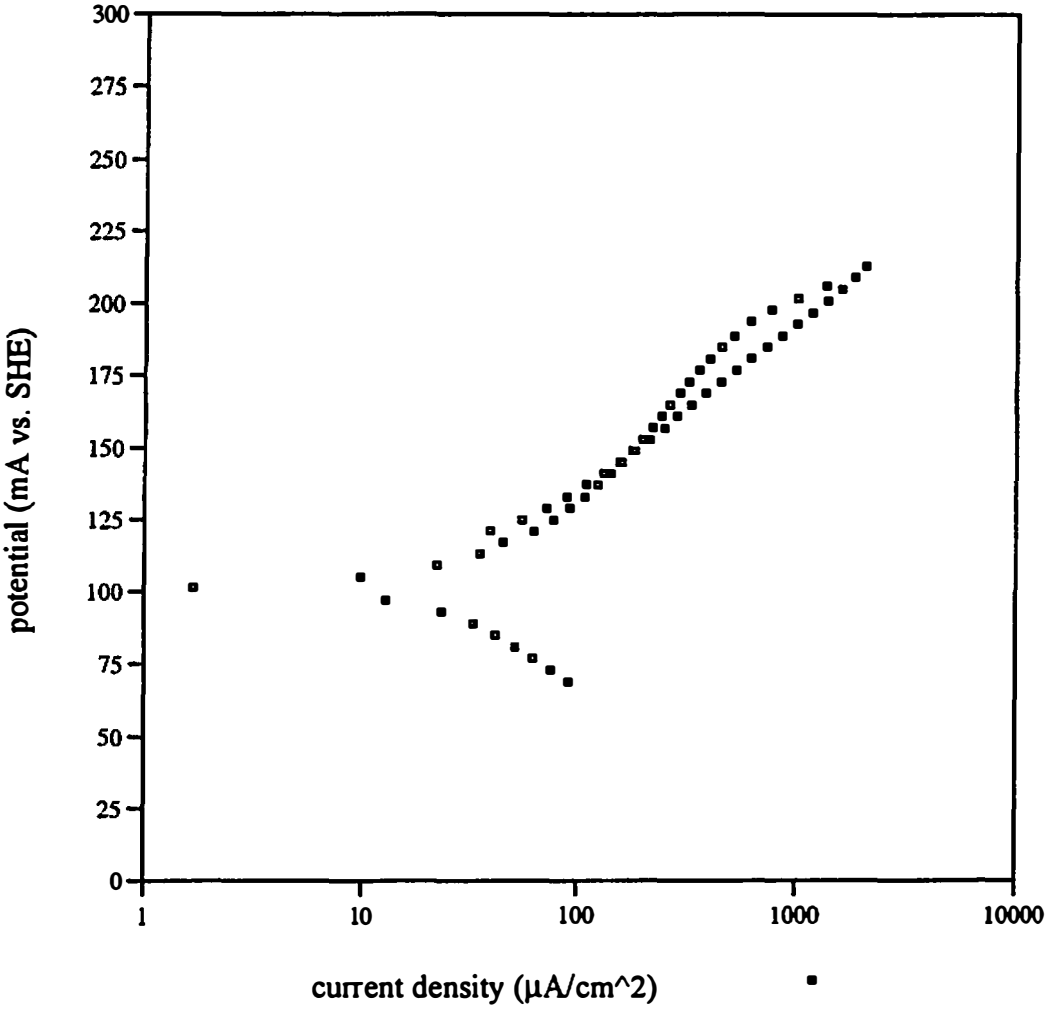



Figure 4-157. Cyclic polarization behavior of 5 at.% Al alloy in 14% hydrochloric solution after aging at 750°C for 100 hours.

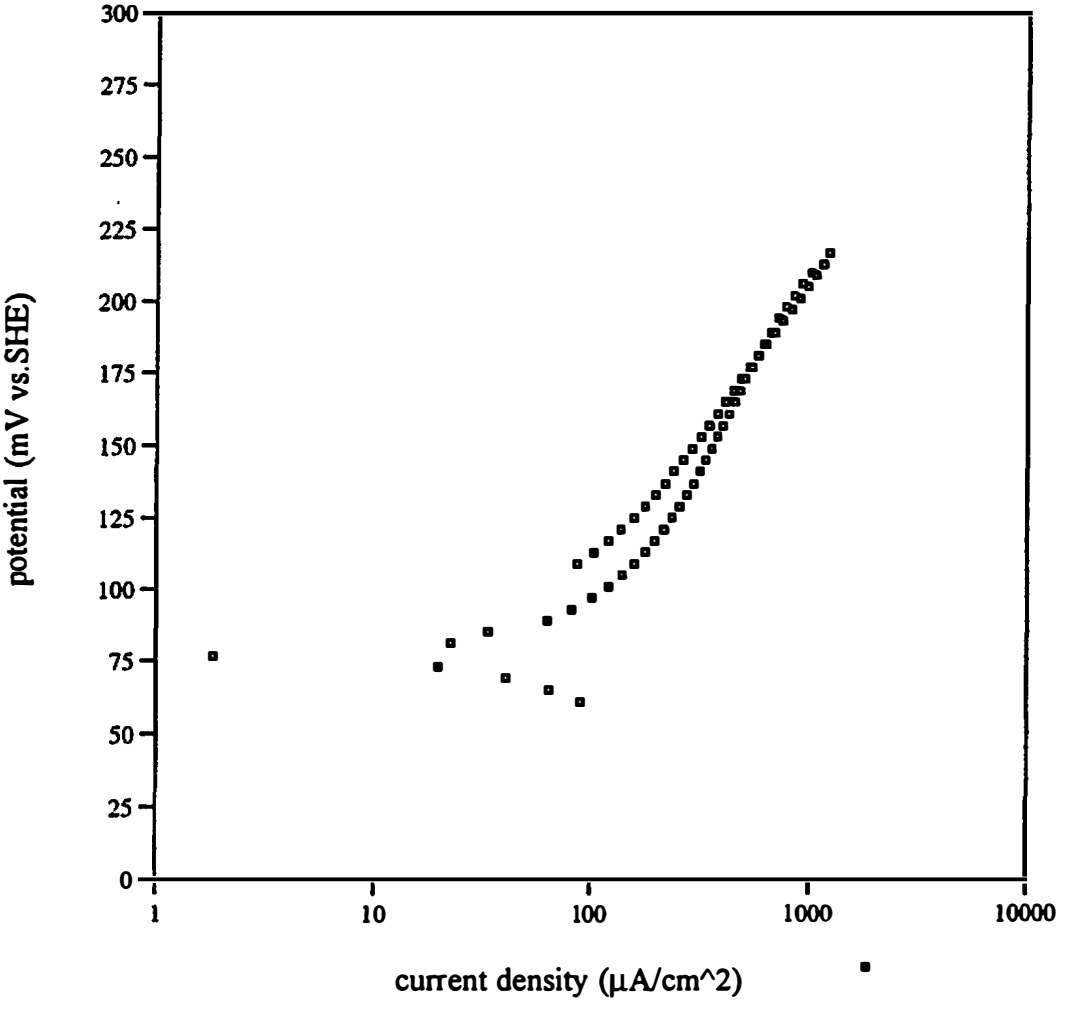



Figure 4-158. Cyclic polarization behavior of 7 at.% Al alloy in 14% hydrochloric solution after aging at 750°C for 100 hours.

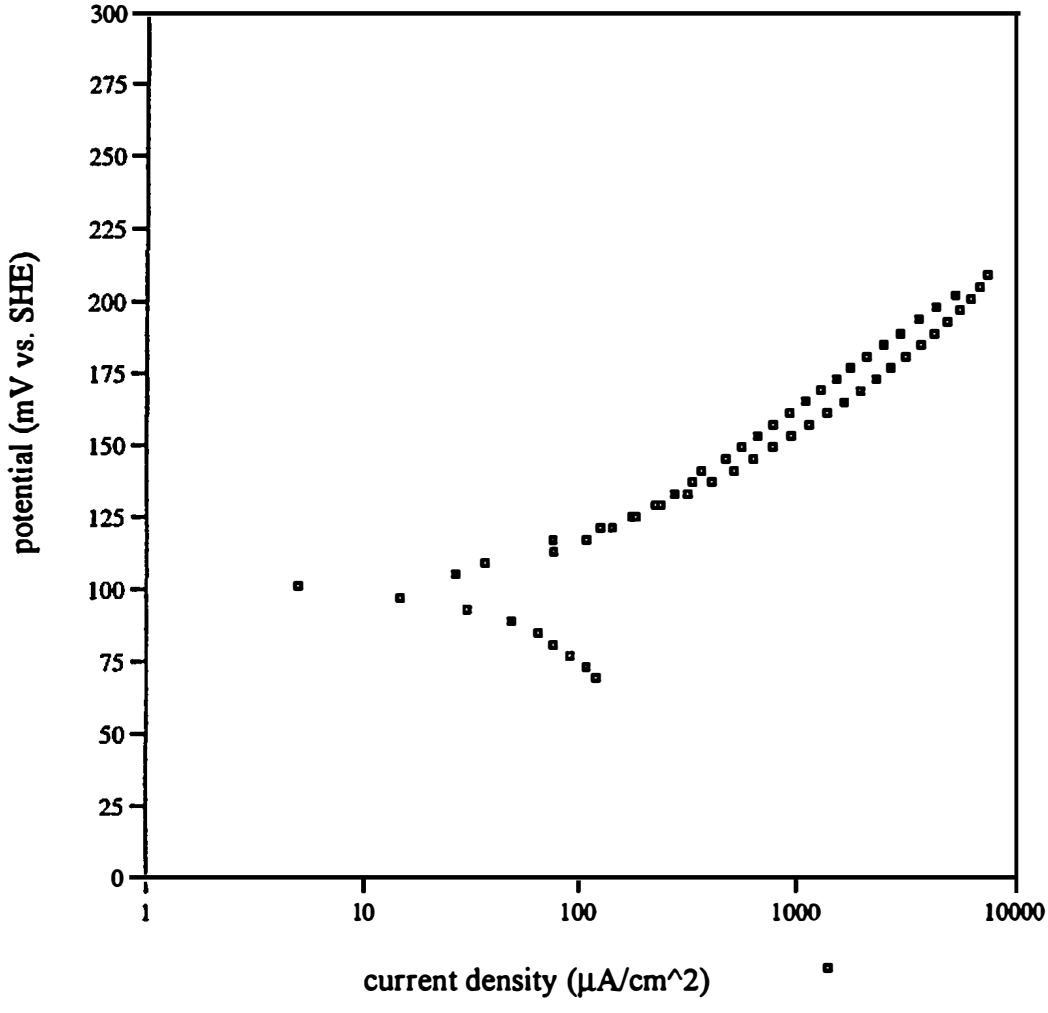



Figure 4-159. Cyclic polarization behavior of 9 at.% Al alloy in 14% hydrochloric solution after aging at 750°C for 100 hours.

different for the Ni-Mo-Al alloys. The differences in corrosion resistance are associated with the difference in as microstructures related to the aluminum content.

The microstructure in $Ni_4Mo$ alloy is a mixture of β and $Ni_2Mo$ phases and it shows good corrosion resistance . The 2 at.% Al alloy is β, $Ni_2Mo$ and $DO_{22}$ mixture structure and shows fair corrosion resistance. The 5 at.% Al alloy is two phase structure (lamellar structure) and its corrosion resistance is fair compared to the $Ni_4Mo$ alloy. As indicated from previous sections, the 7 at.% Al alloy contains $DO_{22}$ and $Ni_2Mo$ phases with an amount of lamellar structure along the grain boundaries. The 7 at.% Al alloy showed somewhat better corrosion resistance than 2 and 5 at.% Al alloy. Nevertheless, this observation indicates that the lamellar structure may decrease the corrosion resistance. It also should be noted that 7 at.% Al alloy showed a relatively larger grain size (Figure 4-45) with fewer lamellar structure regions. Thus, greater corrosion resistance is shown in 7 at.% Al alloy. Therefore, the materials possessing a lamella structure usually showed a higher corrosion tendency compared to the single phase materials for the same aging condition. The microstructure in 9 at.% Al alloy showed 50% lamellar structure and 50% $DO_{22}$ and $Ni_2Mo$ phases. The corrosion resistance of 9 at.% Al alloy was slightly better than that of 5 at.% Al alloy.

However, the corrosion resistances for all samples showed only small differences. A range of 5 to 20 mpy is considered good corrosion resistance and $Ni_4Mo$ and 7 at.% Al alloys were within this range. A range of 20 to 50 mpy is considered fair corrosion resistance and the other Ni-Mo-Al alloys fell in this range. The effect of aluminum did not significantly influence the corrosion behavior for the $Ni_4Mo$ alloy. However, it is noted that aluminum as an oxide-film-forming element has beneficial influence on corrosion resistance, but aluminum also enhances the formation of the lamellar structure which degrades the corrosion resistance (for example: the 5 at.% Al alloy).

Table 4-16 Summary of Polarization Resistance Results (average values based on 2 to 4 independent tests for each alloy)

| | $E_{corr}$ (mV (SHE)) | $i_{corr}$ (μA/cm^2) | corrosion rate (mpy) | relative corrosion resistance | microstructure |
|---|---|---|---|---|---|
| $Ni_4Mo$ | +52 | 40 | 16 | good | $\beta + Ni_2Mo$ |
| 2 at.% Al | +66 | 70 | 27 | fair | $\beta + DO_{22} + Ni_2Mo$ |
| 5 at.% Al | +75 | 112 | 41 | fair | $\gamma + \gamma'$ |
| 7 at.% Al | +86 | 54 | 19 | good | $Ni_2Mo + DO_{22}$, $\gamma+\gamma'$ (10%) |
| 9 at.% Al | +69 | 93 | 33 | fair | $Ni_2Mo + DO_{22}$, $\gamma+\gamma'$ (50%) |

corrosion rate = 0.129 i (M / n) D

i = current (μA/cm$^2$)

M= atomic weight

n = the number of equivalent exchanged ( Ni=2, Mo=3, Al =3)

D = density of the alloy (g/cm$^3$) (The density of Hastelloy B = 9.22 g/cm$^3$ was used)

for alloy: equivalent weight = $\sum \left( \frac{f_i}{M_i / n_i} \right)$

$f_i$ = mass fraction

$n_i$ = electrons exchanged

$M_i$ = atomic weight

## CHAPTER 5

# CONLUSIONS AND RECOMMENDATIONS

## CONLUSIONS

1. The binary alloy contained only SRO $\alpha$ in the solution treated condition, but with increased aluminum content the structure changed to a very fine domain mixture of the non-equilibrium $DO_{22}$ and $Ni_2Mo$ phases. Apparently the addition of aluminum to $Ni_4Mo$ enhances the kinetics of the decomposition of the SRO $\alpha$ during quenching from a solution heat treatment temperature.

2. In the solution heat treated condition, aluminum increased the hardness considerably. The $Ni_4Mo$ alloy had a hardness of about 220HV while the 9 at.% Al alloy had a value of about 460 HV. All the alloys in the solution heat treated condition appeared to be ductile. Thus the addition of Al significantly increases the hardness in the solution heat treated condition yet good ductility is retained. This implies that these Al alloys could be heated into the a range (e.g., 1000°C) then quenched, and a structure would be obtained which would have a hardness significantly higher than the binary alloy yet have good ductility.

3. After aging for 100 hours from 600 to 950°C, all alloys were harder than the solution heat treated condition. Also, for a given aging treatment, the hardness increased with aluminum content, or in some case remained about the same for

the higher aluminum alloys. The highest hardness was obtained after aging at 700°C, attaining a value of about 650 HV for the 5, 7 and 9 at.% Al alloys. Thus to obtain maximum hardness upon aging for 100 hours (but see 4. below), the aging temperature should be near 700°C.

4. upon aging for 10, 50 and 100 hours at 750°C for all alloys the hardness increased significantly after 10 hours, then in 50 hours attained a value about twice that of the solution heat treatment condition, then remained about the same after aging 100 hours. Thus an optimum aging time is somewhere between 10 and 50 hours at this temperature.

5. However, in all the aged condition, the $Ni_4Mo$ alloy and all the aluminum alloys were brittle. Thus, the addition of aluminum dose not prevent embrittlement during aging.

6. The structure of the solution heat treated condition of the higher aluminum alloys changed to a mixture of the intermetallic phases $\gamma$ and d and matrix of a fine domain structure of the non-equilibrium $DO_{22}$ and $Ni_2Mo$ phases. In the 7 and 9 at.% Al alloys, the aluminum-rich $Ni_3(Al + Mo)$ $\gamma'$ phase formed as well as pure molybdenum particles. The morphology of these phases varied, with some as precipitates in the grain boundaries, some as a lamellar structure, and some as relative fine precipitates. The hardness associated with aging is accused by the formation of these complex microstructures. However, these brittle intermatallic phases with a complex morphology is the cause of the accompanying embrittlement.

7. The $Ni_4Mo$ and Ni-Mo-Al alloys show similar good corrosion resistance and no pitting corrosion initiation. The aluminum can influence the microstructure formation in Ni-Mo alloy upon aging. After 5 at.% Al was added in the $Ni_4Mo$ alloy, the lamellar structure ($\gamma + \gamma'$) formed and the corrosion resistance reduced slightly. The fine domain of $DO_{22}$ and $Ni_2Mo$ showed the corrosion resistance. Thus, the corrosion resistance was found to be slightly dependent on aluminum content.

## RECOMMENDATIONS

1. A detailed evaluation of the tensile mechanical properties of these alloys after equilibrating in the a region (e.g., 1 hours at 1000°C and quenching) should be conducted.

2. A careful examination of the effect of cooling rate from the a region on the mechanical properties and structure should be undertaken. From a practical standpoint, it is important to know what range can be tolerated without inducing structural change on cooling which cause embrittlement.

3. Stress corrosion cracking evaluation of the 7 and 9 at.% Al alloys should be studied

# REFERENCES

# REFERENCES


1. W. L. Mankins and S. Lamb, "Nickel and Nickel Alloys", ASM Handbook, 10th Edition, Vol. 2, Properties and Selection: Nonferrous Alloys and Special-Purpose Materials, pp. 428-445 (1990).

2. C. R. Brooks, J. E. Spruiell, and E. E. Stansbury, "Physical Metallurgy of Nickel-Molybdenum Alloys", Metals Reviews, 29:210-248 (1984).

3. C. T. Liu and J. O. Stiegler, "Ordered Intermetallics", ASM Handbook, 10th Edition, Vol. 2, Properties and Selection: Nonferrous Alloys and Special-Purpose Materials, pp. 913-936 (1990).

4. S. J. Matthews, " Selection of Nickel Base Corrosion-Resistant Alloys Containing Molybdenum," ASM Handbook, 10th Edition Vol. 6, Welding, pp. 593-597 (1990).

5. Hastelloy Alloy B2, The Technology Materials Division, Cabot Corporation, Kokomo, IN (1977).

6. S. Cao, C. R. Brooks and G. Whittaker, "The Structure of the Heat-Affected Zone in Welds of a Ni-29wt.% Mo Commercial Alloy (Hastelloy B2)", Materials Characterization, 33:21-32 (1994).

7. W. Z. Friend, Corrosion of Nickel and Nickel-Base Alloys, John Wiley and Sons Inc., New York (1980).

8. A. I. Asphahani, "Corrosion of Nickel-Base Alloys," Metals Handbooks 9th Edition, Vol. 13, Corrosion, pp. 641-657 (1984).

9. M. Raghavan, B. J. Berkowitz and J. C. Scanlon, "Electron Microscopic Analysis of Heterogeneous Precipitates in Hastelloy C-276", Metallurgical Transaction A, 13A:979-984 (1982).

10. M. J. Cieslak, T. J. Headley and A. D. Roming, "The Welding Metallurgy of Hastelloy Alloy C-4, C-22 and C-276", Metallurgical Transactions, 17A:2035-2047 (1986).

11. Hastelloy Alloy S, Technical Information, Haynes International, Inc., Kokomo, IN (1988).

12. Hastelloy Alloy W, Technical Information, Haynes International, Inc. Kokomo, IN (1989).

13. H. M. Tawancy, "Identification of Eta-Carbide in a Commercial Ni-Mo Alloy (Hastelloy Alloy B2)," Journal of Materials Science, 16:1117-1118 (1981).

14. ASM Handbook, 10th Edition, Vol. 3, Alloy Phase Daigrams, Metals Park, Ohio (1992).

15. P. V. Guthrie and E. E. Stansbury, "X-ray and Metallographic Study of the Nickel-rich Alloys of the Nickel-Molybdenum System II', Report ORNL 3078, Oak Ridge National Laboratory, TN (1961).

16. R. E. W. Casselton and W. Hume-Rothery, "The Equilibrium Diagram of the System Molybdenum-Nickel", J. Less-Common Metals 7:212-224 (1964).

17. W. E. Norem, Ph.D. Dissertation, University of Tennessee, 1963.

18. T. S. Lei, Ph.D. Dissertation, University of Tennessee, 1979.

19. M. Brauwers, J. Giner, J. V. Rest and F. Brouers, "Influence of Long Range Order on Electrical Resistivity in Alloys", Solid State Communication 17:229-232 (1975).

20. C. R. Brooks and Y. M. Wang, "Tensile Properties and Fractograply of Aged Hastelloy B2 (550°C-850°C for up to 1200H)", Materials Characterization 25:185-197 (1990).

21. W. E. Clayton and C. R. Brooks, "The Effect of Aging on the Tensile Mechanical Properties of High-Purity Binary Ni-10, -20, and -30 wt Pct Cr Alloy", Metallurgical Transactions 2:531-535 (1971).

22. C. R. Brooks and Y. M. Wang, "Effect on the Miocrostructure of Aging Hastelloy B2 from 550 to 850°C", Metallography 23:57-86 (1989).

23. D. F. Roan and C. R. Brooks, "The Effect of Aging on the Mechanical Properties of a Ni-Mo-Fe Alloy (Hastelloy B)", Metallurgical Transactions, 6A:1829-1831 (1975).

24. Siqi Cao and C. R. Brooks, "Recrystallization of the Disordered and Ordered Structure in Ni-20 at.% Mo Alloy", Microstructural Science, 21:277-288 (1994).

25. M. Sanganeria and C. R. Brooks, "The Effect of Cold Working on the Ordering Reaction in $Ni_4Mo$", Microstructural Science, 18:237-253, Editors, T. A. Place, J. D. Braun, W. E. White and G. F. Vander Voort, ASM International, Materials Park, OH, (1990).

26. Fu-Wen Ling, R. S. Irani and R. W. Cahn, "Ordering Kinetic of Cold-Worked $Ni_4Mo$", Materials Science and Engineering 15:1181-1186 (1974).

27. C. R. Brooks and S. Cao, "The Development of the Ordered Structure from Cold Worked Disordered Alpha in $Ni_4Mo$", Philosophical Magazine A, 65:327-353 (1992).

28. J. E. Spruiell and E. E. Stansbury, "X-ray Study of Short-Range Order in Nickel Alloys Containing 10.7 and 20.0 at.% Molybdenum", J. Phys. Chem. Solids 26:811-822 (1965).

29. T. Saburi, E. Kanai and S. Nenno, "Domain Structure in $Ni_4Mo$ Alloy", Journal of the Less-Common Metals, 37:59-70 (1974).

30. J. Lecomte-Beckers, "Study of Solidification Features of Nickel-Base Superalloys in Relation with Composition", Metallurgical Transactions, 19A:2333-2340 (1988).

31. V. I. Kiriyenko, E. E. Poplavskaya and L. P. Potapov, "Influence of Alloying Elements on Ordering in Nickel-Molybdenum Alloys", Phys. Met. Metall., 33:12360-1266 (1972).

32. H. H. Uhlig and R. W. Revie, Corrosion and Corrosion Control, John Wiley and Sons Inc. New York (1985).

33. H. M. Tawancy, "Effect of Cr on the Ordering Behavior and Ductility of an Ni-$Ni_4Mo$ Alloy", Metallurgical Transactions, 23A:1892-1833 (1992).

34. K. Vasudevan and E. E. Stansbury, "Influence of Chromium on Ordering of $Ni_4Mo$", Scripta Metallurgica, 19:1101-1106 (1985).

35. J. Kolts, J.B. C. Wu and A. I. Asphahani, "Highly Alloyed Austenitic Materials for Corrosion Service", Met. Prog. 25-36 (1983).

36. J. A. Shields, Jr., "Surface Engineering of Refractory Metals and Alloys", ASM Handbook, 10th Edition, Vol. 5, Surface Engineering, pp. 856-862 (1990).

37. H. M. Tawancy, "Ductilization of Ni-$Ni_4Mo$ Alloys by Boron Additions", Metallurgical Transactions, 22A:3067-3071 (1991).

38. S. K. Das, L. A Davis, J. R. Y. Wang, and D. Kapoor, "Ni-Mo-B Alloys: Metallic Glass to Ductile Crystalline Solid," Source unknown.

39. W. Betteridge and J. Heslop, The Nimonic Alloys, Crane, Russak and Company, New York (1974).

40. R. B. Herchenroeder, G. Y. Lai and K. V. Rao, "A New, Wrought, Heat Resistance Ni-Cr-Al-Fe-Y Alloy", J. Met., 35:16-22 (1983).

41. A. Choudhury, H. P. Kao, C. R. Brooks and C. L. White, "Auger Analysis of the Fracture Surface of Ordered $Ni_4Mo$", Scripta Metallurgica, 22:1057-1062 (1988).

42. C. R. Brooks and M. Sanganeria, "Intergranular Fracture Along Migrated Boundaries in Ordered $Ni_4Mo$", Scripta Metallurgica, 22:1683-1688 (1988).

43. E. E. Stansbury, "Kinetics of the SRO-LRO Transformation in $Ni_4Mo$, High-Temperature Ordered Intermetallic Alloys", High-Temperature Ordered Intermetallic Alloys, pp. 93-107, Editors, C. C. Koch, C. T. Liu and N. S. Stoloff, Mateial Research Society, Pittsburgh Pennsylvania (1985).

44. H. H. Kao, "Dislocation Structure, Deformation Structure, Strengthening Mechanisms and Embrittlement Cause of Ordered $Ni_4Mo$ Alloy," Ph.D., Dissertation, University of Tennessee, (1986).

45. D. J. Tillack, J. M. Manning and J. R. Hensley, "Heat Treating of Nickel and Nickel Alloys", ASM Handbook 10th Edition, Vol. 4, Heat Treating, pp. 907-912 (1990).

46. R. S. Irani, Fu-wen Ling and R. W. Cahn, "Domain Structures and Hardening in Ordered $Ni_4Mo$", Metallography 6:141-153 (1973).

47. E. Ruedl, P. Delavignette and S. Amelinckx, "Electron Microscopic Study of the Defect Structure due to Ordering in the Alloy $Ni_4Mo$", Mat. Res. Bull., 2:1045-1054 (1967).

48. S. Cao, C. R. Brooks and L. Allard, "An in situ Transmission Electron Microscopy Study of Ordering in a Splat Cooled Ni 20 at.% Mo Alloy", Microstructure Characterization, 34:87-95 (1995).

49. E. V. Kozlov and V. M. Kushnarenko, "Crystallographic X-ray Analysis of the Order-Disorder Phase Transition in the Alloy $Ni_4Mo$", Phys. Met. Metall., 46:80-85 (1978).

50. K. Vasudevan, H.P. Kao, C.R. Brooks and E.E. Stansbury, "Domain Coarsening by Grain Boundary Migration in Ordered $Ni_4Mo$," Ed., G.W. Bailey, Proceedings of the 44th Annual Meeting of the Electron Microscopy Society of America, San Francisco Press, Inc. (1986).

51. M. Sundararaman, S. Banerjee and H. Wollenberger, "Order-Disorder Transformations in $Ni_4Mo$ under Self Ion Irradiation," Acta Metall. Mater., 43:107-119 (1995).

52. K. Vasudevan, H.P. Kao and C.R. Brooks, "Kinetics of Domain Growth in Ordered $Ni_4Mo$," Metallurgical Transactions A, 19:941-952 (1988).

53. R. D. Ridder, G.V. Tendeloo and S. Amelinckx, "A Cluster Model for the Transition from the Short-Range Order to the Long Range Order State in F.c.c. Based Binary Systems and its Study by Means of Electron Diffraction," Acta Crystallographica, A32:216-224 (1976).

54. K. Vasudevan, E. E. Stansbury and C. R. Brooks, "Domain Coarsening at Grain Boundaries in Ordered $Ni_4Mo$," Acta Metall. Mater., 40:2113-2122 (1992).

55. G. V. Tendeloo and S. Amelinckx, "Lattice Relaxation at Glide Antiphase Boundaries and Stacking Faults in $Ni_3Mo$ and $Ni_4Mo$," phys. stat. sol. (a) 27:93-98 (1975).

56. H. M. Tawancy, "Formation on the $DO_{22}$-Type Superlattice during Long-Range Ordering to $Ni_4Mo$ in a Ni-Mo Alloy," Scripta Metallurgica, 18:343-346 (1984).

57. P. R. Okamoto and G. Thomas, "On Short Range Order and Micro-Domains in the $Ni_4Mo$ System," Acta Metallurgica, 19:825-841 (1971).

58. N. Sridhar, "Behavior of Nickel-base Alloy in Corrosion Enviroments", Metals Handbooks 9th Edition, Vol. 13, Corrosion, pp. 643-647 (1989).

59 . Hastelloy Alloy B-2, Haynes, Corrosion-resistant Alloy, Haynes, International Inc. (1987).

60. "ASTM A262 Practice A," Annual Book of ASTM Standards, Vol. 03.02, ASTM, Philadelphia, PA (1994).

61. "ASTM C5-87," Annual Book of ASTM Standards, Vol. 03.02, ASTM, Philadelphia, PA (1994).

62. "ASTM G-30," Annual Book of ASTM Standards, Vol. 03.02, ASTM, Philadelphia, PA (1994).

6.3. Metals Handbook Ninth Edition, Vol. 13, Corrosion, ASM International, Metals Park, OH (1987).

64. W. B. Snyder and C. R. Brooks, pp.275, Editors by B.H. Kear, C.T. Sims, N.S. Stoloff, and J.H. Westbrook, Ordered Alloys, Baton Rouge, LA, Claitor's Publishing Division (1970).

65. P. Villars, A. Prince, and H. Okamoto, Handbook of Ternary Alloy Phase Diagrams, 4:4046-4066, ASM International, Materials Park, OH (1995).

66. D. S. Miracle, K. A. Lark, V. Srinivasan, and H. A. Lipsitt, "Nickle-Aluminum-Molybdenum Phase Equilibria," Metallurgical Transactions A, 15A:481-486 (1984).

67 K. Vasudevan, "The Effect of 0-4 wt.% Chromium on Transformations of a Phase Ni-Mo-Cr Alloys with Nickle-Molybdenum Atom Ratio Equal to 4:1," M.S. Thesis, University of Tennessee (1982).

68. K. A. Williams, D. S. Miracle and H. A. Lipsitt, "Partitioning and Precipitation of TCP Phase in Rapidly Solidified Alloys, Rapid Solidification Processing Principles and Technologies, II," Ed. by R. Mehrabian, B.H. Kear and M. Cohen, Reston, Claitor's Publishing Division, Virginia (1980).

69. D. A. Porter and K. E. Easterling, "Phase Transformations in Metals and Alloys," Chapman and Hall, New York (1991).

70. M. Yamamoto, S. Nenno, M. Futamoto, and S. Nakamura, "Field-Ion Microscope Study of Early Stages of Ordering in $Ni_4Mo$ Alloy," Japanese Journal of Applied Physics, 11:437-444 (1972).

71. R. De Ridder, G. Van Tendeloo, and S. Amelinckx, "A Cluster Model for the Transition fron the Short-Range Order to the long-Range order state in F.c.c. Based Binary Systems and its Study by Means of Electron Diffraction," Acta Crystallographica, A32:216-224 (1976).

72. S. Banerjee, K. Urban and M. Wilkens, proc. Int. conf. Solid-Solid Phase Treansformations, A.I.M.E. Warrendale, pp. 311, Pittsburgh, PA (1982).

73. B. Chakravarti, E. A. Starke, C. J. Sparks, and R. O. Williams, "Short Range Order and the Development of Long Range Order in $Ni_4Mo$," J. Phys. Chem. Solids, 35:1317-1326 (1974).

74. P. L. Martin and J. C. Willams, "Long Range Order in $Ni_3Mo$ Based Ternary Alloys-I. Isothermal Aging respones," Acta Metall, 32:1681-1693 (1984).

75. P. L. Martin and J. C. Willams, "Long Range Order in $Ni_3Mo$ Based Ternary Alloys-II. Coherent Phase Solvii," Acta Metall, 32:1695-1702 (1984).

76. E. Ruedl, P. Delavignette, and S. Amelinckx, "Electron Diffraction and Electron Microscopic Study of Long- and Short-Range Order in $Ni_4Mo$ and of the Substructure Resulting from Ordering," phys. stat. sol., 28:305-328 (1968).

77. P. R. Okamoto and G. Thomas, "On Short Range Order and Micro-Domains in the $Ni_4Mo$ System," Acta Metallurgica, 19:825-841 (1971).

78. M. Sundararaman, S. Banerjee and H. Wollenberger, "Order-Disorder Transformations in $Ni_4Mo$ underSelf Ion Irradiation," Acta Metall. Mater., 43:107-119 (1995).

79. J. P. Chevalier and W.M. Stobbs, "Short-Range Order and the Disorder-Order Transformation in Stoichiometric $Ni_4Mo$," Scripta Metallurgica, 22:1197-1217 (1979).

80. S. Branerjee, K. Urban, and M. Wilkens, "Order-Disorder Transformation in $Ni_4Mo$ under Electron Irradiation in A High-Voltage Electron Microscope," Acta Metall., 32:299-311 (1984).

81. G. Thomas and M. J. Goringe, Transmission Electron Microscopy of Materials, John Wiley Sons, Inc., New York (1979).

82. G. Van Tendeloo, R. De Ridder, and S. Amelinckx, "The $DO_{22}$ Intermediate Phase in the Ni-Mo System," phys. stat. sol. (a), 27:457-468 (1975).

83. G. Van Tendeloo, "Short Range Order Considerations and Development of Long Range Order in Different Ni-Mo Alloys," Materials Science and Engineeing, 26:209-220 (1976).

84. G. Van Tendeloo, J. Van Landuyt, P. Delavignette, and S. Amelinckx, "Compositional Change Associated with Periodic Antiphase Boundaries in the Intial Stages of Ordering in $Ni_3Mo$," phys. stat. sol. (a), 25:697-707 (1974).

85. M. Fahrmann, P. Fratzl, O. Paris, E. Fahrmann and W. C. Johnson, "Influence of Coherency Stress on Microstructural Evolution in Model Ni-Al-Mo Alloys," Acta Metall. Mater., 43:1007-1022 (1995).

86. K. A. Williams, D. B. Miracle and H. A. Lipsitt, "Partitioning and Precipitation of TCP Phases in Rapidly Solidfied Alloys," pp. 129-134, Rapid Solidification Processing Principles and Technologies, II, Ed. by, R.Mehrabian, B.H. Kear, and M.Cohen, Baton Rouge, Claitor's Publishing Division (1980).

87. E. H. Aigeltinger, S. R. Bates, R. W. Gould, J. J. Hren and F. N. Rhines, "Phase Equilibria in Rapidly Solidified Nickel Rich Ni-Mo-Al Alloy," pp. 291-305, Rapid Solidification Processing Principles and Technologies, Ed. by, R. Mehrabian, B. H. Kear, and M. Cohen, Baton Rouge, Claitor's Publishing Division (1977).

88. K. Vasudevan, "Transmission Electron Microscopy Study of Phase Transformations in Ternary $Ni_4Mo$-based Alloys Containing 0 to 4 Weight Percent Chromium," Ph.D Dissertation, The University of Tennessee (1986).

89. M. Yananoto, s.Nenno, T. Saburi, and Y. Mizutani, Trans. Japanese Inst. of Metals, 11:120-126 (1970).

90. A. G. Khachaturyan, "The Problem of Symmetry in Statistical Thermodynamics of Substitutional and Interstitial Ordered solid Solutions," phys. stat. sol., (b), 6:9-37 (1973).

91. N.S.Mishra and S. Ranganathan "Electron Microscopy and Diffraction of Ordering in a Ni-25 wt.% Mo Alloy," Materials Science and Engineering, A150:75-85 (1992).

92. J. E. Hatch, Aluminum Properties and Physical Metallurgy, American Society for Metals, Metals Park, Ohio, 1984.

93. Dennya A. Jones, Principles and Prevention of Corrosion, New York, Macmillan Publishing Company, 1992.

94. R. A. Buchanan and J. G. Kim, "Chloride-Induced Localized Corrosion of $Fe_3Al$-Type Iron Aluminides: Beneficial Effects of Cr and Mo Additions," High Temperature Ordered Intermetallic Alloys IV, Editors: L.A. Johnson, D.P. Pope, and J.O. Stiegler, Materials Research Society, Pittsburgh, Pennsylvania 1991.

# VITA

Ye-Lin Shen was born on May 27. 1960, in Taiyuan city, Shanxi province, China. In June, 1978, she graduated from Jin Shan High School as the Salutatorian of her class. In the July 1978, she began her undergraduate study at Taiyuan University of Technology with a major of Physical Metallurgy and Metallography at the Secondary Mechanical Engineering (now Materials Science and Engineering) Department. She received her Bachelor of Physical Metallurgy and Metallography in June 1982. In August 1982, she joined the R&D team at Shanxi Central Power Lab where she worked for more than 5 years in the Metallogrphy Group. She was leader of young activity in Shanxi Central Power Lab. In August 1994, she entered the master's program in Metallurgical Engineering at the University of Tennessee, Knoxville. Her Master of Science degree was received in August 1996. She is a member of ASM and TMS.